

# **ENHANCED TRANSPORT PHENOMENA IN CO<sub>2</sub> SEQUESTRATION AND CO<sub>2</sub> EOR**

**Rouhollah Farajzadeh**

پدیده های انتقال پیشرفته در فرآیندهای ذخیره سازی دی اکسید کربن و ازدیاد  
برداشت نفت با دی اکسید کربن

روح اله فرج زاده



# **ENHANCED TRANSPORT PHENOMENA IN CO<sub>2</sub> SEQUESTRATION AND CO<sub>2</sub> EOR**

## **Proefschrift**

ter verkrijging van de graad van doctor  
aan de Technische Universiteit Delft  
op gezag van de Rector Magnificus prof. dr. ir. J. T. Fokkema  
voorzitter van het College voor Promoties  
in het openbaar te verdedigen op dinsdag 2 juni 2009 om 10:00 uur

**door**

**Rouhollah FARAJZADEH**

Master of Science in Petroleum Engineering, Delft University of Technology, The Netherlands

&

Bachelor of Science in Petro-Chemical Engineering, Tehran Polytechnic, Iran

Geboren te Ahar, Iran

## **Dit proefschrift is goedgekeurd door de promotoren**

Prof. dr. P. L. J. Zitha

en

Prof. dr. J. Bruining

## **Samenstelling promotiecommissie**

Rector Magnificus

Prof. dr. P. L. J. Zitha

Prof. dr. J. Bruining

Prof. dr. P. K. Currie

Prof. dr. A. Firoozabadi

Prof. dr. W. R. Rossen

Dr. R. Krastev

Dr. W. M. Schulte

Voorzitter

Technische Universiteit Delft, promotor

Technische Universiteit Delft, promotor

Technische Universiteit Delft

Yale University, VS

Technische Universiteit Delft

NMI Naturwissenschaftliches und Medizinisches Institut an  
der Universität Tübingen, Duitsland

Shell International E&P

The work described in this thesis has been carried out in the group of Petroleum Engineering at Delft University of Technology, Faculty of Civil Engineering and Geosciences. This research was financially supported by DelftEarth Research Center and by Shell International Exploration and Production. A travel grant was provided by Max Planck Institute of Colloid and Interface Sciences.

ISBN: 978-90-9024-337-5

Copyright © 2009 R. Farajzadeh

Printed by Print & Design House Co., Tehran, Iran

Cover design by srnt110@gmail.com

Picture: [www.elephantjournal.com](http://www.elephantjournal.com)

To those, who care about Peace, Humanity and Science

**ONENESS OF MANKIND**

Human beings are members of a whole,  
In creation of one essence and soul.

If one member is afflicted with pain,  
Other members uneasy will remain.

If you have no sympathy for human pain,  
The name of human you cannot retain.

-----

Once I was complaining about not having shoes,  
I saw a man who didn't have a leg.

*Sa'di, Persian poet of the 13<sup>th</sup> century*



# CONTENTS

<b>Chapter 1: Introduction: CO<sub>2</sub> Storage &amp; CO<sub>2</sub> EOR</b>	1
1.1. GLOBAL WARMING AND THE ROLE OF CO <sub>2</sub> SEQUESTRATION	2
1.2. CO <sub>2</sub> SEQUESTRATION IN AQUIFERS	4
1.3. CO <sub>2</sub> ENHANCED OIL RECOVERY	5
1.4. CO <sub>2</sub> FOAM AS A PROFILE MODIFIER	6
1.5. OBJECTIVES OF THE THESIS	7
1.6. OUTLINE OF THE THESIS	8
1.7. REFERENCES	9
<b>PART I: MASS TRANSFER ASPECTS OF CO<sub>2</sub> SEQUESTRATION</b>	
<b>Chapter 2: Mass Transfer of CO<sub>2</sub> into Water, Oil and Surfactant Solutions</b>	13
2.1. INTRODUCTION	14
2.2. EXPERIMENTS	15
2.2.1. Experimental set-up	15
2.2.2. Materials and Methods	15
2.2.3. Experimental procedure	16
2.3. PHYSICAL MODEL	17
2.3.1. Formulation	17
2.3.2. Equations	18
2.3.3. Analytical solution	19
2.4. RESULTS AND DISCUSSION	20
2.4.1. Pressure decline	20
2.4.2. Deviation from the square root of time	21
2.4.3. Estimated diffusion coefficients	22
2.4.4. Influence of surfactant	24
2.4.5. CO <sub>2</sub> mass transfer into oil	25
2.5. PROPOSED MECHANISMS	25
2.6. CONCLUSIONS	26
2.7. NOMENCLATURE	27
2.8. REFERENCES	27
<b>Chapter 3: Modeling of Natural Convection Flow of CO<sub>2</sub> in Water</b>	29
3.1. INTRODUCTION	30
3.2. NUMERICAL MODEL	31
3.2.1. Formulation	31
3.2.2. Governing equations	33

3.2.3. Boundary and initial conditions	34
3.2.4. Henry's law (CO <sub>2</sub> solubility) at the interface	35
3.2.5. Numerical scheme and solution procedure	36
3.3. EXPERIMENTAL	36
3.3.1. Materials	36
3.3.2. Set-up and procedure	36
3.4. RESULTS AND DISCUSSION	37
3.4.1. Experimental observations	37
3.4.2. Results of the model	38
3.5. CONCLUSIONS	43
3.6. NOMENCLATURE	43
3.7. REFERENCES	44
<b>Chapter 4: Density-Driven Natural Convection of CO<sub>2</sub> in Aquifers</b>	47
4.1. INTRODUCTION	48
4.2. EXPERIMENTAL	49
4.3. NUMERICAL MODEL	50
4.3.1. Formulation	50
4.3.2. Governing equations	50
4.3.3. Dimensionless form of the equations	52
4.3.4. Boundary and initial conditions	52
4.3.5. Solution procedure	53
4.4. RESULTS AND DISCUSSION	53
4.4.1. Effect of Rayleigh number	55
4.4.2. Effect of aspect ratio	59
4.4.3. Growth of the disturbance	60
4.5. COMPARISON WITH BULK RESULTS	62
4.6. CONCLUSIONS	63
4.7. NOMENCLATURE	64
4.8. REFERENCES	65
<b>PART II: FOAM FILMS</b>	
<b>Chapter 5: Foam Films Stabilized with an Alpha Olefin Sulfonate (AOS) Surfactan</b>	69
5.1. INTRODUCTION	70
5.2. MATERIALS AND METHODS	71
5.3. RESULTS AND DISCUSSION	75
5.4. CONCLUSIONS	81
5.5. REFERENCES	81

---

<b>Chapter 6: Gas Permeability of Foam Films Stabilized with AOS</b>	83
6.1. INTRODUCTION	84
6.2. GAS PERMEABILITY OF SINGLE SURFACTANT MONOLAYERS	85
6.2.1. Simple diffusion theory	86
6.2.2. Energy barrier theory	87
6.2.3. Density fluctuation and accessible area theories	88
6.3. GAS PERMEABILITY OF FOAM FILMS	91
6.3.1. Sandwich model	91
6.3.2. Nucleation theory of fluctuation formation of holes	92
6.3.3. Freely standing film diffusion theory	95
6.4. EXPERIMENTAL	98
6.4.1. Principle and set-up	98
6.4.2. Materials	99
6.5. RESULTS AND DUSCUSSION	100
6.5.1. Effect of NaCl concentration	100
6.5.2. Effect of surfactant concentration	102
6.5.3. Effect of temperature	104
6.6. CONCLUSIONS	105
6.7. REFERENCES	106
<b>PART III: FOAM IN POROUS MEDIA</b>	
<b>Chapter 7: Effect of Gas Type on Foam Flow in Porous Media</b>	111
7.1. INTRODUCTION	112
7.2. EXPERIMENTAL	113
7.2.1. CT Imaging	113
7.2.2. Materials	114
7.2.3. Experimental set up	115
7.2.4. Experimental procedure	117
7.3. RESULTS	118
7.3.1. Low-pressure foam development	118
7.3.2. High-pressure foam development	123
7.4. GENERAL DISCUSSION	127
7.5. CONCLUSIONS	132
7.6. REFERENCES	132
<b>Chapter 8: Foam Assisted Enhanced Oil Recovery (EOR)</b>	137
8.1. INTRODUCTION	138

8.2. FOAM STABILITY	139
8.2.1. Disjoining pressure	139
8.2.2. Effect of oil on foam stability	140
8.3. EXPERIMENTS	147
8.3.1. Calculation of oil saturation	147
8.3.2. Experimental procedure	147
8.4. RESULTS AND DISCUSSION	148
8.4.1. Low pressure experiments	149
8.4.2. Supercritical CO <sub>2</sub> experiments	153
8.5. CONCLUSIONS	157
8.7. REFERENCES	158
<b>Chapter 9: Summary &amp; Conclusions</b>	161
9.1. PART I: MASS TRANSFER ASPECTS OF CO <sub>2</sub> SEQUESTRATION	161
9.2. PART II: FOAM FILMS	162
9.3. PART III: FOAM IN POROUS MEDIA	163
9.4. IMPLICATIONS FOR EOR	163
<b>Appendix A: Solution of the MODIFIED Fick's Law</b>	165
<b>Appendix B: Numerical Scheme of Natural Convection in Porous Media</b>	171
<b>Appendix C: Derivation of Foam Film Permeability Coefficient</b>	175
<b>Synopsis van het proefschrift</b>	179
چکیده پایان نامه	181
<b>Acknowledgements</b>	185
<b>Scientific Contribution</b>	187
<b>About the author</b>	191

---

# Chapter 1

## INTRODUCTION: CO<sub>2</sub> STORAGE & CO<sub>2</sub> EOR

---

### ABSTRACT

*The growing concern about global warming has increased interest in the geological storage of carbon dioxide (CO<sub>2</sub>), with or without simultaneous production of fossil fuels. This thesis is confined to CO<sub>2</sub> storage in aquifers and extra benefits from CO<sub>2</sub> or CO<sub>2</sub> foam enhanced oil recovery (EOR) in water-flooded reservoirs. From the fundamental point of view the focus is on the mass transfer mechanisms that play role in these processes. We consider the rate of transfer between the bulk gas phase and bulk liquid phase and the transfer through thin liquid films separating the two phases. Chapters 2-4 are concerned with enhanced transport of CO<sub>2</sub> into bulk liquid (water or oil) and porous media saturated with these liquids. Chapters 5 and 6 describe the physico-chemical characteristics of; and transport properties in, thin liquid films (lamellae) stabilized with an Alpha Olefin Sulfonate (AOS) surfactant. Chapters 7 and 8 are devoted to CO<sub>2</sub> foam flow in porous media, under sub- and supercritical conditions, in the absence and presence of oil respectively. Then general conclusions are presented in Chapter 9.*

**KEYWORDS:** *CO<sub>2</sub>, CO<sub>2</sub> sequestration, CO<sub>2</sub> EOR, CO<sub>2</sub> foam, Porous media, Aquifer, Surfactant, Transport phenomena, Foam films, Mass transfer, Modeling, Experiments*

### 1.1. GLOBAL WARMING AND THE ROLE OF CO<sub>2</sub> SEQUESTRATION

An ongoing controversy persists with the cause of the *global warming* in the scientific community. According to the United Nations (UN) report in 2007, human activities and so-called greenhouse effects are very likely (with the probability of over 90%) the source of global warming [1,2]. The idea is inspired on the increasing amount of greenhouse gases (e.g., CH<sub>4</sub>, CO<sub>2</sub>, H<sub>2</sub>O, etc.) in the atmosphere and the corresponding temperature rise measured over the last hundred years [1]. Nonetheless, other scientists dismiss the idea and sustain that the global warming could be caused by increased solar activity such as a massive eruption [3]. Regardless of the causing phenomena, the publicity of the issue and growing concerns over it have increased the number of research projects devoting to the global warming particularly over the last decade.

If greenhouse gases are responsible for the global temperature rise, their emission to the atmosphere should be reduced accordingly [4-9]. Compared to the other greenhouse gases CO<sub>2</sub> is the most important one as it is responsible for about 64% of the enhanced greenhouse effects as inferred from its radiative forcing [10]. CO<sub>2</sub> concentration has increased from around 280 parts per million by volume (ppmv) in the 18<sup>th</sup> century to over 360 ppmv by 1997. Half of this increase has occurred since the mid 1960's [1,10,11]. Fossil fuels supply about 86% of the current global energy demand and account for 75% of current CO<sub>2</sub> emissions [1,9,12]. According to the IPCC report, achieving the European Union (EU) target of no more than 2°C temperature increase would require an emission reduction of between 85% and 50% starting from 2000 levels by 2050 [1]. Achieving long term stabilization at a doubling of pre-industrial levels (approximately 550 ppmv CO<sub>2</sub>), would require emissions to be approximately the same as in 2000 or lower despite any growth that would otherwise occur. According to the IPCC report this would result in a warming of 2.8 to 3.3°C [1].

One way to reduce CO<sub>2</sub> emission will be to replace fossil fuels by clean sources of energy. However, a rapid move away from oil, natural gas and coal is unlikely to be achievable without serious disruption to the global economy. Therefore, an achievable option is to reduce CO<sub>2</sub> emissions. IPCC report suggests the following options [1]:

- Improve energy efficiency by reducing the fossil fuel consumption
- Switching from high carbon to low carbon fuels
- Increased use of low or near zero carbon fuels
- Sequester CO<sub>2</sub> through the enhancement of natural, biological sinks
- CO<sub>2</sub> capture and storage (CCS)

In selecting the mitigation option one should take into account variety of factors such as the potential and capacity of the option, social acceptance, environmental side effect and more importantly the associated costs [1,13].

One potential solution to reduce the amount of emitted CO<sub>2</sub> in the atmosphere is to store it in the geological formations. Geological sequestration means “the capture of CO<sub>2</sub> directly from anthropogenic sources and disposing of it deep into the ground for geologically significant periods of time” [14]. These geological formations include

- Deep saline aquifers
- Depleted oil and gas reservoir
- CO<sub>2</sub> driven enhanced oil recovery
- Deep unmineable coal seams
- CO<sub>2</sub> driven enhanced coal bed methane (ECBM) recovery
- Deep saline filled basalts formation and other formations

The following mechanisms may contribute to the sequestration of CO<sub>2</sub> in the geological formations [15]:

*Hydrodynamic trapping:* When CO<sub>2</sub> is injected into a geological formation CO<sub>2</sub> will (eventually) accumulate under a low permeable cap rock because of the capillary forces. This mechanism relies on the physical displacement of pore fluids. The crucial concern for hydrodynamic trapping is the possible leakage of CO<sub>2</sub> through the cap rock. This problem becomes more serious when CO<sub>2</sub> alters the wettability of the rock or reacts chemically with it reducing its mechanical integrity.

*Dissolution trapping:* This occurs when CO<sub>2</sub> dissolves in the fluids present in the formation. The rate of CO<sub>2</sub> dissolution determines how fast CO<sub>2</sub> can be stored. Chapters 2-4 of this thesis mainly focus on this mechanism. We argue that CO<sub>2</sub> dissolution may increase the fluid density and lead to accelerated mass transfer rates.

*Mineralization-based trapping:* CO<sub>2</sub> reacts with minerals in the rock, other solutes in the formation fluids, or the formation fluids themselves. It sometimes forms stable minerals called carbonates in a process called mineralization. This is the most permanent form of trapping, since the CO<sub>2</sub> has been chemically incorporated into nonreactive minerals, and can no longer enter the atmosphere without undoing those chemical reactions.

*Chemical sorption in coals:* In coal seams, methane molecules are sorbed within the coal matrix; however, since the chemical bond between the coal and CO<sub>2</sub> is favorable, CO<sub>2</sub> will replace

methane when it is injected into a coal layer. This mechanism is referred to as CO<sub>2</sub> sorption on coal. Sorption of CO<sub>2</sub> causes coal swelling and can have a detrimental effect on its permeability [16].

Table 1.1 presents the range of capacity estimates and the main trapping mechanisms for different geological sequestration methods of CO<sub>2</sub>. The data are collected from different sources including Refs. [17-23].

**Table 1.1:** Summary of geological CO<sub>2</sub> storage capacity (adapted from Ref. [15])

Formation	Trapping mechanism(s)	The US (Gt CO <sub>2</sub> )	Worldwide (Gt CO <sub>2</sub> )
Saline Aquifers	Hydrodynamic, dissolution, mineralization	3630	9500
Depleted Oil + Gas Reservoirs	Hydrodynamic, dissolution, mineralization	12+35	120+700
Deep Unmineable Coal Seams	Primarily chemical adsorption	30	140
Deep Saline Filled Basalts Formations	Hydrodynamic, dissolution, mineralization	240	NA
Other (Caverns, Organic Shales, gas hydrates etc.)	Various	NA	NA

This thesis confines its interest in the sequestration of CO<sub>2</sub> in the *saline aquifers* and more specifically on the mass transfer between CO<sub>2</sub> and the brine. Therefore, some introductory explanations are provided about this topic in the next section.

## 1.2. CO<sub>2</sub> SEQUESTRATION IN AQUIFERS

Saline aquifers are the most abundant subsurface formations with large storage capacities. A saline aquifer is a geological formation with a sufficient porosity and permeability which contains water with large amounts of dissolved solids [15]. Due to the presence of these solids, the water in aquifers (*brine* or *formation water*) is not suitable for industrial or drinking purposes. Nevertheless, presence of large volumes of water and high pressures of the aquifers make them an excellent candidate for storing CO<sub>2</sub>.

For CO<sub>2</sub> storage in aquifers the following issues should be considered [24]:

- the rate at which CO<sub>2</sub> can be disposed (inclusive dissolution of CO<sub>2</sub> into brine),
- the available storage capacity,
- the presence of cap rock of low permeability to prevent leakage,

- identification and characterization of suitable aquifer formations and cap rock structures,
- uncertainty and possibility of failure due to incomplete knowledge of subsurface conditions and processes,
- sensitivity of the injection facilities towards corrosion.

When CO<sub>2</sub> is injected into an aquifer the competition between viscous, capillary and buoyancy forces determines the flow pattern. Due to buoyancy forces CO<sub>2</sub> migrates upwards and is trapped under the cap rock due to the capillary forces. An interface between a CO<sub>2</sub> rich phase and brine exists. Then CO<sub>2</sub> dissolves into brine by molecular diffusion when it is in contact. The dissolution of CO<sub>2</sub> increases the density of brine [25]. This density increase together with temperature fluctuations in the aquifer (which may only partially be compensated by pressure gradients [26]) destabilize the CO<sub>2</sub>-brine interface and accelerate the transfer rate of CO<sub>2</sub> into the brine by natural convection [27]. The occurrence of natural convection significantly increases the total storage rate the aquifer since convection currents bring the fresh brine to the top. Natural convection will eventually stop as the brine becomes fully saturated with CO<sub>2</sub>. The quantification of mixing due to convection is the subject of Chapters 2-4 in this thesis.

### **1.3. CO<sub>2</sub> ENHANCED OIL RECOVERY**

An attractive method to reduce the amount of CO<sub>2</sub> is to combine CO<sub>2</sub> sequestration and enhanced oil recovery. Typically only around one third of the oil is produced after primary (natural depletion) and secondary (mainly water flooding) oil recovery methods. Much of the remaining oil is trapped by capillary forces as disconnected blobs, surrounded by water, or as a continuous phase at low saturation with gas occupying the larger fraction of the pore space [28]. As a result, a high water-oil ratio (WOR) occurs in the producing wells and most of the oil remains in the reservoir. Injection of a fluid miscible with oil can reduce the interfacial tension (i.e. capillary forces) in the reservoir. In some regions the hydrocarbon gases produced along with the oil are re-injected to the reservoir to produce part of the oil that is left behind. Nevertheless, in some regions, e.g., North Sea, the enriched hydrocarbon displacement is not an option because the gas is sold [29] and the gas itself is also a valuable source of energy. The alternative can then be CO<sub>2</sub> injection as it combines EOR with removal of CO<sub>2</sub> from the environment. Much CO<sub>2</sub> is produced during operation of an oil field or for providing the energy to compress the produced CO<sub>2</sub>. The advantage of CO<sub>2</sub> is that it can become miscible with oil at lower pressures compared to CH<sub>4</sub> or N<sub>2</sub>. CO<sub>2</sub> injection near critical conditions causes a significant reduction in the capillary forces and therefore the oil is easily displaced towards the production well.

The first industrial CO<sub>2</sub> EOR project was commenced in 1972 in SACROC field in the USA. Currently the petroleum industry operates CO<sub>2</sub> EOR projects in 79 fields. Nearly all of them, 70

miscible and 1 immiscible CO<sub>2</sub> EOR projects were implemented in the USA [30]. Table 1.2 shows the number of active CO<sub>2</sub> EOR projects and their production rates in 2004. CO<sub>2</sub> EOR produces more than 230,000 barrels (~0.3% of the current daily world production) of incremental oil a day by injecting over 76 million cubic meters of CO<sub>2</sub> per day [30,31]. This implies that more than 3 barrels of additional oil is produced for every thousand cubic meter of CO<sub>2</sub> injected. The results of projects from the US indicate that the average incremental oil recovery lies within the range of 4-12% of OIIP while the net volume of injected CO<sub>2</sub> is in the range 10-45% of the volume occupied by the hydrocarbons in the reservoir [32]. The current use of CO<sub>2</sub> for oil recovery is limited by the cost and availability of CO<sub>2</sub>.

**Table 1.2:** Active CO<sub>2</sub> EOR projects and production rates (adapted from Ref. [30])

Location	Project Type	Number	Production rate [bbl/day]
USA	Miscible and immiscible	70 (1)	206000 (105)
Canada	Miscible	2	7200
Turkey	Immiscible	1	6000
Trinidad	Immiscible	5	320

CO<sub>2</sub> can be either miscible or immiscible with the oil in the reservoir. Miscibility is the ability of the crude oil to form a single homogenous phase when mixed with CO<sub>2</sub> in all proportions at a specific temperature and pressure [33]. When CO<sub>2</sub> is directly miscible with oil the interface between the two phases ceases to exist and theoretically the oil recovery factor reaches unity. CO<sub>2</sub> can be indirectly miscible with the oil as explained below. The pressure at which indirect miscible displacement takes place is called Minimum Miscibility Pressure (MMP). The MMP essentially depends on purity of CO<sub>2</sub>, composition of oil and reservoir pressure and temperature. CO<sub>2</sub> is not miscible directly with most of crude oils. For a miscible CO<sub>2</sub> flood, the pressure should be above the MMP. This corresponds to minimum of 800 meter reservoir depth. If the pressure is below MMP only swelling and viscosity reduction happens and the recovery drops drastically compared to the pressure above the MMP, though the process could still be economically attractive.

#### 1.4. CO<sub>2</sub> FOAM AS A PROFILE MODIFIER

A critical problem associated with many secondary and tertiary gas (e.g. CO<sub>2</sub>) EOR processes is the high mobility of the gas (displacing phase) compared to oil (displaced phase). The lower viscosity and density of the gas (even at reservoir conditions) result in unfavorable viscous fingering and gravity segregation. Another problem is the heterogeneity of the reservoir rock. Consequently a large part of the reservoir remains untouched and the sweep efficiency becomes poor. This can be improved by injecting alternating slugs of liquid and CO<sub>2</sub>. If the liquid contains no chemicals the process is called Water Alternating Gas (WAG) and if the liquid contains

surfactant it is called Surfactant Alternating Gas (SAG or SAG foam). The gas and surfactant solution can also be injected continuously (co-injection foam) [e.g. 34-39].

WAG can eventually suffer from viscous instabilities and gravity segregation and therefore has not always been a successful method of controlling the gas mobility. Addition of surfactant into water, however, can potentially overcome the problems encountered in WAG by foaming the gas. Foam reduces the gas mobility by immobilizing or trapping a large fraction of the gas without compromising its efficiency.

Figure 1.1 shows the simulation results of CO<sub>2</sub> EOR (left) and CO<sub>2</sub> foam EOR (right) processes for a North Sea oil field with high permeability (around 7 D). The simulations using models implemented in STARS. Gas and oil saturations are shown after 12 years of pure CO<sub>2</sub> and CO<sub>2</sub> foam injection. In this simulation the residual oil saturation to water injection was assumed to be 0.18. This figure shows the fundamental difference between CO<sub>2</sub> gas and CO<sub>2</sub> foam recovery techniques. While in the case of CO<sub>2</sub> injection, the gas overrides the liquid and breaks through without contacting most of the oil, in the case of CO<sub>2</sub> foam a (semi)-sharp front is formed between CO<sub>2</sub> and liquids in the reservoir and displaces the oil more efficiently. Figure 1.2 compares incremental oil recovery of the two processes after 12 years. Although the oil production in the case of CO<sub>2</sub> foam is delayed (5 years) its ultimate oil recovery is higher than CO<sub>2</sub> gas. Therefore, the key properties of foam in porous media are also subject of this thesis.

### 1.5. OBJECTIVES OF THE THESIS

The objectives of this thesis are the following:

1. To quantify, experimentally and numerically, the mass transfer rate of CO<sub>2</sub> to water, oil and surfactant solutions when CO<sub>2</sub> is put on top of the liquid layer,
2. To investigate the effect of surfactant molecules on the transfer rate of gases through gas-liquid interface,
3. To model natural-convection-enhanced mass-transfer rate of CO<sub>2</sub> to bulk liquid and a saturated porous medium,
4. To measure the transfer rate of gases through foam films (lamellae) and quantify the effects of adsorption of surfactant molecules and surface forces on the transfer rate by varying surfactant and electrolyte concentrations,
5. To compare different literature theories on gas permeability of foam films,
6. To measure the mobility and sweep efficiency of CO<sub>2</sub> and N<sub>2</sub> foams in the absence and presence of oil in porous media.

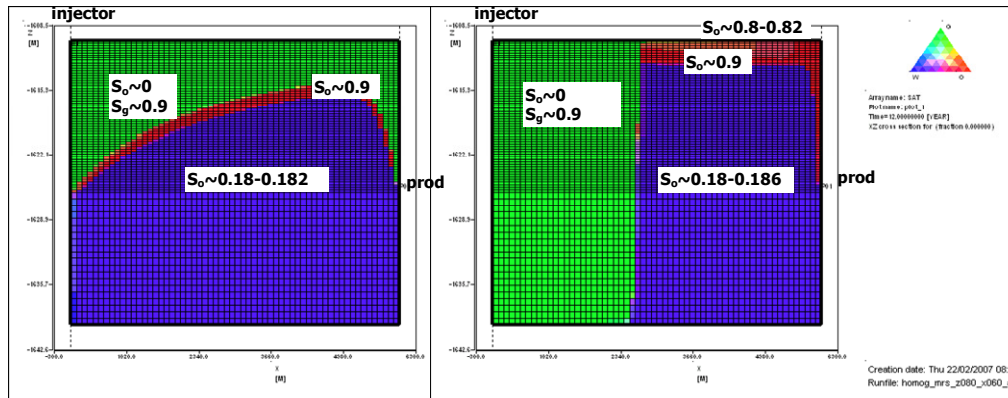


Fig. 1.1: CO<sub>2</sub> gas recovery (left) vs. CO<sub>2</sub> foam (right) recovery

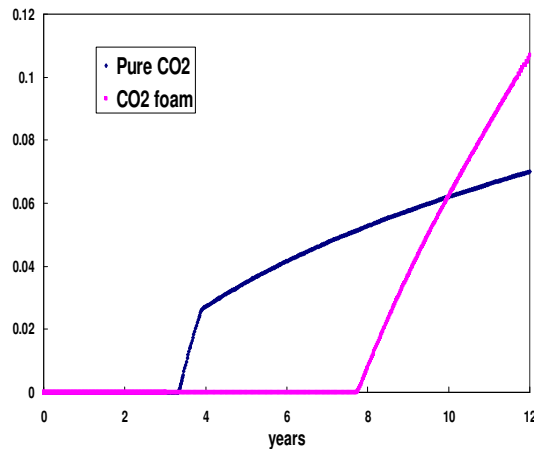


Fig. 1.2: CO<sub>2</sub> gas recovery (left) vs. CO<sub>2</sub> foam (right) recovery

## 1.6. OUTLINE OF THE THESIS

This thesis is based on a number of articles published by the author describing results in the area discussed in previous sections. The thesis consists of three main parts: Part I is concerned with density-driven natural convection and its importance for *CO<sub>2</sub> sequestration in aquifers* (Chapter 2-4). Part II presents a detailed study of an Alpha Olefin Sulfonate (AOS) surfactant with an emphasis on the measurements of the diffusion rate of gases through the *foam films* (Chapter 5&6). Finally Part III discusses the dynamics of *foam in porous media* with and without oil present (Chapter 7&8).

Chapter 2 introduces a simple PVT set-up which was developed to quantify the transfer rate of gases into liquids by tracking the gas pressure. With some preliminary calculations we show that the experimentally measured pressures cannot be modeled by Fick's law with a single diffusion coefficient when CO<sub>2</sub> is put on top of a liquid layer. Furthermore, for first time we present a few experiments highlighting the significance of density-driven natural convection on the transfer rate of CO<sub>2</sub> into oil. This phenomenon could be important to EOR. In Chapter 3 we develop a

theoretical model to simulate the pressure history of the experiments. Chapter 4 introduces the natural-convection concept for a porous medium that is fully saturated with brine.

Chapter 5 deals with the basic properties of an Alpha Olefin Sulfonate (AOS) surfactant. AOS surfactants are widely used in petroleum industry for several reasons such as their low costs and satisfactory foaming and wetting properties. The surface tension and adsorption of the surfactant solution are measured simultaneously with the thickness and contact angle of the foam films made from that surfactant solution by varying the amounts of surfactant and electrolyte (NaCl). This knowledge is taken to explain the unexpected gas-permeability behavior of the foam films stabilized by AOS in Chapter 6. The gas permeability of foam films is important in describing the differences in foaming properties of different gases in the presence and absence of a porous medium.

Chapter 7 discusses experiments to define the foaming properties of CO<sub>2</sub> and N<sub>2</sub> in porous media in the absence of oil. The experiments are done under surfactant alternating gas (SAG) scheme above and below critical point of CO<sub>2</sub> by means of X-ray tomography (CT scan). The mechanisms causing the observed differences are explained in detail. Chapter 8 reports the results of a number of experiments in which porous media with water-flood residual oil saturation are flooded by surfactant followed by a gas (CO<sub>2</sub> or N<sub>2</sub>).

Finally, the main conclusions of the thesis are summarized in Chapter 9.

## 1.7. REFERENCES

1. IPCC special report on Carbon Dioxide capture and storage, Edited by B. Metz, O. Davidson, H. de Coninck, M. Loos, L. Meyer, *Cambridge University Press* (2005).
2. UNFCCC. Climate change information kit. Technical report, United Nations Framework Convention on Climate Change (2002).
3. S. Kroonenberg, “*De menselijke maat; de aarde over tienduizend jaar*”, revised and expanded edition 12, March (2008), in Dutch.
4. K. Pruess and J. Garcia, *Environ. Geol.*, 42 (2002) 282.
5. R.G. Bruant, A.J. Guswa, M.A. Celia, C.A. Peters, *Environmental Science and Technology*, June 1 (2002) 241A..
6. A. Naderi Beni, M. Kühn, R. Meyer, C. Clauser, *Proceedings of the Sino-German Workshop, Goslar, Germany*, 17-20 September 2007.
7. M.I. Hoffert, K. Caldeira, A.K. Jain, E.K. Haites, *Nature*, 395 (1998) 881.
8. C. Green, S. Baksi, M. Dilmaghani, *Energy Policy*, 35(1), (2007) 616.
9. B.S. Fisher et al., *Issues related to mitigation in the long term context*, in *Climate Change 2007: Mitigation. Contribution of Working Group III to the Fourth Assessment Report of the Intergovernmental Panel on Climate Change*, B. Metz, et al., Editors. 2007, Cambridge University Press: Cambridge. p. 169-250.
10. F.M. Orr, *SPE 101630*, SPE Annual Technical Conference and Exhibition, Houston, Texas USA (2004).

11. J. T. Houghton, Y. Ding, D.J. Griggs, M. Noguera, and P. J. van der Linden, editors. *Climate Change 2001: The Scientific Basis*. Cambridge University Press, 2001.
12. <http://www.energy.gov/energysources/fossilfuels.htm>, (US department of energy).
13. S. McCoy, PhD Dissertation, Carnegie Mellon University, Pittsburgh, PA (2008).
14. S. Bachu, *Energy Conversion & Management*, 43, (2002) 87.
15. J.J. Dooley, R. T. Dahowski, C. L. Davidson, M. A. Wise, N. Gupta, S. H. Kim, E. L. Malone, *Carbon dioxide and geological storage*, [www.pnl.gov/gtsp/docs/ccs\\_report.pdf](http://www.pnl.gov/gtsp/docs/ccs_report.pdf), last visited on 17-10-2008.
16. S. Mazumder, P. v. Hemert, J. Bruining, K.H. Wolf, K. Drabe, *Fuel*, 85 (2006).
17. H. Koide, Y. Tazaki, Y. Noguchi, S. Nakayama, *Energy Conversion & Management*, 33(5-8), (1992) 619.
18. S. Bachu, W.D. Gunter, E.H. Perkins, *Energy Conversion & Management*, 35(4), (1994) 269.
19. C.A. Hendriks and K. Blok, *Energy Conversion & Management*, 36, (1995) 539.
20. S. Holloway, *Annual Review of Energy & Environment*, 26, (2001) 145.
21. S.H. Stevens, et al., *Environmental Geosciences*, 8(3), (2001) 200.
22. J. Shaw and S. Bachu, *Journal of Canadian Petroleum Technology*, 41(9), (2002) 51.
23. S. Benson, et al., Underground geological storage, in IPCC Special Report on Carbon Dioxide Capture and Storage, B. Metz, et al., Editors. 2005, Cambridge University Press: Cambridge, U.K.
24. K. Pruess, T. Xu, J. Apps, J. García, *SPE Journal* (2003), SPE 66537.
25. L. Gmelin, in: Gmelin *Handbuch der anorganischen Chemie*, 8. Auflage. Kohlenstoff, Teil C3, Verbindungen. ISBN 3-527-81419-1 (1973).
26. E. Lindeberg and D. Wessel-Berg, *Energy Convers. Mgmt.*, 38, (1997) S229.
27. L.D. Landau and E.M. Lifshitz, *Fluid mechanics, Volume 6 of course of theoretical physics*, translated from Russian by Sykes J.B. and Reid W.H., pp. 212-218, 4<sup>th</sup> Edition, Pergamon Press (1975).
28. P.L. Bondor, *Energy Convers. Mgmt.*, 33, (1992) 579.
29. M.F. Blunt, F.J. Fayers, F.M. Orr, Jr., *Energy Convers. Mgmt.*, 34 (9-11), (1993) 1197.
30. E. Tzimas, A. Georgakaki, C. Garcia Cortes and S.D. Petevs, *Enhanced Oil Recovery using Carbon Dioxide in the European Energy System*, Report EUR 21895 EN, Dec. 2005.
31. K. Jessen, A.R. Kavscek, F.M. Orr, Jr., *Energy Convers. Mgmt.*, 46, (2005) 293.
32. ECL Technology, CO<sub>2</sub> EOR Issues: Phase 1 – Literature Review, DTI SHARP Website, CO<sub>2</sub> Dissemination, May 2001.
33. L.W. Holm, *J. Petr. Tech.*, Pages 817-818, August 1986.
34. G.G. Bernards and L.W. Holm, *SPE Journal*, pp 267-274, September 1964.
35. A.H. Falls, J.J. Musters, J. Ratulowski, SPE 16048, August 1986.
36. G.J. Hirasaki and J.B. Lawson, *SPE Journal*, pp 175-190, April 1985.
37. W.R. Rossen, *Foams in Enhanced Oil Recovery*, In: *Foams: Theory Measurement and Applications*, R.K. Prud'homme and S. Khan (Eds), Marcel Dekker, New York City (1996).
38. A.R. Kavscek and C.J. Radke, *Fundamentals of foam transport in porous media*, In: *Foams: Fundamentals and applications in the Petroleum Industry*, ACS Advances in Chemistry Series, N.242, American Society (1994).
39. S.L. Wellington and H.J. Vinegar, *Surfactant-Induced Mobility Control for Carbon Dioxide Studied with Computerized Tomography*. In: *Surfactant Based Mobility Control – Progress in Miscible Flood Enhanced Oil Recovery*; Smith, D.H., Eds.; ACS Symposium Series 373; American Chemical Society: Washington, 1988; pp.344-358.

## **PART I.**

# **Mass-Transfer Aspects of CO<sub>2</sub> Sequestration**



---

## Chapter 2

# MASS TRANSFER OF CO<sub>2</sub> INTO WATER, OIL AND SURFACTANT SOLUTIONS

---

### ABSTRACT

*The mass transfer of CO<sub>2</sub> into water, oil (nC<sub>10</sub> and nC<sub>16</sub>) and aqueous solutions of Sodium Dodecyl Sulphate (SDS) is experimentally studied using a PVT cell at different initial pressures and a constant temperature (T=25°C). It is observed that initially the transfer rate is much larger than expected from a diffusion process alone. The model equations describing the experiments are based on Fick's law and Henry's law. The experiments are interpreted in terms of two effective diffusion coefficients, one for the early stages of the experiments and the other one for the later stages. The results show that at the early stages the effective diffusion coefficients are one order of magnitude larger than the molecular diffusivity of CO<sub>2</sub> in water. Nevertheless, in the later stages the extracted diffusion coefficients are close to literature values. It is asserted that at the early stages density-driven natural convection enhances the mass transfer. A similar mass transfer enhancement was observed for the mass transfer between gaseous CO<sub>2</sub> rich phase with an oil (n-decane) phase. It is also found that at the experimental conditions studied addition of pure SDS does not have a significant effect on the mass-transfer rate of CO<sub>2</sub> in water.*

**KEYWORDS:** *Mass Transfer, CO<sub>2</sub>, Natural Convection, Effective Diffusion Coefficient, Surfactant*

**Published in:** *Petroleum Science and Technology, 25(12), (2007) 1493.*

## 2.1. INTRODUCTION

The mass transfer of a gas through a gas-liquid interface (with and without monolayers of surfactant) is of great importance in many fields of science and engineering. Examples include CO<sub>2</sub> sequestration, to reduce CO<sub>2</sub> concentration in the atmosphere [1-5], oil recovery [6] and gas absorption [7]. There is a vast literature on the mass transfer between gases and liquids. We confine our interest to the experimental determination of the mass transfer rate of CO<sub>2</sub> into water in a PVT cell. It has been suggested in the literature that natural convection enhances the mass transfer [2,4].

Unfortunately there are only few experimental data in the literature involving mass transfer between water and CO<sub>2</sub> under conditions of natural convection. Lindeberg and Wessel-Berg [2] demonstrated the importance of natural convection for sequestration of CO<sub>2</sub> in aquifers and studied the conditions under which natural convection occurs as a result of CO<sub>2</sub> injection in saline aquifers. They found the following sequence of events: initially the injected CO<sub>2</sub> accumulates under the cap rock. Then, CO<sub>2</sub> dissolves into the reservoir brine by molecular diffusion. As a result, the density of brine increases, and therefore, natural convection occurs. Nevertheless, Lindeberg and Wessel-Berg [2] did not quantify the effects of the natural convection in terms of enhanced mass transfer of CO<sub>2</sub> into the reservoir brine. Yang and Gu [4] studied the mass transfer of CO<sub>2</sub> into water at high pressures and temperatures. They interpreted the experimental results in terms of a modified diffusion equation and found an effective diffusion coefficient for each experiment. The effective diffusion coefficients were two orders of magnitude larger than the molecular diffusion coefficient. However the duration of their experiments were short (*3-4 hours*) and they did not study the long-time behavior of the CO<sub>2</sub> mass transfer into water. Nghiem et al. [5] gave a field example to show that natural convection is an important mechanism in CO<sub>2</sub> sequestration. They also observed downward migration of high-density saturated plumes in their simulations.

When surfactants are added to a quiescent liquid the total resistance to the transfer of gas molecules is the sum of the liquid phase resistance, the gas resistance and the interfacial resistance which arises from the adsorption of surfactant molecules to the interface. It has been shown that the presence of soluble surfactants has no measurable effect on the passage of gas molecules through the gas-liquid interface [8-10]; however, insoluble surfactants can offer resistance to mass transfer [11-15]. To our knowledge the reported experiments in this area are conducted under atmospheric pressure and the effect of surfactants on mass transfer at higher pressures (especially in the cases where diffusion is not the only transport mechanism) apparently has not been reported in the literature.

In this chapter we study the mass transfer of CO<sub>2</sub> into bulk water and surfactant solutions experimentally to avoid the complex adsorption mechanism between surfactants and the porous medium. The emphasis of the first section is on the experimental results and procedure. In order to quantify the results we interpret the results in terms of two effective diffusion coefficients using a modified diffusion equation. However, in Chapter 3 we model the experiments by considering natural convection effects. This chapter adds three contributions to the experimental knowledge base: Firstly, by extending the duration of the experiments we investigate the long-term behavior of CO<sub>2</sub> mass transfer and investigate whether enhanced transfer persists over time or whether it dies out. Secondly, we perform the experiments with an oil phase and show experimentally the enhancement of CO<sub>2</sub> mass transfer to the oil phase. Thirdly, this chapter reports the effect of surfactants at high pressures. In Section 2.2 we describe the experimental setup, materials and experimental procedure. In Section 2.3 we define a model to interpret the experiments and in Section 2.4 the obtained experimental data are incorporated into a physical model. This allows us to obtain two diffusion coefficients for the mass-transfer process of CO<sub>2</sub> through the interface; one for the early stages of the experiments and one for the late stages of the experiments. The possible mechanisms for the observed phenomena are discussed in Section 2.5. We end this chapter with some remarks and conclusions.

## **2.2. EXPERIMENTS**

### **2.2.1. Experimental setup**

The experimental apparatus is shown in Fig. 2.1. It consists of a transparent scaled glass tube with an inner diameter of  $7.0\text{ mm}$ , an outer diameter of  $11.0\text{ mm}$  and a length of  $45.0\text{ cm}$ . The tube was embedded in Teflon at the top and bottom and was sealed with o-rings and fitted inside a stainless steel cylinder. The glass tube has the capability of withstanding pressures up to  $50\text{ bar}$ . To assure that the liquid is stagnant the stainless steel cylinder was mounted into a heavy ( $10\text{ kg}$ ) steel holder. The bottom of the cell was equipped with a valve and a piston pump, which permitted injection of liquid into the cell. The top of the cell was connected to a high-pressure gas cylinder. The gas pressure was measured with a calibrated pressure transducer with an accuracy of  $5\text{ mbar}$ . Moreover, a safety valve was placed at the top part of the setup. A calibrated data-acquisition system was provided to record the pressure and temperature in the cell during the experiment. The experimental data were recorded every  $10\text{ seconds}$  by the computer. To avoid thermal fluctuations the cell was located inside a liquid bath. In all experiments the bath was kept at  $25\pm 0.1^\circ\text{C}$ .

### **2.2.2. Materials and methods**

*Gas:* The gas used to carry out the experiments was 99.98% pure carbon dioxide. CO<sub>2</sub> is highly soluble in water [16], i.e., the Henry constant is  $2980.1\text{ Pa}/(\text{mol}\cdot\text{m}^3)$  [17]. The diffusion coefficient

of CO<sub>2</sub> in water is  $(1.97 \pm 0.10) \times 10^{-9} \text{ m}^2/\text{s}$  [18]. Nitrogen (N<sub>2</sub>) was used to detect possible leakages in the setup.

**Surfactant:** The surfactant used to perform the surfactant experiments was Sodium Dodecyl Sulfate (SDS) with the chemical formula of C<sub>12</sub>H<sub>25</sub>SO<sub>4</sub>Na and a molecular weight of 288 g/mol. It was dissolved in distilled water (pH=5.5±0.1).

Before starting the experiments the Critical Micelle Concentration (CMC) of the surfactant was determined. To that end, solutions of SDS and distilled water with the concentrations of 2, 2.5, 3, 3.5, 4, 5 and 6 mM were prepared. The surface tension of these solutions was measured by the DuNouy Ring method at room temperature. The apparatus was first calibrated with distilled water (the surface tension of distilled water at the room temperature is 72.6 mN/m). The critical micelle concentration of the SDS was measured to be ~3 mM (~0.085 wt%) under our experimental conditions.

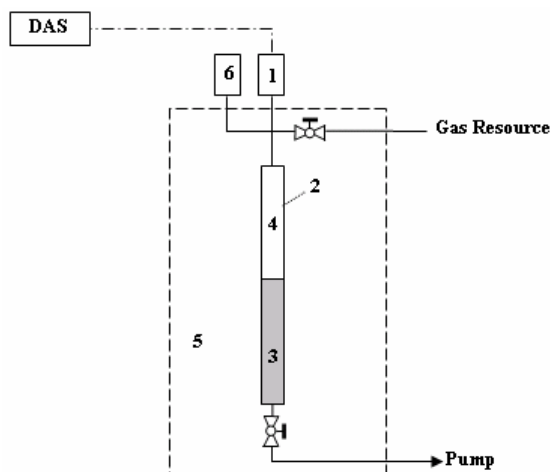


**Fig. 2.1:** Schematic of the experimental setup: (1) Pressure Transducer, (2) Cell, (3) Liquid Phase, (4) Gas Phase, (5) The liquid Bath, (6) Pressure Safety Valve and (7) Data Acquisition System connected to a computer

### 2.2.3. Experimental procedure

In the pressure-depletion experiments, the liquid phase was either distilled water or surfactant solutions of different surfactant concentrations with or without NaCl as salt. The concentration of the surfactant in some experiments was above the CMC and in some experiments below the CMC. For this purpose an appropriate amount of SDS was weighed and dissolved in distilled water. Originally some bubbles were formed at the surface, which collapses after leaving it undisturbed for a few minutes.

Before performing the experiments, the dry cell was filled with nitrogen to a certain pressure to assure that there is no leakage in the system. Figure 2.2 shows the pressure versus time plot for a leakage test. The small fluctuations in the first part of the plot are due to small fluctuations in the temperature and the difference between the temperature of the gas cylinder and the liquid bath. The experimental procedure is as follows:

First, the liquid was injected from the bottom via an accurate piston pump into the cell until it reached the desired level. After that, pumping of the liquid was stopped and the valve at the bottom of the cell was closed. Next CO<sub>2</sub> was slowly injected into the cell from the top, for about 30 seconds. When the CO<sub>2</sub> pressure reached the desired value, the valve was closed and the cell was isolated. This was the starting time of the experiment. Each experiment was run for several days. All the experiments were repeated to show the reproducibility.

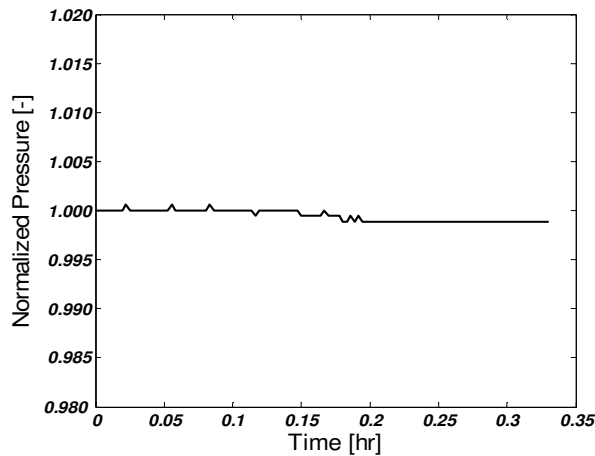


**Fig. 2.2:** Normalized pressure vs. time in a leakage test before starting the experiments

## 2.3. PHYSICAL MODEL

### 2.3.1. Formulation

A numerical model has been developed to describe the mass transfer based on Fick's law taking into account the solubility of the gas by Henry's law. The geometry of the problem under scrutiny is depicted in Fig. 2.3. The vessel consists of an upper column filled with gas and a lower column filled with a stagnant liquid layer. The model disregards convection and capillary effects. Moreover, it is assumed that the density of CO<sub>2</sub> in the gas phase only depends on time (i.e. pressure). We disregard both water evaporation (the contribution of water vapor to the gas pressure is 0.03 bar at 25°C [19]) and water swelling due to CO<sub>2</sub> dissolution. Consequently we assume that the boundary remains fixed. The CO<sub>2</sub> concentration at the liquid surface is related to the gas pressure by assuming instantaneous thermodynamic equilibrium at the interface. We assert that the transfer of gas molecules through the gas-liquid interface can be described as a one dimensional

unsteady-state diffusion process, i.e., by Fick's law. We take  $z$  positive in the downward direction ( $z=0$  at the gas-liquid interface) and assume that diffusion coefficient does not change significantly with concentration. Since the liquid column is large the concentration is taken zero at the bottom of the vessel. The gas inside the vessel follows the real gas law and the gas pressure can be calculated by  $PV = ZRT$ .

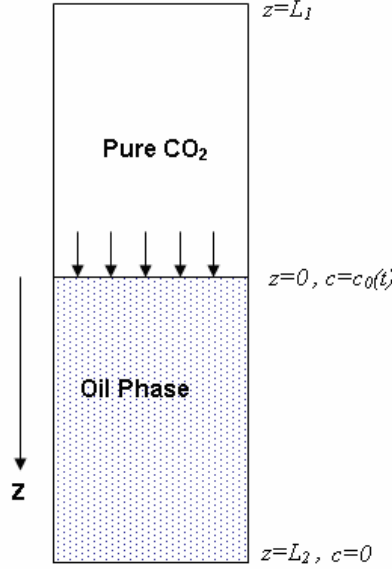


**Fig. 2.3:** Geometry of the process

### 2.3.2. Equations

For this system Fick's second law can be written as

$$\frac{\partial c}{\partial t} = D \frac{\partial^2 c}{\partial z^2} \quad 0 \leq z \leq L_2, \quad 0 \leq t \leq \infty, \quad (2.1)$$

where  $D$  is the effective diffusion coefficient and  $c$  is the concentration of CO<sub>2</sub> in the liquid phase. Initially there is no gas inside the liquid, i.e.

$$c(z, t = 0) = 0 \quad 0 \leq z \leq L_2. \quad (2.2)$$

Since the diffusion process is slow and the liquid column is large, we can assume that the concentration of the gas is zero at the end of the tube ( $L_2 \rightarrow \infty$ ). The second boundary condition is given by Henry's law which states that the pressure of a gas above a solution is proportional to the mole fraction (concentration) of the gas in the solution, i.e.,

$$P(t) = k_H c(t), \quad (2.3)$$

where  $k_H$  is taken as Henry's law proportionality constant. An additional condition to the present problem can be written in accordance with the fact that the change of the total moles of gas in the system is due to diffusion into the liquid. The mass flux of the gas at the interface for real gas can be written as

$$\left. \frac{dn_g}{dt} \right|_{z=0} = \frac{V}{ZRT} \left. \frac{dP_g}{dt} \right|_{z=0} = -DS \left. \frac{\partial c}{\partial z} \right|_{z=0}, \quad (2.4)$$

where  $V$  and  $S$  are the gas volume and the cross-sectional area of the cell respectively,  $R$  is the universal gas constant and  $Z$  is the compressibility factor.  $V$  is also assumed to be constant (no moving boundary). By substituting Henry's law for the gas pressure in Eq. (2.4) we obtain

$$-DS \left. \frac{\partial c}{\partial z} \right|_{z=0} = \frac{Vk_H}{ZRT} \left. \frac{\partial c}{\partial t} \right|_{z=0}. \quad (2.5)$$

### 2.3.3. Analytical solution

Equation (2.1) has a time-dependent boundary condition and can be solved by Laplace transform method (The complete solution is presented in Appendix A). Laplace form of Eq. (2.1), with initial condition Eq. (2.2), is

$$\frac{\partial^2 \bar{C}}{\partial z^2} - \frac{s}{D} \bar{C} = 0. \quad (2.6)$$

The final solution of Eq. (2.6) with the given boundary conditions is

$$\bar{C}(s) = \frac{1}{\frac{k_H}{P_i} s - \frac{ZRT\sqrt{D}}{L_1 P_i} \sqrt{s}} \exp\left(-\sqrt{\frac{s}{D}} z\right). \quad (2.7)$$

Applying Laplace transform to Eq. (2.4) and using Eq. (2.7) yields

$$\frac{L_1}{ZRT} (s\bar{P}_g - P_i) = -\frac{1}{\frac{k_H}{P_i \sqrt{D}} \sqrt{s} - \frac{ZRT}{P_i L_1}}, \quad (2.8)$$

from which we can obtain

$$\frac{\bar{P}_g(s)}{P_i} = \frac{1}{s} - \frac{1}{\frac{L_1 k_H}{ZRT\sqrt{D}} s^{3/2} - s}. \quad (2.9)$$

The gas pressure as a function of time is found by Laplace inversion as

$$P_g(t) = P_i \left[ 2 - \exp(\chi^2 t) \operatorname{erfc}(-\chi\sqrt{t}) \right], \quad (2.10)$$

where

$$\chi = \frac{ZRT\sqrt{D}}{L_1 k_H}. \quad (2.11)$$

Due to our boundary condition –that the concentration is zero at the bottom of the cell ( $z = L_2$ )– we find as long time behavior that the pressure is declining indefinitely. However, that occurs for times much longer than relevant for the experiment.

It should be also mentioned that the solution of Fick's second law assuming a constant concentration at the gas-liquid interface suggests that after a long time the concentration at the interface is linearly proportional to the square root of time, i.e., the plot of gas pressure versus the square root of time will be a straight line [20].

## 2.4. RESULTS AND DISCUSSION

### 2.4.1. Pressure decline

In this study, the quantification of the mass-transfer rate is based on the measurement of the gas pressure in a closed volume containing a column of liquid below a gas column. The changes in the gas pressure are assumed to be only due to transfer of gas into the liquid phase. The measured gas pressure versus time for both distilled water and the surfactant solution are plotted for all experiments. The general trends of the curves for different initial pressures were similar. Thus due to these similarities only the curves of Exp-02 will be presented. However, the extracted data will be reported for all experiments (Table 2.1 and Table 2.2).

**Table 2.1:** List of experiments with water

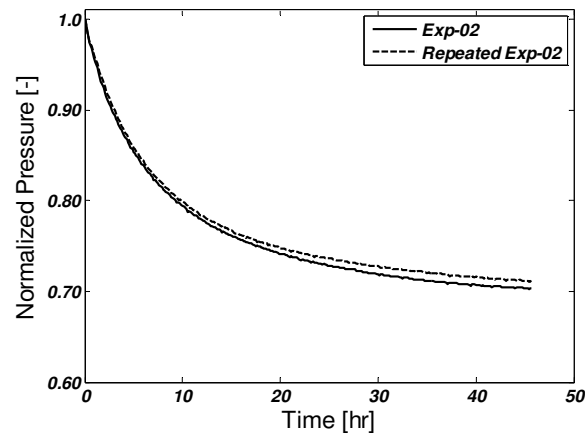
Experiment Number	Initial Pressure [bar]	Temperature [°C]
Exp-01	7.7	25±0.1
Exp-02	11.7	25±0.1
Exp-03	20.1	25±0.1

Figure 2.4 shows normalized CO<sub>2</sub> pressure versus time during pressure decline measurements for Exp-02. It shows that the gas pressure decreases with time due to the transfer of the CO<sub>2</sub> molecules into water. Comparison between the solid and dashed lines in the figure shows the reproducibility of the experiment. The small difference between these two curves is due to the difficulties in setting the initial pressure to exactly the same value for the two experiments.

It becomes clear from Fig. 2.5 that the gas pressure declines significantly at the initial stages of the experiment, i.e., has a steep slope at the early times of the experiment. However, the slope of the curve becomes less steep with time, meaning that also the mass-transfer rate decreases with time. Figure 2.5 shows the comparison between the measured pressures and the model using the known diffusion coefficient of CO<sub>2</sub> in water (in this curve  $D=1.97 \times 10^{-9} \text{ m}^2/\text{s}$ ). The curve shows significant discrepancy between experimental and predicted values.

**Table 2.2:** List of experiments with SDS solution

Experiment Number	Initial Pressure [bar]	Temperature [°C]	SDS Concentration
Exp-04	11.8	25±0.1	30mM > CMC
Exp-05	11.7	25±0.1	2mM < CMC
Exp-06	11.7	25±0.1	30mM + 0.5M NaCl



**Fig. 2.4:** Reproducibility of the experiments,  $P_i=11.7 \text{ bar}$

#### 2.4.2. Deviation from the square root of time

Figure 2.6 shows the plot of the measured gas pressure versus the square root of time for Exp-02. It shows that the initial behavior of this curve is faster than the square root of time. This is an indication of the higher mass transfer of CO<sub>2</sub> into water, which cannot be explained by a diffusion like process. Interestingly, after about one day the pressure vs. square root of time curve becomes linear. It can be expected that at longer times the mass transfer of CO<sub>2</sub> into water is determined by molecular diffusion.

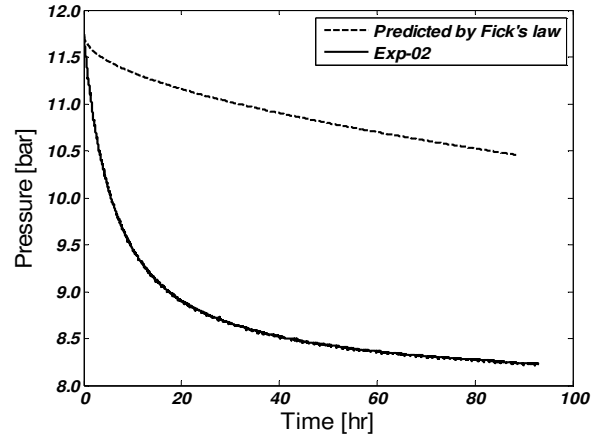


**Fig. 2.5:** Comparison between the experimental data and the physical model

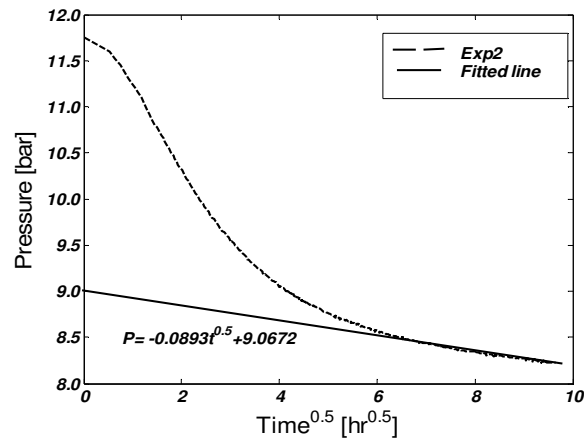


**Fig. 2.6:** Deviation of the experimental data from the square root of time rule. The later stages of the experiment can be fitted to a straight line.

### 2.4.3. Estimated diffusion coefficients

Two effective diffusion coefficients are extracted from the experimental data describing the initial and long-time behavior of the CO<sub>2</sub> mass transfer into water and surfactant solutions. The procedure is as follows:

In the plots of pressure versus square root of time (for example Fig. 2.6 for Exp-02), the late-stage experimental data are fitted to a straight line. The intercept of the fitted line in Fig. 2.6 is the initial pressure with which the mass transfer process would have started if diffusion had been the only responsible mechanism for mass transfer of CO<sub>2</sub> into the liquid (no convection case). Therefore, to obtain the late-stage diffusion coefficient this pressure is put as initial pressure in the physical model, for which the model equation is Fick's second law with a time dependent boundary condition. The lower solid curve in Fig. 2.7 is the predicted gas pressure by Eq. (2.10) using the initial pressure obtained from Fig. 2.6 and choosing  $D=2.75 \times 10^{-9} \text{ m}^2/\text{s}$  and inserting the literature value of Henry's coefficient ( $k_H=2980.1 \text{ Pa}/(\text{mol} \cdot \text{m}^3)$ ). The dashed line in Fig. 2.7 shows the

experimentally measured pressure data versus time. With a diffusion coefficient close to the molecular diffusion coefficient of CO<sub>2</sub> into the water the predicted values by the model are in excellent agreement with the measured pressure values. To obtain the effective coefficients for early stages of the experiments the experimental initial pressure was put in the model and the effective diffusion coefficient was obtained with the help of the data. The upper solid curve in Fig. 2.7 is the predicted gas pressure by Eq. (2.10) choosing  $D=8.35\times 10^{-8} \text{ m}^2/\text{s}$  and  $k_H=2980.1 \text{ Pa}/(\text{mol.m}^3)$ . Alternatively we can use the later stage diffusion coefficient  $D=2.75\times 10^{-9} \text{ m}^2/\text{s}$  but then the Henry's coefficient needs to be modified to  $k_H=552.01 \text{ Pa}/(\text{mol.m}^3)$ . Such a small value has not been reported in the literature for CO<sub>2</sub> solubility in water. Therefore, we have chosen to use the literature value of Henry's coefficient in the interpretation of the experiments.

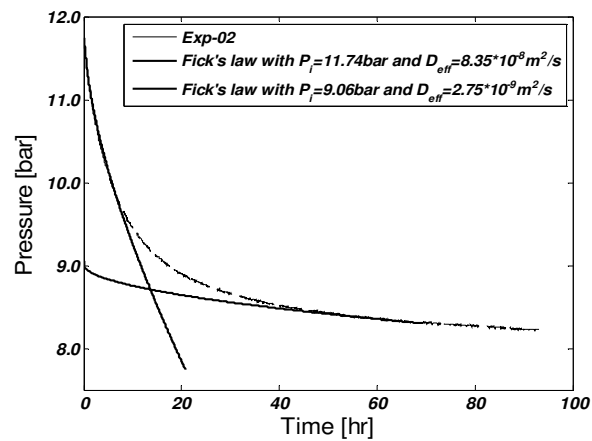


**Fig. 2.7:** The fitted curves to extract the effective diffusion coefficients.

The extracted effective diffusion coefficients for different experiments are shown in Table 2.3. The obtained effective diffusion coefficients for the early stages of the experiments are about two orders of magnitude larger than the actual molecular diffusion of CO<sub>2</sub> into water, again indicating the faster mass transfer rate of CO<sub>2</sub> into water at the early stages of the experiment. However, the obtained effective diffusion coefficients for the later stages of the experiments imply that after a certain time, the mass transfer of CO<sub>2</sub> into aqueous solutions becomes slower compared to the initial stages. The early-stage diffusion coefficients increase with increasing initial pressure proving the fact that even at slightly high pressures for CO<sub>2</sub>-water system the effective diffusion coefficient is a strong function of the initial pressure, i.e., the initial concentration of CO<sub>2</sub> in the system. This means that at higher pressures the effective diffusion coefficients will be even higher. This observation is also supported by the experimental results in Ref. [4] in which the authors found diffusion coefficients which were two orders of magnitude larger than the molecular diffusion coefficient of CO<sub>2</sub> into water at higher pressures. In addition, regardless of the initial pressure, after a certain time, diffusion becomes the dominant mechanism for mass transfer of CO<sub>2</sub> into

water. The diffusion coefficient extracted from the long time behavior turns out to be independent of the initial experimental pressure.

**Table 2.3:** The late- and early stage effective diffusion coefficients extracted from experimental data. The effective diffusion coefficients in the third and fourth columns were extracted by choosing the literature value of Henry's coefficient,  $k_H = 2980.1 \text{ Pa/mol/m}^3$

Experiment Number	$\sqrt{D} / k_H$	<b>D<sub>eff</sub> for early stages</b> [m <sup>2</sup> /s]	<b>D<sub>eff</sub> for late stages</b> [m <sup>2</sup> /s]
Exp-01	$7.00 \times 10^{-8}$	$4.35 \times 10^{-8}$	$2.05 \times 10^{-9}$
Exp-02	$9.50 \times 10^{-8}$	$8.35 \times 10^{-8}$	$2.75 \times 10^{-9}$
Exp-03	$1.10 \times 10^{-7}$	$10.70 \times 10^{-8}$	$2.05 \times 10^{-9}$
Exp-04	$9.46 \times 10^{-8}$	$7.95 \times 10^{-8}$	$2.50 \times 10^{-9}$
Exp-05	$9.37 \times 10^{-8}$	$7.80 \times 10^{-8}$	$3.50 \times 10^{-9}$
Exp-06	$9.00 \times 10^{-8}$	$7.20 \times 10^{-8}$	$1.95 \times 10^{-9}$

#### 2.4.4. Influence of surfactant

To study the influence of the soluble surfactants on the interfacial mass-transfer some of the experiments were done using surfactant (SDS) solutions with and without salt (NaCl). Figure 2.8 shows the normalized pressure decline curve for the experiments with surfactant solution together with the experiment with pure water. It is evident from Fig. 2.8 that at our experimental conditions the addition of soluble surfactant (SDS) has no significant effect on mass transfer rate of CO<sub>2</sub> into water. However, the addition of salt seemingly retards the mass transfer. Several reasons can be responsible for this behavior: (a) the addition of NaCl increases the viscosity of the solution and therefore the effective diffusion coefficient decrease by adding NaCl, (b) the addition of NaCl decreases the solubility of CO<sub>2</sub> in water. Therefore, less CO<sub>2</sub> is dissolved in water in the experiment with NaCl compared to experiments without NaCl and (c) the addition of salt increases the adsorption of the surfactant molecules at the interface [21] and the interface becomes more packed which could be another possible reason for the differences of the curves in Fig. 2.8. Our results are consistent with the results of other researchers [12,22,23], i.e., the surface resistance for soluble surfactants is very small. However, the insoluble surfactants do have a significant effect on the transfer rates of gas through the gas-liquid interface.

The same procedure as discussed above was also followed to extract the effective diffusion coefficients for surfactant solutions. Indeed, the obtained diffusion coefficient values for surfactant solutions are about the same as for the experiments with water and are presented in Table 2.3.

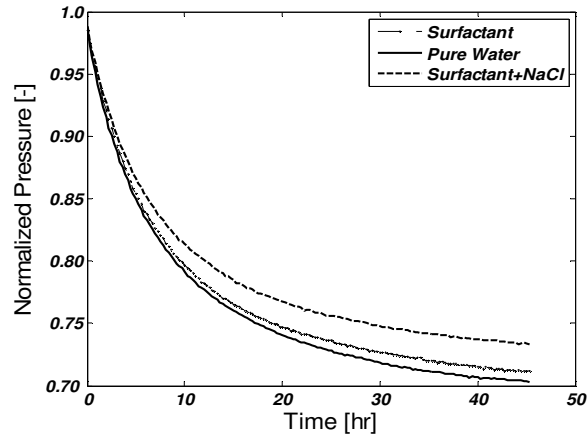


**Fig. 2.8:** Comparison of the pressure decline for experiments with and without surfactant and salt

#### 2.4.5. CO<sub>2</sub> mass transfer into oil

To study the mass transfer of CO<sub>2</sub> we carried out experiments with n-decane (n-C<sub>10</sub>) and n-hexadecane (n-C<sub>16</sub>). The dissolution of CO<sub>2</sub> increases the density of the hydrocarbons [14]. The experimental procedure and conditions were the same as explained in Section 2.2. Figure 2.9 shows the pressure decline curve for n-C<sub>10</sub> at 12.0 and 20.0 bar together with an experiment with n-C<sub>16</sub> at 12.0 bar. Like for the CO<sub>2</sub> mass transfer into aqueous media, it can be concluded from Fig. 2.9 that initially the mass transfer of CO<sub>2</sub> is faster than at the later stages for both hydrocarbons. As expected the mass transfer of the CO<sub>2</sub> into n-C<sub>10</sub> increases with increasing pressure. However the general trend remains similar. The mass transfer of CO<sub>2</sub> in n-C<sub>16</sub> is slower than in n-C<sub>10</sub> due to the higher viscosity of n-C<sub>16</sub>.

During the experiments with an oil phase the interface was monitored. Contrary to the water case, the volume change in oil phase was significant. The volume of n-C<sub>10</sub> increased by  $4.7 \pm 0.1\%$  at 20 bar and  $1.8 \pm 0.1\%$  at 12 bar. The volume of n-C<sub>16</sub> increased by about  $1.0 \pm 0.1\%$  of the initial volume. We believe that this result has implications for enhanced oil recovery for CO<sub>2</sub> flooding and improved oil recovery in fractured oil reservoirs.

#### 2.5. PROPOSED MECHANISMS

In order to explain the observed discrepancy between the physical model and the experimental data in Fig. 2.5 several mechanisms have been considered. Firstly, CO<sub>2</sub> might be absorbed into the water “lining” the gas filled part of the glass tube wall. This explanation is however unlikely because it would require a water layer with a thickness of 2 mm; our estimate of the water layer thickness is in the order of 10-100 nm instead. Secondly, the validity of Henry’s law used to relate surface concentration of the fluid to the gas pressure. Even if we consider these possibilities less likely, they have to be investigated. Thirdly, it has been shown repeatedly that when CO<sub>2</sub> is brought

into contact with water, the dissolution and diffusion of CO<sub>2</sub> leads to a concentration gradient in the water and also a density gradient [25]. As the density increases with increasing dissolution of CO<sub>2</sub> at the interface, the fluid overlaying the water or oil phase near the interface becomes denser. The density gradient induces natural convection in the liquid phase. In this thesis we assert that this density-driven natural convection is the main mechanism for the enhanced mass-transfer of CO<sub>2</sub> into water, and results in higher flux of CO<sub>2</sub> at the interface. However, the density gradient, and therefore natural-convection effects, decrease with time and after a certain time the density gradient is not large enough to sustain convection to the system.

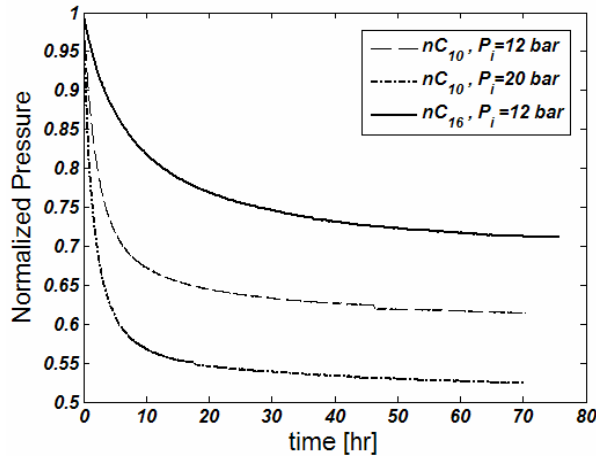


**Fig 2.9:** Pressure decline curve for n-decane and n-hexadecane

In addition to the natural convection, the time-dependency of the boundary condition in Eq. (2.4) can be another reason why the early pressure history is not proportional to the square root of time. However, as we can see from Fig. 2.6 the pressure decline is slow at the later stages and then the gas pressure can be considered constant for the boundary condition.

## 2.6. CONCLUSIONS

The mass transfer of gaseous CO<sub>2</sub> into aqueous and oleic phases was investigated using a PVT cell enabling accurate monitoring of the evolution of the gas pressure over time, under isothermal conditions. It was found that the transfer rate at the initial stages of the experiments is much faster than at the late stages. Moreover, the transfer rate increases with increasing the gas pressure. A physical model based on the Fick's second law and Henry's law was developed to interpret the experimental data. The mass transfer process could not be modeled with a modified Fick's second law, using a single effective diffusion coefficient. Nevertheless, by considering separately the short-time and long-time mass transfer behavior, we could model them individually with the proposed model and two effective diffusion coefficients. The measured short-time effective diffusion coefficients were about two orders of magnitude larger than the molecular diffusivity, whereas the

long-time effective diffusion coefficients agree with the molecular diffusivity of CO<sub>2</sub> into water. It was suggested that at the early stages of the experiments density-driven natural convection enhances the mass transfer of CO<sub>2</sub> into water. After a certain time, the density-driven natural convection becomes less important and at the later stages diffusion becomes the dominant mechanism for the mass transfer experiments of CO<sub>2</sub> into water and surfactant solutions. The same behavior was seen from the surfactant solution experiments. Moreover, the results of experiments show that the addition of SDS to water has no measurable effect on the mass transfer rate in our experimental setup. A similar mass-transfer enhancement was observed for the mass transfer between gaseous CO<sub>2</sub> rich phase with two hydrocarbons (n-decane and n-hexadecane). The effect is less significant for n-hexadecane due to its higher viscosity. This has implications for the oil recovery.

## 2.7. NOMENCLATURE

$c$	Gas concentration [M]
$\bar{C}$	Laplace transform of $c$ [M]
$D_{eff}$	Effective diffusion coefficient [m <sup>2</sup> /s]
$k_H$	Henry's constant [Pa/(mol.m <sup>3</sup> )]
$L$	Length of the experimental tube [m]
$L_1$	Height of the gas in the experimental tube [m]
$L_2$	Height of the liquid in the experimental tube [m]
$P_g$	Gas pressure [Pa]
$P_i$	Initial gas pressure [Pa]
$R$	Universal gas constant [J/mol/K]
$S$	Cross sectional area of the tube [m <sup>2</sup> ]
$t$	Time [sec]
$T$	Temperature [K]
$V$	Volume of the gas in tube [m <sup>3</sup> ]
$Z$	Gas compressibility factor [-]

## 2.8. REFERENCES

1. T. Holt, J. Jensen and E. Lindeberg, *Energy Convers. Manage.*, 36 (1994) 535.
2. E. Lindeberg and D. Wessel-Berg, *Energy Convers. Manage.*, 38 (1997) S229.
3. S. Bachu, J.J. Adams, *Energy Convers. Manage.*, 44 (2003) 3151.
4. Ch. Yang and Y. Gu, *Ind. Eng. Chem. Res.*, 45 (2006) 2430.
5. L. Nghiem, P. Sammon, J. Grabensetter, H. Okhuma H, *SPE 89474* (2004).
6. Y.P. Zhang, C.L. Hyndman, B.B. Maini, *J. Petroleum Sci. and Eng.*, 25 (2000) 37.
7. G. Vazquez, G. Antorrena, J.M. Navaza, *Ind. Eng. Chem. Res.*, 39 (2000) 1088.

8. T.G. Springer and R.L. Pigford, *Ind. Eng. Chem. Fundam.*, 9 (1970) 458.
9. J.A. Caskey and W.B. Jr. Barlage, *J. Colloid Interface Sci.*, 41 (1972) 52.
10. J. Hanwight, J. Zhou, G.M. Evans, K.P. Galvin, *Langmuir*, 21 (2005) 4912.
11. K. Koide, Y. Orito and Y. Hara, *Chem Engng Sci.*, 29 (1974) 417.
12. V.K. La Mer, L.A.G. Aylmore, T.W. Healy, *J. Phys. Chem.*, 67 (1963) 2793.
13. M.J. Blank, *Phys. Chem.*, 66 (1962) 1911.
14. G.T. Barnes and D.S. Hunter, *J. Colloid Interface Sci.*, 129 (1989) 585.
15. G.T. Barnes, *Colloids Surf. A*, 126 (1997) 149.
16. P.G.T. Fogg and W. Gerrard, *Solubility of gases in liquids*, Wiley, New York, 1991, pp 281-314.
17. R. Sander, *Compilation of Henry's Law Constants for Inorganic and Organic Species of Potential Importance in Environmental Chemistry*, available online at: <http://www.mpch-mainz.mpg.de/%7Esander/res/henry.html>, Version 3, 1999, p57 (last date accessed Jan. 2009)
18. Kh. Gertz and Hh. Loeschcke, *Helv. Physiol. Pharmacol. Acta.*, 12(4) (1954) C 72-4.
19. N.N. Greenwood and A. Earnshaw, *Chemistry of the elements*, 2<sup>nd</sup> Ed. Butterworth Heinemann, Oxford, 1997.
20. J.M. Coulson and J.F. Richardson, *Chemical Engineering*, 3<sup>rd</sup> ed., Pergamon Press, Oxford, 1977, Vol. 1, pp 281-286.
21. Santanu Paria and Pak K. Yuet, *Ind. Eng. Chem. Res.*, 45 (2006) 712.
22. E. Molder, T. Tenno, P. Nigu, *Critical Rev. Anal. Chem.*, 28 (1998) 75.
23. D.R. Raymond and S.A. Zieminski, *A.I.Ch.E.J.*, 17 (1971) 57.
24. S. Ashcroft and M. Ben Isa, *J. Chem. Eng. Data* (1997) 1244.
25. Gmelin L., *Gmelin Handbuch der anorganischen Chemie*, 8. Auflage. Kohlenstoff, Teil C3, Verbindungen., 1973, pp 64-75.

---

## Chapter 3

# MODELING OF NATURAL-CONVECTION FLOW OF CO<sub>2</sub> IN WATER

---

### ABSTRACT

*In the previous chapter, it was proposed that the dissolution of CO<sub>2</sub> into water (or oil) causes a density increase with respect to pure water (or oil). It was further asserted that the increase in density causes natural convection, and therefore, the experiments cannot be modeled with Fick's law using a single diffusion coefficient. This chapter elaborates on these ideas. It reports a new set of expert experiments performed in a cylindrical PVT-cell at a pressure range of  $p_i=10-50$  bar, where a fixed volume of CO<sub>2</sub> gas was brought into contact with a column of distilled water. A theoretical interpretation of the observed effects based on diffusion and natural-convection phenomena is developed. The CO<sub>2</sub> concentration at the interface is estimated from the gas pressure using Henry's solubility law, in which the coefficient varies with both pressure and temperature. Good agreement between the experiments and the theoretical results has been obtained.*

**KEYWORDS:** *CO<sub>2</sub>, Enhanced mass transfer, Natural convection, Henry's law, Navier-Stokes equation, Effective diffusion coefficient*

**Published in:** Industrial and Engineering Chemistry Research, (2009).

### 3.1. INTRODUCTION

Geological storage of CO<sub>2</sub> is considered to reduce the concentration of CO<sub>2</sub> in the atmosphere [1-4]. The quantification of CO<sub>2</sub> dissolution in water and understanding the transport mechanisms are crucial in predicting the potential and long-term behavior of CO<sub>2</sub> in aquifers. When CO<sub>2</sub> is injected into saline aquifers or water-flooded oil reservoirs, brine will be overlaid by CO<sub>2</sub> due to gravity segregation. Then, CO<sub>2</sub> dissolves into the brine by molecular diffusion. The density of the water-CO<sub>2</sub> solution exceeds the density of pure water and increases with increasing CO<sub>2</sub> concentration [5], leading to natural convection [5-7].

Arendt et al. [8] applied a Schlieren method and a three-mode magnetic suspension balance connected to an optical cell to analyze the mass transfer of the CO<sub>2</sub>-water system up to 360 bar. A good agreement between their model (linear superposition of *free convection* and Marangoni convection) and the experiment was obtained. The addition of surfactant suppressed the Marangoni convection in their experiments; while in our experiments addition of surfactant did not have a significant effect on the transfer rate of CO<sub>2</sub>. Yang and Gu [9] performed experiments in bulk where a column of CO<sub>2</sub> at high pressure was in contact with water (brine). A modified diffusion equation with an effective diffusivity was used to describe the mass-transfer process of CO<sub>2</sub> into the brine. A good agreement between the experiments and the model was observed by choosing effective diffusion coefficients two orders of magnitude larger than the molecular diffusivity of CO<sub>2</sub> into water. However, the authors pointed out that the accurate modeling of the experiments should consider natural convection effects. In the previous chapter we reported experimental results for the same system, in a slightly different geometry, showing initially enhanced mass transfer and subsequently a classical diffusion behavior for long times. We showed that, although the initial stages and later stages of the experiments can be modeled individually with the described model and two effective diffusion coefficients could be obtained from the experimental data, the mass transfer process cannot be modeled with a modified Fick's second law with a single effective diffusion coefficient for the CO<sub>2</sub>-water system at high pressures. The extracted diffusion coefficients are only fitting parameters and have no physical meaning.

The theoretical description of temperature-driven natural-convection flow uses the Navier-Stokes equation and can be found in classical books on fluid mechanics [10,11]. Several numerical approaches have been proposed to solve the governing Navier-Stokes and continuity equations. Guçeri and Farouk [12] derived a numerical model for steady-state natural (turbulent) convection in various geometries. By the symmetry of the geometries considered they can use the stream function-vorticity approach. From the mathematical point of view these geometries allow a 2-D description. Patankar [13] proposed a semi-implicit numerical method, which can also be used to

(non-steady) 3-D problems. Bairi [14] used Patankar's method to study the transient natural convection in a 2-D vertical cylinder. Increasingly, the Finite Element Method (FEM), which was originally developed for solid-mechanics calculations, is being applied in this area. This method facilitates the modeling of the problem in complex geometries with irregularities [15-17]. Moreover, non-uniform meshes can easily be used in this method which allow for the resolution of flow details in the regions of interest.

The objective of this chapter is to develop a model that can fully describe the experiments without having to introduce (semi) empirical parameters, in spite of disregarding surface-tension-gradient and temperature effects. It turns out that this is possible by considering density-driven natural-convection phenomenon. Therefore, this chapter focuses on describing the phenomena, both experimentally and numerically, when a CO<sub>2</sub>-rich gaseous phase is on top of a water layer. Section 3.2 describes the geometry of the system and the physical model to study natural convection in a vertical cylinder. Section 3.3 explains the experimental setup, i.e., a vertical cylindrical PVT cell, and the experimental procedures. Section 3.4 presents the experimental results and compares it with the numerical computations. Finally we draw the main conclusions of this study.

## 3.2. NUMERICAL MODEL

### 3.2.1. Formulation

There can only be mechanical equilibrium in a fluid in a gravitational field if the concentration of CO<sub>2</sub> inside the liquid only varies in the vertical coordinate, i.e.,  $c = c(z)$ . However if the concentration gradient exceeds a certain value mechanical equilibrium in the fluid will be impossible [11]. The instability will initiate a convection current. This process will develop into natural convection throughout the entire fluid and the concentration becomes dependent on the radial coordinate as well. The driving force for natural convection is due to the fact that dissolution of CO<sub>2</sub> into water causes a density increase. Consequently fresh (no-CO<sub>2</sub>-containing) water moves to the interface and CO<sub>2</sub>-containing water moves downwards, accelerating the diffusion process, and hence the mass transfer rate. The mixing of the water finally leads to a constant CO<sub>2</sub> concentration in the water.

We try to formulate such motions inside the water when it is brought into contact with a CO<sub>2</sub>-rich gaseous phase in the geometry depicted in Fig. 3.1. The cylindrical vessel with radius  $R$  consists of an upper column filled with gaseous CO<sub>2</sub> and a lower column filled with a stagnant water layer. We disregard both water evaporation (the contribution of water vapor to the gas pressure is 4.25 kPa at  $T=30^\circ\text{C}$  which is negligible compared to the experimental pressure drop [18]) and water swelling due to CO<sub>2</sub> dissolution. Consequently we assume that the boundary remains fixed. This assumption arises from the fact that the volume change of CO<sub>2</sub>-water binary mixture is very small

at the range of our experimental pressures [19]. It is assumed that capillary effects are absent and therefore the interface is flat. Fast transfer rate is assumed at the upper part of the cell so that it can be adequately described by Fick's law with a high constant diffusion coefficient. CO<sub>2</sub> will be removed at the CO<sub>2</sub>-water interface. This decreases the concentration of CO<sub>2</sub> at the interface and increases concentration of water. However, water concentration cannot deviate too far from equilibrium, as otherwise water will condense. Consequently, even with slow diffusion rates (of the order of  $10^{-5} \times P_{\text{atm}}/P_{\text{exp}} \text{ m}^2/\text{s}$ ) the concentration of CO<sub>2</sub> will not significantly deviate from its equilibrium value at the time scale of the experiment. The CO<sub>2</sub> concentration at the liquid surface is related to the gas pressure by assuming instantaneous thermodynamic equilibrium at the interface by applying Henry's law. The characteristic time for conversion of  $\text{CO}_2 + \text{H}_2\text{O} \rightarrow \text{H}_2\text{CO}_3$  is  $1/0.039 \sim 25$  seconds, which is much smaller than the experimental times. Moreover, only very small amount of CO<sub>2</sub> is converted to H<sub>2</sub>CO<sub>3</sub>. The dissociation into HCO<sub>3</sub><sup>-</sup> and CO<sub>3</sub><sup>2-</sup> is negligible and therefore the rates of their formation can be ignored. We assert that the transfer of gas through the CO<sub>2</sub>-water interface can be described as an unsteady-state diffusion process, i.e., by Fick's law.

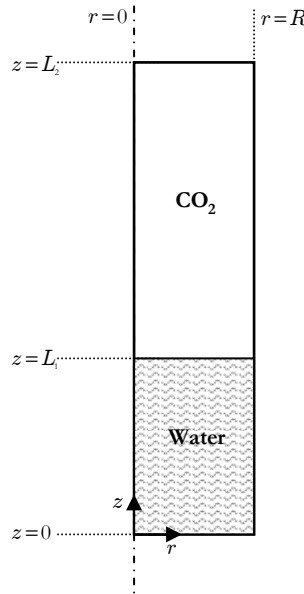


**Fig. 3.1:** Schematic layout of the process: The total length of the tube is  $L$ , the height of water is  $L_1$ . There is no gas flowing out at the end of the tube. The gas-liquid interface is fixed. The liquid concentration at the interface is related to the gas pressure through Henry's Law and changes with time.

The conservation laws for the two components (CO<sub>2</sub> and water) and momentum in the liquid are the governing equations to describe the diffusion and natural convection; the analogy between mass and heat transfer allows us to use the equations in Refs. [10-12]. Only a laminar regime is expected, as the Rayleigh number is of the order of  $10^6$ . The density difference is normally the

driving force for natural convection. Consequently, the density cannot be considered constant. A simplification (the Boussinesq approximation) can be used. This approximation considers density variations only when they contribute directly to the fluid motion. Moreover we assume that there is a linear relationship between density change and concentration

$$\Delta\rho = \beta_c \rho_i \Delta c \quad (3.1)$$

Symbols are defined at the end of the chapter. The characteristic behavior of the density of a CO<sub>2</sub>-water solution on pressure and temperature can be found in Ref. [5]. For the pressure and temperatures of interest the data are presented in Fig. 3.2.

The time dependent governing equations for a 2D diffusion and natural convection system can be written in radial coordinates (see Fig. 3.1 for a schematic of the setup and the area of interest), as described below.

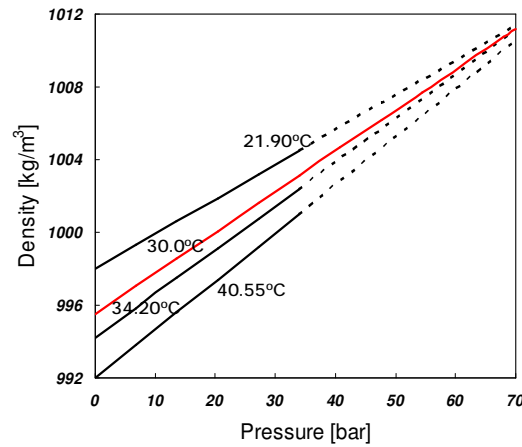


**Fig. 3.2:** Density of water as a function CO<sub>2</sub> concentration (equilibrium pressure). The dashed lines are extrapolated from the solid lines reproduced from the data in Ref. [5].

### 3.2.2. Governing equations

#### 3.2.2.1. Liquid phase

##### (a) Continuity equation

$$\text{div } \mathbf{v} = 0. \quad (3.2)$$

##### (b) Conservation of momentum

$$\frac{\partial \mathbf{v}}{\partial t} + (\mathbf{v} \cdot \mathbf{grad}) \mathbf{v} = -\frac{1}{\rho} \mathbf{grad} p + \nu \Delta \mathbf{v} - \beta_c \mathbf{g} \Delta c \quad . \quad (3.3)$$

(c) Concentration equation

$$\frac{\partial c}{\partial t} + \mathbf{v} \cdot \mathbf{grad} c = D \Delta c \quad . \quad (3.4)$$

3.2.2.2. Gas phase

$$\frac{\partial c_g}{\partial t} = D_g \Delta c_g \quad . \quad (3.5)$$

One important dimensionless number in fluid dynamics is the Rayleigh number, which is dependent on the fluid properties and geometry of the system (characteristic length of the system) with the following relation

$$Ra = \frac{\beta_c g \Delta c R^3}{\nu D} = \frac{\Delta \rho g R^3}{\rho_i \nu D} \quad , \quad (3.6)$$

where, we use Eq. (3.1) to replace  $\beta_c$ . Equation (3.6) states that the magnitude of Rayleigh number depends on the geometry of the experimental setup, in this case the radius of the tube, and properties of the fluid. These properties include the diffusion coefficient of gas into water, viscosity of water and its density change due to gas dissolution. As mentioned before in our case this density change is a strong function of the CO<sub>2</sub> concentration, i.e., the initial pressure of the CO<sub>2</sub>. This means that a high Rayleigh number is due to a large radius of the tube or a high initial pressure or the combination of both parameters.

### 3.2.3. Boundary and initial conditions

3.2.3.1. Liquid phase

Initially the liquid is at rest and there is no CO<sub>2</sub> dissolved in the water, i.e.,

$$\mathbf{v} = c = 0 \text{ at } t = 0 \quad . \quad (3.7)$$

The boundary conditions of the problem are

$$\begin{aligned} \partial_r c &= 0 \text{ at } r = 0, \\ \mathbf{v} &= 0, \partial_r c = 0 \text{ at } r = R, \\ \mathbf{v} &= 0, \partial_z c = 0 \text{ at } z = 0, \\ c &= p_g / k_H = (Z_g R_B T / k_H) c_g \text{ at } z = L_1. \end{aligned} \quad (3.8)$$

3.2.3.2. Gas phase

Initially the gas part is filled with gas at pressure  $p_i$  and therefore the molar gas concentration reads,

$$c_g(x, t = 0) = \frac{p_i}{Z_g R_B T} \quad . \quad (3.9)$$

The boundary conditions are

$$\begin{aligned} \partial_r c_g &= 0 \quad \text{at } r = 0, \\ \partial_r c_g &= 0 \quad \text{at } r = R, \\ J_z &= -D \partial_z c_g \quad \text{at } z = L_1, \\ \partial_z c_g &= 0 \quad \text{at } z = L_2. \end{aligned} \quad (3.10)$$

### 3.2.4. Henry's law (CO<sub>2</sub> solubility) at the interface

The solubility of CO<sub>2</sub> in water can be expressed by using Henry's law as:

$$x_{CO_2(aq)} = \frac{f_{CO_2(P,T)} y \gamma_y}{k_{H(P,T)}^* \gamma_{CO_2(aq)}} \quad , \quad (3.11)$$

where,  $x_{CO_2}$  and  $y$  are the mole fractions of CO<sub>2</sub> in liquid and gas phases, respectively,  $k_H^*$  is Henry's constant [in Pa] that is dependent on pressure and temperature,  $\gamma_{CO_2}$  is the asymmetric (Henry's law) activity coefficient of aqueous CO<sub>2</sub> such that  $\gamma_{CO_2(aq)} \rightarrow 1$  as  $x_{CO_2(aq)} \rightarrow 0$  and  $\gamma_y$  is the symmetric (Raoult's law) activity coefficient of CO<sub>2</sub> in the non-aqueous phase, such that  $\gamma_y \rightarrow 1$  as  $y \rightarrow 1$  and  $f_{CO_2}$  is the fugacity of pure CO<sub>2</sub> at specified P-T conditions. Henry's coefficient,  $k_H^*$ , can be calculated from the virial-like equation of state of Akinfiev and Diamond [20]

$$\ln(k_H^*) = (1 - \xi) \ln f_w + \xi \ln \left( \frac{R_B T}{M_w} \rho_w \right) + 2 \rho_w \left[ a + b \left( \frac{1000}{T} \right)^{0.5} \right]. \quad (3.12)$$

Diamond and Akinfiev [21] developed a thermodynamic model that reproduces 362 published experimental solubility data with a precision of better than 2% over the entire  $P$ - $T$ - $x$  considered. We used their model to calculate Henry's coefficient (the model is available as a computer code at [www.geo.unibe.ch/diamond](http://www.geo.unibe.ch/diamond)). The dependency of Henry's coefficient,  $k_H$  [in Pa/(mol.m<sup>3</sup>)], on pressure at a constant experimental temperature of  $T=30^\circ\text{C}$  is shown in Fig. 3.3. Henry's coefficient varies slightly with pressure at a constant temperature.

### 3.2.5. Numerical Scheme and solution procedure

The finite volume method (FVM) was first used to solve the model equations numerically. The validity of the model was confirmed by comparing to benchmark solutions. This model was used to validate the finite element method (FEM) in COMSOL Multiphysics., which is a software package that can solve various coupled engineering and physics problems, e.g., here a combination of Navier-Stokes, convection-diffusion and diffusion equations in the geometry depicted in Fig. 3.1. The advantage of FEM is that local grid refinement is easier and the simulation times are much smaller than FVM, especially when the Rayleigh values are large.

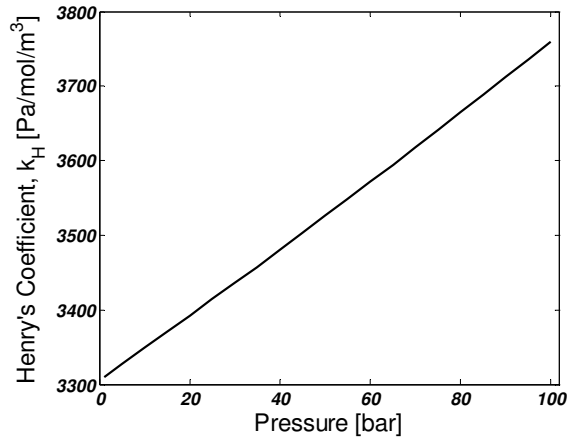


**Fig. 3.3:** Henry's coefficient,  $k_H$ , as a function of pressure calculated using Eq. (3.12) at a constant temperature of  $T=30^\circ\text{C}$ .

## 3.3. EXPERIMENTAL

### 3.3.1. Materials

The gas used to carry out the experiments was 99.98% pure carbon dioxide. The diffusion coefficient of CO<sub>2</sub> in water is  $D=(1.97\pm 0.10)\times 10^{-9}$  m<sup>2</sup>/s [22]. Nitrogen (N<sub>2</sub>) was used to detect possible leakages in the setup. Water with pH=6.8±0.1 was used in the experiments.

### 3.3.2. Set-up and procedure

In the experimental setup described in Chapter 1, the ratio between height of the water column and the radius of the tube was 55. Unfortunately the developed numerical code did not give satisfactory results for aspect ratios larger than 10. Therefore, we performed new experiments with the set-up described here to test the validity of the model explained in previous section.

Figure 3.4 shows the schematic of the experimental set-up. It consists of two stainless steel vessels, the measurement vessel with inner diameter of  $D_1=30$  mm and the gas storage vessel with an inner diameter of  $D_2=40$  mm. The length of both vessels is 10 cm. The vessels are sealed and kept at constant temperature of  $T=30\pm 0.1$  °C in an oven. The characteristic time at which

temperature equilibrates ( $\sim 1500$  sec) has been determined by numerical simulation, where the vessel was subjected to conductive and radiation heat loss. To ensure that the vessels remain in a fixed position they were attached to a board. Before starting the measurements a leakage test was performed with nitrogen. A valve at the bottom of the measurement cell was used to fill the vessel with double-distilled water up to the desired height ( $L_1=43$  mm) using a pump with a known flow rate. A waiting time of approximately 1 hour was then respected, in order to let the liquid come into thermal equilibrium with the oven. CO<sub>2</sub> was slowly injected into the measurement vessel from the storage vessel. The gas pressure is measured with two calibrated pressure gauges, which are connected to the top of the vessels. When the CO<sub>2</sub> pressure reached the desired value, the valve connecting the vessel containing the water was closed and the cell was isolated. This was the starting time of the experiment. The gas pressure was recorded every 100 seconds in a computer.

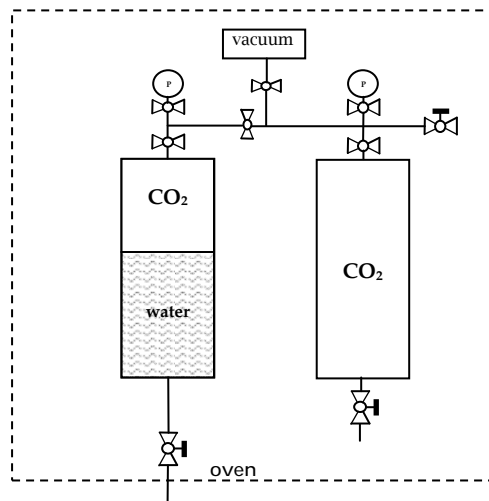


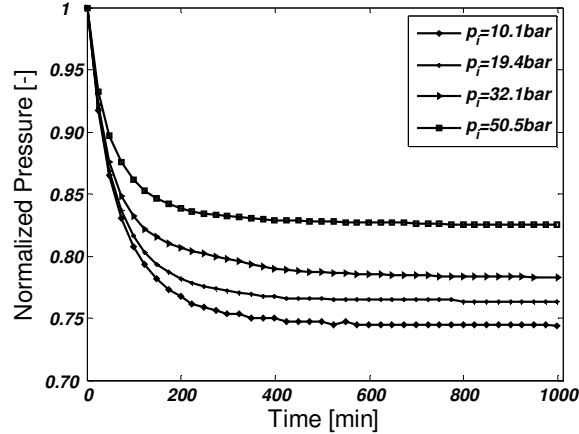
**Fig. 3.4:** Schematic of the set-up: The set-up consists of two steel vessels, a storage vessel (right) and a measurement vessel (left). The gas at pressure  $p_i$  is injected from the right vessel to the left vessel. Mass transfer occurs through the interface in the left vessel. The set-up is held in an oven at a constant temperature. The pressure of the gas at the top part is monitored by a pressure transducer.

### 3.4. RESULTS & DISCUSSION

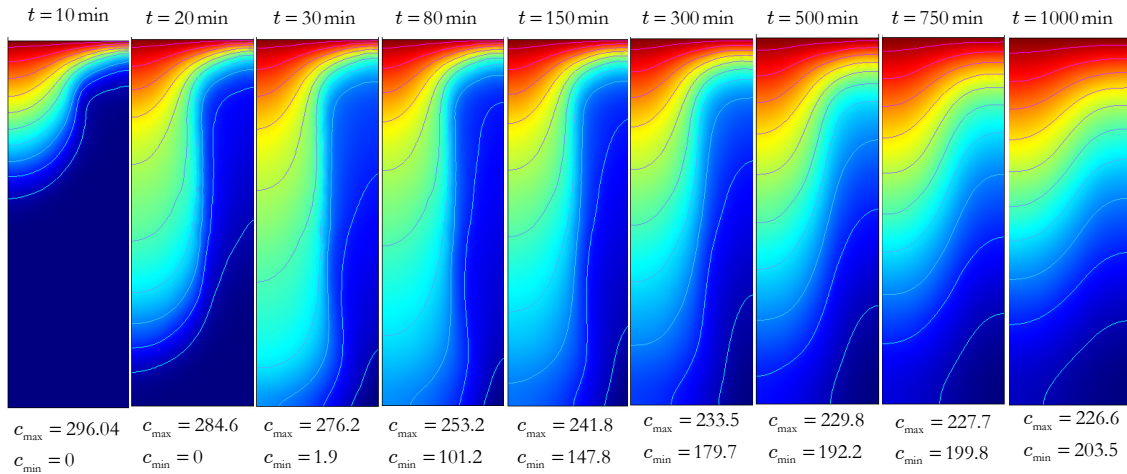
#### 3.4.1. Experimental observations

Figure 3.5 shows the normalized CO<sub>2</sub> pressure versus time during the experiments with different initial pressures. The gas pressure declines significantly at the initial stages of the experiment, i.e., it has a steep slope at the early times of the experiment. However, the slope of the curve becomes less steep with time, meaning that the mass transfer rate decreases with time. The time needed for an over-pressurized gas to reach equilibrium with the liquid below can be calculated using Fick's second law. However, in our experiments the measured mass-transfer rate over the interface turned out to be substantially larger than predicted using Fick's second law (see Figs. 3.11-3.14). An interpretation in terms of *two effective diffusion coefficients* was presented in Chapter 2. The

effective diffusion coefficient for the early stages of the experiments is two orders of magnitude higher than the molecular diffusivity of the CO<sub>2</sub> into water, indicating the presence of natural convection. The effect of natural convection increases as the initial pressure of the experiments increases. Nevertheless in all experiments the influence of the convection decreases as time elapses regardless of the initial pressure of the experiment.



**Fig. 3.5:** Pressure history of the experiments with different initial pressures. The pressure decline indicates the transfer of CO<sub>2</sub> into water.



**Fig. 3.6:** Evolution of CO<sub>2</sub> concentration profiles inside water with time at an initial pressure of  $p_i = 10.1 \text{ bar}$ . The maximum (red) and minimum (blue) concentration values are different in each panel. The concentration values are expressed in [mol/m<sup>3</sup>].

### 3.4.2. Results of the model

#### 3.4.2.1. CO<sub>2</sub> concentration inside the liquid

The general trend of the concentration profiles for all experiments is similar and therefore only the curves of the experiment with  $p_i = 10.1 \text{ bar}$  will be presented. Nonetheless, the explanation

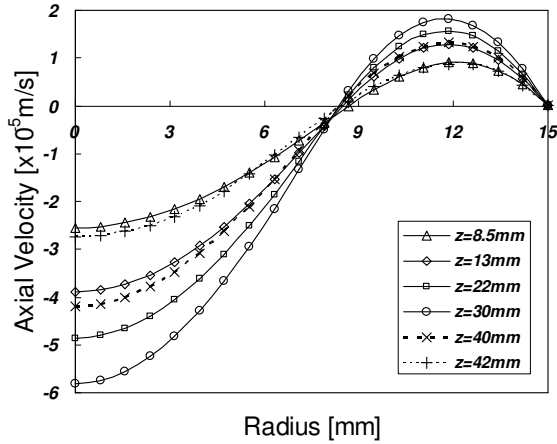
holds for all experiments. Figure 3.6 shows the evolution of CO<sub>2</sub> concentration inside the water with time. The maximum and minimum concentrations are given below each image. These maximum (red) and minimum (blue) concentration values are different in each panel. This procedure allows using the full color span for displaying the results. When analyzing this profile, it is observed that as soon as CO<sub>2</sub> is put above the water, it starts to dissolve. The CO<sub>2</sub> concentration is higher near the center of the vessel. This increases the density of the liquid near the center, which induces an anti-clockwise vortex in the vessel.

The CO<sub>2</sub> concentration decreases at the interface (and near the interface) as the pressure in the gas chamber decreases while CO<sub>2</sub> is transferred far into the liquid. After about 30 minutes CO<sub>2</sub> reaches the bottom of the vessel. At this time the fluid has its maximum velocity (see Fig. 3.9). With a simple scaling analysis it is possible to evaluate the significance of natural convection. The time scale for CO<sub>2</sub> diffusion through a water layer with thickness of  $L_l=43\text{ mm}$  at our experimental condition is  $\sim L_l^2/D \approx 9.24 \times 10^5\text{ sec} \approx 256\text{hr} \gg 30\text{ minutes}$ . As time elapses, the difference between the minimum and maximum values of the concentration becomes less, i.e., the distribution of CO<sub>2</sub> becomes more uniform in the liquid. This implies that convection effect die out with time.

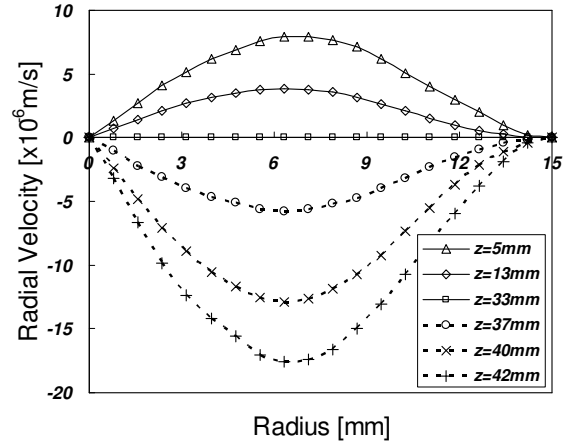
#### 3.4.2.2. Velocity profiles

Figure 3.7 presents the calculated vertical velocity,  $v_z$ , at different vertical positions as a function of the vessel radius for the experiment with the initial pressure of  $p_i=10.1\text{ bar}$ . In accordance with the concentration profile, the flow is much faster in the center, obviously to ensure (water) mass conservation in a horizontal cross section. In the entire volume of the vessel the ascending fluid flow has a low velocity close to the wall, where it approaches zero corresponding to the adherence of the fluid. The vertical velocity increases as fluid moves down in the region  $43 < z < 33\text{ mm}$ . From  $z=33\text{ mm}$  downwards the fluid starts to slow down again until it stops at the bottom of the vessel ( $z=0$ ). In other words the flow is slower at the upper part close to the CO<sub>2</sub>-water interface. A similar velocity pattern was numerically observed for a cylindrical cavity when its upper face was cooled by thermoelectrical Peltier effect following an exponential law [14]. It appears from the simulation results that at  $z=33\text{ mm}$  there is no flow in the radial direction (see Fig. 3.8). The radial velocity is one order of magnitude smaller than the vertical velocity and it has different signs below and above  $z=33\text{ mm}$ . This means that the vertical flow is mainly responsible for the enhancement of transfer rate of CO<sub>2</sub> into water. The velocity change with time is shown in Fig. 3.9 at a fixed position of  $z=30\text{ mm}$ . Initially the liquid is at rest. When CO<sub>2</sub> is brought in contact with the liquid it starts to move. The liquid velocity increases until the CO<sub>2</sub> front reaches the bottom of the vessel at  $t \sim 30\text{ minutes}$ . After that the fluid velocity decreases as more CO<sub>2</sub> is dissolved in the

water with time. Note that at the end of our experiment the liquid velocity is very low but not zero. The fluid motion stops after about 3000 minutes when the water is fully saturated with CO<sub>2</sub>. As can be seen from Fig. 3.10 the liquid velocity increases as the initial pressure of the experiment (or the Rayleigh number) increases. Obviously, the relation is not linear. The pressure decline becomes faster as the Rayleigh number increases, i.e., the time to reach the equilibrium state for a constant volume of water decreases with increasing Rayleigh number, a result which can also be concluded from Fig. 3.5.



**Fig. 3.7:** Axial velocity,  $v_z$ , at different positions at time  $t=60\text{min}$  for the experiment with an initial pressure of  $p_i=10.1\text{ bar}$ .



**Fig. 3.8:** Radial velocity,  $v_r$ , at different positions at time  $t=60\text{min}$  for the experiment with an initial pressure of  $p_i=10.1\text{ bar}$ .

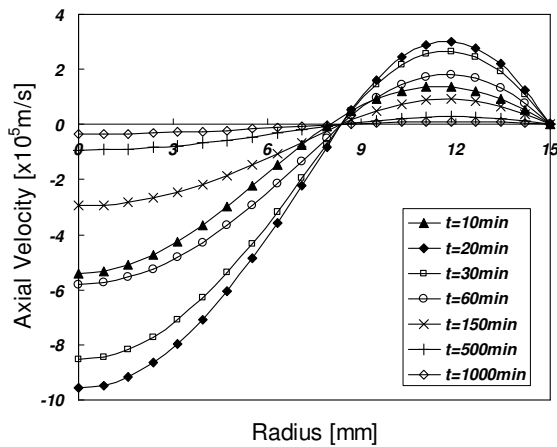


**Fig. 3.9:** Axial velocity,  $v_z$ , at different times at  $z=30\text{mm}$  for the experiment with an initial pressure of  $p_i=10.1\text{ bar}$ .

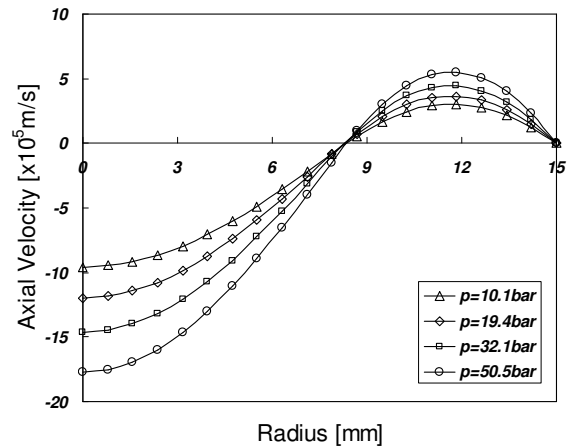


**Fig. 3.10:** The calculated axial velocity,  $v_z$ , at  $z=30\text{mm}$  and  $t=20\text{min}$  for the experiments with different initial pressures

### 3.4.2.3. Pressure decline

As already mentioned CO<sub>2</sub> was injected from the storage vessel to the measurement vessel that was initially filled with water at atmosphere pressure. The sudden opening of the valve between the two vessels causes adiabatic compression of CO<sub>2</sub> which temporarily increases the temperature of the vessel [23]. As a result the system requires a short time to equilibrate. This effect is more significant at higher pressure as larger mass of CO<sub>2</sub> is injected to the system. Our system measures pressures with *100 second* intervals; therefore, we ignored the first two data points. This time is equivalent to the time at which CO<sub>2</sub> reaches equilibrium in the storage vessel (the pressure remains constant). In Ref. [9] the authors ignored first *180* seconds of their experiments due to a similar effect.

Figures 3.11-3.14 plot the pressure history for the experiments with the initial pressures of  $p_i=10.1, 19.4, 32.1$  and  $50.5$  bar respectively. These pressures are well below the critical pressure of CO<sub>2</sub>. The experimental data are compared with the theory described in Section 3.2 with and without taking into account natural convection effects. In all cases the pressure decline rate is much larger than predicted by a Fickian diffusion process. For the computations values of  $\beta_c$ ,  $k_H$  and  $Z_g$  are required. Note that by choosing  $\beta_c = 0$  in the simulation, diffusion will be the only transport mechanism. In the case of natural convection, the density differences are read from Fig. 3.2 and then the concentration dependent  $\beta_c$  is calculated for the conditions of each experiment using Eq. (3.1). Henry's coefficient,  $k_H$ , is obtained from Fig. 3.3. The compressibility factor,  $Z_g$ , is calculated using the Span-Wagner EoS [24] for all pressures at the experimental temperature ( $T=30$  °C). For all of the experiments the match between the experimental data and the theory is within the experimental error (solid lines). It is also possible to fit the experimental data by choosing *effective diffusion coefficients* and switching off the convection currents (dotted lines), similar to the models explained in Ref. [9] and Chapter 1. Such models are not physically justified, because comparing the values reported in Chapter 1 for  $p_i=10.1$  and  $19.4$  bar and the values obtained from our simulations reveal that the magnitude of the diffusion coefficient depends on the geometry of the system (in this case radius and aspect ratio). Moreover, these models fail in accurately explaining the later stages of the experiments, because allowing an effective diffusion coefficient two orders of magnitude larger than molecular diffusivity of CO<sub>2</sub> results in equilibration times that are much shorter than the experiments [see Figs. 3.11-3.14]. In Ref. [9] the authors simulate experiments with duration of only one hour. The extracted effective diffusion coefficients increase with increasing initial pressure and they are in good agreement with the values reported in Ref. [9].

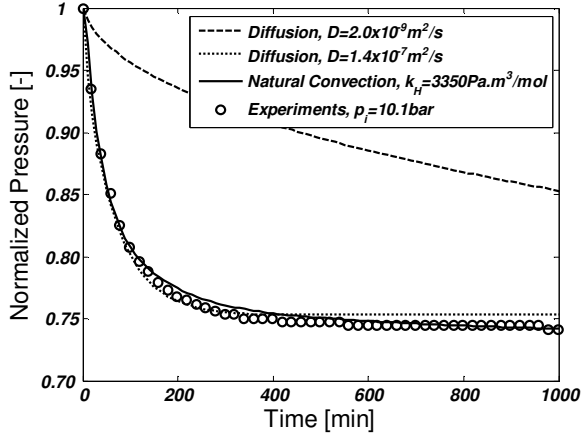


**Fig. 3.11:** Comparison between the measured pressure data and the numerical model for  $p_i=10.1$  bar,  $T=30^\circ\text{C}$ ,  $k_H=3350$  Pa.m<sup>3</sup>/mol and  $D=2.0\times 10^{-9}$  m<sup>2</sup>/sec. The dotted line is obtained with an effective diffusion coefficient of  $D=1.40\times 10^{-7}$  m<sup>2</sup>/sec.

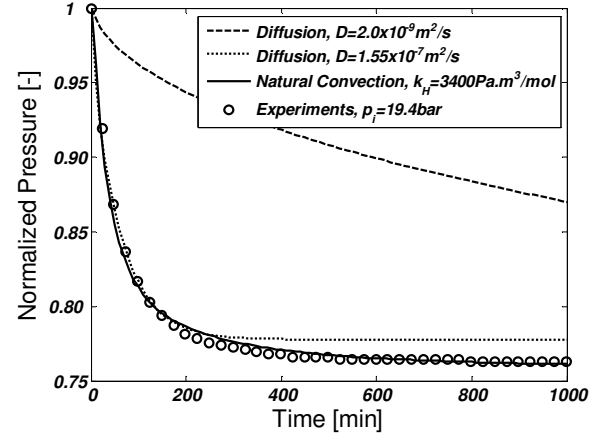


**Fig. 3.12:** Comparison between the measured pressure data and the numerical model for  $p_i=19.4$  bar,  $T=30^\circ\text{C}$ ,  $k_H=3400$  Pa.m<sup>3</sup>/mol and  $D=2.0\times 10^{-9}$  m<sup>2</sup>/sec. The dotted line is obtained with an effective diffusion coefficient of  $D=1.55\times 10^{-7}$  m<sup>2</sup>/sec.

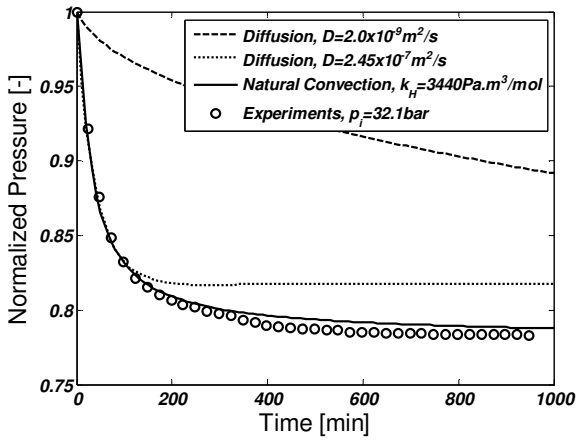


**Fig. 3.13 :** Comparison between the measured pressure data and the numerical model for  $p_i=32.1$  bar,  $T=30^\circ\text{C}$ ,  $k_H=3440$  Pa.m<sup>3</sup>/mol and  $D=2.0\times 10^{-9}$  m<sup>2</sup>/sec. The dotted line is obtained with an effective diffusion coefficient of  $D=2.45\times 10^{-7}$  m<sup>2</sup>/sec.

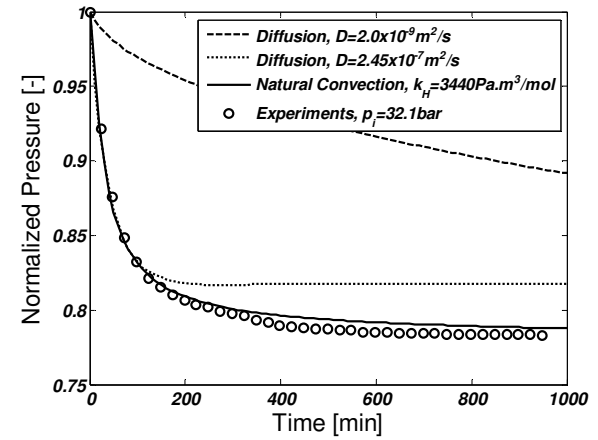


**Fig. 3.14:** Comparison between the measured pressure data and the numerical model for  $p_i=50.5$  bar,  $T=30^\circ\text{C}$ ,  $k_H=3530$  Pa.m<sup>3</sup>/mol and  $D=2.0\times 10^{-9}$  m<sup>2</sup>/sec. The dotted line is obtained with an effective diffusion coefficient of  $D=2.80\times 10^{-7}$  m<sup>2</sup>/sec.

It should be mentioned that we also considered the possible contributions of Marangoni effect in our experiments. A rough calculation, based on a paper by Arendt et al. [8] shows that at our experimental conditions the mass transfer coefficient due to natural (or free) convection is 1-2 orders of magnitude larger than the mass transfer coefficient due to Marangoni convection. The reason could be that the interfacial tension between CO<sub>2</sub> and water does not change significantly

at our experimental pressures but it does change significantly from 1 bar to 100 bar. Strictly speaking at pressures above 100 bar the IFT has asymptotic behavior [25].

### 3.5. CONCLUSIONS

The mass transfer of CO<sub>2</sub> into water was studied for the pressure range of 10-50 bar at a constant temperature of  $T=30^{\circ}\text{C}$  in a relatively simple PVT cell. The gas pressure was monitored continuously to investigate the transport phenomena. It was observed that initially, the mass-transfer rate is larger than expected from Fick's law. For long times the convection effects are no longer dominant and the behavior becomes diffusion like. This confirms the hypothesis that the increase in density of water (due to the dissolution of CO<sub>2</sub>) causes convective currents inside water that accelerate the transfer of CO<sub>2</sub> molecules. It is possible to develop a physical model that can explain the experiments. The model considers mechanical equilibrium in the upper gas phase such that it can be described by Fick's law with a sufficiently large diffusion coefficient. Furthermore, the model considers density-driven natural convection in the liquid phase that is based on the Navier-Stokes equations. The gas pressure was related to the CO<sub>2</sub> concentration at the gas-liquid interface applying Henry's solubility law, in which the coefficient varies with both pressure and temperature. According to the simulations the velocity increases until it reaches a maximum and then diminishes gradually as natural convection effect become less important. The maximum velocity corresponds to the time in which CO<sub>2</sub> front reaches the bottom of the vessel. There is a strong correlation between the fluid velocity and the concentration profile with the experimental pressure decline rates. The experiments and pressure decline in the gas phase predicted by the theory agree within the experimental error.

### 3.6. NOMENCLATURE

$c$	Concentration [mol/m <sup>3</sup> ]
$c_p$	Heat capacity [J/K/m <sup>3</sup> ]
$D$	Diffusion coefficient [m <sup>2</sup> /s]
$f$	Fugacity [Pa]
$g$	acceleration due to gravity [m/s <sup>2</sup> ]
$k_H$	Henry's constant
$L$	Length of the tube [m]
$M$	Molecular weight [kg/mol]
$p$	Pressure [Pa]
$r$	Distance from center of the tube [m]
$R$	Radius of the tube [m]
$Ra$	Rayleigh number [-]

$T$	Temperature [K, °C]
$t$	Time [sec]
$v$	Velocity [m/s]
$z$	Distance from the bottom of the tube [m]
$Z_g$	Gas compressibility factor [-]

### **Greek symbols**

$\rho$	Density of the fluid [ $kg / m^3$ ]
$\beta_c$	Volumetric expansion coefficient [ $m^3/mol$ ]
$\xi, a, b$	Empirical fitting parameters
$\mu$	Viscosity of the fluid [ $kg / m - sec$ ]
$\nu$	Kinematic viscosity [ $m^2/s$ ]

### **Subscripts**

0	Reference value of the quantity
$g$	Gas
$i$	Initial value of the quantity
$w$	Water
$r$	Quantity in $r$ -direction
$z$	Quantity in $z$ -direction

## **3.7. REFERENCES**

1. IPCC special report on Carbon Dioxide capture and storage, Edited by B. Metz, O. Davidson, H. de Coninck, M. Loos, L. Meyer, *Cambridge University Press* (2005).
2. K. Pruess and J. Garcia, *Environ. Geol.*, 42 (2002) 282.
3. R.G. Bruant, A.J. Guswa, M.A. Celia, C.A. Peters, *Environmental Science and Technology*, June 1, (2002) 241A.
4. A. Naderi Beni, M. Kühn, R. Meyer, C. Clauser, *Proceedings of the Sino-German Workshop, Goslar, Germany, 17-20 September 2007*.
5. L. Gmelin, in: *Gmelin Handbuch der anorganischen Chemie*, 8. Auflage. Kohlenstoff, Teil C3, Verbindungen. ISBN 3-527-81419-1 (1973).
6. R. Farajzadeh, H. Salimi, P.L.J. Zitha, J. Bruining, *Int. J. Heat and Mass Transfer*, 50 (2007) 5054.
7. E. Lindenberg and D. Wessel-Berg, *Energy Convers. Mgmt*, 38 (1997) S229.
8. B. Arendt, D. Dittmar, R. Eggers, *Int. J. Heat and Mass Trans.*, 47 (17-18), (2004) 3649.
9. C. Yang and Y. Gu, *Ind. Eng. Chem. Res.*, 45 (8), (2006) 2430.
10. R.B. Bird, W.E. Stewart and E.N. Lightfoot, *Transport phenomena*, 2<sup>nd</sup> rev. ed., New York: Wiley, (2007).
11. L.D. Landau and E.M. Lifshitz, *Fluid mechanics, Volume 6 of course of theoretical physics*, translated from Russian by Sykes J.B. and Reid W.H., pp. 212-218, 4<sup>th</sup> Edition, Pergamon Press (1975).
12. S. Güçeri and B. Farouk, *Numerical solutions in laminar and turbulent natural convection*, In: Natural convection, Fundamentals and applications, S. Kakac, W. Aung, R. Viskanta, Hemisphere publication, pp. 615-655 (1985).
13. S.V. Patankar, *S.V. Numerical Heat Transfer and Fluid Flow*, Hemisphere, New York, 1980.

14. A. Bairi, *Applied Thermal Engineering*, 23 (2003) 431.
15. B.R. Becker and J.B. Drake, *Mathematical Modelling*, 8 (1987) 245.
16. S. Ferreira, *Nuclear Engineering and Design*, 31 (1974) 346.
17. B. Ramaswamy, *Finite Elements in Analysis and Design*, 6 (1989) 319.
18. N.N. Greenwood and A. Earnshaw, *Chemistry of the elements*, 2nd Ed. Butterworth Heinemann, Oxford (1997).
19. A. Tegetmeier, D. Dittmar, A. Fredenhagen, R. Eggers, *Chem. Eng. and Processing*, 39 (2000) 399.
20. N.N. Akinfiev and L.W. Diamond, *Geochim. Cosmochim. Acta*, 67 (2003) 613.
21. L.W. Diamond and N.N. Akinfiev, *Fluid Phase Equilibria*, 208 (2003) 265.
22. Kh. Gertz and Hh. Loeschcke, *Helv. Physiol. Pharmacol. Acta.*, 12(4) (1954) C 72.
23. W.C. Edmister and B.I. Lee, *In: Applied Hydrocarbon Thermodynamics*, 2nd Ed., Gulf Publishing Company: Houston, TX, Vol1 (1984).
24. R. Span and W. Wagner, *J. Phys. Chem. Ref. Data*, 25 (6), (1996) 1509.
25. P. Chiquet, J.L. Daridon, D. Broseta, Thibeau, *Energy Convers. Mgmt.*, 48 (2007) 736.



---

# Chapter 4

## DENSITY-DRIVEN NATURAL CONVECTION OF CO<sub>2</sub> IN AQUIFERS

---

### ABSTRACT

*In this chapter we investigate the mass transfer of CO<sub>2</sub> injected into a (sub)-surface porous formation saturated with a liquid. In almost all cases of practical interest CO<sub>2</sub> is present on top of the liquid. Therefore, we perform our analysis to a porous medium that is impermeable from sides and that is exposed to CO<sub>2</sub> at the top. For this configuration density-driven natural convection enhances the mass transfer rate of CO<sub>2</sub> into the initially stagnant liquid. The analysis is done numerically using mass and momentum conservation laws and diffusion of CO<sub>2</sub> into the liquid. The effects of layering, anisotropy, aspect ratio and the Rayleigh number, which is dependent on the characteristics of the porous medium and fluid properties, are studied. This configuration leads to an unstable flow process. Numerical computations do not show natural convection effects for homogeneous initial conditions. Therefore a sinusoidal perturbation is added for the initial top boundary condition. It is found that the mass transfer increases and concentration front moves faster with increasing Rayleigh number. The results of this chapter have implications in enhanced oil recovery and CO<sub>2</sub> sequestration in aquifers.*

**KEYWORDS:** *CO<sub>2</sub>, Porous media, Density-driven natural convection, Rayleigh number, Aquifer, Enhanced mass transfer, Global warming*

**Published in:** International Journal of Heat and Mass Transfer, 50 (25-26), (2007) 5054.

#### 4.1. INTRODUCTION

We now turn to the case where CO<sub>2</sub> injected into a porous formation accumulates under the cap rock and subsequently dissolves into the formation liquid by molecular diffusion. As we have discussed in Chapters 2 and 3, CO<sub>2</sub> dissolution increases the liquid density [1,2] and eventually CO<sub>2</sub>-liquid interface becomes unstable [3-5]. For favorable conditions, natural convection occurs and enhances the mass transfer of CO<sub>2</sub>.

Several authors have studied the problem of occurrence of natural convection in a saturated porous layer subject to a sudden temperature rise from the bottom. Foster [6] showed that the critical time that elapses before the onset of the instability is independent of the depth of fluid layer for large Rayleigh numbers, a result which was verified experimentally [7]. Lapwood [8] determined the criterion for the onset of natural convection, which occurs at Rayleigh numbers above  $4\pi^2 \approx 40$ . Elder [9] and Wooding [10] suggested imposing small perturbations to the initial condition to observe the fingers of hot fluid protruding into the porous medium. Foster [6] stated that the fluid manifests convective behavior or “onset of instability” when the averaged vertical velocity disturbance had increased by a factor between one and three orders of magnitude of its initial value. Results of Foster [6] and Lapwood [8] showed that the critical time required for the onset of natural convection is inversely proportional to the square of permeability of the porous medium. Indeed the interface of two immiscible fluids can be unstable due to several mechanisms in the porous medium. The stability of saturated porous layer under natural convection effects by means of a linear stability analysis, the energy method and a two dimensional numerical model have been studied by several researchers and the criteria in which the boundary becomes unstable have been reported in the literature [11-15]. The results of these investigations show that the critical (fastest growing) wavelength for the onset of natural convection is inversely proportional to the Rayleigh number or the permeability of the porous medium. This means that for the high permeable reservoirs the conventional simulators will not give satisfactory results, since a very high resolution is required to numerically simulate such a problem.

The analogy between heat and mass transfer phenomena allows us to use the equations for the temperature-driven natural convection to treat the concentration-driven natural convection. We have applied this analogy to study the effects of natural convection in a porous medium saturated with liquid (water or oil) when over-pressurized CO<sub>2</sub> rich gaseous phase is in contact with the top. We investigate the effect of natural convection on the flow regime and quantify it numerically. The theory and the results described in this chapter are highly relevant to CO<sub>2</sub> sequestration in aquifers and CO<sub>2</sub> flooding for enhancing oil recovery in porous media. Before we turn to the

theory, we describe one experimental result in detail. This single experiment aims to emphasize the significance of natural convection on  $\text{CO}_2$  transport in porous media. Therefore, we do not use the theory for the interpretation of the experiments, because (a) the theory is in Cartesian system coordinates, whereas the experiments are in cylindrical coordinates, which poses difficult numerical problems and (b) the comparison would entail only a few experiments which can possibly lead to premature conclusions. Therefore, we leave the comparison between theory and experiments for future work.

## 4.2. EXPERIMENTAL

The experimental set-up introduced in Chapter 2 was used to perform the experiment. The glass tube was filled with sand grains (with an average diameter of  $1\text{ mm}$ ) up to the desired height ( $L=20\text{ cm}$ ) and then saturated with water. The small diameter of the glass tube allowed high pressure ( $11.6\text{ bar}$ ) experiments, but possibly introduces boundary effects as much less than 50 grains (some 10 grains) are in a horizontal cross-section. The porosity of the sand pack was measured as  $\varphi = 0.42$ . Using the Karman-Kozeny correlation the permeability was calculated to be  $k = 1200\text{ Darcy}$ .  $\text{CO}_2$  was slowly injected into the cell from the top, for about 30 seconds. When the  $\text{CO}_2$  pressure reached the desired value, the valve connecting to the gas source was closed and the cell was isolated. This was the starting time of the experiment. The gas pressure was recorded every 10 seconds in a computer.

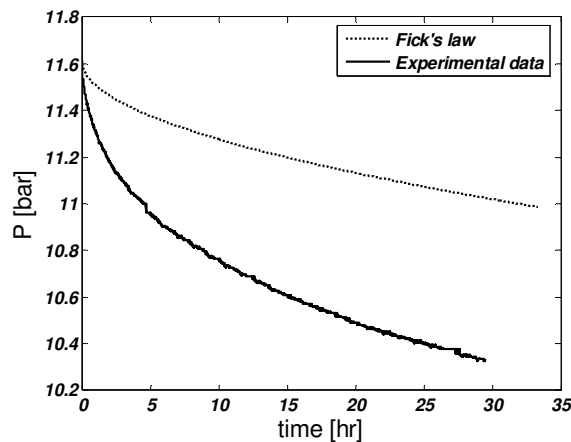


**Fig. 4.1:** Enhanced mass transfer of  $\text{CO}_2$  into a porous medium saturated with water; the experimental pressure decline for the porous medium is faster than the diffusion model prediction.

Figure 4.1 shows the experimental data (solid line) and the predicted pressure decline (dotted line) as calculated by Fick's law for stagnant water for an initial pressure  $p_i=11.6\text{ bar}$ . The dotted line was plotted by inserting a diffusion coefficient of  $D = 2.0 \times 10^{-9}\text{ m}^2/\text{s}$  and Henry's solubility constant  $k_H = 2980.1\text{ Pa}/(\text{mole} \cdot \text{m}^3)$  in the 1-D diffusion model described in detail in Chapter 2.

It can be seen from Fig. 4.1 that the mass transfer of CO<sub>2</sub> in a porous medium saturated with water at slightly elevated pressure is significantly higher than the mass transfer expected in stagnant water in a porous medium, calculated by Fick's law at the same pressure, but much slower than the mass transfer in the absence of a porous medium. As mentioned in the introduction we assert that density-driven natural convection is the responsible mechanism for enhanced mass transfer of CO<sub>2</sub> into the water present in porous media.

### 4.3. NUMERICAL MODEL

#### 4.3.1. Formulation

If the fluid in the porous medium is in mechanical equilibrium in a gravitational field the concentration in the  $z$  direction will be merely a function of the distance from the interface, i.e.,  $c = c(z)$ . Nevertheless, if the concentration varies in the  $x$  direction or if the vertical concentration gradient value exceeds a certain value, mechanical equilibrium is not possible and the fluid inside the porous medium starts to move to return the system to equilibrium. We try to formulate the occurrence of such phenomena.

Under consideration is the natural convection flow in a porous medium saturated with a fluid with a height  $H$  and length  $L$ . The permeability of the porous medium is  $k$  and its porosity is  $\varphi$ . The porous medium is impermeable on the left and right side. Initially the fluid is at rest and there is no CO<sub>2</sub> dissolved in the fluid. CO<sub>2</sub> is continuously supplied from the top, i.e., CO<sub>2</sub> concentration at the top is kept constant. We assume that CO<sub>2</sub>-liquid interface is relatively sharp and fixed. Moreover, we assume a no-flow boundary at the bottom of the porous medium. We disregard the presence of a capillary transition zone between the gas and the liquid phase. Hence we only model the liquid phase and the presence of the gas phase at the top is represented by a boundary condition for the liquid phase. The motion of fluid is described by Darcy's law driven by a density gradient. Darcy's law is combined with the mass conservation laws for the two components (CO<sub>2</sub> and either water or oil) to describe the diffusion and natural convection processes in the porous medium. We only expect a laminar regime since Rayleigh's number is low. The density gradient is the source of natural convection and therefore the density cannot be considered constant. However, we use Boussinesq approximation which considers density variations only when they contribute directly to the fluid motion.

#### 4.3.2. Governing equations

For the 2-D porous medium depicted in Fig. 4.2, the governing equations can be written as

(a) *Continuity Equation*

$$\varphi \frac{\partial \rho}{\partial t} + \frac{\partial(\rho U_x)}{\partial X} + \frac{\partial(\rho U_z)}{\partial Z} = 0 \quad , \quad (4.1)$$

(b) Darcy's law

$$U_x = -\frac{k}{\mu} \frac{\partial p}{\partial X} \quad , \quad (4.2)$$

$$U_z = -\frac{k}{\mu} \left( \frac{\partial p}{\partial Z} + \rho g \right) \quad , \quad (4.3)$$

(c) Concentration

$$\frac{\varphi \partial c'}{\partial t} + U_x \frac{\partial c'}{\partial X} + U_z \frac{\partial c'}{\partial Z} = \varphi D \left( \frac{\partial^2 c'}{\partial X^2} + \frac{\partial^2 c'}{\partial Z^2} \right) \quad . \quad (4.4)$$

The fluid becomes denser when CO<sub>2</sub> is present at the top part of the porous medium. We assume that the liquid density changes linearly with the increasing CO<sub>2</sub> concentration, i.e.,

$$\rho = \rho_0 (1 + \beta_c (c' - c'_0)) \quad , \quad (4.5)$$

from which we obtain

$$\frac{\partial \rho}{\partial X} = \rho_0 \beta \frac{\partial c'}{\partial X} \quad . \quad (4.6)$$

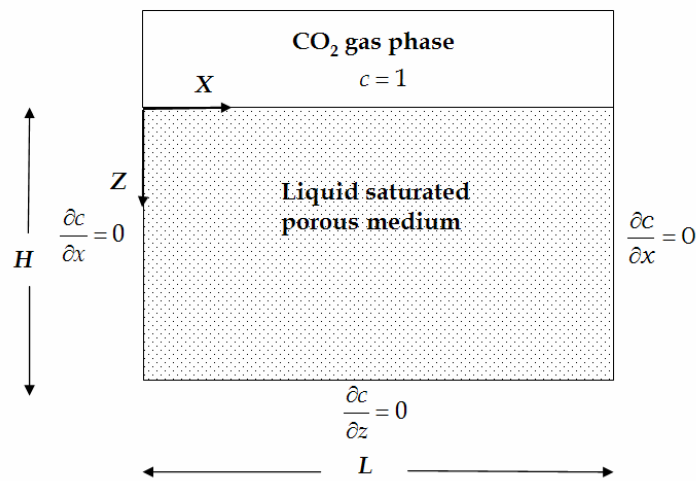


**Fig. 4.2:** Schematic of the system and coordinates

In Eqs. (4.1) to (4.4) there are four unknowns ( $U_X$ ,  $U_Z$ ,  $p$  and  $c'$ ). We eliminate the pressure by cross-differentiating Eqs. (4.2) and (4.3) (Eq. (4.2) with respect to  $Z$  and Eq. (4.3) with respect to  $X$ ). This leads to

$$\frac{\partial U_Z}{\partial X} - \frac{\partial U_X}{\partial Z} = \frac{kg\rho_0\beta}{\mu} \frac{\partial c'}{\partial X}. \quad (4.7)$$

Therefore, the equations to be solved are Eqs. (4.1), (4.4) and (4.7) to obtain  $U_X$ ,  $U_Z$  and  $c'$ .

#### 4.3.3. Dimensionless form of the equations

We take  $H$  as characteristic length and define the following dimensionless variables

$$x = \frac{X}{H}, \quad z = \frac{Z}{H}, \quad u_x = \frac{H}{\varphi D} U_X, \quad u_z = \frac{H}{\varphi D} U_Z, \quad \tau = \frac{D}{H^2} t, \quad c = \frac{c' - c'_i}{c'_0 - c'_i}$$

$$u_x = -\frac{\partial \psi}{\partial z}, \quad u_z = \frac{\partial \psi}{\partial x}, \quad \text{Ra} = \frac{k\rho_0\beta g H \Delta c'}{\varphi D \mu} = \frac{\Delta \rho g k H}{\varphi D \mu} \quad (4.8)$$

Thus, after applying the Boussinesq approximation the dimensionless form of the equations can be written as

$$\frac{\partial^2 \psi}{\partial x^2} + \frac{\partial^2 \psi}{\partial z^2} = \text{Ra} \frac{\partial c}{\partial x}, \quad (4.9)$$

$$\frac{\partial c}{\partial \tau} + \frac{\partial \psi}{\partial z} \frac{\partial c}{\partial x} - \frac{\partial \psi}{\partial x} \frac{\partial c}{\partial z} = \frac{\partial^2 c}{\partial x^2} + \frac{\partial^2 c}{\partial z^2}. \quad (4.10)$$

#### 4.3.4. Boundary and initial conditions

The initial condition of the problem is

$$\psi = 0, \quad c = 0 \quad \text{at } \tau = 0, \quad (4.11)$$

The boundary conditions of the problem are

$$\psi = 0, \quad \frac{\partial c}{\partial z} = 0 \quad \text{at } x = 0,$$

$$\psi = 0, \quad c = 1 \quad \text{at } z = 0,$$

$$\psi = 0, \quad \frac{\partial c}{\partial x} = 0 \quad \text{at } z = 1,$$

$$\psi = 0, \quad \frac{\partial c}{\partial x} = 0 \quad \text{at } x = A. \quad (4.12)$$

#### 4.3.5. Solution procedure

A modified version of the numerical method explained by Guçeri and Farouk [16] was applied to solve the system of Eqs. (4.9) and (4.10), i.e., the finite volume approach. A fully implicit method was used to obtain the transient values in Eq. (4.10). For each time step, we first compute the stream function from Eq. (4.9) and then we obtain the concentration profile by solving Eq. (4.10). The calculation procedure for each time step was repeated until the following criteria were satisfied

$$\left| \frac{c_{i,j}^{\tau+\Delta\tau} - c_{i,j}^{\tau}}{c_{i,j}^{\tau+\Delta\tau}} \right|_{\max} \leq \varepsilon \quad \text{and} \quad \left| \frac{\psi_{i,j}^{\tau+\Delta\tau} - \psi_{i,j}^{\tau}}{\psi_{i,j}^{\tau+\Delta\tau}} \right|_{\max} \leq \varepsilon.$$

$\varepsilon$  was set to  $10^{-5}$  in the numerical computations reported in this paper and the time step was chosen to be as small as  $10^{-5}$  (for small Rayleigh numbers) and  $10^{-6}$  (for  $Ra=1000$ ) for greater accuracy of the results. The developed code was checked with the literature benchmark [17,18] and the results were in excellent agreement with the published simulations independent of the number of grid cells.

To observe the non-linear behavior, i.e., the fingering behavior it was necessary to disturb the interface. Therefore in the numerical simulations, we start with a wavy perturbation on the top interface, i.e.

$$c(x, z = 0, t = 0) = 1 + A_0 \sin(2\pi x / \lambda) \quad (4.13)$$

where  $A_0 = 0.01$  and  $\lambda = 1/12$ . In reality fluctuations are caused by thermodynamic fluctuations (see Refs. [19, 20]) and porelevel perturbations. We ignore instabilities on the pore level (see, however, e.g. Refs. [21,22]).

#### 4.4. RESULTS AND DISCUSSION

In this section we show the results of our simulation for a 2-D isotropic homogeneous porous medium. We study the stability behavior by imposing small initial perturbations. This idea is following the normal mode method which is an analytical method that investigates the stability of a system of equations to infinitesimally small perturbations. It uses the idea that any perturbation can be decomposed into its Fourier components, i.e., in our 2-D example sinusoidal perturbation. We used wavenumbers ( $\alpha = 2\pi / \lambda$ ) between 10 and 270 to investigate the effect of the

wavelength. The normal mode method also uses the concept of fastest growing wavelength as the characteristic wave length which will emerge as the result of an arbitrary perturbation. Following this idea it is asserted that the long term behavior does not depend on the initial perturbation and hence reflects a material or structural property. For instance we observe (see for instance Fig. 4.7) that after some time the number of fingers are less than the number of periods in the initial perturbation. However, Fig. 4.14 shows that the growth rate of the perturbations is a weak function of the wavelength. Hence there will be some tenacity of the initial behavior and the pattern observed in the figures persists for some time before the number of fingers starts to decrease and starts to reflect structural properties.

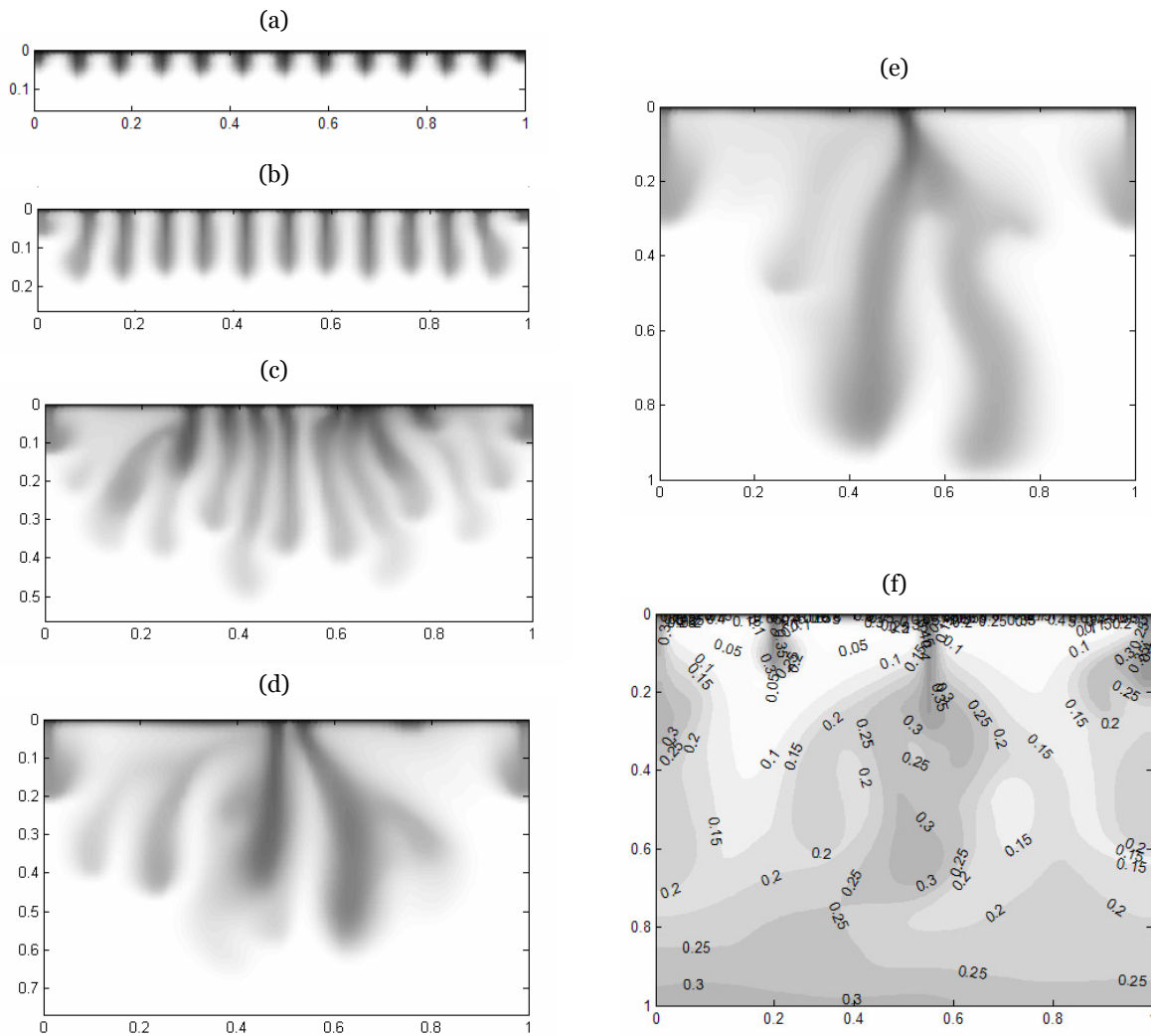


**Fig. 4.3:** Concentration profiles for  $Ra=10^4$  at  $\tau =$  (a)  $5 \times 10^{-5}$ , (b)  $1.5 \times 10^{-4}$ , (c)  $5 \times 10^{-4}$ , (d)  $7.5 \times 10^{-4}$ , (e)  $1.06 \times 10^{-3}$  and (f)  $0.002$

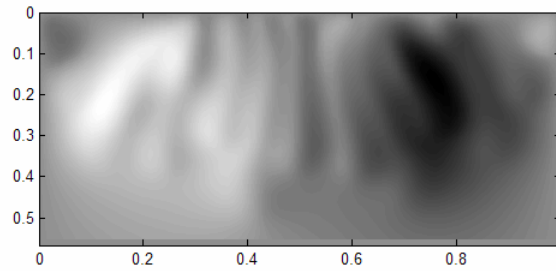


**Fig. 4.4:** Stream function profile for  $Ra=10000$  at  $\tau = 5 \times 10^{-4}$  with maximum value of 100 and minimum value of -120.

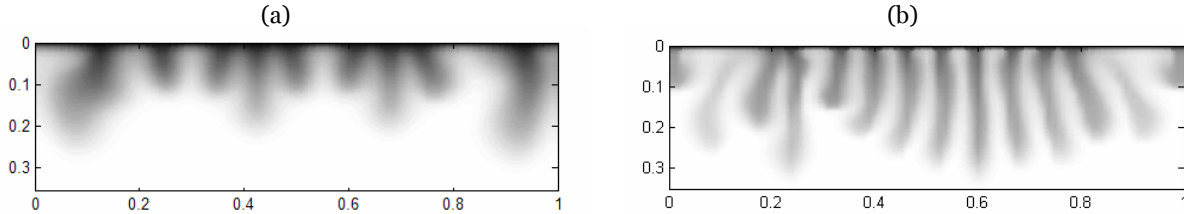
It is well established that for a certain fluid the dynamics of flow in the porous medium is strongly dependent on the characteristics of the porous medium, i.e., the permeability and for the non-cubic medium the ratio of length over height ( $L/H$ ). In this section we discuss the effect of the Rayleigh number ( $Ra$ ) and the aspect ratio ( $A$ ).

#### 4.4.1. Effect of Rayleigh number

Figure 4.3 shows the concentration profiles for  $Ra=10000$  and  $A=1$  at different times. This simulation was performed with  $81 \times 81$  grid cells. An initial perturbation, too small to be visible in the plots, was introduced in the system. Although the interface is disturbed and unstable, initially the imposed perturbation is damped and the  $\text{CO}_2$ -rich front moves in diffusion like manner. Therefore, in the simulations some time elapses before the small fingers appear. At early times, e.g.,  $\tau = 5 \times 10^{-5}$  (Fig. 4.3a) and  $\tau = 1.5 \times 10^{-4}$  (Fig. 4.3b), the number of fingers remain equal to the number put in the initial perturbation, i.e., 11. Nevertheless some fingers grow faster than the others (Fig. 4.3c). The laboratory results in the absence of a porous medium show that natural convection effects die out with time [5]. This can also be concluded from the experiment performed in a porous medium (Fig. 4.1). Therefore, it appears that the density difference, i.e., the driving force for natural convection decreases with time. This means that the concentration of  $\text{CO}_2$  is distributed more evenly as more  $\text{CO}_2$  is dissolved. In the numerical simulations this effect is also observed. In the simulations the number of fingers decreases with increasing time. It appears that the neighboring fingers coalesce by mutual interaction, a process which is governed by diffusion. This behavior has been also observed in Refs. [9-11]. A noticeable feature in our simulations is that the merging starts at the “trunk” rather than at the tip of the finger and from there it proceeds to the rest of the system. The merging of fingers continues until the end of the simulation.

Figure 4.4 shows a grey level plot of the stream function for  $\tau = 5 \times 10^{-4}$ . Dark areas correspond to high positive values of the stream function, with a maximum value of 100. Light areas correspond to negative values, with the lowest value of -120. Comparison with Figure 4.3d shows

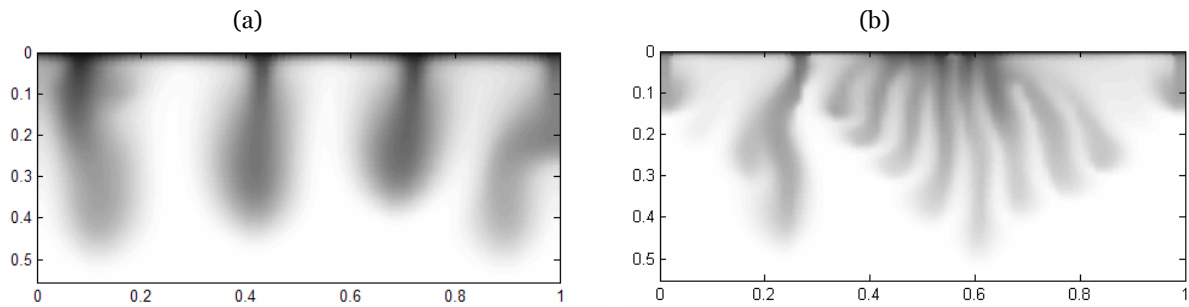
a similarity in the contours between concentration profiles and stream function profiles. This shows the importance of natural convection for the spreading of CO<sub>2</sub> in the cell. Moreover, it means that the dynamics of the non-linear behavior, i.e., the fingering of the CO<sub>2</sub> in the porous medium is governed by the flow field. Simulation results show that at  $\tau = 0.002$  the maximum and minimum values of the stream function are 80 and -90 respectively. This indicates that the values of stream function, i.e., the velocity components, decrease with increasing time due to the increasingly more homogeneous concentration distribution as time progresses.



**Fig. 4.5:** Concentration profiles for (a)  $Ra=2000$  at  $\tau = 1.4 \times 10^{-3}$  and (b)  $Ra=20000$  at  $\tau = 1.3 \times 10^{-4}$

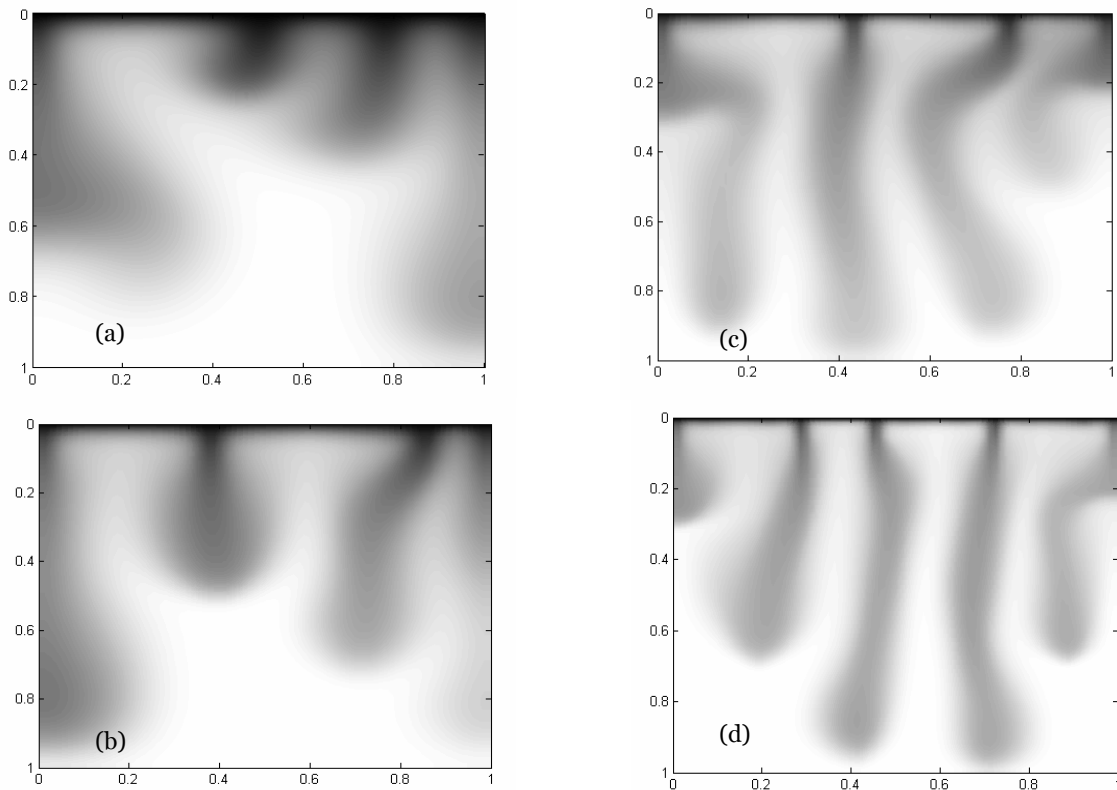
The concentration contours shown in Fig. 4.3 suggest that the late-stage behavior of the mass transfer process cannot be precisely predicted by the early-stage behavior of the system. This complexity in the flow behavior is strongly dependent on the Rayleigh number. To show the effect of different Rayleigh numbers we plot the early-stage concentration profiles of  $Ra=2000$  and  $Ra=20000$  and compare them with the base case  $Ra=10000$ . Furthermore, to show the late-stage flow behavior, in Fig. 4.7 we plot the concentration profile for  $Ra=500, 1000, 2000, 5000$  and  $20000$  when the CO<sub>2</sub> concentration of the bottom of the cell for the first time reaches 10% of the initial concentration at the top.

Figure 4.5 shows the concentration contours for  $Ra=2000$  at  $\tau = 2.5 \times 10^{-3}$  and  $Ra=20000$  at  $\tau = 1.3 \times 10^{-4}$ . Comparison of these profiles with Fig. 4.3c indicates that concentration front moves faster for the larger Rayleigh numbers. This means that natural convection affects the mass transfer significantly for larger Rayleigh numbers. For  $Ra=2000$  the number of fingers has been already decreased (Fig. 4.5a). However, some fingers merge together and form large fingers (Fig. 4.6a) and move without any further interactions until they reach the bottom (Fig. 4.7c). Comparing Fig. 4.5b and Fig. 4.6b shows that the nonlinear behavior of the fingering is more pronounced at higher Rayleigh numbers. The stream function profiles corresponding to the concentration profiles shown in Fig. 4.6 preserve a similar pattern to the concentration profiles, as discussed previously in Fig. 4.4. However, the values of the stream function increase with increasing Rayleigh number.



**Fig. 4.6:** Concentration profiles for  $Ra=2000$ , at (a):  $\tau = 2.5 \times 10^{-3}$  and (b)  $Ra=20000$  at  $\tau = 2.2 \times 10^{-4}$

The late-stage flow behavior of different Rayleigh numbers is shown in Fig. 4.7. As discussed above, for  $Ra < 5000$  at the initial stages the smaller fingers merge together and progress without any significant interactions with the neighboring fingers. An interesting feature in the simulation results is that for smaller Rayleigh numbers  $CO_2$  flows downwards close to the boundaries. In another words, the flow is faster close to the boundaries than near the center for the small Rayleigh numbers. The time in which the  $CO_2$  front (10%) reaches the bottom of the cell is plotted in Fig. 4.8 for different Rayleigh numbers. This figure suggests that given the conditions of our simulations (the initial perturbation, number of grid cells and etc.) there is a linear relation between the inverse of this time and Rayleigh number. This linear relation emphasizes the importance of the convection effect compared to diffusion.



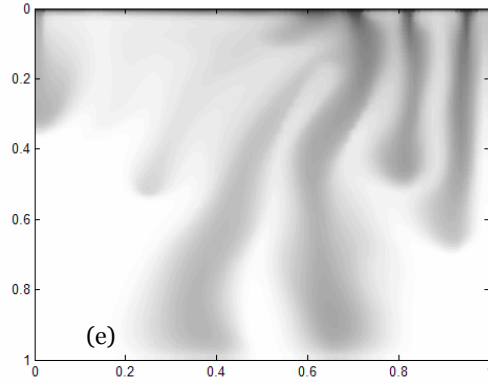


**Fig. 4.7:** Concentration profiles for (a)  $Ra=500$  at  $\tau = 2.47 \times 10^{-2}$  (b)  $Ra=1000$  at  $\tau = 1.06 \times 10^{-2}$ , (c)  $Ra=2000$  at  $\tau = 5.1 \times 10^{-3}$ , (d)  $Ra=5000$  at  $\tau = 2.0 \times 10^{-3}$  and (e)  $Ra=20000$  at  $\tau = 6.25 \times 10^{-4}$  (Figs. 4.7a-4.7d are in the previous page)

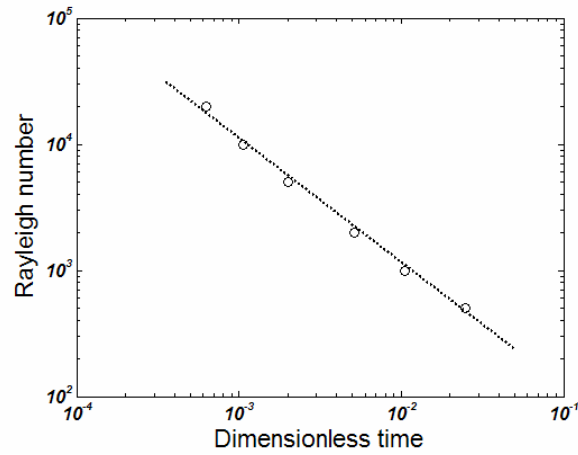


**Fig. 4.8:** The time required for the CO<sub>2</sub> concentration to reach to  $0.1c_0$  at the bottom for the first time for different Rayleigh numbers

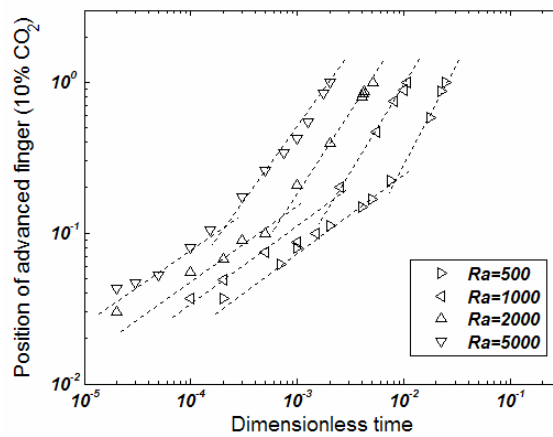


**Fig. 4.9:** Progress of the tip of the most advanced finger for different Rayleigh numbers as a function of time and the change from square-root behavior to linear behavior.

Figure 4.9 shows the progress of the tip position of the most advanced finger with time for different Rayleigh numbers in a log-log plot. With the term *advanced tip position* we mean the distance from the gas-liquid interface to the contour in which the  $\text{CO}_2$  reaches 10% of the initial concentration at the top boundary. This plot shows that initially the  $\text{CO}_2$  front moves proportional to the square-root of time, i.e., the initial behavior is controlled by diffusion. In all cases, after some time the relation becomes linear, i.e., convection starts to play a role in the system. The time, in which the relation changes to linear behavior, decreases with increasing Rayleigh number. For the number of grid cells used in our simulation it was difficult to get the exact point of the front for higher Rayleigh numbers; therefore these values are not plotted in Fig. 4.9.

#### 4.4.2. Effect of aspect ratio (A)

Figures 4.10 and 4.11 show the simulation results for  $Ra=10000$  and different aspect ratios. Comparison of these plots with concentration profiles in Fig. 4.3 yields that the interaction between fingers decreases with increasing aspect ratio. The number of fingers that survive to reach the bottom of the cell in the  $A=4$  case is equal to the number of the initially imposed fingers indicating that the interaction between the fingers decreases with increasing the aspect ratio. Nevertheless, the time required for the 10%  $\text{CO}_2$  front to reach the bottom increases with increasing aspect ratio.

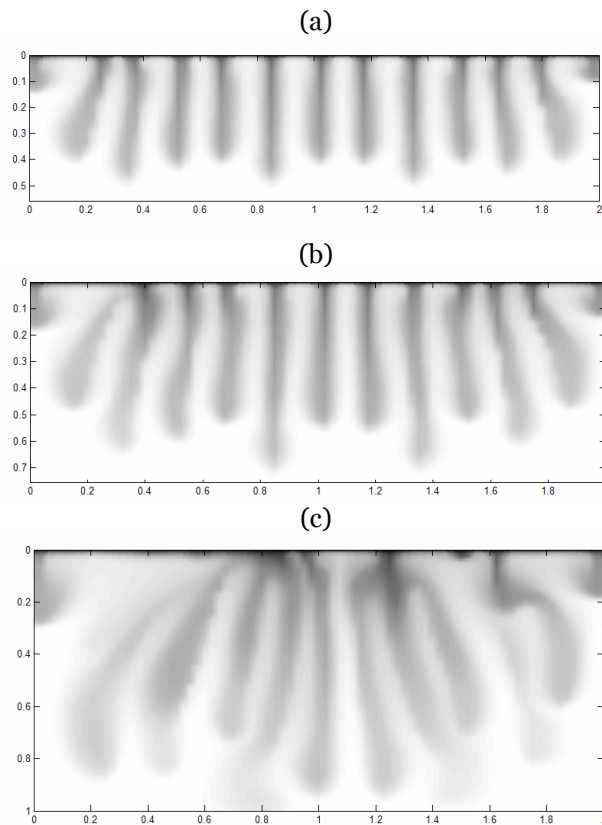


**Fig. 4.10:** Concentration profiles for  $A=2$  and  $Ra=10^4$  at  $\tau =$  (a)  $5 \times 10^{-4}$ , (b)  $7.5 \times 10^{-4}$  and (c)  $1.39 \times 10^{-3}$

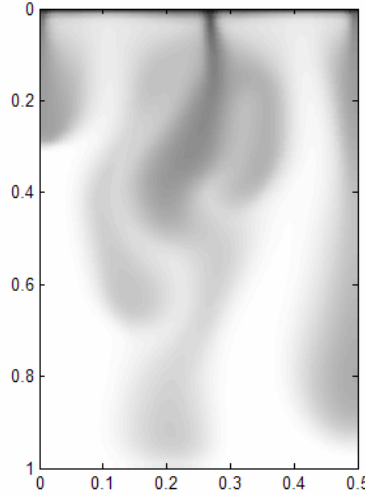


**Fig. 4.11:** Concentration profiles for  $A=0.5$  and  $Ra=10000$  at  $\tau = 9.3 \times 10^{-4}$

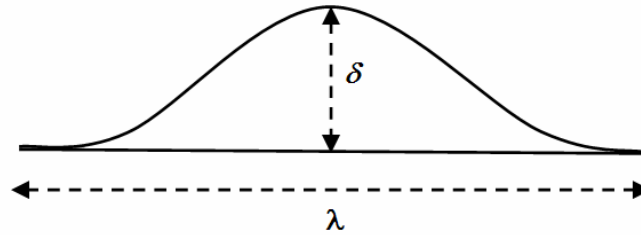


**Fig. 4.12:** Schematic of the imposed sinusoidal perturbation at the interface

#### 4.4.3. Growth of the disturbance

In the numerical simulations presented in this paper the imposed initial disturbance was the sinusoidal disturbance with wavelength  $\lambda$  and amplitude  $\delta$  (Fig. 4.12). The wave-number is defined as  $\alpha = 2\pi / \lambda$ . We assume that any disturbance grows exponentially

$$\delta(\tau) = \delta_0 \exp(\sigma\tau). \quad (4.14)$$

$\delta_0$  is a constant, which can be determined by the initial condition of the interface, and  $\sigma(\alpha)$  is the wavelength dependent disturbance growth factor. Equation (4.14) means that a plot of  $\ln(\delta)$  versus time is a straight line. The slope of this straight line gives the growth factor  $\sigma$ . Depending on the scope of  $\sigma$  it is possible to find the fastest growing wave-number at which the first derivative of  $\sigma$  towards the wave number  $\alpha$  becomes zero. The determination of the fastest growing wave-number is as follows:

In the simulations for a certain Rayleigh number we determine the average amplitude of one arbitrary contour line of the concentration profile (in this paper  $c = 0.4$  line) for different wave numbers. We plot the average amplitudes of the  $c = 0.4$  contour line versus time in a semi-

logarithmic plot. The slope of the obtained lines gives  $\sigma$  of the selected wave-number. We plot the obtained growth factors versus wave-number to get the value of the fastest growing wave-number.

In Fig. 4.13 we present plot of  $\ln(\delta)$  vs. time only for  $Ra=2000$  for different wave-numbers. The regression coefficient of the fitted lines were all larger than 0.97. This means that the imposed instabilities grow linearly in agreement with Eq. (4.14). However, it was noticed that in some simulations when we considered the late-stage points the regression coefficients became less than 0.95, suggesting that at the later stage the growth of the instabilities is not linear. Therefore, in order to find fastest growing wave-number we omitted the late-stage points when the regression coefficient was less than 0.95. The non-linear growth of fingers at later stages has been also reported by Park et al. [23]. Figure 4.14 shows the growth factor as a function of wave-number for  $Ra=2000$  and  $Ra=1000$ . The extracted growth rates are presented in Table 4.1 and Table 4.2 for  $Ra=1000$  and  $Ra=2000$  respectively. It is clear from these Tables and Fig. 15 that the fastest growing wave-number is between 50-75 for  $Ra=1000$  and 25-37 for  $Ra=2000$ .

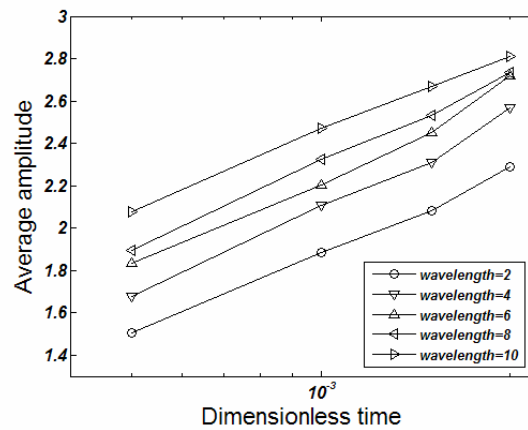


**Fig. 4.13:** Logarithm of the average amplitude (distance from interface) of the growing fingers versus time for  $Ra=2000$

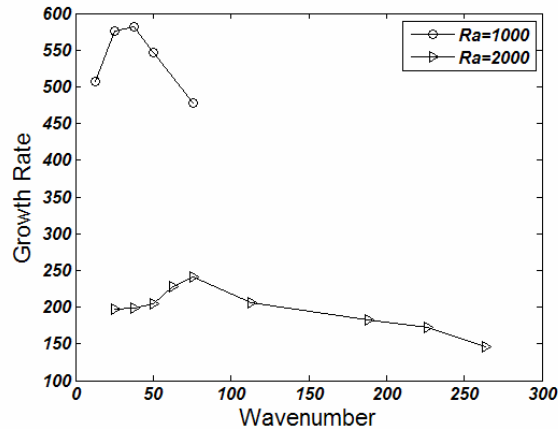


**Fig. 4.14:** Growth rate coefficient as a function of wave-number for  $Ra=1000$  and  $Ra=2000$

**Table 4.1:** Wavelengths and corresponding growth rates for  $Ra=1000$ 

$1/\lambda$	$\sigma$
4	196.95
6	198.122
8	203.82
10	227.2
12	241.66
18	206.24
30	183.22
36	173.13
42	145.68

**Table 4.2:** Wavelengths and corresponding growth rates for  $Ra=2000$ 

$1/\lambda$	$\sigma$
2	507.68
4	575.78
6	582.32
8	547.16
10	477.72

#### 4.5. COMPARISON WITH BULK RESULT

In Fig. 4.15 we plot the pressure history of two experiments in a glass tube with radius of 3.5mm. In one experiment the glass tube is filled with only water (Chapter 1) and in the other one the tube is filled with porous media of the same height and saturated with water (this chapter). This figure shows that, although natural convection enhances the transfer rate in water-saturated porous media, its significance is less compared to bulk liquid. One has to remember that the critical time for the onset of natural convection is inversely proportional to the Rayleigh number. The Rayleigh number,  $Ra$ , appears in the flow equations of both cases and therefore the rate of flow is an increasing function of  $Ra$ . The equations of  $Ra$  imply that:  $(Ra)_{pm} \propto kL$  and  $(Ra)_{bulk} \propto L^3$ . In the comparison of the pressure behavior of the experiments with and without porous media the following points should be considered: First, the critical  $Ra$  for onset of convection in porous media is about 40, while for a clear fluid (or bulk liquid) convection occurs beyond a critical  $Ra$  of approximately 1700 [24]. Secondly, from Hagen–Poiseuille equation the permeability of the tube with radius of  $r_t$  is  $k = r_t^2 / 8$ , which gives the value of  $k=1.5 \times 10^6$  Darcy for a tube with radius of 3.5mm, whereas for porous medium the permeability is 1200 Darcy, i.e., a factor of 1000 difference. This can explain a factor of 10 difference in the transfer rates of the two systems

presented in Fig. 4.15. It should be also mentioned that the amount of water in porous media experiment is much less than bulk experiment and therefore the equilibrium pressures are different.

Nevertheless in both experiments, the early time behavior is governed by diffusion before the onset of the natural convection. Vella and Huppert [25] show that for Sleipner field, in which around  $10^9$  kg of  $\text{CO}_2$  is injected to a 200 m thick layer each year, with the typical measured values for the porosity ( $\varphi = 0.31$ ) and permeability of  $0.7 \leq k \leq 5$  Darcy, the onset of convection may vary between few days and 14.2 years. This suggests that the effect of gravity instabilities (convection) is indeed important in the field. Similar to the experiments with the *bulk fluid*, natural convection effects in a saturated porous media also die out with time and eventually stops as more  $\text{CO}_2$  is dissolved in brine (the driving force for convection decreases). This is one of the most important findings of our experiments, which is confirmed with the recent experiments conducted in porous media saturated with water [26] and shown by simulation results in this chapter.

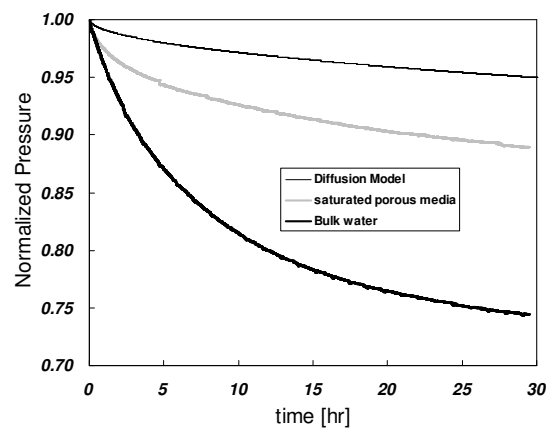


**Fig. 4.15:** Comparison of the pressure history of the experiments with and without porous media. The experiments are done in a glass tube with radius of 3.5 mm at  $P_i=11$  bar.

#### 4.6. CONCLUSIONS

In this chapter we studied the transient density-driven natural convection problem when the top of the porous medium initially saturated with a liquid is exposed to a  $\text{CO}_2$ -rich gaseous phase. With the aid of dimensionless groups it is possible to study the effect of different parameters on the fate of injected  $\text{CO}_2$  into the porous medium. It is shown that the density-driven natural convection with the boundaries used in this paper has a significant effect on the mass transfer. The effect of natural convection increases with increasing Rayleigh number that depends both on the characteristics of the porous medium, mainly the permeability, and the fluid properties. With increasing aspect ratio, the time to see the beginning of the natural convection decreases. The

simulation results show that the non-linear behavior of the flow is strongly dependent on the Rayleigh number. With increasing Rayleigh number natural convection effects become more significant. However, as time elapses the number of the fingers decreases due to the decreasing effect of natural convection. This effect can be also observed from the decreasing values of the stream function. Initially, the CO<sub>2</sub> front moves proportional to the square root of time for different Rayleigh numbers and then the relationship becomes linear. However, the time in which the switching happens decreases with increasing Rayleigh number.

#### 4.7. NOMENCLATURE

$A$	Aspect ratio, $H / L$ [-]
$c$	Dimensionless concentration [-]
$c'$	Concentration [mole/m <sup>3</sup> ]
$D$	Diffusion coefficient [m <sup>2</sup> /s]
$g$	acceleration due to gravity [m/s <sup>2</sup> ]
$Gr$	Grasshof number [-]
$H$	Height of the porous medium [m]
$k$	Permeability of the porous medium [ $m^{-2}$ ]
$k_H$	Henry's solubility constant [Pa/(mole.m <sup>3</sup> )]
$L$	Length of the porous medium [m]
$P$	Pressure [Pa]
$Ra$	Rayleigh number [-]
$t$	Time [sec]
$u$	Dimensionless velocity [-]
$U$	Velocity [m/s]
$z$	Distance from the bottom of the tube [m]
$x$	Dimensionless distance in X coordinate
$z$	Dimensionless distance in Z coordinate

#### **Greek symbols**

$\alpha$	Wave-number
$\beta_c$	Volumetric expansion factor [m <sup>3</sup> /mole]
$\delta$	Amplitude [-]
$\varphi$	Porosity of the porous medium [-]
$\lambda$	Wavelength [-]
$\mu$	Viscosity of the fluid [ $kg / m - sec$ ]
$\psi$	Stream function [m <sup>3</sup> m <sup>-1</sup> sec <sup>-1</sup> ]

$\rho$	Density of the fluid [ $kg / m^3$ ]
$\sigma$	Dimensionless growth rate [-]
$\tau$	Dimensionless time [-]

### Subscripts

$0$	Value of the quantity at the boundary
$i$	Reference value of the quantity
$x$	Quantity in $x$ -direction
$z$	Quantity in $z$ -direction

### 4.8. REFERENCES

1. L. Gmelin, *Gmelin Handbuch der anorganischen Chemie*, 8. Auflage. Kohlenstoff, Teil C3, Verbindungen., pp 64-75 (1973).
2. S. Ashcroft and M. Ben Isa, *J. Chem. Eng. Data*, (1997) 1244.
3. E. Lindeberg and D. Wessel-Berg, *Energy Convers. Manage.*, 38, (1997) S229.
4. Ch. Yang and Y. Gu, *Ind. Eng. Chem. Res.*, 45, (2006) 2430.
5. R. Farajzadeh, A. Barati, H.A. Delil, J. Bruining, P.L.J. Zitha, *Petrol. Sci. and Technol.*, 25 (2007) 1493.
6. T.D. Foster, *Physics of fluids*, vol. 8, no. 7, 1249-1257 (1965).
7. T.D. Foster, *Physics of fluids*, vol. 8, no. 8, (1965) 1770.
8. E.R. Lapwood, *Proc. Camb. Phil. Soc.*, 44, (1948) 508.
9. J. W. Elder, *J. Fluid Mech.*, 32, (1968) 69.
10. R. A. Wooding, *J. Fluid Mech.*, 39, (1969) 477.
11. A. Riaz, M. Hesse, A. Tchelepi, F.M. Orr, *J. Fluid Mech.*, 548, (2006) 87.
12. K.L. Walker and G.M. Homsy, *J. Fluid Mech.*, 87, (1978) 449.
13. J. Ennis-King, I. Preston and L. Paterson, *Physics of Fluids*, 17, (2005) 84107.
14. J. P. Caltagirone, *J. Mech. Appl. Math.*, vol. XXXIII, Pt. 1., (1980) 47.
15. X. Xu, Sh. Chen, D. Zhang, *Adv. Water Res.*, 29, (2006) 397.
16. S. Guçeri and B. Farouk, *Numerical solutions in laminar and turbulent natural convection*, In: Natural convection, Fundamentals and applications, S. Kakac, W. Aung, R. Viskanta, Hemisphere publication, 615-655 (1985).
17. M. Sathiyamoorthy, T. Basak, S. Roy, I. Pop, *Int. J. Heat and Mass Trans.*, 50 (3-4) (2007) 766.
18. A. Bahloul, *Int. J. Thermal Sci.*, 45, (2006) 635.
19. L.D. Landau and E.M. Lifshitz, *Statistical Physics: Course of Theoretical Physics*, Volume 5, 2en revised English Ed., Pergamon Press (1969).
20. R. D. Gunn, W. B. Krantz, *SPE 6735-PA* (1980).
21. Y. C. Yortsos, B. Xu and D. Salin, *Physical Review Letters*, Vol 79, No. 23 (1997).
22. M. Parlar, Y. C. Yortsos, *SPE 16969* (1987).
23. Park C.W., Gorell S and Homsy G.M., *J. Fluid Mech.*, 141, (1984) 275.
24. H. Ozoe, M. Takemoto, S.W. Churchill, *Numerical Heat Transfer, Part B: Fundamentals*, 9 (3) (1986), 323.
25. D. Vella and H.E. Huppert, *J. Fluid. Mech.*, 555 (2006) 333.
26. R. Farajzadeh, F. Farshbaf Zinati, P.L.J. Zitha, J. Bruining, Proc. 11th European Conference on Mathematics in Oil Recovery (ECMOR X1), Bergen, Norway, 8-11 September 2008.



## **PART II.**

### **Foam Films**



---

## Chapter 5

# PROPERTIES OF FOAM FILMS STABILIZED WITH ALPHA OLEFIN SULFONATE (AOS)

---

### ABSTRACT

*Alpha Olefin Sulfonate (AOS) surfactants have shown outstanding detergency, lower adsorption on porous rocks, high compatibility with hard water and good wetting and foaming properties. These properties make AOS an excellent candidate for foam applications in enhanced oil recovery. This chapter summarizes the basic properties of foam films stabilized by an Alpha Olefin Sulfonate surfactant. The foam film thickness and contact angle between the film meniscus and film-forming solution were measured as a function of NaCl and AOS concentrations. The critical AOS concentration for formation of stable films was obtained. The critical NaCl concentration for formation of stable Newton black films was found. The dependence of the film thickness on the NaCl concentration was compared to the same dependence of the contact angle between the film and its meniscus. With increasing NaCl concentration the film thickness decreases gradually while the contact angle (and respectively the free energy of film formation) increases, in accordance with the classical DLVO theory. The surface tension isotherms of the AOS solutions were measured at different NaCl concentrations. They coincide on a single curve when plotted as a function of mean ionic activity product. Our data imply that the adsorption of AOS is independent of NaCl concentration at a given mean ionic activity.*

**KEYWORDS:** *Foam film, AOS surfactant, Monolayer, Film thickness, Surface tension, Adsorption, Ionic activity*

**Published in:** *Colloids and Surfaces A: Engineering Aspects*, 324 (2008) 35.

## 5.1. INTRODUCTION

Foam is a dispersion of a gas phase in a continuous liquid phase stabilized by surfactants and/or nano-particles [1,2]. The gas breaks into bubbles that are separated by thin liquid films, also called lamellae. During foam flow in porous media the foam films bridging the pore throats tend to block flow path for the gas [3,4]. Because pushing a large number of lamellae through complex pores requires a lot of energy, foam in porous media is characterized by a yield stress and, for stresses larger than the yield stress, by a high effective viscosity. Owing to these characteristics foam is an excellent mobility control agent, which was extensively used to control fluid flow during oil and gas recovery [3,4] and during the cleaning up of contaminated soils [5]. Foam is capable of improving the CO<sub>2</sub> spreading during geological storage.

The key factor for the success of the above foam processes in the geosciences realm are the choice of surfactant with respect to the injected gas, type of the porous medium and chemical/physical properties of the fluids in the porous medium, i.e., water and oil. A suitable surfactant should be capable of generating ample and stable foam in the reservoir rock and in presence of oil at high pressures and temperatures. Furthermore, the adsorption of surfactant on the rock should be as low as possible. Surfactant adsorption decreases the surfactant concentration and therefore limits the distance the surfactant will propagate into the oil reservoir before its concentration becomes too low for an effective foam generation [6]. The stability of foam in the presence of oil is an important challenge for scientists and engineers intending to use foam as an enhanced oil recovery (EOR) method. Note that in a simplistic view oil is often regarded as an anti-foam. In general, the selected surfactant in EOR foam has to balance chemical costs against the expected gas mobility reduction, taking into account surfactant adsorption and foam-oil interaction.

The long-term stability of foam is subsidiary to the stability of the single separating liquid films-lamellae. Therefore, to have a better control on the foam properties, it is essential to understand the basic properties of the lamella. Furthermore foam films are rather good model systems for studying the interfacial phenomena and the interactions between interfaces [2,7]. The structure and the properties of foam films have been intensively studied, and they are well documented in the literature. The main results are summarized in books and review articles [e.g. Refs. 2,8-13].

There are two equilibrium states of foam films that are defined by the thermodynamic conditions. Common films are usually formed when the salt concentration in the film forming solution is low. These films have a sandwich-like structure and consist of two monolayers of adsorbed surfactant molecules stabilizing the film separated by an aqueous layer. The film thickness decreases when the salt concentration in the film-forming solution increases. The reflectivity from the film

decreases so much at a certain film thickness (respectively, salt concentration) that the films look black in reflected light. Hence, these films are called Common Black Films (CBF). The interactions in these films are adequately described by the classical DLVO approach [14]. Their stability is due to the interplay between a repulsive electrostatic ( $\Pi_{EL}$ ) and an attractive van der Waals ( $\Pi_{vW}$ ) contributions to the disjoining pressure,  $\Pi$ .  $\Pi_{EL}$  decreases with the addition of salt to the film forming surfactant solution, until it is fully suppressed. Very thin Newton Black Films (NBF) are formed at that point. These films have bilayer structures: the two surfactant monolayers are close to each other, separated only by few layers of hydration water. The stability of these films is governed by short-range interaction forces. The application of DLVO theory to such thin foam films is not possible because this theory does not take into account both spatial and or surfactant density fluctuations [13,15]. The two states of foam films are shown schematically in Fig. 5.1. In both cases the transition from thicker common film to the thinner black films (either CBF or NBF) occurs through the formation of black spots in the thicker film.

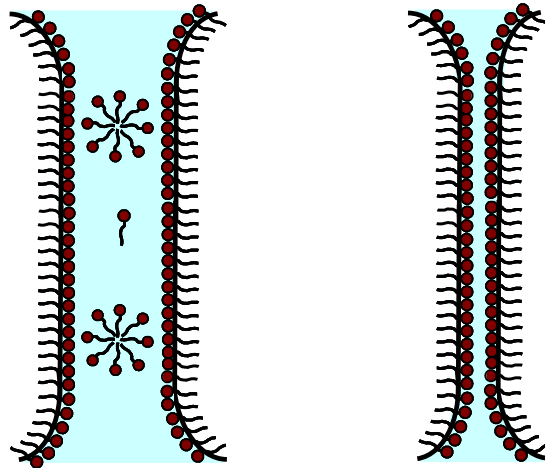


**Fig. 5.1:** Schematic of two equilibrium states of the foam films: A common black film (left) has a central aqueous layer which is sandwiched between two surfactant monolayers. A Newton black film (right) has a bilayer structure where two surfactant monolayers are close to each other separated only by few layers of hydration water.

In this chapter the properties of foam films prepared from AOS solutions in presence of different amounts of electrolyte (NaCl) are investigated. The thickness and contact angle of the films (Fig. 5.2) were measured. Complementary studies on surface tension of AOS surfactant solutions were performed for better understanding of the results. Thus, the surface density of the surfactant in their adsorption layers on water surface was estimated.

## 5.2. MATERIALS AND METHODS

*Choice of the surfactant:* Alpha Olefin Sulfonate (AOS) surfactant was chosen to carry out the experiments because it has comparatively lower adsorption on sandstones than other commercial

surfactants like, for instance, Sodium Dodecyl Sulfate (SDS) [16]. Moreover, AOS surfactants have outstanding detergency, high compatibility with hard water and good wetting and foaming properties with  $\text{CO}_2$  even when the porous medium is partially saturated with oil (see Chapter 8). These properties make AOS an excellent candidate for  $\text{CO}_2$ -foam applications, e.g., EOR projects that aim to produce more oil from underground reservoirs.

*Surface Tension:* The surface tensions were measured using a K11 tensiometer (Krüss GmbH, Germany) using the DuNouy ring method. The solutions were prepared at least 12 hours prior to the experiments and sonicated for 30 minutes. The solutions remained still in the Teflon vessels for two hours before the measurements to assure the equilibrium adsorption at the liquid/air surface. The solution remained still for at least 30 minutes between every single measurement to recover the equilibrium.

*Foam Film Experiments:* The experiments were performed in a Scheludko-Exerowa ring cell [2,17] with an inner radius of the ring ( $R_{cap}$ ) of 2.5 mm. Detailed description of the cell and the used experimental procedures are given in [2,17]. The ring cell was placed in a closed thermostat vessel saturated with vapor of the studied solution. Two hours were allowed for reaching equilibrium, before the measurement was started. A horizontal microscopic film with constant radius was formed in the glass ring, by suction of the film forming solution from the ring through the capillary at a low capillary pressure. The film starts thinning after its formation due to drainage. It either ruptures during the thinning process or an equilibrium film is formed at the end of the drainage process.

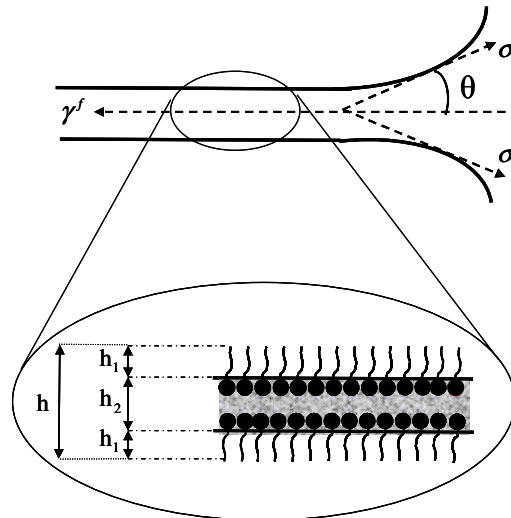


**Fig. 5.2:** A single foam film consists of an aqueous core with thickness  $h_2$  sandwiched between two adsorbed monolayers of surfactant with the thickness of  $h_1$ . In this model the Plateau borders are neglected. The liquid layer and the surfactant monolayers are assumed to be homogenous. The contact angle,  $\theta$ , is formed at the transition between the film and the bulk solution.

*Film Thickness:* The equivalent solution film thickness  $h_w$  was measured micro-interferometrically [2,17-19] by assuming an optically homogeneous film with the same refractive index  $n$  as that of the bulk solution from which the film was formed.

$$h_w = \frac{\lambda}{2\pi n} \arcsin \sqrt{\frac{I/I_m}{1 + \frac{4R_h}{(1-R_h)^2}(1-I/I_m)}} \quad (5.1)$$

where  $R_h = (n-1)^2 / (n+1)^2$ ,  $\lambda$  is the wavelength of the light (in this study  $546 \text{ nm}$ ),  $I_m$  and  $I$  are the maximum intensity of the light and the intensity of the light reflected from the film at each moment during the thinning process or in equilibrium.

In fact the film consists of two surfactant monolayers and an aqueous layer in between. Thus, the film thickness  $h$  is different from that of  $h_w$ . The film thickness  $h$  was calculated by assuming a three-layer model of the film [18] where the aqueous solution core of thickness  $h_2$  and refractive index  $n_2$ , is flanked by two layers of hydrophobic alkyl chains of the adsorbed surfactant molecules, with thickness  $h_1$  and refractive index  $n_1$ . The aqueous core includes the hydrophilic head groups of the surfactant molecules. This three-layer model was used to calculate the film thickness  $h$  from the experimentally obtained  $h_w$  values using the relation [19]:

$$h = 2h_1 + h_2; \quad h_2 = h_w - 2h_1 \frac{n_1^2 - 1}{n_2^2 - 1} \quad (5.2)$$

The correction is especially important for thin NBFs. We assumed that the thickness  $h_1 = 1.35 \text{ nm}$  [19] as used for similar films and the refractive index  $n_1$  as that of pure tetradecane  $n_1 = 1.4290$  [20].  $n_2 = n$  is the refractive index of the surfactant solution.

*Contact Angle:* The contact angle between the film and bulk solution,  $\theta$ , (Fig. 5.2) was measured by the expansion method at constant pressure [21]. During the drainage process, due to local fluctuation of the film thickness black spots appear. These spots grow and finally cover the whole film. The film expands shortly (in less than a second) at that moment because of the new force balance between the film and the bulk meniscus. Thereafter the film size remains constant without any further change. The radius of the thinner equilibrium black film  $r_2$  is greater than the radius of the thicker film  $r_1$  just before the first black spot appears. The contact angle was evaluated using the relation [21]

$$\sin \theta = \frac{\delta_2^2 - \delta_1^2}{\delta_2} \quad (5.3)$$

where,  $\delta_1 = r_1 / R_{cap}$  and  $\delta_2 = r_2 / R_{cap}$ . This calculation is based on the estimation of the pressure in the system foam film/meniscus before and after the film expansion which supplement the formation of the black films and the assumption that this pressure does not change during the film transition. It should be mentioned that the method is more precise when  $\theta > 1^\circ$ .

All measurements (thickness, contact angle and surface tension) were conducted at room temperature ( $T = 25 \pm 0.5^\circ C$ ) and every point presented is average of at least 10 single measurement. The standard deviation is less than 5% of the mean values.

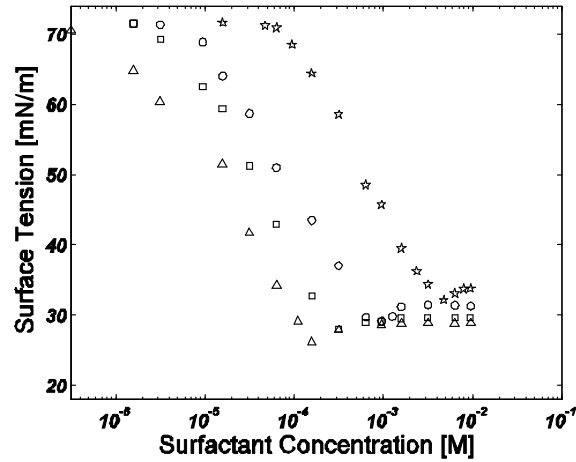


**Fig. 5.3:** The measured surface tension isotherms ( $T=25^\circ C$ ) vs. surfactant concentration with different NaCl concentrations: (\*) no salt, (o)  $c_{NaCl}=0.05 M$ , (□)  $c_{NaCl}=0.20 M$  and (Δ)  $c_{NaCl}=0.50 M$ . The addition of NaCl alters the shape of the curves. Higher amount of NaCl shifts the surface tension curves to lower surfactant concentrations.

**Table 5.1:** CMC values of AOS solutions at different NaCl concentrations obtained from the surface tension isotherms presented in Fig. 5.3.

NaCl concentration [M]	CMC [wt% AOS]
0.50	0.004
0.20	0.007
0.05	0.018
0.00	0.100

**Materials:** The surfactant used was (C<sub>14</sub>-C<sub>16</sub>)-alpha-olefin sulfonate, AOS (Stepan company, USA). This surfactant is anionic, with industrial purity and was used as received without any further purification. The general structure of olefin surfactants is  $R-SO_3^-Na^+$ , where  $R$  represents the hydrophobic group. In our case, the number of the carbon atoms in the surfactant structure is between 14 and 16 and the molecular weight of the surfactant is  $M_w=315$  gr/mol. Sodium chloride (NaCl) GR grade (Merck, Darmstadt, Germany) was roasted at  $600^\circ C$  for 5 hours to remove the

organic impurities, some of which might be surface active. All solutions were prepared with deionized water from a Milli-Q purification setup (Elga Labwater, Germany). The specific resistance of the water was  $18.2 \text{ M}\Omega\text{cm}$ , the pH was 5.5 and the total organic carbon (TOC) value was  $<10 \text{ ppb}$ .

### 5.3. RESULTS AND DISCUSSION

*Surface Tension:* The measured surface tension isotherms for different concentrations of the added electrolyte, NaCl, are presented in Fig. 5.3. The value of surface tension decreases with increasing surfactant concentration for all electrolyte concentrations until it reaches a minimum. The existence of a minimum in the curves indicates that the surfactant contains diverse surface active molecules with different activity or contains some impurities. The surface tension values increase slightly after this minimum and remain constant afterwards. The addition of NaCl does not change the slope of the curve but only shifts them toward lower values of the surfactant concentrations. This means that the critical micelle concentration (CMC) decreases with increasing NaCl concentration, as shown in Table 5.1. A similar behavior has been reported for other ionic surfactant-electrolyte systems [23-25].

We followed the thermodynamic method explained in Ref. [24] to determine the adsorption of the surfactant at liquid/air interface which is an extension of the approach of Rehfeld [26]. According to the theory the Gibbs adsorption isotherm in a suitable form which accounts for the added inorganic salt is given by

$$\Gamma_s = -\frac{1}{RT} \left( \frac{d\sigma}{d \ln(aa_t)} \right)_T \quad (5.4)$$

here  $R$  is the universal gas constant,  $T$  is temperature,  $\sigma$  is the measured surface tension and  $a$  and  $a_t$  are ionic activities of the surfactant (AOS) and surfactant+electrolyte (AOS+NaCl) solutions respectively defined by

$$a = \gamma_{\pm} c_{AOS} \quad \text{and} \quad a_t = \gamma_{\pm} (c_{AOS} + c_{NaCl}) \quad (5.5)$$

with  $\gamma_{\pm}$  the mean ionic activity coefficient. An equation accurately representing measured values of  $\gamma_{\pm}$ , up to  $2 \text{ M}$  solutions of NaCl is provided by Debye-Hückel formula corrected for short-range interactions [27,28]

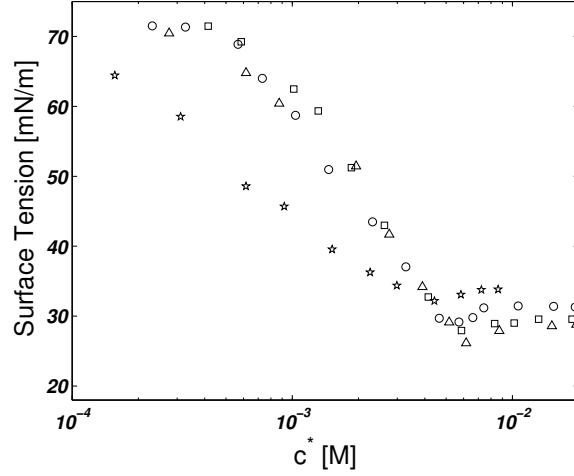


**Fig. 5.4:** The measured surface tension isotherms ( $T=25^{\circ}\text{C}$ ) vs. mean ionic activity  $c^*$ . (\*) no salt, (o)  $c_{\text{NaCl}} = 0.05 \text{ M}$ , (□)  $c_{\text{NaCl}} = 0.20 \text{ M}$  and (Δ)  $c_{\text{NaCl}} = 0.50 \text{ M}$ . All curves with NaCl follow a master curve.

$$\log \gamma_{\pm} = -\frac{0.5115\sqrt{I}}{1+1.316\sqrt{I}} + 0.055I \quad (5.6)$$

where,  $I$  is the ionic strength in moles and the numerical constants correspond to  $25^{\circ}\text{C}$ . For consistency sake we also define so-called “mean ionic activity” as

$$c^* = (aa_t)^{1/2} = \gamma_{\pm} (c_{\text{AOS}} (c_{\text{AOS}} + c_{\text{NaCl}}))^{1/2} \quad (5.7)$$

Equation (5.4) suggests a way to determine the adsorption from the surface tension measurements. Gurkov et al. [23] proposed that the isotherm of  $\sigma$  versus  $\ln(aa_t)$  can be fitted with a polynomial function

$$\sigma = z_0 + z_1 \ln(aa_t) + z_2 (\ln(aa_t))^2 + z_3 (\ln(aa_t))^3 + \dots \quad (5.8)$$

Therefore, to determine the adsorption we fitted our measured surface tension data to a quadratic function and calculated the adsorption using Eq. (5.4).

Fainerman and Lucassen-Reynders [25,29] pointed out that for solutions of a single ionic surfactant with inorganic electrolyte the measurements of surface tension (or surface pressure) vs. mean ionic activity ( $c^*$ ) at different electrolyte concentrations coincide on a single curve. The measured surface tension data of AOS solutions are presented in Fig. 5.4 as a function of the mean ionic activity ( $c^*$ ). The isotherms of  $\sigma$  pass through a master curve for different NaCl concentrations, except for the solution without NaCl. This implies that at a given mean ionic activity, both adsorption and surface tension are independent of electrolyte concentration, i.e. the

ionic atmosphere contribution to the surface pressure is negligible. This is confirmed in Fig. 5.5 where the calculated adsorptions (from Eq. (5.4)) are plotted vs. mean ionic activity,  $c^*$ . The adsorption  $\Gamma_s$  continuously increases with the addition of either salt or surfactant by  $c^*$ . The complete absence of inert electrolyte in the studied solutions results in an adsorption curve very different from that in presence of salt. The adsorption is lower in this case. Similar effect was already observed in Ref. [24] and the authors attributed it to “enhanced electrostatic screening in the double layer and decreased repulsion between the surfactant ions” upon addition of salt.

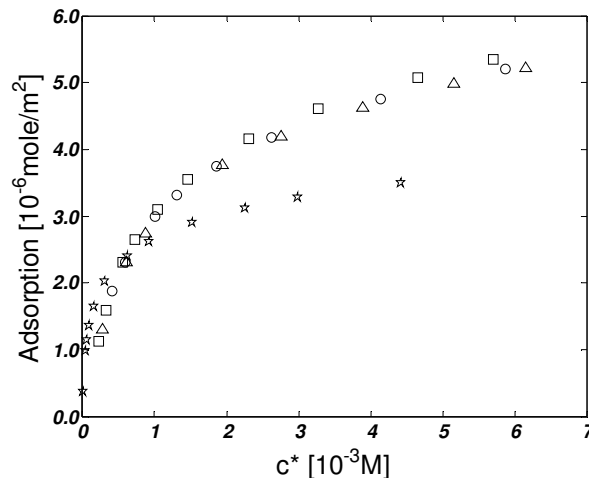


**Fig. 5.5:** Calculated adsorption,  $\Gamma_s$ , vs. mean ionic activity for AOS solutions and different NaCl concentrations: (\*) no salt, (o)  $c_{NaCl} = 0.05 M$ , (□)  $c_{NaCl} = 0.20 M$  and (Δ)  $c_{NaCl} = 0.50 M$ .  $\Gamma_s$  is less for the solution without NaCl compared to the solution with NaCl.  $\Gamma_s$  is independent of NaCl concentration at a given  $c^*$ .

*Foam Film Experiments:* The dependence of the equivalent solution film thickness  $h_w$  on the NaCl concentration was investigated for two surfactant concentrations, one ( $c_{AOS} = 0.01 wt\% = 3 \times 10^{-4} M$ ) below and the other ( $c_{AOS} = 0.30 wt\% = 9.5 \times 10^{-3} M$ ) above the CMC of the AOS solution in the absence of NaCl. The results are shown in Fig. 5.6 and the calculated  $h$  and  $h_1$  are summarized in Table 5.2. Thick films are formed at low salt concentration. The thickness of these films depends on the AOS concentration in the solution. Those made from AOS solutions with a concentration of  $0.01 wt\%$  are thicker than those prepared in presence of  $0.3 wt\%$  solution. This is because the AOS surfactant is an electrolyte itself and at low salt concentration its concentration determines the ionic strength of the solutions. Following the classical DLVO theory the electrostatic double layer repulsion is weaker when the salt concentration is higher.

In both cases the film thickness decreases smoothly with increasing NaCl concentration. In the case of  $c_{AOS} = 0.01 wt\%$  common black films with an equivalent thickness of  $11.1 nm$  are formed when concentration of NaCl is between  $0.10$  and  $0.30 M$  while in the case of  $c_{AOS} = 0.30 wt\%$  CBFs

with an equivalent thickness of  $11.7 \text{ nm}$  are formed when concentration of NaCl is between  $0.05$  and  $0.20 \text{ M}$ . The film thickness is  $5.1 \text{ nm}$  in the case of  $c_{AOS} = 0.01 \text{ wt\%}$  above  $c_{NaCl} = 0.40 \text{ M}$  and in the case of  $c_{AOS} = 0.30 \text{ wt\%}$  above  $c_{NaCl} = 0.30 \text{ M}$  and it is independent of NaCl and surfactant concentrations. We identify these films as NBFs which consist of two hydrophobic hydrocarbon layers of molecules with a thickness of about  $1.35 \text{ nm}$  and a core of bound water which includes the hydrophilic head groups of the AOS molecule with a thickness of  $1.4 \text{ nm}$ .

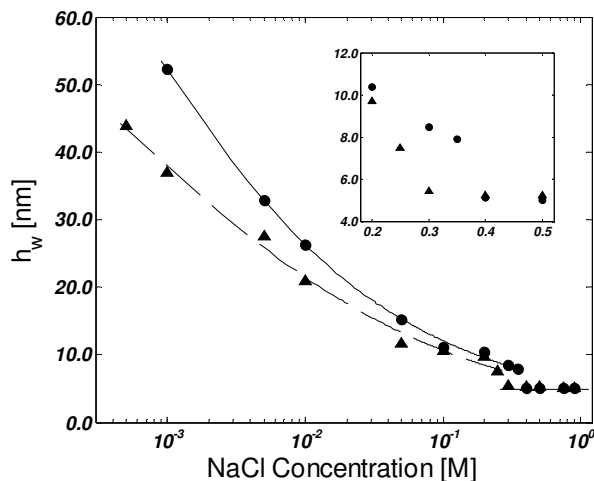


**Fig. 5.6:** Dependence of the experimentally obtained equivalent film thickness,  $h_w$ , on NaCl concentration for constant AOS concentrations of (●)  $c_{AOS} = 0.01 \text{ wt.}\%$  ( $3.0 \times 10^{-4} \text{ M}$ ) and (▲)  $c_{AOS} = 0.30 \text{ wt.}\%$  ( $9.5 \times 10^{-3} \text{ M}$ ) at a constant temperature of  $T = 25 \text{ }^\circ\text{C}$ . The concentrations in which the transition from CBF to NBF happens are more clear in the small figure. The solid (—) and dashed (---) lines are only guides for the eyes.

The critical concentration of formation of NBF is similar to that reported for other ionic surfactant like the classical sodium dodecylsulphate (SDS) which is  $0.25 \text{ M}$  of NaCl [30,31], but it is much higher than that reported for some non-ionic surfactants. For example it is  $0.05 \text{ M}$  NaCl for  $\beta$ -dodecyl maltoside [32]. The transition concentration of NaCl above which only NBF are formed is higher in the case of the lower surfactant concentration ( $c_{AOS} = 0.30 \text{ wt.}\%$ ). This is a result of the contribution of the surfactant ions and counter ions to the total electrolyte concentration of the solutions.

The dependence of the thickness of the foam films on the AOS concentration was also investigated at fixed NaCl concentration of  $c_{NaCl} = 0.50 \text{ M}$ . The equivalent film thickness remained the same (with the average value of  $5.1 \text{ nm}$ ) for all surfactant concentrations above  $c_{AOS} = 0.003 \text{ wt.}\%$  ( $9.5 \times 10^{-5} \text{ M}$ ). Formation of stable films below this concentration was not possible.

**Table 5.2:** Foam film thickness,  $h_1$ , and the thickness of the aqueous core,  $h_2$  as a function of the NaCl concentration for films prepared from AOS solutions with concentrations  $c_{AOS}=0.01$  wt.% ( $3.0 \times 10^{-4}$  M) and  $c_{AOS}=0.30$  wt.% ( $9.5 \times 10^{-3}$  M). The thicknesses were calculated from the experimentally obtained  $h_w$  using Eq. 5.2

$c_{NaCl}$ [M]	$c_{NaCl} = 0.01$ wt.% ( $3.0 \times 10^{-4}$ M)		$c_{NaCl} = 0.30$ wt.% ( $9.5 \times 10^{-3}$ M)	
	$h$ [nm]	$H_2$ [nm]	$h$ [nm]	$h_2$ [nm]
0.0005			43.8	40.2
0.001	51.5	47.9	36.9	32.3
0.005	32.9	29.3	27.4	23.8
0.01	26.3	22.7	20.9	17.3
0.05	15.3	11.7	11.7	8.1
0.10	11.1	7.4	10.6	7.0
0.20	10.3	6.7	9.7	6.0
0.25	8.4	4.8	7.5	3.8
0.30			5.4	1.8
0.35	7.9	4.3		
0.40	5.1	1.5	5.2	1.6
0.50	5.0	1.4	5.2	1.6
0.75	5.0	1.4	5.1	1.5
0.90	5.0	1.4	5.1	1.5

The contact angle,  $\theta$ , was measured for two surfactant concentration while the NaCl concentration was varied between  $0.2$  M and  $0.7$  M. The results are shown in Fig. 5.7. For CBFs the contact angle is less than  $\theta < 1^\circ$ . It increases with increasing NaCl concentration for both cases until it faces a jump. This jump is usually accepted as an indication of formation of NBFs [2, 22,33]. The jump is between  $c_{NaCl} = 0.35$  M and  $c_{NaCl} = 0.40$  M for  $c_{AOS}=0.01$  wt% and between  $c_{NaCl} = 0.30$  M and  $c_{NaCl} = 0.35$  M for  $c_{AOS}=0.30$  wt% which proves the transition from CBF to NBF. After the well pronounced jump in the curves, the contact angle increases slower further. This indicates changes in the interactions between the film surfaces even after the formation of the NBF. It might be attributed to a further decrease in the electrostatic component of the disjoining pressure in this range of salt concentrations as already shown for films prepared from sodium dodecylsulphate (SDS) in presence of NaCl [30].

When the two film surfaces approach each other the surface forces cause appearance of a disjoining pressure ( $\Pi$ ) in the film [30]. It is related to the film tension  $\gamma^f$  (see Fig. 5.2) by

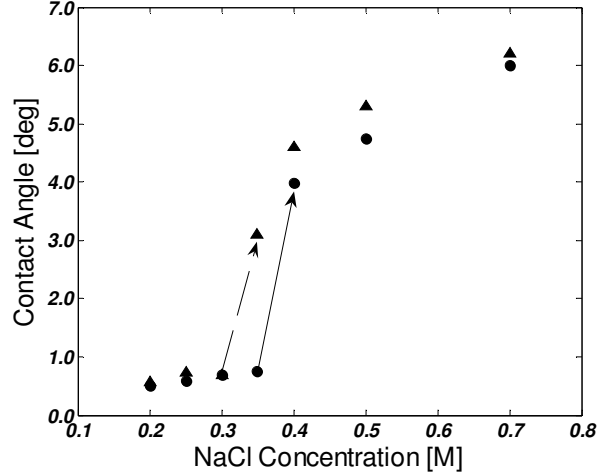


**Fig. 5.7:** Dependence of the experimentally obtained contact angle between the film forming solution and the film meniscus,  $\theta$ , on NaCl concentration for constant AOS concentrations of (●)  $c_{AOS}=0.01$ wt.% ( $3 \times 10^{-4}$  M) and (▲)  $c_{AOS}=0.3$ wt.% ( $9.5 \times 10^{-3}$ ). The temperature is constant ( $T=25^\circ\text{C}$ ). The solid (—) and dashed (---) arrows are only guides for the eyes and show the jump in contact angle.

$$\gamma^f = 2\sigma - \int_{\infty}^h \Pi dh + \Pi h = 2\sigma + \Delta g^f + \Pi h \quad (5.9)$$

The free energy of film formation,  $\Delta g^f$ , provides useful information for studying the interaction forces in the films [33]. Usually, the term  $\Pi h$  is some orders of magnitude smaller than  $\Delta g^f$  and can be neglected. The forces balance in lateral direction at the line of intersection (see Fig. 5.2) requires that

$$2\sigma \cos \theta = \gamma^f \quad (5.10)$$

Combining Eqs. (5.9) and (5.10) one obtains the following equation which relates  $\Delta g^f$  to the easily accessible experimentally contact angle

$$\Delta g^f = 2\sigma (\cos \theta - 1) \quad (5.11)$$

The dependence of  $\Delta g^f$  on the NaCl concentration is presented in Table 5.3. The free energy of film formation has small value at low electrolyte concentrations. It increases sharply at a certain NaCl concentration. Similar to the contact angle behavior the jump is between  $c_{NaCl} = 0.35$  M and  $c_{NaCl} = 0.40$  M for  $c_{AOS} = 0.01$  wt% and between  $c_{NaCl} = 0.35$  M and  $c_{NaCl} = 0.30$  M for  $c_{AOS} = 0.3$  wt%. The increase in the absolute value of  $\Delta g^f$  emphasizes the fact that with increasing electrolyte concentration the contribution of the electrostatic repulsive forces ( $\Pi_{EL}$ ) to the total film interaction free energy decreases and the formation of NBF from the initially

formed CBF is energetically favorable process. The values of the specific interaction free energies are lower compared to that of films prepared from SDS. For example, it is  $-0.9 \text{ mJ/m}^2$  at  $0.5 \text{ M}$  NaCl in the film formed from SDS compared to ca.  $-0.20 \text{ mJ/m}^2$  depending on the surfactant concentration in the case of AOS stabilized films. This comparison shows that formation of NBF stabilized with SDS is energetically favorable than in the case of AOS stabilized films.

**Table 5.3:** Values of the contact angle,  $\theta$ , the surface tension,  $\sigma$  and the specific interaction film free energy,  $\Delta g^f$  as a function of NaCl concentration for two surfactant concentrations

$c_{NaCl}$ [M]	$c_{AOS} = 0.01 \text{ wt\% } (3.0 \times 10^{-4} \text{ M})$			$c_{AOS} = 0.30 \text{ wt\% } (9.5 \times 10^{-5} \text{ M})$		
	$\theta$ [deg]	$\sigma$ [mN/m]	$\Delta g^f$ [mJ/m <sup>2</sup> ]	$\theta$ [deg]	$\sigma$ [mN/m]	$\Delta g^f$ [mJ/m <sup>2</sup> ]
0.20	0.5	27.5	$-2.2 \times 10^{-3}$	0.6	29.1	$-2.8 \times 10^{-3}$
0.25	0.6	28.5	$-3.0 \times 10^{-3}$	0.7	29.0	$-4.7 \times 10^{-3}$
0.30	0.7	28.6	$-4.0 \times 10^{-3}$	0.7	28.8	$-4.3 \times 10^{-3}$
0.35	3.1	28.8	$-4.9 \times 10^{-3}$	0.8	28.7	-0.09
0.40	4.0	28.6	-0.14	4.6	28.5	-0.18
0.50	4.7	27.5	-0.19	5.3	28.4	-0.24
0.70	6.0	28.4	-0.31	6.2	28.4	-0.33

## 5.4. CONCLUSIONS

We calculated the adsorption of AOS surfactant at air/water interface using the surface tension data. It was shown that, except for the solution without salt, the addition of salt does not alter the adsorption  $\Gamma_s$ . Moreover, we studied the properties of foam films stabilized by AOS. It was observed that the films are not stable when  $c_{AOS} < 0.03 \text{ wt\%}$  at a fixed concentration of  $c_{NaCl} = 0.50 \text{ M}$ . The film thickness and contact angle, which is formed at the transition between the film and the bulk solution, were measured as a function of NaCl and surfactant concentration. The thickness of the films remains constant for a concentration range of  $c_{AOS} > 0.03 \text{ wt\%}$  at a fixed concentration of  $c_{NaCl} = 0.50 \text{ M}$ . However, the film thickness decreases with addition of NaCl due to the screening of the repulsive forces. The concentrations in which the NBFs are formed were also determined. Measurements of contact angle were used to calculate the free energy,  $\Delta g^f$ , of film formation. The results show that  $\Delta g^f$  changes even when the conditions for the formation of NBF with constant thickness are achieved. This implies that the formation of NBF is not a state which ensures the minimum in the film energy.

## 5.5. REFERENCES

1. B. P. Binks and T.S. Horozov, *Angew. Chem.*, 117, (2005) 3788.
2. D. Exerowa and P.M. Kruglyakov, *Foam and Foam Films*, Elsevier Science, 1998
3. D. Cohen, T. W. Patzek and C. J. Radke, *Transport in Porous Media*, 28 (1997) 253.

4. W. R. Rossen, In: R. K. Prud'homme and S.A. Khan, Editors: Foams, theory, measurements and application, New York, Marcel Dekker, Inc., 1996, p.413-463.
5. J. R. Calvert, *International Journal of Heat and Fluid Flow*, 11 (3), (1990) 236.
6. J. Frieditis and G.S. Paulett, SPE 24178, presented at SPE/DOE Eighth Symposium on Enhanced Oil Recovery, Tulsa, Oklahoma, 1992.
7. J. Israelachvili, *Intermolecular and Surface Forces*, Academic Press: London, 1991.
8. D. Exerowa, T. Kolarov and Khr. Khristov, *Colloids Surf.* 22 (1987) 171.
9. A. Sheludko, *Advan. Colloid Interface Sci.*, 1 (1967) 391.
10. C. Stubenrauch and R. von Klitzing, *J. Phys. Condens. Matter*, 15 (2003) R1197.
11. V. Bergeron, *J. Phys. Condens. Matter*, 11 (1999) R215.
12. I.B. Ivanov (Ed.), *Thin Liquid Films*, Chapter 11, Surfactant Science Series Vol. 29, Marcel Dekker, New York 1988.
13. V. Bergeron, *Langmuir*, 13 (1997) 3474.
14. B.V.Derjaguin, L.D.Landau Acta Physicochem. USSR 14 (1941) 633; E.J.W. Verwey and J.Th.G., *Theory of stability of Liophobic colloids*, Elsevier, Amsterdam, 1948.
15. J. Israelachvili and H. Wennerstrom, *J. Phys. Chem.*, 96 (1992) 520.
16. D.X. Du, *Private Communication*, 2008.
17. A. Scheludko, *Adv. Colloid Interface Sci.*, 1 (1967) 391.
18. J.L. Toca-Herrera, H.J. Müller, R. Krustev, D. Exerowa, H. Möhwald, *Colloids and Surfaces A*, **144**, (1998), 319.
19. S.P. Frankel and K.J. Mysels, *J. Appl Phys*, 81 (1966) 3725-3748; E.M. Duyvis, *The equilibrium thickness of free liquid films*, PhD thesis, Utrecht University, (1962)
20. J. Benattar, A. Schalchli, O. Belorgey, *J. Phys. I France*, 2 (1992) 955
21. Lide, D., Ed., *Handbook of Chemistry and Physics*, 73rd ed., CRC Press Inc.: Cleveland, OH, (1993).
22. T. Kolarov, A. Scheludko, D. Exerowa, *Tans Faraday Soc*, 64 (1968) 2864; R. Krustev, H. -J Müller, J.L. Toca-Herrera, *Colloid Polym Sci*, 276 (1998) 518
23. A.J. Prosser and E.I. Franses, *Colloids and Surfaces A: Physicochemical and Engineering Aspects*, 178 (2001) 1-40.
24. T. D. Gurkov, D.T. Dimitrova, K.G. Marinova, C. Bilke-Crause, C. Gerber, I. B. Ivanov, *Colloids and Surfaces A: Physicochemical and Engineering Aspects*, 261 (2005) 29.
25. V. B. Fainerman and E. H. Lucassen-Reynders, *Adv Colloid Interface Sci*, 96 (2002) 295
26. S.J. Rehfeld, *J. Phys. Chem.* 71 (1967) 738.
27. R.A. Robinson, R.H. Stokes, *Electrolyte Solutions*, Butterworths, London, 1959.
28. E.A. Moelwyn-Hughes, *Physical Chemistry*, Pergamon Press, London, 1961.
29. V. B. Fainerman, R. Miller, E. V. Aksenenko, A. V. Makievski, in: V. B. Fainerman, D. Mobius, R. Miller (Eds.), *Surfactants: Chemistry, Interfacial Properties, Applications*, Elsevier, Amsterdam, 2001, p. 189, Chapter 3.
30. M.N. Jones, K. Mysels, P.C. Scholten, *Trans. Faraday Soc.*, 62 (1966) 1336.
31. H.G. Bruil, *Specific Effects in Free Liquid Films*, Meded. Landbouwhogeschool, Wageningen, Vols. 70-9, 1970.
32. N.C. Mishra, R.M. Muruganathan, H.-J. Müller, R. Krustev, *Colloids and Surfaces A*: 256 (2005) 77.
33. J.A. De Feijter, in: Ivanov I (Ed) *Thin Liquid Films*, Surfactant Science Series, Vol. 29: Marcel Dekker, New York, pp. 1-47 (1988).

---

## Chapter 6

# GAS PERMEABILITY OF FOAM FILMS

## STABILIZED WITH AOS

---

### ABSTRACT

*The mass transfer of gas through foam films is important in various industrial and biological processes. The aim of this chapter is to give a perspective and critical overview of studies carried out to date on the mass transfer of gas through foam films. A comprehensive overview of the theoretical models used to explain the observed effects is given. A detailed description of the processes that occur when a gas molecule passes through each layer that forms a foam film is shown. Moreover, the measured gas permeability coefficient,  $k$  (cm/s), of foam films stabilized by an alpha olefin sulfonate (AOS) surfactant is reported as a function of the electrolyte (NaCl) concentration, surfactant concentration and the temperature. The addition of salt to the film forming solution leads to decrease of the film thickness which was complemented by an increase of  $k$  up to a certain value. Above that critical salt concentration, the film thickness and its gas permeability coefficient both decrease. We explain this effect as a result of interplay of the film thickness and the adsorption monolayer permeability for the permeability of the whole film, i.e. the thermodynamic state of the film. The classical theories which explain the process were applied. Furthermore, the gas permeability of the film showed an unexpected increase at surfactant concentrations well above the CMC.*

**Keywords:** *Foam film, AOS surfactant, Gas permeability, Monolayer, Adsorption, Electrolyte concentration, Disjoining pressure*

**Published in:** *Advances in Colloid and Interface Science, 137 (1), (2008) 27 and Langmuir 25(5), (2009) 2881.*

## 6.1. INTRODUCCION

From thermodynamics point of view foams are unstable systems which evolve with time via coarsening, drainage and lamellae rupture. The long-term stability of foam is a result of the stability of the thin liquid films. One factor for the long-term stability of foam is the gas permeability of the foam films [1-3]. The measurement of the gas permeability of the foam films gives valuable information about the stability and lifetime of the foams. The permeation of gas through foam films is a matter of interest in many physical, chemical, and biological studies, as well as in many technological applications. Examples include gas separation processes [4-8], chemical sensing [9-12], medical research- (breathing) [13-15], stabilization of ultrasonic contrast agents for medical diagnostics [16,17], cosmetics (stabilization of foams against coarseness) [18], and petroleum engineering, where for instance, gas bubbles arise as the pressure decreases below the bubble point during the production of (highly) viscous and dense oils, and inter-bubble diffusion gives rise to the coalescence of the gas bubbles, which is undesirable [19,20], etc.

Foam in porous media is indeed made up of gas bubbles that are separated by thin liquid films, i.e., lamellae which span across pores. To maintain foam flow in a porous medium a high pressure gradient is required. Therefore, when the pressure gradient is not high enough to keep lamella moving, the lamella become trapped in the pores and gas flow is blocked. While the fraction of the trapped gas depends on many parameters including type of gas and porous media, experimental measurements reveal that the fraction of the gas that is not flowing during foam flow may vary between 0.60 and 0.95 [21,22]. In this case gas transport through the system is limited to diffusion through the foam films [22-24]. These processes show how important is the detailed knowledge of the foam properties for precise tuning of different processes. Moreover, as we will discuss in the next chapters, the nature of gas affects the foam behavior in porous media, e.g. CO<sub>2</sub> foam builds up lower pressure gradient along the porous medium compared to N<sub>2</sub>. The difference in diffusion rates of gases through foam films can be used to explain the differences.

The transfer of gases through a foam film depends on the gas permeability of the two surfactant monolayers, which build the film and the central aqueous core (Fig. 5.1). The first part of this chapter focuses on detailed description of the processes that occur when a gas molecule passes through each of the foam film forming layers. A summary of the existing theoretical models used to explain the experimentally observed effects are also given. The permeability of the film-forming surfactant monolayers plays an important role for the whole permeability process. It can be successfully described by the models used to explain the permeability of surfactant monolayers on an aqueous sub phase. For this reason, we briefly discuss the surfactant-induced resistance to the mass transfer of gases through gas-liquid interface and review the theories proposed in the

literature to interpret the experimental observations. After presenting a review of the theories and mechanisms of the permeability of foam films, we report experimental results of the effects of salt and surfactant concentration on the gas permeability of foam films stabilized with AOS.

## 6.2. GAS PERMEABILITY OF SINGLE SURFACTANT MONOLAYERS

The first studies on gas permeation through foam films were reported in 1924 by Hedestrand [25]. The author undertook repeated efforts to determine the influence of surfactant monolayers on the evaporation rate of water but found no measurable effect. He found no measurable effect; however, his technique was subject to criticism from Adam [26] and Rideal [27]. These authors pointed out that the stagnant air over the water surface might have had a greater effect on the water evaporation than the spread monolayer. In 1925, Rideal [27] modified Hedestrand's technique [25] and demonstrated for the first time that the presence of a monolayer at the water-air interface retards the water evaporation, although the mechanism of the retardation was not completely clear. Subsequently, in 1927 Langmuir and Langmuir [28] reported the effect of an insoluble monolayer on the evaporation of ethyl ether from saturated solutions in water (5.5%). They observed that the rate of evaporation of ether from the solution in the presence of an insoluble oleic acid monolayer was 10 times lower than the case when no monolayer was present. Moreover, Langmuir and Langmuir [28] proposed for first time the energy barrier theory for the permeation of the water molecules through the layer covered by fatty acids and alcohols. The theory was later modified by Langmuir and Schaefer [29] and has been extensively used since.

The effect of surfactant monolayers on the water evaporation rate has been studied extensively [for example, see Refs. 30-45]. Most of the concepts, which describe the effect of surfactant monolayers on the water evaporation rate, remain the same for the mass transfer rate of other gases into a surfactant solution [46-62]. The common view is that when a surfactant is spread onto a quiescent liquid, the total resistance to the passage of the gas molecules is a sum of a series of three resistances: liquid phase resistance, gas phase resistance, and interfacial resistance, which arises from the adsorption of surfactant molecules to the interface (Fig. 6.1). The retardation of the mass transfer of gas through a gas-liquid interface by addition of surfactant to the liquid phase is often specified as "*monolayer resistance*" or its reciprocal "*monolayer permeability*". The magnitude of the monolayer permeability is related to the molecular structure of the surfactant: the polarity of the hydrophilic group [47,56], the molecular weight of the hydrophilic group and the hydrophobic chain length (number of the CH<sub>2</sub> group) [41,48], temperature [48-50], the monolayer surface pressure [51], and the size of the permeant (gas molecule) [52].

Many experiments support the view that insoluble surfactants impede the mass transfer of gas molecules through the gas-liquid interfaces. Nevertheless, there is a difference between the probable effects of soluble and insoluble surfactants. Relatively little work has been done on the effects of the soluble surfactants on the mass transfer of gas molecules. Some papers even suggest that the soluble surfactants have no measurable resistance on the mass transfer of gas across gas-liquid interfaces [47, 63-67].

Different theories describe the permeability of surfactant monolayers. The main theories are the simple diffusion theory, the energy barrier theory, the density fluctuation theory, and the accessible area theory, which will be discussed subsequently.

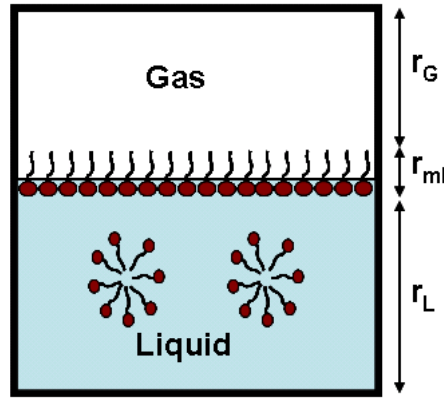


**Fig. 6.1:** Surfactant solution: when a surfactant is added to a quiescent liquid there are three main resistances to the mass transfer of gas: the gas phase resistance ( $r_G$ ), the interfacial resistance induced by surfactant molecules ( $r_l$ ), and the resistance in the bulk liquid ( $r_L$ ).

### 6.2.1. Simple diffusion theory

The first simple approach to treat the experimental data is to assume that the monolayer is a homogenous phase with a thickness  $h_{ml}$ . The gas molecules diffuse through this thin uniform layer with a diffusion coefficient  $D_{ml}$ . According to Fick's first law, the rate of mass transfer is inversely proportional to the monolayer thickness:

$$\frac{dN_g}{dt} = -\frac{D_{ml}}{h_{ml}} \Delta C_g = -k_{ml} \Delta C_g \quad (6.1)$$

where,  $N_g$  is the number of moles of gas passing across the film per unit area and time  $t$ ,  $\Delta C_g$  is the difference in the gas concentrations on the both sides of the monolayer, i.e. the driving force for the diffusion process, and  $k_{ml} = D_{ml} / h_{ml}$  (cm/sec) is the permeability coefficient for a monolayer [68,69].

The thickness of the monolayer can be related to the length of hydrocarbon chain of the surfactant molecule by the simple relation of

$$h_{ml} = a_{hg} + b_{hc} (n_C - 1) \quad (6.2)$$

Here,  $n_C$  is the number of carbon atoms in a linear hydrocarbon chain of a surfactant molecule. The constant  $a_{hg}$  account for the size of the polar group as well as the terminal methyl group of the alkyl chain. The constant  $b_{hc}$  accounts for the size of a single methylene group in the chain. According to Eqs. (6.1) and (6.2), gas permeability has to be inversely proportional to the length of its hydrocarbon chain, i.e.

$$k_{ml} = D_{ml}/h_{ml} = f\left(1/n_C\right) \quad (6.3)$$

Langmuir and Schaefer [29] could explain some of their experimental data, mainly those for gas permeation through thick oil films on water surface, using the above theory based on Fick's law. Nevertheless, several works [29,31] have shown that the relationship between monolayer permeability and the chain length is exponential. This raises doubts about the accuracy of the simple diffusion theory in interpreting the experimental results. Seemingly when the size of permeant gas molecules is comparable to the thickness of the barrier (surfactant monolayer), Fick's law is not adequately accurate. Even more, it was observed that the diffusion coefficient of monolayers differs from that of the bulk material from which the monolayer is prepared [55]. However, Fick's law is a good approximation for thick films [47] and can also be applied to explain the effects of impurities and external additives on liquid surface that enhance the permeability of the monolayers [38].

### 6.2.2. Energy barrier theory

The concept of the existence of an activation energy barrier due to the presence of surfactant monolayers at the gas-liquid interface was first introduced by Langmuir and Langmuir [28] and developed further by Langmuir and Schaefer [29]. Their experimental results showed that gas permeability of a surfactant monolayer is exponentially proportional to the length of the surfactant hydrocarbon chain and inverse of the temperature. Although Archer and La Mer [31] proved that the low permeability coefficients obtained by Langmuir and Langmuir [28] were a result of impurities on the water surface, they confirmed the existence of an energy barrier that opposes the penetration of the gas molecules into the monolayer or some part of it. Consequently, they proposed the following relationship for the coefficient of monolayer gas permeability:

$$k_{ml} = \zeta \alpha_c \exp\left(\frac{E_a}{R_B T}\right) \quad (6.4)$$

where,  $E_a$  is the energy needed to permeate a monolayer,  $R_B$  is the universal gas constant,  $T$  is the absolute temperature,  $\alpha_c$  is the condensation coefficient which accounts for the condensation of water molecules on a monolayer free surface and cannot exceed unity, and  $\zeta$  is a constant that depends on the cross-sectional area of the permeant molecule [28]. According to the gas kinetics theory [70], each gas molecule carries a certain amount of energy. When this molecule reaches a surfactant monolayer, it needs space to pass through the monolayer. The gas molecules in the gas phase strike the surfactant molecules in the monolayer. Some of the molecules are reflected back to the gas phase, and only a certain fraction of the molecules that have certain energy can permeate. This activation energy is dependent on the length of the hydrocarbon chain, the surface pressure, the cross-sectional area of the permeant, and some properties intrinsic to the monolayer (phase state, compressibility, free surface area, and polar group) [28, 29, 71-73].

By combining the gas kinetics theory and energy barrier theory, Eq. (6.4) can be modified to

$$k_{ml} = \frac{\chi H}{(2\pi M_g R_B T)^{1/2}} \exp\left(-(\Delta E_a + \Pi_s \Delta A) / R_B T\right) \quad (6.5)$$

where  $\chi$  is a constant and depends on the frequency of collision,  $M_g$  is the molecular weight of the gas,  $H$  is Henry's solubility coefficient, and  $\Pi_s$  is the surface pressure. Equation (6.5) provides a direct relation between the monolayer permeability and the properties of the permeating gas, and the characteristics of the monolayer.

A modified version of the energy barrier theory was proposed by considering the dependence of the monolayer permeability in terms of the activation free energy,  $\Delta G'$  [71,72]. This model formulates the coefficient of monolayer permeability as

$$k_{ml} = \zeta' \exp(\Delta G' / R_B T) \quad (6.6)$$

where  $\zeta'$  is a constant. The excess Gibbs energy of activation is given by  $\Delta G' = \Delta U - T\Delta S + \Pi_s \Delta A$  with  $\Delta U$ ,  $\Delta S$  and  $\Delta A$  internal energy, entropy, and area of activation, respectively.  $\Delta A$  is the area by which the monolayer must expand to form the required space between the surfactant molecules to let the gas molecules pass through. The value of  $\Delta A$  decreases as the packing density of the monolayer decreases [72].

### 6.2.3. Density fluctuation and accessible area theories

A large number of factors influence the energy barrier. For this reason the energy barrier theory proved to be inadequate for giving a unified physical mechanism for the permeability of the monolayers. Blank [74], Blank and Britten [75], and Barnes [35,36] pointed out that the permeation is allowed only when the permeating molecule reaches a hole with a sufficiently large size to pass through, i.e. the permeation process is assumed to be all-or-none. Respectively, the gas permeability is related to the probability,  $P$ , of a gas molecule finding such hole in the monolayer. Thus, the monolayer permeability coefficient is defined as

$$\frac{1}{k_{ml}} = r_{ml} = \left( \frac{1}{\alpha_v Q} \right) \left( \frac{1}{P} - 1 \right) \quad (6.7)$$

where,  $Q = \sqrt{R_B T / 2\pi M_g}$  and the condensation coefficient  $\alpha_v$  is the fraction of the gas molecules which can enter the monolayer. Equation (6.7) shows that the permeability of a monolayer can be predicted if the probability of finding a free space in the surfactant monolayer is known.

Blank [74] proposed a “*density fluctuation theory*” by which he could explain his experimental results. The model was derived in terms of equilibrium properties of the monolayers. Blank [74] and Blank and Britten [75] stated that the free space in the monolayer can arise by three different mechanisms: (i) the natural free area in the lattice; (ii) local fluctuations in the monolayer concentration; and (iii) the kinetic energy of the permeant molecule forcing the monolayer molecules apart.

The probability of a gas molecule finding a free space formed by mechanisms (i) and (ii) is proportional to the entropy change,  $\Delta S$ , due to expansion of the monolayer

$$\Delta S = \int \frac{dE'}{T} - \int \frac{\sigma dA}{T} \quad (6.8)$$

where  $E'$  is the enthalpy of monolayer expansion,  $\sigma$  is the surface tension of the bulk surfactant solution, and  $A$  is the area of monolayer. Thus,

$$P = P_0 \exp \left( - \frac{\sigma_i \Delta A}{k_B T} \right) \quad (6.9)$$

with  $\sigma_i = fA - Td\sigma / dT$ ,  $f$  is a constant and is related to the monolayer compressibility,  $k_B$  is the Boltzmann constant, and  $P_0$  is the probability of the equilibrium ( $\Delta S = 0$ ). In Eq. (6.9),  $\Delta A$  is the local expansion of the area necessary for the gas molecules to pass through.

The density fluctuation model gives reasonable results when dealing with equilibrium properties of the monolayers such as surface pressure (as part of the fluctuation frequency calculation), the diffusion coefficient, and the permeability. However, the model does not provide useful information when dealing with the dynamic properties such as the viscosity of the monolayer and thermal conductivity. The permeability obtained by the density fluctuation model is smaller than the experimental values. It appears that the calculation of the probability for the formation of a hole from the bulk entropy of the expansion of the monolayer [74] underestimates the number of permeable gaps. To get closer values, Bockman [76] suggested using experimental entropy values rather than calculated ones, which makes the model more accurate. There is no explicit allowance for the temperature or the alkyl chain length, and the model does not explain the impurity effects.

The “*accessible area theory*” [35,36] also calculates the probability of a gas molecule finding a gap between the surfactant molecules. The only difference to the “*density fluctuation theory*” is that in this theory the gaps exist in the monolayer because of the non-perfect arrangement of the molecules. The sum of areas of the available holes is called *accessible area*. These holes are formed spontaneously at the surface. According to this theory, the probability for a gas molecule to meet a gap is

$$P = \frac{A_{ac}}{A} \quad (6.10)$$

where  $A_{ac}$  is the accessible area and  $A$  is the area of the monolayer. Any decrease in the rate of gas transfer is due to the reduction of the accessible area. A model for the monolayer structure is required in order to predict the accessible area. Barnes et al. [35] proposed a random hard-disk model in which the surfactant molecules are represented by hard disks that are randomly distributed on the liquid surface. Liquid (water) molecules are represented by hard spheres. The interaction energy between a surfactant molecule and a liquid molecule is equal to that between two liquid molecules. However, this model ignores the interaction forces between the surfactant molecules and, as a result, the clumping of the surfactant molecules into closely packed clusters. Gas molecules can permeate through the existing holes, but they cannot form new holes. This model does not include the effect of the hydrocarbon chain length of the surfactants in the gas permeation rate, while experiments show the dependency of the permeability of monolayers to the chain length [28,29]. The absolute value of the calculated permeability by this model is in a satisfactory agreement with the experimental data, and it is remarkably successful in predicting the dependence of the monolayer permeability on the surface density, although it is inaccurate in high concentrations due to the small numbers of holes in the arrays.

In Ref. [36] it was assumed that the surfactant molecules are not randomly distributed and exist in loose hexagonal packing so that the centers of the molecules form a regular hexagonal lattice with areas per molecule larger than the crystallographic values. The holes are formed because of the independent vibrations of the disks about their mean positions. Examining of the calculated values from this model with experimental results reveals that it cannot accurately predict the permeability of monolayers to gas molecules. The model presented in Ref. [35] was more satisfactory, giving more realistic permeation rates.

### 6.3. GAS PERMEABILITY OF FOAM FILMS

#### 6.3.1. Sandwich model

A single foam film consists of an aqueous core with thickness  $h_2$  sandwiched between two adsorbed monolayers of surfactant with the thickness of  $h_1$  (Fig. 5.2). The permeability of such a foam films at equilibrium can be calculated by [77,78]

$$k = \frac{DH}{h_2 + 2D/k_{ml}} \quad (6.11)$$

taking into account the solubility of gas and applying Fick's first law for a *homogenous* layer, while neglecting the gas resistance on both sides of the film. Here,  $k$  is the permeability of the whole foam film to gas,  $D$  is the diffusion coefficient of the gas in the liquid phase,  $H$  is the Henry's solubility coefficient, and  $k_{ml}$  is the permeability of the monolayer to gas. This equation shows that the permeability of the foam films depends on the thickness of the aqueous layer as well as on the solubility and diffusion of the gas in the aqueous phase. Higher  $D$  and  $H$  of the bulk liquid results in higher permeation rates, respectively  $k$ . It appears from Eq. (6.11) that for thick foam films ( $2D/k_{ml} \ll h_2$ ) the rate of permeation is controlled by the liquid layer via  $D$  and  $H$  ( $k = DH/h_2$ ), while for thin foam films ( $2D/k_{ml} \gg h_2$ ) the permeability of monolayer ( $k = Hk_{ml}/2$ ) is the limiting permeability process. Equation (6.11) shows that the total foam film resistance is the sum of the resistance in the liquid core and the resistance of the monolayers. This is similar to the equations proposed in [79, 80] for the permeation of rubber membranes by gases and polymer membranes by water vapor.

Princen et al. [77,78] performed detailed measurements on the gas permeability of foam films, varying concentrations of the surfactant and salt and also the temperature. The authors emphasized that Fick's law is applicable in macroscopic systems and accounts for the transport of gas through soluble monolayers. The sandwich model is adequately accurate for soluble monolayers, and the values calculated by this theory are in good agreement with experimental data, although such a simple model may not be accurate for the permeation of gases through

insoluble monolayers [77]. The authors reported some values for the permeability of various gases through foam films. It was observed that the permeability of monolayers inversely changes with the collision diameter of the gas molecules, a fact that cannot be explained by the simple Fick's mechanism they proposed.

### 6.3.2. Nucleation theory of fluctuation formation of holes

The sandwich structure model of the film used by Princen and Mason [77] to explain the foam film permeability is not adequate to describe the structure of the very thin Newton Black Films (NBF). These films consist only of two monolayers of adsorbed surfactant molecules and some layers of hydration water. The properties of such films (e.g. electroconductivity [81]) are very different to those of the thicker CBF, which means that the mechanism of their permeability could be different than that of single surfactant monolayers. Several authors [82-84] have mentioned that a possible mechanism of permeability of such surfactant bilayers (NBF) is the existence of microscopically small holes in the bilayer. Nucleation theory of fluctuation formation of holes in the NBF assumes that molecular defects in the adsorbed monolayers exist. They are called vacancies. These vacancies move in the monolayers and aggregate, forming holes with different size  $i$  (here  $i$  is the number of vacancies which form a single hole). The theory gives relations to calculate the probability for the formation of holes of certain size  $i$  [85-87]. The permeability occurs by two regions in the foam bilayers (NBF): (a) hole-free area with a permeability coefficient  $k_0$  (coefficient of background permeability) and (b) area which consists of holes with different sizes. The gas flux of holes with size  $i$  is given by the permeability coefficient  $k_i$ . Thus, the permeability of a bilayer is a sum of the permeabilities of each part of the film  $k_0$  and  $k_i$  by:

$$k = k_0 + \sum_{i=0}^{\infty} k_i \quad (6.12)$$

where the permeability coefficients are defined as

$$k_0 = \frac{S_0 D_0}{Sh}, \quad k_i = \frac{S_i D_i}{Sh_i} \quad (6.13)$$

and in these equations  $h$  and  $S$  are the thickness and total area of a bilayer film, respectively.  $S_0 = S - \sum_{i=0}^{\infty} S_i$  is the hole-free area of the film,  $S_i$  is the overall area of the holes of size  $i$ , and  $D_0$  and  $D_i$  are the diffusion coefficients of the permeant gas through hole free bilayer and holes of size  $i$ , respectively.

Equation (6.13) is valid only in the case that the permeability obeys Fick's law. Earlier studies [28, 29,31,47] on the permeability of insoluble monolayers and foam films [88] show that this usually

is not obeyed. The permeability is not a linear function of the surfactant chain length, but  $D$  varies with the number of  $\text{CH}_2$  groups in the hydrophobic part of the surfactant molecules [29,31]. Thus, it is more suitable to describe the results as permeability rather than as diffusion.

The background permeability of the bilayer could be described by any of the mechanisms of permeability of surfactant monolayers. The problem of finding  $k_i$  and, respectively,  $k$  according to nucleation theory is reduced to that of finding

$$S_h = \sum_{i=1}^{\infty} S_i \quad (6.14)$$

The area  $S_i$  is determined using nucleation theory of hole formation in bilayers [85-87, 89] as

$$S_i = (iA_{ef})n_iS \quad (6.15)$$

where  $A_{ef} = iA_m / 2$  ( $A_m$  is the area occupied by a single surfactant molecule) is the effective area of an  $i$ -sized hole. The density of the  $i$ -sized holes in the bilayer  $n_i$  ( $\text{m}^{-2}$ ) is given by [85, 86]

$$n_i = \left( \frac{1}{A_m} \right) \exp \left( - \frac{W_i}{k_B T} \right) \quad (6.16)$$

where  $W_i$  is the work of the formation of an  $i$ -sized hole in the bilayer. Equation (6.16) is valid when  $n_i \ll (1/A_m)$ . The work of formation of an  $i$ -sized hole depends on the surfactant concentration in the solution and is calculated from the thermodynamics of fluctuation formation of holes in the bilayer [85-87]

$$W_i = -i\Delta\mu + P_i, \quad \Delta\mu = k_B T \ln \left( \frac{C_{se}}{C_s} \right) \quad (6.17)$$

where  $C_s$  is the surfactant concentration, and subscript  $e$  stands for the equilibrium surfactant concentration in the solution. At  $C_s = C_{se}$  there is no driving force for the formation of large holes in the film. Above this concentration the film is stable with respect to rupture by hole nucleation. Equation (6.17) shows that the work  $-i\Delta\mu$  is gained ( $C_s < C_{se}$ ) or lost ( $C_s > C_{se}$ ) due to clustering of  $i$  single vacancies to form an  $i$ -sized hole, and during this process work  $P_i$  is needed to create the hole periphery. The quantity  $P_i$  can be determined only if the shape of the hole and the interaction energies of the molecules in the bilayer are known [89]. For large enough holes, it can be assumed that  $P_i$  is simply proportional to hole perimeter

$$P_i = (4\pi A_{ef} i)^{1/2} \gamma \quad (6.18)$$

where  $\gamma$  (J/m) is the specific free energy of the hole edge. Combining Eqs. (6.12)-(6.18) provides the following expression for the bilayer film permeability

$$k = \frac{D_0}{h} + A_{ef} \sum_{i=1}^{\infty} i D_i n_i \quad (6.19)$$

Equation (6.19) states that the permeation of the gas through the holes of size  $i$  depends on the hole density  $n_i$ . The possibility of the formation of large holes in the bilayer is small, and their density is low. Therefore, the main contribution to the film permeability will be due to the existence of a large number of sufficiently small holes. From Eqs. (6.16), (6.17), and (6.19) an equation is obtained, which expresses the relation between surfactant concentration and foam film permeability

$$k = k_0 + \sum_{i=1}^{\infty} \varepsilon_i \left( \frac{1}{C_s} \right)^i \quad (6.20)$$

where,

$$\varepsilon_i = \left( \frac{A_{ef}}{A_m h} \right) i D_i C_{se}^i \exp\left( -\frac{P_i}{k_B T} \right) \quad (6.21)$$

Physically  $\varepsilon$  is the permeability coefficient of certain holes of the bilayer at  $C_s = C_{se}$ . It can be obtained as a fitting parameter of the experimental data.

Equation (6.20) shows that the foam film permeability increases with decreasing surfactant concentration because the required work for formation of a hole decreases. When the concentration of surfactant increases, the density of holes decreases, and the required work for the formation of a hole increases. As a result, permeability of the gases through the bilayer decreases. The permeability of the bilayers decreases with the increase of surfactant concentration until it reaches its minimum value, i.e.,  $k_0$ . After this, minimum permeability of the foam film is independent of surfactant concentration and remains constant. Furthermore, Eq. (6.20) implies that the dependence of foam film permeability on temperature is not a simple Arrhenius dependence. The nucleation theory of fluctuation formation of holes in foam bilayers also explains the stability of the NBF. It shows that there is a range of surfactant concentrations where the film is in metastable equilibrium. In this range the film is stable and permeable even though some holes are formed, which can rupture the film [86]. This can be seen from Fig. 6.2.

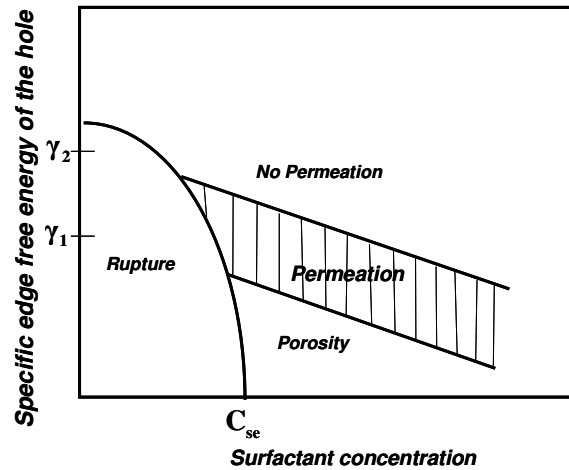


**Fig. 6.2:** Bilayer permeability: the shaded area shows the area in which the bilayer is permeable to gases.  $\gamma$  is the hole specific edge energy [86].

### 6.3.3. Freely standing film diffusion theory

Nguyen et al. [19, 20] studied a special case of interest, e.g. a train of foam films in a matrix. They developed a “freely standing film diffusion” model to investigate the resistance of one or more films to the mass transfer in this case. The model allows experiments on vapor components, extending the range of investigated gases. This mechanistic model relates the effective gas diffusivity to foam film density (number of foam films per unit of length) and permeability, which itself is a complex function of electrolyte concentration, gas solubility, surfactant concentration, and temperature.

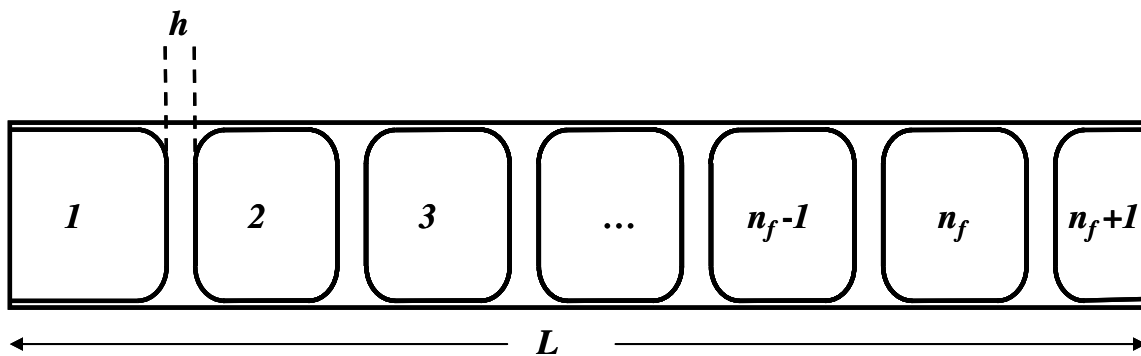


**Fig. 6.3:** Schematic of a train of foam films with the equal thickness of  $h$  in cylinder with the length of  $L$ . In the presence of  $n_f$  intervening foam films the 1-D gas space is separated to  $n_f+1$  sections.

In the presence of  $n_f$  intervening foam films with the equal thickness of  $h$ , the one dimensional gas space is separated to  $n_f + 1$  sections (Fig. 6.3). The gas flux will be reduced as a result of film resistance  $1/k_{eff}$  with  $k_{eff}$  being the effective coefficient of the gas transfer across  $n_f$  films. The whole system is assumed to have an effective diffusion of  $D_{eff}$ . The difference between  $D_{eff}$  and

the diffusion coefficient of the gas in the gaseous mixture,  $D_g$ , is the measure of the film resistance. The effective resistance mass transfer coefficient of the gas  $k_{eff}$  through  $n_f$  foam films of thickness  $h$  in a cylinder with a length  $L$  can be written as

$$\frac{1}{k_{eff}} = \frac{(L - n_f h)}{D_g} + \frac{n_f H}{k} \quad (6.22)$$

where  $H$  is the Henry's coefficient of gas solubility in the aqueous core of the film. Equation (6.22) is obtained under steady-state condition, assuming that the mass transfer rate is linearly proportional to the driving force and the equilibrium relationship is a straight line. Assuming that the permeability of a single film follows the sandwich model, its permeability coefficient,  $k$ , is defined as

$$\frac{1}{k} = \frac{2}{k_{ml}} + \frac{1}{k_w} \quad (6.23)$$

where  $k_w$  is the background mass transfer coefficient in the bulk. When the film thickness is much smaller than the length of the cylinder, Eq. (6.22) reads

$$\frac{L}{D_{eff}} = \frac{1}{k_{eff}} = \frac{1}{k_g} + n_f H \left( \frac{1}{k} \right) \quad \text{for } h \ll L \quad (6.24)$$

where,  $k_g = D_g/L$  is the mass transfer coefficient of the investigated gas in the gaseous mixture. Since the film thickness  $h$  is neglected in Eq. (6.24), the quantity  $k$  reduces to the permeability of a bilayer film (respectively Eq. (6.23) reduces to  $1/k = 2/k_{ml}$  and is determined from the adsorption density of the surfactant molecules at the film interfaces.

Nguyen et al. [19, 20] assumed that the state of unsaturated monolayers varies considerably with the dynamic adsorption behavior of the surfactant, which depends in turn on the presence of electrolytes in the solution. As a result, similar to the monolayer permeability, the permeability of a foam film to gas is also dependent on the surface coverage of the surfactant or adsorption density.

The adsorption density,  $\theta$ , is defined as the ratio of the equilibrium density,  $n_{eq}$ , to the closed packed density,  $n_0$ , of the surfactant molecules at the interface, provided that the effective area per molecule of the surfactant,  $A_m$ , is constant. However, it is well known that the effective area per molecule of surfactant in the interface varies significantly with surface pressure and decreases with the increasing  $\theta$  [90]. The authors proposed the following form of the effective fraction of

the occupied sites:  $\theta$  to the power of  $1/(\lambda - 2\theta)$  where  $\lambda (= 4)$  shows the maximum change in the effective area per surfactant molecule with varying surfactant concentration. Therefore, from the kinetics theory, the overall penetration rate of gas molecules across this interface can be written as

$$k = \left(1 - \theta^{\frac{1}{\lambda - 2\theta}}\right)^2 F e^{(-E_w / R_B T)} + \left(\theta^{\frac{1}{\lambda - 2\theta}}\right) F e^{(-E_f / R_B T)} \quad (6.25)$$

where,

$$F = \frac{H}{\sqrt{2\pi M R_B T}} \quad (6.26)$$

and,

$$H = H_0 e^{\left(\frac{-\Delta H}{R_B} \left(\frac{1}{T} - \frac{1}{T_0}\right)\right)} \quad (6.27)$$

$E_f$  and  $E_w$  are respectively the penetration activation energies across the occupied and unoccupied sites, and  $\Delta H$  is the enthalpy of the solution. The power two of the unoccupied sites in Eq. (6.25) considers both of the film surfaces. However, depending on the overlapping structure of the two monolayers, a power other than 2 can be also taken. This number should be lower for sufficient thick films and vice versa. The fraction of occupied sites can be obtained by a Langmuir type of adsorption equation [91]

$$\theta = \frac{(B/n_0) C_s e^{(E_a / R_B T)}}{1 + (B/n_0) C_s e^{(E_a / R_B T)}} \quad (6.28)$$

$$\text{where, } E_a = \frac{521 n_{hc}}{N_A} + 12 \times 10^{-6} n_{hc} n_0^{0.5} - z e \psi_0$$

In these equations  $C_s$  is the surfactant concentration,  $E_a$  is the desorption activation energy,  $B$  is the adsorption-desorption equilibrium constant,  $n_0$  is the closed-packed adsorption density, and  $z$  and  $e$  are the valence number and electric charges, respectively.  $\psi_0$  is the Gouy potential and is expressed as a function of electrolyte concentration, temperature, and effective area per surfactant molecule [90]. This model is capable of explaining the effect of surfactant concentration, the length of hydrocarbon chains, as well as the effect of temperature and electrolyte concentration.

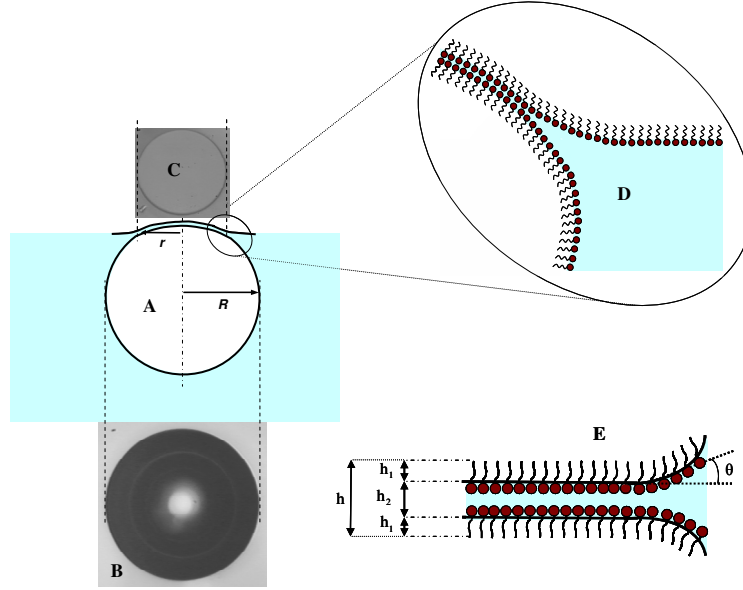


**Fig. 6.4:** Sketch of the “diminishing bubble” experiment. The free floating bubble A) is imaged from the top B) and from the bottom C) using reflected and transmitted light microscopes. The film contacts the bulk solution via meniscus at a contact angle  $\theta$  (D). The film consists (E) of two surfactant monolayers (thickness  $h_1$ ) separated by an aqueous core (thickness  $h_2$ ).

## 6.4. EXPERIMENTAL

### 6.4.1. Principle and set-up

*Gas Permeability:* We used diminishing bubble method [92-94] to measure the film permeability. In this method a bubble with the radius of  $R$  is blown on the surface of the solution with a fine capillary tube. On the top of the bubble a foam film with the radius of  $r$  is formed (Fig. 6.4). Due to the difference between inside and outside pressures of the bubble (capillary pressure) the gas molecules permeate through the film and the bubble, and respectively the film, shrink. We assume that the liquid is fully saturated with the gas at the start and therefore the rate of the bubble shrinkage is only related to the outward diffusion of gas molecules through the film. Thus the driving force, i.e.  $\Delta C_g$  in Eq. (6.1), is provided by

$$\Delta C_g = \frac{1}{R_B T} \frac{2\sigma}{R} \quad (6.29)$$

where,  $\sigma$  is the surface tension of the bulk solution,  $R$  is the radius of the bubble and  $R_B$  and  $T$  are universal gas constant and temperature respectively. Assuming that the gas inside the bubble is an ideal gas the following expression is obtained to calculate the gas permeability coefficient (for derivation see Appendix C)

$$k = \frac{\frac{P_{atm}}{2\sigma} (R_0^4 - R_t^4) + \frac{8}{9} (R_0^3 - R_t^3)}{\int_0^t r^2(t) dt} \quad (6.30)$$

In this equation  $r$  is the radius of the formed film and  $R_0$  and  $R_t$  are the bubble radii at the beginning ( $t = 0$ ) and at the end of experiment ( $t = t$ ) respectively. Two microscopes, one from top and the other from the bottom, are used to monitor the changes in bubble radius and film radius. These microscopes are connected to digital cameras. The obtained images are recorded with a video which is connected to a monitor. The temperature of the cell is kept constant with an accuracy of  $\pm 0.1^\circ\text{C}$ .

The denominator of Eq. (6.30) is solved numerically from the experimental  $r(t)$  dependence. An example of such dependence is shown in Fig. 6.5. The experimental resolution of the technique is  $\pm 0.002$  cm/s. The experiments were performed at constant temperature controlled with a precision of  $\pm 0.1^\circ\text{C}$ . All presented K values are arithmetical mean values from more than 10 single experiments. The standard deviations of the mean values are presented as error bars in the figures. The permeating gas was always air.

### 6.3.2. Materials

The same materials explained in Chapter 5 were used to perform the experiments, i.e., AOS as surfactant, NaCl as electrolyte and deionized water with pH of 5.5.

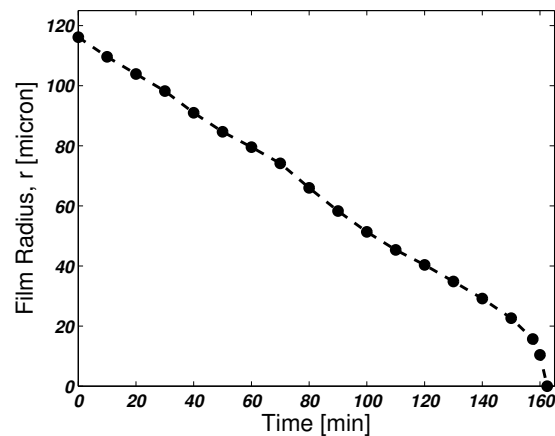


**Fig. 6.5:** Experimental dependence of the radius of the film  $r$  on the time  $t$ . The gas pressure in the bubble is higher because of the capillary pressure. This causes permeation of gas through the thin foam film and  $r$  decrease with time. Such sets of data were used to calculate numerically the denominator in Eq. 6.30.

## 6.4. RESULTS AND DISCUSSION

### 6.4.1. Effect of NaCl concentration

The film permeability is strongly dependent upon the film thickness (see Eq. 6.11). The film thickness can be precisely tuned by changing the concentration of electrolyte in the surfactant solution according to the predictions of the classical DLVO theory. The gas permeability of the films was measured in large range of electrolyte (NaCl) concentrations. Two AOS surfactant concentrations were used to stabilize the films –  $3.0 \times 10^{-4} M$  and  $9.5 \times 10^{-3} M$ , one below and the other above the CMC of the salt-free solution. The NaCl concentration was varied from  $0 M$  (salt free solution) to  $0.50 M$ . As was shown in Chapter 5, in this range of electrolyte and surfactant concentrations the foam film thickness varies from ca.  $50 nm$  (CBF) down to  $5.0 nm$  (NBF). The dependence of the film permeability on the NaCl concentration is shown in Fig. 6.6. The results show sharp increase of the film permeability  $k$  with increase of the salt concentration up to a certain point followed by a decrease in  $k$ . This result is similar to that already observed for films stabilized with sodium dodecyl sulfate (SDS). The film thickness was varied in these earlier experiments either by changing the NaCl concentration [89] or by applying additional pressure on the film surfaces [92].

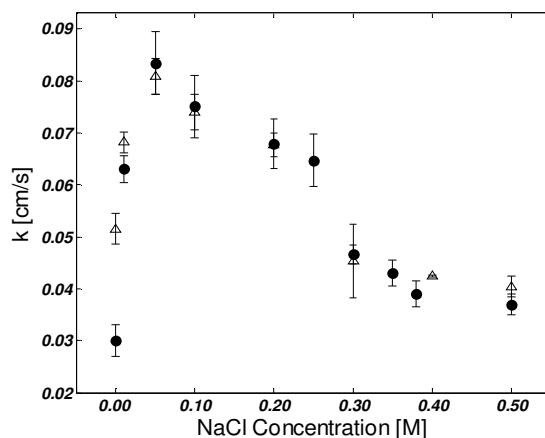


**Fig. 6.6:** Film permeability as a function of the NaCl concentration. Films were prepared from AOS surfactant solutions with concentrations: ● -  $3.0 \times 10^{-4} M$  (0.01 wt%) and △ -  $9.5 \times 10^{-3} M$  (0.3 wt%).

The increase of the NaCl concentration in the surfactant solution has a dual effect. Firstly, it suppresses the repulsive electrostatic double-layer component of the disjoining pressure in the film, and the film thickness decreases [95,96]. The film permeability has to increase with decreasing film thickness according to Eq. 6.11. The dependence of the film permeability on the film thickness is shown in Fig. 6.7. The figure shows that indeed the film permeability slightly increases when the film thickness decreases up to a thickness of  $15 nm$ , where CBFs start to form. In this range of thicknesses, the gas permeability of the films is governed by the permeability of

the central aqueous layer of the film. After that point the gas permeability strongly decreases, most probably because the permeability of the surfactant adsorbed monolayers controls the permeability rate of the whole film.

Secondly, the salt concentration influences the adsorption of the surfactant (in the case of ionic surfactants) due to the screening of the electrostatic repulsion between the adsorbed ions. Generally, the surfactant adsorption has to increase when the salt concentration increases. Higher adsorption at the film surfaces has to decrease the film permeability, as predicted from different theories of the permeability of gas molecules through layers of surfactant molecules.

The data of adsorption of the molecules of AOS on the surface of a bulk solution at different NaCl concentrations were presented in Chapter 5. As pointed out, for solutions of a single ionic surfactant with inorganic electrolyte the measurements of surface tension vs.  $c^*$  at different electrolyte concentrations fall on a master curve. The mean ionic activity is defined as  $c^* = \gamma_{\pm} (c_{AOS} (c_{AOS} + c_{NaCl}))^{1/2}$  with  $\gamma_{\pm}$  being the mean ionic activity coefficient and,  $c_{AOS}$  and  $c_{NaCl}$  – surfactant and salt concentrations. This implies that at a given mean ionic activity the surfactant adsorption is independent of electrolyte concentration, i.e. the ionic atmosphere contribution to the surface pressure is negligible. This was confirmed in Chapter 5 for the case of AOS surfactant and in Ref. [97] for the case of SDS surfactant.

The adsorption,  $\Gamma_s$ , continuously increases with the addition of either salt or surfactant by changing  $c^*$ . However, precisely in this range of surfactant and NaCl concentration the film permeability increases first of then sharply decreases. One has to remember that the surface tension of the solutions changes only up to point of the CMC, which changes with the addition of salt. The higher surfactant concentration we used ( $9.5 \times 10^{-3} M$  (0.30 wt%)) is always well above the CMC of AOS independent of the salt concentration of the solution. The lower surfactant concentration ( $3.0 \times 10^{-4} M$  (0.01 wt%)) is above CMC for the higher salt concentration of 0.5 M NaCl and below CMC for the lower salt concentration of 0.05 M NaCl. These data allowed the surfactant adsorption to be estimated using the surface tension and adsorption data presented in Chapter 5. The  $c^*$  varies between  $4.3 \times 10^{-3}$  and  $1.5 \times 10^{-2} M$  and respectively the adsorption varies with less than 10% from  $4.8 \times 10^{-6}$  to  $5.2 \times 10^{-6} \text{ mole/m}^2$  (see Fig. 6.5). This minor increase in the surfactant adsorption cannot explain the two-fold decrease of the gas permeability of the films at high salt concentration. This could mean that the change in the surfactant adsorption at the film surfaces with the increase of the surfactant concentration is different than that at the surface of a bulk solution of AOS.

An alternative explanation of the sharp decrease of the gas permeability of the films was given in Ref. [98]. It has been shown that the gas permeability is influenced by an increasing adsorption density of the surfactant at the film surfaces, if the free energy of film formation becomes negative with increasing salt concentration. This quantitatively explains the remarkable finding that the film permeability decreases with decreasing thickness. The monolayer permeability which governs the permeability through very thin films depends on the area in the monolayers accessible for gas molecules to go through. This area can be described by the number of unoccupied sites in the adsorption layer. At the transition to the Newton black film this number and therefore the accessible area decrease significantly due to the effect of the film interaction on the state of the monolayers. The proposed mechanism describes the variation of film permeability at the CBF to NBF transition. Indeed the transition in the gas permeability occurs at salt concentrations of ca. 0.05 M which is lower than that estimated to be defined as critical for the transition from CBF to NBF ( $c_{NaCl} = 0.35$  to  $0.40$  M). Similar effect was also observed in Ref. [92] and might be explained by the assumption that the strong attractive interaction between the film surfaces can change the surfactant adsorption at the film surfaces even before the transition from CBF to NBF.

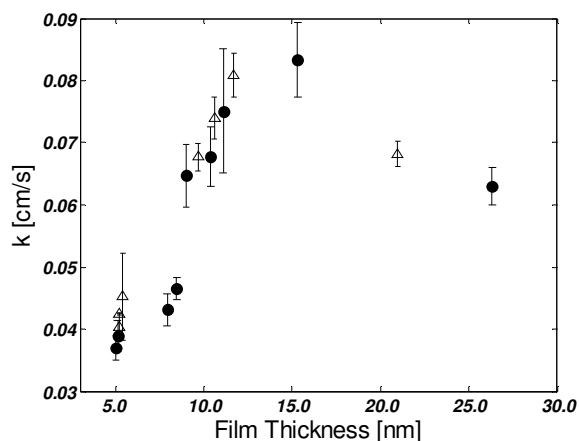


**Fig. 6.7:** Film permeability as a function of the film thickness. The film permeability values are the same as in Fig. 3. The thickness is taken from Ref. [30]. Films were prepared from AOS surfactant solutions with concentrations: ● -  $3.0 \times 10^{-4}$  M (0.01 wt%) and △ -  $9.5 \times 10^{-3}$  M (0.3 wt%).

#### 6.4.2. Effect of surfactant concentration

The film permeability coefficients were measured for different AOS concentrations at a constant NaCl concentration of  $c_{NaCl} = 0.50$  M. The dependence of foam film permeability on AOS concentration is presented in Fig. 6.8. The temperature remained constant during the experiments ( $T = 24$  °C). Newton black films with the equilibrium thickness of ca. 5 nm are formed at this NaCl concentration (Chapter 5). The surfactant concentration was changed from  $9.5 \times 10^{-5}$

to  $1.3 \times 10^{-2} M$ . The entire studied range of concentrations was above the CMC, which is  $1.3 \times 10^{-4} M$  at the conditions of the experiment, since formation of stable films was not possible below the CMC. This is most likely due to the fact that the adsorption surfactant monolayers are not saturated below the CMC [95]. Another reason might be existence of impurities in the surfactant solution, which was confirmed by the appearance of a minimum in the surface tension vs. surfactant concentration curves in Chapter 5.

Figure 6.8 shows that the permeability of film remains constant for concentrations above CMC similar to other experiments with different surfactants [89,94] and predicted theoretically as explained previously. However, above a certain AOS concentration ( $3.0 \times 10^{-3} M$ ) the film permeability increases with increasing surfactant concentration.

This observation contradicts the previous theoretical predictions and experimental observations. The mechanism of this effect is not known. One can speculate and propose different mechanisms to explain the experimental observation. In general, the micelles can change the properties of either the adsorbed surfactant monolayers or the aqueous layer or the whole films.

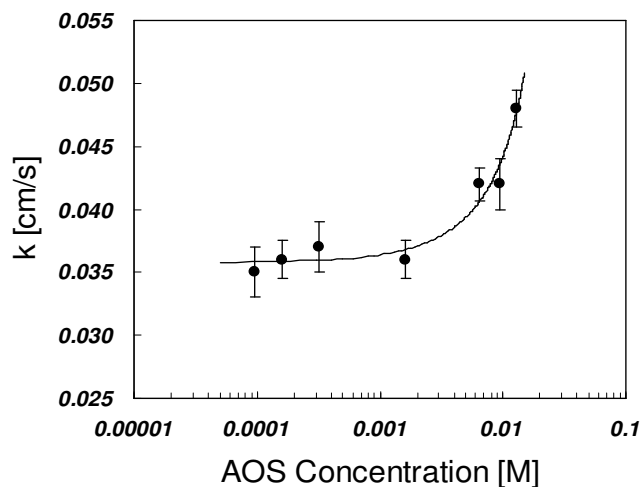


**Fig. 6.8:** Gas permeability of foam films on AOS concentration at a constant NaCl concentration of  $c_{NaCl}=0.50 M$  and constant temperature of  $T=24 ^\circ C$ . At these conditions only NBF are formed. The points are experimentally determined values. The solid line is only a guide for the eye.

As an explanation for the observed phenomenon few possible mechanisms could be considered. The solubility of air in the bulk solution increases when the surfactant concentration increases, similar to the observation reported for SDS solutions [99,100]. Therefore, some part of the gas diffuses into the bulk to satisfy the enhanced solubility. This explanation is, however, unlikely

because the solutions were made at least one day prior to the experiments and left at least for 24 hours for gas saturation.

The films which we studied are very thin NBF. In general they have to only consist of two surfactant layers separated by few layers of hydration water. However, at high surfactant concentrations when the concentration of micelles in the film forming solution is high some micelles could be captured in the film during the thinning process. Similar behavior was already observed and reported in the literature [101]. The existences of such captured micelles can change the properties of the films and their permeability. We have no direct observation of such effects in our films because the film thickness was measured at much lower surfactant concentrations. Even though, we believe that presence of micelles in the NBF at very high surfactant concentration might be possible and can explain the increased permeability.

The nucleation theory of formation of holes in the NBF [89,95] postulates that gas permeability occurs through small holes, which consist of molecular vacancies in the film [95]. The formation of these holes depends on the work used for their formation. One of the important contributions to this work is the linear energy at the line that separates the hole from the non-defect film. If this line binds to a micelle attached to the film surface, the linear energy might be decreased, thus increasing the probability of formation of a hole in the film. This will increase the rate of the permeability through the film [86].

Another hypothesis could be that the micelles captured in the film enhance its permeability similar to mechanisms presented in several recent studies which have reported that presence of micelles enhances the mass transfer between emulsion droplets. According to the hypothesis micelles facilitate mass transfer by acting as carriers of oil molecules [102,103]. Therefore it is possible that micelles act as carriers of gas molecules, thus increasing the permeability of foam films.

#### **6.4.3. Effect of temperature**

To investigate the effect of temperature gas permeability coefficient of AOS films was measured in the temperature range from 22-32 °C at a constant AOS concentration of  $c_{AOS}=3.2 \times 10^{-4}$  M and a constant NaCl concentration of  $c_{NaCl}=0.50$  M. In the whole range of temperatures NBFs were formed. The results are presented in Fig. 6.9.

The foam film permeability increases with increasing temperature. According to the gas kinetics theory, with increasing temperature the average energy of the gas molecules and the collision frequency of the gas molecules with the surfactant molecules at the interface increase. Therefore,

the number of the gas molecules that can overcome the energy barrier and pass through the film increases. The energy barrier theory relates the film permeability to temperature by Eq. (6.4). Using Arrhenius coordinate  $\Delta E$  was calculated to be  $\Delta E=35.5$  kJ/mol in the case of the NBF stabilized with AOS. This energy is different than that estimated for NBF formed from other surfactant solutions [88,94,104,105] some of them with film permeability similar to that of AOS. Obviously, the pre-exponential factor plays an important role describing the temperature dependence of the gas permeability of the foam films.

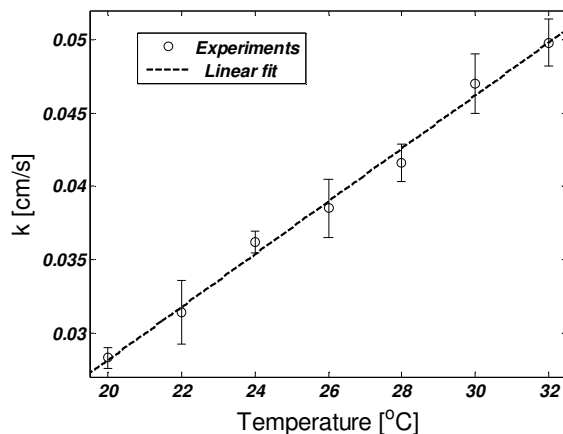


**Fig. 6.9:** Dependence of the film permeability on the temperature for Newton Black Films from  $3.2 \times 10^{-4}$  M AOS in presence of 0.5 M NaCl.

## 6.5. CONCLUSIONS

We studied the gas permeability of foam films stabilized with (C<sub>14</sub>-C<sub>16</sub>)-alpha olefin sulfonate (AOS) to air. According to the film permeability model of Princen and Mason [77] the permeation process depends on the permeability and thickness of the film aqueous core and the permeability of the surfactant adsorption layers which form the film. Varying the film thickness by changing the electrostatic double layer repulsion in the film we changed the contribution of these different components to the whole permeability of the films. We observed that the gas permeability of the films increases when the film thickness decreases until certain value. The film permeability coefficient sharply decreases after that critical value. We conclude that after that critical point the film permeability is governed by the monolayer permeability, respectively the adsorption density of the surfactant monolayers. The decrease of the  $k$  after this point can be explained by decreased permeability of the monolayers. This might be a result of increased adsorption upon increase of the electrolyte concentration most probably because of the stronger interactions between the film surfaces. The film permeability shows an unexpected increase at high surfactant concentrations well above the CMC. We hypothesize that this is a result of faster gas transport via the aqueous film core facilitated by the micelles. Experiments at different temperatures allowed the energy of

the permeability process to be estimated using the simple energy barrier theory. Comparison with other similar systems shows that the pre-exponential factor in the theoretical description also plays an important role for the whole gas permeability.

## 6.6. REFERENCES

1. F. E. Fox and K. F. Herzfeld, *J. Acoust. Soc. Am.*, 26 (1954) 984.
2. D. E. Yount, *J. Colloid Interface Sci.*, 193 (1997) 50.
3. R. K. Prud'homme and S. A. Khan, *Foams: Theory, Measurements and Applications, Surfactant Science Series*, Eds.; Marcel Dekker: New York, Basel, Hong Kong, 1996, Vol. 57.
4. K. Sujatha, T. R. Das, R. Kumar and Gandhi, K. S., *Chem. Eng. Sci.*, 43 (1988) 1261.
5. N. Ramachandran, A. K. Didwania and K. K. Sirkar, *J. Colloid Interface Sci.*, 83 (1981) 94.
6. G. D. Rose and J. A. Quinn, *J. Colloid Interface Sci.*, 27 (1968) 193.
7. N. N. Li, *AIChE J.*, 17 (1971) 459.
8. O. Albrecht, A. Laschewsky and H. Ringsdorf, *Macromolecules*, 17 (1984) 937.
9. J. S. Do and W. B. Chang, *Sensors and Actuators B: Chemical*, 72 Issue 2 (2001) 101.
10. A. W. Snow and W. R. Barger, in: *C.C. Leznoff, A.B.P. Lever (Eds.) , Phthalocyanine*, Vol. I, VCH Publishers, 1989, p. 345.
11. T. Moriizumi, *Thin Solid Films*, 160 (1988), 413.
12. M. C. Petty, *Thin Solid Films*, 210-211 (1992) 417.
13. E. M. Scarpelli, *Surfactants and the Lining of the Lung*, The John Hopkins University Press: Baltimore, MD, 1988.
14. D. Exerowa and Z. Lalchev, *Langmuir*, 2 (1986) 668.
15. E. M. Scarpelli, *Pediat. Res.*, 12 (1978) 1070.
16. E. G. Schutt , D. H. Klein, R. M. Mattrey, J. G. Riess, *Angewandte Chemie International Edition*, 42 (28), (2003) 3218.
17. Sh. Qin and K. W. Ferrara, *Phys. Med. Biol.*, 51 (2006) 5065.
18. A. S. Angelatos, A. P. R. Johnston, Y. Wang and F. Caruso, *Langmuir*, 23 (2007) 4554.
19. P. Q. Nguyen, *Dynamics of foam in porous media*, PhD Dissertation, Delft University of Tech., The Netherlands, 2004.
20. P. Q. Nguyen., P. L. J. Zitha and P. K. Currie, *J. Colloid Interface Sci.*, 248 (2002) 467.
21. Q. P. Nguyen, P.K. Currie, M. Buijse, P.L.J. Zitha, *J. Petrol. Sci. Eng.*, 58 (2007) 119.
22. G.-Q. Tang and A. Kovscek, *Transport in Porous Media*, 65 (2006) 287.
23. D. Cohen, T.W. Patzek, C.J. Radke, *J. Colloid Interf. Sci.*, 179 (1996) 357.
24. D. Cohen, T.W. Patzek, C.J. Radke, *Transport in Porous Media*, 28 (1997) 253.
25. G. Hedestrand, *J. Phys. Chem.*, 28 (1924) 1585.
26. N. K. Adam, *J. Phys. Chem.*, 29 (1925) 610.
27. E. K. Rideal, *J. Phys. Chem.*, 29 (1925) 1585.
28. I. Langmuir and D. B. Langmuir, *J. Phys. Chem.*, 31 (1927) 1719.
29. I. Langmuir and V. J. Schaefer, *J. Franklin Inst.*, 235 (1943) 119.
30. F. Sebba and H. V. A. Briscoe, *J. Chem. Soc.* 106 (1940) 128.
31. R. J. Archer and V. K. La Mer, *J. Phys. Chem.* , 59 (1955) 200.
32. V. K. La Mer and M. L. Robbins, *J. Phys. Chem.*, 62 (1958) 1291.
33. V. K. La Mer, L. A. G. Aylmore and T. W. Healy, *J. Phys. Chem.*, 67 (1963) 2793.
34. V. K. La Mer and T. W. Healy, *Science*, 148 (1965) 36.
35. G. T. Barnes, T. I. Quickenden and J. E. Saylor, *J. Colloid Interface Sci.*, 33 (1970) 236.
36. G. T. Barnes and T. I. Quickenden, *J. Colloid Interface Sci.*, 37 (1971) 581.
37. T. I. Quickenden and G. T. Barnes, *J. Colloid Interface Sci.*, 67 (1978) 415.
38. G. T. Barnes, *Adv. Colloid Interface Sci.*, 25 (1986) 89.
39. G. T. Barnes and D. S. Hunter, *J. Colloid Interface Sci.*, 129 (1989) 585.
40. G. T. Barnes, *Colloids Surf., A*, 126 (1997) 149.
41. M. Blank, *J. Phys. Chem.*, 66 (1962) 1911.
42. M. Blank, *Tech. Surf. Colloid Chem. Phys.*, 1 (1972) 41.
43. E. Sada and D. M. Himmelblau, *AIChE J.*, 12 (1966) 894.

44. V. K La Mer (Ed.), *Retardation of Evaporation by Monolayers: transport Process*, Academic Press, New York, 1962.
45. H. L. Rosano and V. K. La Mer, *J. Phys. Chem.*, 60 (1956) 348.
46. T. G. Springer and R. L. Pigford, *Ind. Eng. Chem. Fundam.*, 9 (1970) 458.
47. J. Li, H. Schuring and R. Stannarius, *Langmuir*, 18 (2002) 112.
48. J. G. Hawke and I. White, *J. Phys. Chem.*, 74 (1970) 2788.
49. J. G. Hawke and H. J. L. Wright, *Nature*, 212 (1966) 810.
50. J. G. Hawke and I. White, *J. Phys. Chem.*, 70 (1966) 348.
51. J. G. Hawke and A. E. Alexander, in V. K La Mer (Ed.), *Retardation of Evaporation by Monolayers: transport Process*, Academic Press, New York, 1962, pp. 67-73.
52. D. H. T. Chen, *Amer. Inst. Chem. Eng. J.*, 15 (1969) 617.
53. G. T. Barnes, *Specialist Periodical Reports: Colloid Science*, 3 (1979) 150.
54. M. Blank, *Proc. 4th Int. Cong. Surface Active Substances*, Brussels, 1964, Vol. 2, pp.969-979.
55. M. Blank, in R.J. Good, R.R. Stromberg and R.L. Patrick (Eds.), *Techniques of Surface and Colloid Chemistry and Physics*, Marcel Dekker, New York, 1972, Vol. 1, pp.41-88.
56. M. Blank and F. J. W. Roughton, *Trans. Faraday Soc.*, 56 (1960) 1832.
57. J. G. Hawke and A. E. Alexander, *Proc. 3rd. Int. Cong. Surface Activity*, Cologne, 1960, Vol. 2, pp.184-188.
58. F. Goodridge and D. J. Bricknell, *Trans. Inst. Chem. Eng.*, 40 (1962) 54.
59. S. Whitaker and R. L. Pigford, *Amer. Inst. Chem. Eng. J.*, 12 (1966) 741.
60. R. E. Plevan and J. A. Quinn, *Amer. Inst. Chem. Eng. J.*, 12 (1966) 894.
61. J. A. Caskey and D. L. Michelsen and Y. P. To, *J. Colloid Interface Sci.*, 42 (1973) 62.
62. J. Petermann and Ber. Bunsen., *J. Phys. Chem.*, 81 (1977) 649.
63. J. A. Caskey and W. B. Jr. Barlage, *J. Colloid Interface Sci.*, 41 (1972) 52.
64. L. A. Crum., *J. Acoust. Soc. Am.*, 68 (1980) 200.
65. B. W. Bussey, *PhD Thesis in Chemical Engineering*, University of Delaware, 1966.
66. J. Hanwright, J. Zhou, G. M. Evans and K. P. Galvin, *Langmuir*, 21 (2005) 4912.
67. R. Farajzadeh, A. Barati, H.A. Delil, J. Bruining, P. L. J. Zitha, *Mass Transfer of CO<sub>2</sub> into water and surfactant solutions*, Petroleum Sci, & Tech. (2007).
68. A. G. Brown, W. C. Thuman and J. W. McBain, *J. Colloid Sci.*, 8 (1953) 491.
69. A. G. Brown, W. C. Thuman and J. W. McBain, *J. Colloid Sci.*, 8 (1953) 508.
70. J. C. Maxwell, *Nature*, (1873) 437.
71. W. J. Moore, and H. J. Eyring, *Chem. Phys.*, 6 (1938) 381.
72. G.T Barnes and V.K. La Mer, in: V.K. La Mer (Ed.), *Retardation of evaporation by Monolayers: transport processes*, Academic press, New York, 1962, p.9
73. M. Blank, in V.K. La Mer (Ed.), *Retardation of Evaporation by Monolayers: Transport Processes*, Academic Press, New York, 1962, pp.75-95.
74. M. Blank, *J. Phys. Chem.*, 68 (1964) 2793.
75. Blank M. and Britten J.S., *J. Colloid Sci.*, 20, 789-800 (1965)
76. D. D. Bockman, *Ind. Eng. Chem. Fundamentals*, 8 (1969) 77.
77. H. M. Princen and S. G. Mason, *J. Colloid Sci*, 20 (1965) 353.
78. H. M. Princen, J. Th. G. Overbeek and S. G. Mason, *J. Colloid Int. Sci*, 24, 125-130, 1967
79. G. J. van Amerongen, Thesis, Delft, 1943.
80. A. E. Korveze and E. A. Mol, *J. Polymer Sci.*, 2 (1947) 371.
81. M. Sidorova, M. Nedyalkov and D. Platikanov, *Colloid Polym. Sci.*, 254 (1976) 45.
82. U. A. Chizmadzhev, L. V. Chernomordik, V. F. Pastushenko, and I. G. Abidor, in: P. G, Kostyuk (Ed.) *Biofizika Membran*, Vol. 2, (Moscow: AN USSR), (1982), p. 161.
83. A. Kotyk and K. Janacek, *Membrane Transport. An interdisciplinary Approach*, New York, Plenum, (1977).
84. H. T. Tien, *Bilayer Lipid Membranes (BLM). Theory and Practice*, New York: Dekker, 1974.
85. D. Kashchiev and D. Exerowa, *J Colloid Interface Sci.*, 77 (1980) 501.
86. D. Kashchiev and D. Exerowa, *Biochim Biophys Acta* 732 (1983) 133.
87. D. Kashchiev, *Coll & Polym Sci*, 265 (1987) 436.

88. R. Krustev, D. Platikanov and M. Nedyalkov, *Colloids and Surfaces A: Physicochem. Eng. Aspects*, 79 (1993) 129.
89. M. Nedyalkov, R. Krustev, D. Kashchiev, D. Platikanov and D. Exerowa, *Coll. & Polym. Sci.*, 266 (1988) 291.
90. C. H. Paul, in: *Principles of colloids and surface chemistry*, vol. 9, Chap. 7, Marcel Dekker, New York, 1986.
91. J. T. Davies and E. K. Rideal, *Interfacial Phenomena*, Academic Press Inc.: New York, 1961, chapter 7, pp. 301-321.
92. R. Krustev, D. Platikanov, M. Nedyalkov, *Langmuir*, 12 (1996) 1688.
93. R. M. Muruganathan, R. Krustev, H.-J. Müller, H. Möhwald, *Langmuir*, 22 (2006) 79819.
94. M. Nedyalkov, R. Krustev, A. Stankova, D. Platikanov, *Langmuir*, 8, 3142 (1992).
95. D. Exerowa and P.M. Kruglyakov, *Foam and Foam Films*, Elsevier Science, 1998
96. G. T. Barnes and D. S. Hunter, *J. Coll. Inter. Sci.*, 136 (1990) 198.
97. T. D. Gurkov, D.T. Dimitrova, K.G. Marinova, C. Bilke-Crause, C. Gerber, I. B. Ivanov, *Colloids and Surfaces A: Physicochemical and Engineering Aspects*, 261 (2005) 29-38.
98. R. M. Muruganathan, R. Krustev, N. Ikeda and H.-J. Müller, *Langmuir*, 19, 3062 (2003).
99. A.D. King, Jr., Solubilization of Gases, in: *Solubilization in Surfactant Aggregates* By Sherril Duane Christian, John F. Scamehorn, Contributor Sherril Duane Christian, Chapter 2, Published by CRC Press, 1995.
100. I.B.C. Matheson and A.D. King, Jr, *J. Colloid Interf. Sci.*, 66 (3), (1978) 464.
101. V. Bergeron, *Langmuir*, 12 (1996) 5751.
102. J.G. Weers, *Molecular diffusion in emulsions and emulsion mixtures*, in: *Modern Aspects of emulsion science*, Ed.: B.P. Binks, Published by Royal Society of Chemistry, 1998.
103. S. Karaborni, N.M. van Os, K. Esselink and P.A.J. Hilbers, *Langmuir*, 19 (1993) 1175.
104. R. Krustev, D. Platikanov, A. Stankova, M. Nedyalkov, *J. Disp. Sci. Technol.*, 18 (1997) 789.
105. R. M. Muruganathan, H.-J. Müller, H. Möhwald, and R. Krustev, *Langmuir*, 21 (2005) 12222.

## **PART III.**

### **Foam in Porous Media**



---

## Chapter 7

# EFFECT OF GAS TYPE ON FOAM FLOW IN POROUS MEDIA

---

### ABSTRACT

*An experimental study of the motion of CO<sub>2</sub> and N<sub>2</sub> foams in granular porous media using X-ray Computed Tomography is reported. In the experiments gas is forced through natural porous media initially saturated with a surfactant solution, a process known as surfactant-alternating-gas or SAG. The CO<sub>2</sub> was either under sub- or super-critical conditions whereas N<sub>2</sub> remained under subcritical conditions at all experimental conditions. We found injection of gas following a slug of surfactant can considerably reduce gas mobility and promote higher liquid recovery at the experimental conditions investigated. Foaming of CO<sub>2</sub> builds-up a lower pressure drop over the core at both low and high pressures than N<sub>2</sub>. Both gases require a certain penetration depth to develop into foam. The space is longer for N<sub>2</sub> (large entrance effect) and increases with increasing gas velocity. Moreover, the ultimate liquid recovery of CO<sub>2</sub> foam is always lower than of N<sub>2</sub> foam. The possible mechanisms explaining the observed differences in foaming behavior of the two gases are discussed in detail.*

**KEYWORDS:** *Foam, Porous media, Surfactant Alternating Gas (SAG), Carbon Dioxide (CO<sub>2</sub>), Nitrogen (N<sub>2</sub>), Gas solubility, Foam stability, Disjoining pressure, X-ray Computed Tomography.*

**Published in:** *Industrial and Engineering Chemistry Research, 48(9) (2009) 4542.*

## 7.1. INTRODUCTION

The environmental issues concerning CO<sub>2</sub> and shortage of energy supply has increased the interest in combined geological CO<sub>2</sub> storage and CO<sub>2</sub> flooding to enhance oil recovery (EOR) [1-3]. Favorable characteristics of CO<sub>2</sub> include miscibility with oil, swelling and the ensuing lowering of viscosity [4-6]. Even at immiscible conditions CO<sub>2</sub> can considerably reduce the oil viscosity and swell the oil volume leading to a significant improvement of oil recovery [4-6]. Nevertheless, due to its low viscosity and density, even at reservoir conditions, CO<sub>2</sub> segregates upwards thus overriding water (and eventually oil) and channels through high permeability streaks [5,7]. Foaming of CO<sub>2</sub> reduces its mobility and can potentially overcome these drawbacks [5,8-10]. The mobility reduction of gas will result in a more favorable sweep efficiency [5,11-13]. Even if the recovery is not improved the costs of handling of the gas will be reduced [14].

Although the geological storage of CO<sub>2</sub> is considered an attractive solution for global warming, the efficiency (or even feasibility) of the process is not yet established [15]. One major problem is the leakage of the injected CO<sub>2</sub> through the walls of abandoned wells or through the cap rock [16]. In this case foaming of CO<sub>2</sub> may temporarily hamper the leakage while other actions are considered.

There are two main injection strategies in EOR-field projects related to foam. These include co-injection of gas and liquid, and surfactant alternating gas (SAG) injection. In the first strategy the gas and the liquid are co-injected at a fixed ratio. The ratio between the gas flowrate and the sum of the gas and the liquid flowrates (total flowrate) determines the foam quality. The foam can also be generated outside the porous medium before injection; however, we categorize this strategy under the co-injection scheme. In the SAG scheme alternating slugs of surfactant solution and gas are injected and therefore foam is generated inside the porous medium (in-situ generation) [9, 17,18]. The SAG foam is sometimes called *drainage foam* in the literature [19]. In a recent EOR application of the foam in the Norwegian Snorre field the SAG phase operations were conducted without any major problem while the co-injection was hampered by operational problems that resulted in unstable injectivity [20,21]. Moreover, the SAG process is similar to water alternating gas process (WAG) and requires little additional effort [5, 17-22]. SAG injection minimizes contact between water and gas in surface facilities and piping which can be important when the gas, e.g. CO<sub>2</sub>, forms an acid upon contact with water [23,24]. The laboratory study of Huh and Handy [25] also revealed that the gas-surfactant co-injection foam can completely block the porous medium under certain conditions, while this never occurs with the SAG foam. It was also shown that the mobility reduction factor is higher for co-injection foam than for SAG foam with the same gas flowrate.

While the co-injection foam has been the center of attention of many experiments [e.g. 26-31], there is only a little data on SAG foam [18,32-34, 93-4]. Moreover, in most of the previous studies on foam flow in porous media the measured pressure drop became stationary only after 10-100 pore volumes of the injected fluids (liquid and gas). In these experiments the pressure drop does not increase significantly until the gas phase reaches the end of the initially surfactant saturated porous medium, a phenomenon that cannot be explained by the existing models [35]. Possibly, this happens due to the high gas flowrates or short length of porous media used in experiments. Indeed, the injected gas needs to travel inside the porous medium before it mixes with the available surfactant and foams. However, when the gas flowrate is high or the porous medium is short, the gas will breakthrough before making a strong foam. The gas will only start to form a strong foam if many pore volumes are injected in the laboratory set-up and therefore the obtained results can only be representative of the initial stages of the injection process. It has been also observed that different gases behave differently, both in bulk [36-38] and porous media [18,39-42] experiments. Recently, Du et al. [27] claimed based on experimental evidence that there is difference between CO<sub>2</sub> and N<sub>2</sub> foams in porous media. In their experiments the gases were co-injected with SDS solution with high gas flowrates. The differences were attributed to the dissimilar physical properties of the gases, mainly higher CO<sub>2</sub> solubility in water than N<sub>2</sub>.

The purpose of this chapter is two-fold. Firstly we aim to add (high P-T) experimental data to the currently small database in the literature. Secondly, our goal is to study the effect of the gas type on the behavior of foam in porous media, at both low and high pressures and temperatures. Therefore, this chapter focuses on describing the experiments when CO<sub>2</sub> or N<sub>2</sub> is injected into a porous medium that is initially saturated with a surfactant solution (SAG foam). Section 7.2 describes the experimental set-up and the experimental procedures. Section 7.3 presents the experimental results for two sets of experiments. The first set of the experiments is performed at atmospheric pressure and a room temperature of  $T=20^{\circ}C$ . The second set of experiments is conducted at  $P=90\text{ bar}$  and  $T=50^{\circ}C$ . This condition is well above the critical point of CO<sub>2</sub>. Section 7.4 provides detailed explanations of the differences observed in the experiments and investigates the relevant physical/chemical properties of gases affecting the foam behavior in the porous medium. Finally we draw the main conclusions of this chapter.

## **7.2. EXPERIMENTAL**

### **7.2.1. CT imaging**

X-ray computed tomography (CT) is a technique of visualization of flow processes within opaque objects by constructing the local attenuation coefficients from multidirectional X-ray transmission data [5]. The variation in X-ray attenuation is closely related to density differences

within the object. Because density contrast usually correspond difference in the materials or phases, these data are often straightforward to interpret. Another important advantage of the CT is its digital output, which leads easily to quantitative analysis. The linear attenuation coefficient  $\mu$  [ $cm^{-1}$ ] can be defined as:

$$\mu = \rho \left( \sigma(E) + b \frac{Z_e}{E^{3.2}} \right)$$

where  $\rho$  is the electron density (bulk density) in electrons/cm<sup>3</sup>,  $\sigma$  is the Klein-Nishina coefficient,  $b$  is a constant ( $= 9.8 \times 10^{24}$ ),  $Z_e$  is the effective atomic number of the chemical species and  $E$  is the X-ray photon energy in keV. The values that come out from the computer attached to the CT scanner are measured in Hounsfield units (HU). The relationship between attenuation coefficient and HU is:

$$HU_m = 1000 \left( \frac{\mu_m}{\mu_w} - 1 \right) \quad (7.1)$$

where  $\mu_w$  displays the water attenuation coefficient: we obtain  $HU_m = 0$  for water and  $HU_m = -1000$  for air. The following equation is used to compute the liquid saturation,  $S_w$ , from the measured HU, eliminating the contribution of the rock by the subtraction:

$$S_w = \frac{HU_{foam} - HU_{dry}}{HU_{wet} - HU_{dry}} \quad (7.2)$$

where the subscripts foam, wet and dry stand for the foam flow, solution saturated and dry core conditions, respectively. Though theoretically the above equation is only valid under the insoluble conditions, it can still give good estimation for solutions with dissolved CO<sub>2</sub> gas under our experimental conditions, due to the fact that there is only negligible density variation coming from the gas dissolution.

### 7.2.2. Materials

**Chemicals:** The surfactant used was alpha-olefin sulfonate, AOS (Stepan company, The USA). This surfactant is anionic and was used as received without any further purification. The general structure of olefin surfactants is  $R-SO_3^-Na^+$ , where  $R$  represents the hydrophobic group. In our case the number of the carbon atoms in the surfactant structure is 12 and the molecular weight of the surfactant is  $M_w = 273$  g/mol. A fixed surfactant concentration of  $c_{AOS} = 1$  wt% (0.035 M) was used in our experiments. Sodium chloride (NaCl) was used to make the Brine. The concentration

of NaCl was a fixed value of 0.5M ( $\sim 3$  wt%) in all experiments reported here. At this concentration very thin (5 nm) Newton Black Films (NBF) are formed [44]. All solutions were prepared with deionized water ( $pH=6.8\pm 0.1$ ). In order to increase the CT attenuation of the solutions, 10 wt% of Sodium Wolframate was added to the solutions.

**Table 7.1:** Properties of sandstone cores (porous media) used in the experiments

Name	Permeability [mD]	Porosity [%]	Diameter [mm]	Length [mm]	Pore Volume [ml]	Main Composition
Long	1010	22 $\pm$ 0.2	40 $\pm$ 1	170 $\pm$ 2	42.5 $\pm$ 0.5	97% Quartz
Short	1010	22 $\pm$ 0.2	40 $\pm$ 1	90 $\pm$ 2	22.5 $\pm$ 0.5	97% Quartz

*Gases:* The gases used to carry out the experiments were 99.98% pure CO<sub>2</sub> and N<sub>2</sub>. The solubility of CO<sub>2</sub> in water is about 55 times higher than that of nitrogen [46].

*Porous Media:* The porous medium used was consolidated, quasi-homogenous and quartz-rich Bentheimer sandstone. The main properties of the porous medium are presented in Table 7.1. The permeability was calculated from the pressure data of a single-phase (brine) flow (with a known flow rate) through the core and the porosity was determined from the CT data. The radius of the pore throats are mainly in the range of 10-30  $\mu$ m.

*Core Holder:* Depending on the length of the cores and the experimental pressures, different core holders were designed and constructed. They were made of PolyEther EtherKetone (PEEK) that combines excellent mechanical properties to a low X-ray attenuation. Seemingly, PEEK also transmits X-ray within a narrow energy window (refiltering the polyenergetic source X-rays) which appreciably minimizes the beam hardening artifact due to the polychromaticity of the X-ray beam [47]. The geometry and structure of the core holder were designed to minimize beam hardening and scattering artifacts. The core holders were placed vertically on the platform of the CT scanner apparatus and kept in place using a polymethyl methacrylate (PMMA) stand.

### 7.2.3. Experimental Set-up

The schematic of the experimental set-up is schematically shown in Fig. 7.1. It consists of four parts: Injection Unit (IU), Test Unit (TU), Pressure Controlling Unit (PCU) and Data Acquisition System (DAS).

*Injection Unit:* In order to ensure the supply of the gas at a stable rate, the gas flow rate is controlled by using a high precision needle valve (for low-pressure experiments) and an ISCO pump (for high pressure experiments) and it is monitored by using a gas flow meter. A high

precision double-effect piston displacement pump (Pharmacia P 500) is used to inject the brine and the surfactant solution at a constant rate.

*Test Unit:* In the test unit, the sample core is placed inside a cylindrical coreholder. The foam is introduced from the injection tube, and the liquid production is collected in a glass cup on an electronic mass balance. Two high precision pressure transducers locate at the inlet and the outlet to monitor the pressure drop along the core.

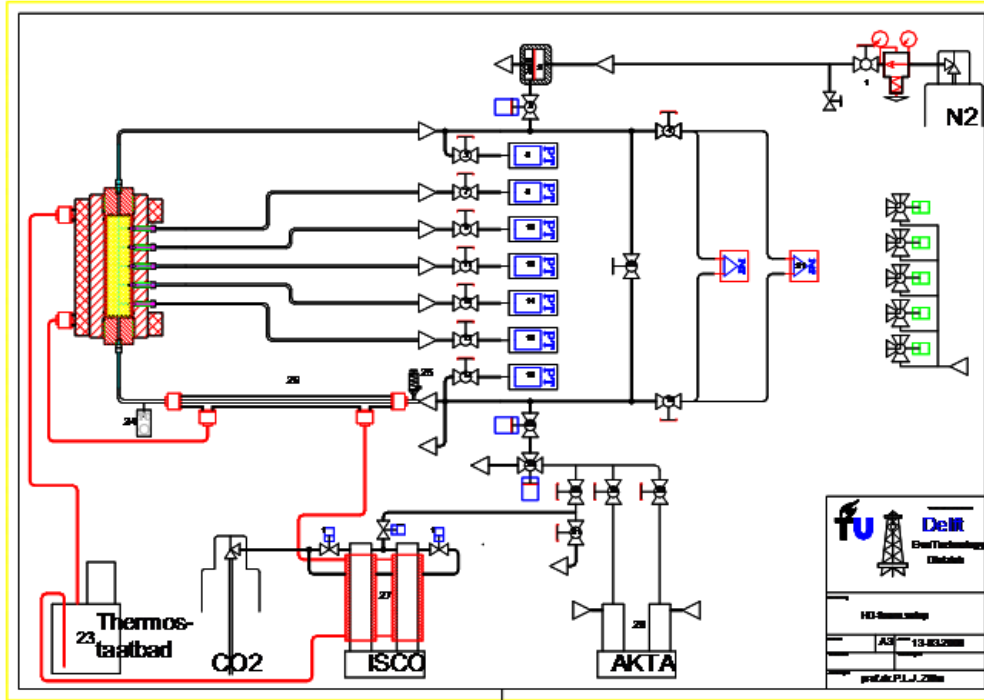


**Fig. 7.1:** Schematic of the foam set-up: It consists of four major units: injection unit (pumps), test unit (the porous medium), pressure controlling unit and data acquisition system (not shown in this Fig.).

**Table 7.2:** Settings of the CT scan measurements

Parameters	CT-scan settings
Energy Levels [keV]	140
Current [mA]	250
Slice Thickness [mm]	3
Number of Slices	4
Filter	B40-medium

*Pressure-Control Unit:* The pressure-control part connects to the outlet of the core. By using a backpressure regulator and a manometer we can measure different pressures in the system. The data-acquisition system records gas and liquid injection rates, pressures and the liquid

production data automatically. All experiments were conducted under isothermal conditions. The low-pressure experiments were done at room temperature of  $T = 20^{\circ}\text{C}$  and the high pressure experiments were performed at a constant temperature of  $T = 50^{\circ}\text{C}$ .

The core-flood set-up is positioned on the couch of the CT scanner. The PEEK core holder is vertically placed, perpendicular to the length of the table, to control gravity-segregation effects. A third-generation SAMATOM Volume Zoom Quad slice scanner is used in our work. The main technical information about this machine has been provided elsewhere [26] and the imaging settings in our experiments are listed in Table 7.2. The X-ray tube of the CT scanner is operated at the voltage of  $140\text{ kV}$  and the current of  $250\text{ mA}$ . The thickness of CT slice is  $3\text{ mm}$  and one series of scan includes  $4$  slices. In the calculations the slice corresponding to the center of the core was used. The spiral scan mode is applied for imaging the dynamic foam flow, instead of the more classical sequential scanning. The spiral scan allows fast and continuous acquisition of the data from a complete volume and generates axial images using standard reconstruction kernel after the data interpolation. One typical slice image consists of  $512 \times 512$  pixels. All  $HU$  values in the pixels are added together and divided by the total amount of pixels to get the average  $HU$  value for one slice image. Due to the fact that the noise for CT images typically ranges from  $3$  to  $20\text{ HU}$ , it can be estimated that the measurement error in water (or gas) saturation is about  $2\%$  for the  $HU$  values in our experiments.

#### 7.2.4. Experimental Procedure

*Core Preparation:* The cores were drilled from a large block and sawn to the dimensions specified in Table 7.1 using a diamond saw cooled with water. The cores were dried in an oven at  $60^{\circ}\text{C}$  for at least  $48$  hours. Then the cores were molded in Araldite glue to avoid production from the axial core sides. Initially some glue penetrated into the core samples and reduced the effective flow area. In the calculation of the total pore volumes (PV) of the cores penetration layer of the glue was assumed to be  $1\text{ mm}$ . The core was then placed in a PEEK core holder. For pressure measurements inside the core, the pressure gauges were connected through a small hole drilled in the glue to the surface of the core. The connectors were also made of PEEK to reduce the beam-hardening effects of X-ray beam.

Before starting the experiments all of the connections in the set-up were checked for possible leakages by keeping the set-up under high pressure and monitoring the measured pressures.

*Core Saturation:* The core was flushed with  $\text{CO}_2$  for at least  $30$  minutes to replace the air in the system. Afterwards, at least  $20$  pore volumes of brine with the flowrate of  $q_w = 2\text{ ml/min}$  were

injected to the system while the backpressure was set  $P_b = 20 \text{ bar}$ . Therefore, all  $\text{CO}_2$  present in the core is dissolved into the brine and carried away. This is confirmed by CT images.

*Surfactant Injection:* After the core was saturated with the brine, 1 pore volume of the surfactant was injected ( $q_s = 2 \text{ ml/min}$ ) to the porous medium from the bottom.

*Foam (gas) Injection:* The gas was injected into the core previously saturated with the surfactant solution (SAG foam) from the bottom.

### 7.3. RESULTS

#### 7.3.1. Low-pressure foam development

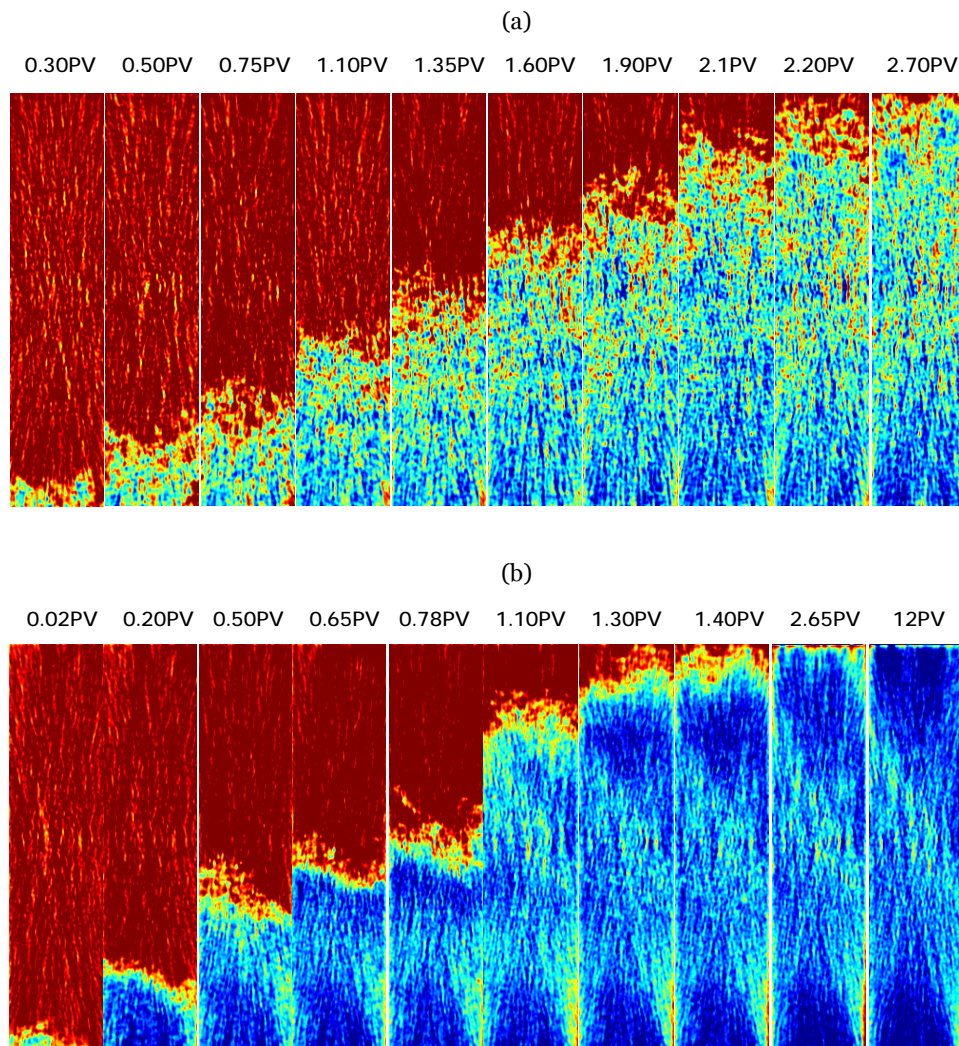
##### 7.3.1.1. CT scan images

Figure 7.2 presents the central CT images of the  $\text{CO}_2$  and  $\text{N}_2$  experiments respectively. The time of each image is also shown in terms of the dimensionless time of pore volumes,  $PV$ , which is the ratio of the cumulative volume of injected fluids (in these experiments only gas) to the volume of the pore space in the porous medium. In these experiments the gas ( $\text{CO}_2$  or  $\text{N}_2$ ) was injected at a flowrate of  $0.5 \text{ ml/min}$  into the core initially saturated with 1  $PV$  of the surfactant solution (SAG scheme). The blue and red colors represent the gas and the liquid phases, respectively. The general features of these experiments (foam advance) are similar to foam experiments in which the surfactant solution and the gas are co-injected into the porous medium [27]. For both  $\text{CO}_2$  and  $\text{N}_2$ , the images show a front-like displacement of the aqueous phase by foam. Three regions can be distinguished in both experiments along the flow direction: 1) an upstream region which is characterized by low liquid saturation, 2) a region downstream of the foam front where the liquid saturation is still unchanged and equals unity and 3) a frontal region characterized by a mixing of flowing foam and liquid and exhibits fine fingering effects. The extent of the fingering behavior is caused by the local rock heterogeneity [26,28] and apparently depends on the type of the foamed gas (foam strength).

Nevertheless, a closer examination of the images reveals the considerable differences between  $\text{CO}_2$  and  $\text{N}_2$  foams. About  $0.30 \text{ PV}$  of  $\text{CO}_2$  is injected before the gas penetrates the core and becomes visible in the images while  $\text{N}_2$  becomes visible much more rapidly as the gas penetrates the core immediately displacing the liquid. This is possibly due to the higher solubility of  $\text{CO}_2$  in water. We return to this point later. The upstream region of  $\text{CO}_2$  foam front is less blue indicating higher water content compared to the upstream region of  $\text{N}_2$  foam. However, similar to  $\text{N}_2$  foam, as the foam front progresses in the core, the gas sweeps parts of the remaining liquid from the upstream region towards the outlet. In the frontal region,  $\text{N}_2$  foam is sharper than  $\text{CO}_2$ . Finally the higher solubility of  $\text{CO}_2$  in the aqueous phase results in its substantially delayed breakthrough.

The gas breakthrough takes places at a time between  $1.30$  and  $1.70$   $PV$  for  $N_2$  foam while the foamed  $CO_2$  breaks through at a time slightly larger than  $2.20$   $PV$ .

The amount of  $CO_2$  that can be dissolved in water can be estimated by Henry's law. The solubility of  $CO_2$  in water is  $\sim 38.4$   $mol/m^3$  at our experimental condition. Using the CT images the volume of water that gas has met was estimated at each  $PV$  and then the amount of dissolvable  $CO_2$  was calculated. The results are summarized in Table 7.3. In these calculations the possible effect of surfactant micelles on  $CO_2$  solubility is disregarded. It turns out that the amount of dissolved  $CO_2$  is considerable and therefore the effect of water solubility cannot be neglected [27]. Indeed, considering also some dead volume in the system, more than  $1$   $PV$  of the injected  $CO_2$  is required to saturate the liquid upstream of the front before it can form foam.



**Fig. 7.2:** CT images of (a)  $CO_2$  and (b)  $N_2$  foam flow (blue) in a porous medium initially saturated with surfactant solution (red) at  $P=1bar$  and  $T=20^\circ C$  ( $q_0=0.5$   $ml/min$ ). The time of each image is shown in pore volumes of the injected gas.

### 7.3.1.2. Saturation profiles

To quantify the evolution of the liquid saturations,  $S_w$ , over the entire core, the CT data of the obtained images were converted to water saturation profiles using Eq. (2). The results are shown in Figs. 7.3a and 7.3b at various times for CO<sub>2</sub> and N<sub>2</sub> respectively. Note that every point on these figures is the averaged water saturation over a disk of the core with  $\sim 8$  mm thickness. These figures show that foamed CO<sub>2</sub> and N<sub>2</sub> displace the liquid, i.e., the surfactant solution from the porous medium. Prior to the gas breakthrough the saturation profiles along the core show a steep increase of  $S_w$  at the foam front, which indicates an effective front-like displacement of the initial liquid for both foams. In the case of CO<sub>2</sub> foam due to more fingering in the foam front, revealed by the CT images, the front is not as sharp as for the N<sub>2</sub> foam.

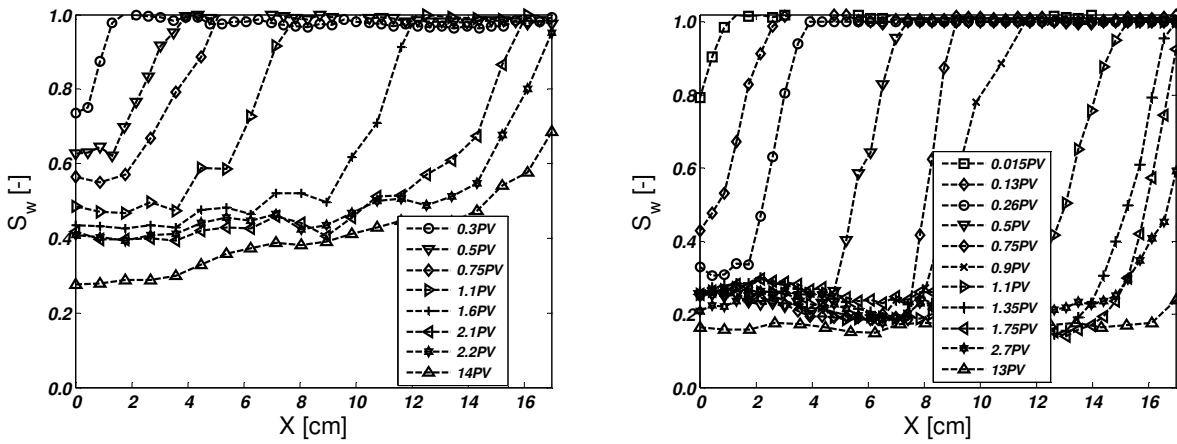


**Fig. 7.3:** The liquid saturation profiles of (a) CO<sub>2</sub> foam (left) and (b) N<sub>2</sub> foam (right), calculated from CT profiles shown in Fig. 2 and Fig.3, respectively.

**Table 7.3:** Amount of CO<sub>2</sub> that can be dissolved in water calculated from Henry's law at  $P=1$  bar and  $T=20^\circ\text{C}$ . The solubility of CO<sub>2</sub> in water at this P-T is estimated to be  $38.4$  mol/m<sup>3</sup>.

PV of CO <sub>2</sub> Injected	Water Content	Amount of dissolved CO <sub>2</sub>	PV of CO <sub>2</sub> dissolved
[-]	[cm <sup>3</sup> ]	(Henry's law) [cm <sup>3</sup> ]	[-]
<b>0.30</b>	2.6	1.2	0.06
<b>0.50</b>	7.5	3.4	0.16
<b>0.75</b>	10.4	4.8	0.23
<b>1.10</b>	15.6	7.2	0.34
<b>1.35</b>	21.6	9.6	0.47
<b>1.60</b>	26.8	12.4	0.59
<b>1.90</b>	30.5	14.1	0.67
<b>2.10</b>	36.5	16.8	0.80
<b>2.20</b>	40.2	18.5	0.92
<b>Breakthrough</b>	42.5	19.6	0.93

Another difference in the saturation profiles of these experiments (SAG scheme) with experiments reported by Refs. [26,48] is the absence of so-called *secondary liquid desaturation* (SLD) stage in our experiments. Considering the differences in the experimental conditions, it may be that SLD is a phenomenon that happens in the experiments with high gas flowrates (and/or short cores).

High values of liquid saturation are found at the region close to the core outlet. This capillary end effect results from the fact that the porous medium retains the liquid in an attempt to maintain equilibrium across the outlet where the capillary pressure is zero or near zero [49-51]. After about  $2 PV$  of gas injection,  $CO_2$  foam removes about 50% of the liquid while  $N_2$  removes more than 70% of the liquid. Further injection of  $N_2$  after (foam) breakthrough removes the liquid retained at the inlet and outlet of the porous medium while further injection of  $CO_2$  produces the liquid from the whole core as the liquid content is still high after foam breakthrough. Finally, comparing the water-saturation profiles of two gases at the same pore volumes, one can conclude that the foamed  $N_2$  displaces more liquid than foamed  $CO_2$ . Indeed, the foamed  $N_2$  produces more than 82% of the initial liquid in the porous medium while the foamed  $CO_2$  sweeps less than 65% of the initial liquid after more than 11  $PV$  of gas injection.

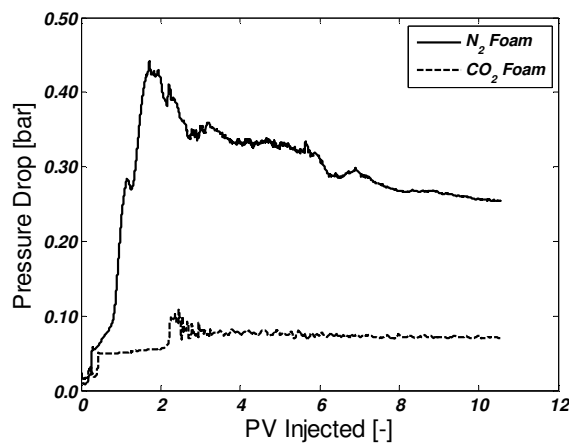


**Fig. 7.4:** Pressure drop across the entire core for  $N_2$  and  $CO_2$  foam ( $q_g=0.5ml/min$ ) at  $P=1bar$  and  $T=20^\circ C$

### 7.3.1.3. Pressure profiles

Figure 7.4 compares the measured pressure drops versus dimensionless time (PV) of the two experiments. It appears that the foamed  $N_2$  builds up larger pressures over the core than foamed  $CO_2$ . The high liquid saturation and the small pressure drop indicate that  $CO_2$  is in the form of relatively weak foam. Although this foam is relatively weak, it does produce a pressure drop higher than expected for the steady state pressure drop with the gas injection to a core initially saturated with water [52]. In both experiments the pressure drop across the core reaches a

maximum and then decline slowly. The maximum point corresponds to the foam breakthrough at the outlet. The pressure decreases after breakthrough because of the coalescence of the bubbles due to diffusion or breaking of the foam films.

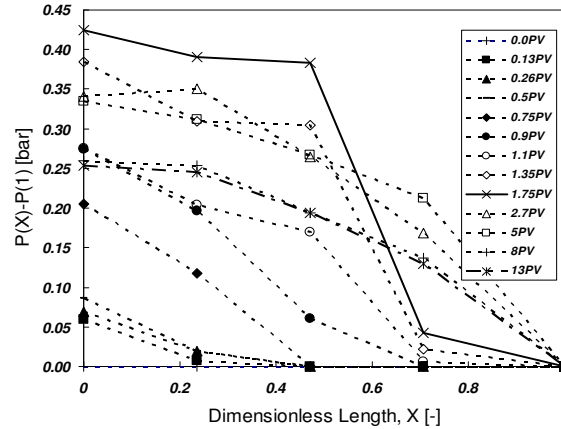


**Fig. 7.5:** The transient pressure profile at different location in the core for  $N_2$  foam experiment at  $P=1\text{bar}$  and  $T=20^\circ\text{C}$ .

For a detailed explanation of foam progress in the core the pressure-drop measurements at different sections of the core are plotted for the  $N_2$  experiments in Fig. 7.5. At early times, until  $0.50\text{ PV}$ , the pressure drop is quite small. This means that foam is still weak. From time  $0.50\text{ PV}$  to  $0.70\text{ PV}$  there is a sharp increase in the pressure drop across the beginning of the core. This is confirmed by the saturation profile in Fig. 7.3b. After  $0.50\text{ PV}$  of gas injection, the foam front moves relatively slower along the core, nevertheless, it produces more water from the upstream region. Comparing the saturation profiles of two gases, this effect is more pronounced in the  $CO_2$  foam, possibly due to the fact that (i)  $CO_2$  foam is weaker and (ii) unlike  $N_2$  foam, the transition from weak to strong foam does not happen for  $CO_2$ . The low pressure drop and relatively high liquid saturation at the core inlet at early experimental times is referred to as the *entrance effect* in the literature [29,35]. Apparently gas needs time and space before it develops into foam. The pressure drop continues to increase as gas moves forward along the core. Again due to the capillary end effect the pressure drop at the last section of the core is low (water saturation is high). The pressure drop reaches maximum of  $0.42\text{ bar}$  which is equal to the overall pressure drop across the core. This means that foam in the last section is weaker than foam in the first half of the core. However, as it is seen from Fig. 7.5 the pressure drop at the last section of the core increases with time indicating that foam becomes stronger with increasing amounts of injected gas. After foam breakthrough the pressure drop decreases due to the destruction of foam films as mentioned previously.

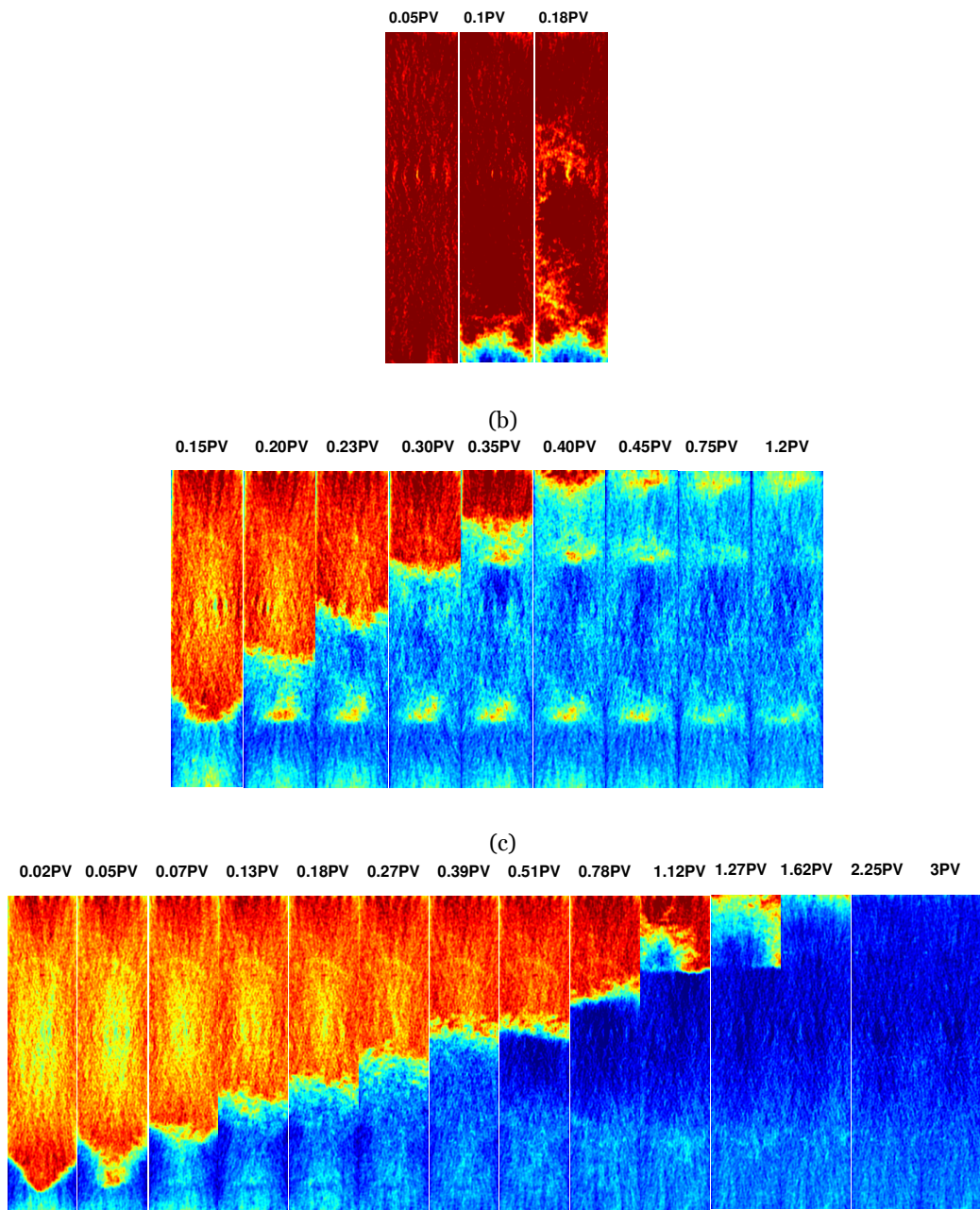


**Fig. 7.6:** CT images of (a)  $\text{CO}_2$  gas, (b)  $\text{CO}_2$  foam and (c)  $\text{N}_2$  foam flow in a porous medium initially saturated with surfactant solution (red) at  $P=90$  bar and  $T=50$  °C ( $q_g=1$  ml/min). The time of each image is shown in pore volumes of the injected gas.

### 7.3.2. High-pressure experiments

The second set of experiments were done at  $P=90$  bar and  $T=50$ °C. This P-T condition is well above the critical point of  $\text{CO}_2$  [53]. The density of  $\text{CO}_2$  is  $286$  kg/ $m^3$  at this condition calculated from the Span and Wagner EoS [54]. Moreover, at this pressure and temperature a water-rich liquid phase coexists with a  $\text{CO}_2$ -rich liquid, where a distinction between the vapor and liquid

phases of  $\text{CO}_2$  disappears [55]. Note that foams formed with dense  $\text{CO}_2$  as the internal phase are strictly emulsions [10], sometimes referred to as *foamulsions* [5]. However, for the sake of consistency we use the term foam here as well.

### 7.3.2.1. CT images

Figure 7.6 presents the central CT images of  $\text{CO}_2$  gas,  $\text{CO}_2$  foam and  $\text{N}_2$  foam flow at  $P=90$  bar and  $T=50^\circ\text{C}$ . The time of each image is also shown in the dimensionless time of pore volumes,  $PV$ . The gas flowrate in these experiments was set to  $1$  ml/min. In the  $\text{CO}_2$  gas experiment the core was initially saturated with brine and  $\text{CO}_2$  was injected into the core afterwards. The images reveal the remarkable effect of the surfactant solution in the porous medium. When  $\text{CO}_2$  is injected to the core initially saturated with the brine, there is no (clear) sharp interface between the gas and the brine.  $\text{CO}_2$  forms channels through the brine and breaks through in less than  $0.20$   $PV$ . When  $\text{CO}_2$  is injected into the core initially saturated with the surfactant solution a clear interface between the moving gas and the liquid appears and  $\text{CO}_2$  breakthrough is delayed until a time between  $0.45$   $PV$  and  $0.50$   $PV$ . The breakthrough time for  $\text{N}_2$  foam is longer than  $1.2$   $PV$ . Similar to the low pressure foam experiments the three regions are again present at high pressure foam experiments. In the  $\text{CO}_2$  foam, the gas bypasses part of the porous medium and therefore the brine content is high at regions near the core inlet and outlet. In the  $\text{N}_2$  foam, the foam front moves a lot slower after  $0.40$   $PV$  which is an indication that the foam has become stronger.

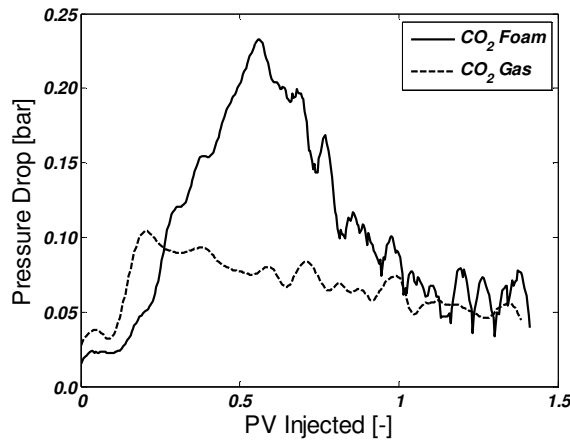


**Fig. 7.7:** Pressure drop across the entire core for  $\text{CO}_2$  gas and  $\text{CO}_2$  foam ( $q_g = 1$  ml/min) at  $P=90$  bar and  $T=50^\circ\text{C}$ .

### 7.3.2.2. Pressure profiles

Figure 7.7 shows the pressure history for  $\text{CO}_2$  gas and  $\text{CO}_2$  foam experiments while Fig. 7.8 compares the pressure drop of  $\text{CO}_2$  and  $\text{N}_2$  foams. The pressure drop along the core follows a similar trend; it reaches a maximum at gas breakthrough and then declines with time. The

maximum value of the pressure in CO<sub>2</sub> foam is about two times larger than that of CO<sub>2</sub> gas. Compared to the low pressure experiment, the pressure peak is higher at the high pressure CO<sub>2</sub> (and N<sub>2</sub>) foam because (i) the gas flowrate is higher and (ii) CO<sub>2</sub> has a higher density (and viscosity) in the latter case. One interesting feature is that after 1.0 PV of CO<sub>2</sub> injection, the pressure drop of the CO<sub>2</sub> foam experiment is comparable to that of CO<sub>2</sub> gas experiment, meaning that after breakthrough there is almost no foam (or emulsion) present in the porous medium due to the shortage of the surfactant. The pressure drop for the N<sub>2</sub> foam is again larger than the CO<sub>2</sub> foam (see Fig. 7.8). In the N<sub>2</sub> foam the pressure drop over the core is low until 0.40 PV, confirming the idea that gas should invade some part of the core before it develops into foam. This effect appears to be less significant for CO<sub>2</sub> than N<sub>2</sub> and as can be seen from Figs. 7.2 and 7.6, the higher the gas flowrate the larger the entrance effect is.

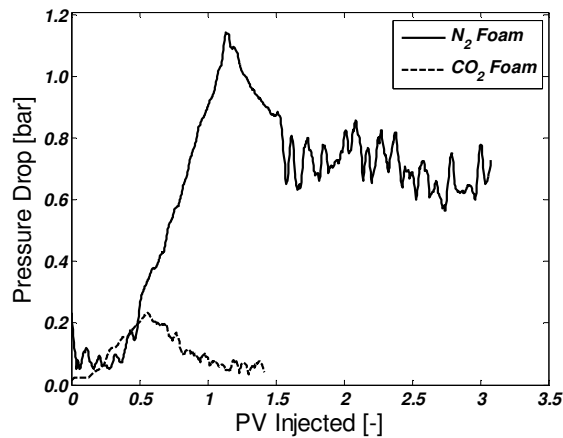


**Fig. 7.8:** Pressure drop across the entire core for N<sub>2</sub> foam and CO<sub>2</sub> foam ( $q_g = 1$  ml/min) at  $P=90$  bar and  $T=50^\circ\text{C}$ .

### 7.3.2.3. Saturation profiles

The calculated liquid saturation profiles,  $S_w$ , for the three experiments are shown in Fig. 7.9. In all three experiments gas displaces the liquid, although when gas is foamed inside the porous medium the amount of the liquid that remains inside the core is less than when the gas is not foamed. Moreover, in the gas injection there is no steep increase of  $S_w$  at the gas front while in foam experiments an effective front-like displacement of the initial liquid by foam takes place. The capillary end effect is present in the experiments as the liquid saturations are high near the core outlet. A detailed analysis of the N<sub>2</sub> foam experiments reveals that when the foam becomes stronger (after 0.40 PV of gas injection), the liquid saturation is reduced to a value as low as 8%; nonetheless due to the capillary end effects the saturation starts to increase to maintain the pressure equilibrium near the core outlet (This would have happened later if the core was longer). After about 1.5 PV of gas injection, CO<sub>2</sub> gas produces about 40% of the initial liquid. Foaming of

CO<sub>2</sub> increases the recovery by 25% and brings out more than 65% of the liquid. The N<sub>2</sub> foam removes more than 80% of the liquid.

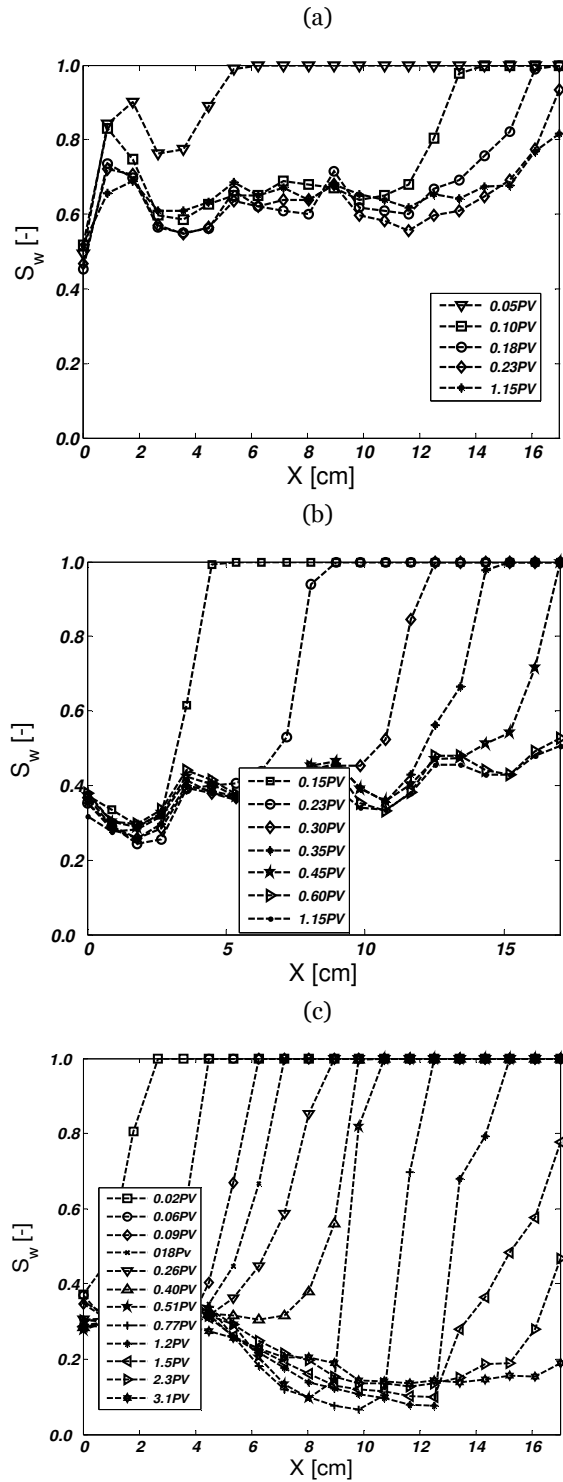


**Fig. 7.9:** The liquid saturation profiles of (a) CO<sub>2</sub> gas (b) CO<sub>2</sub> foam and (c) N<sub>2</sub> foam, calculated from CT profiles shown in Fig. 7.6.

#### 7.4. GENERAL DISCUSSION

The experiments have clearly demonstrated that under a SAG scheme CO<sub>2</sub> foams are *weaker* than N<sub>2</sub> foams at both low and high pressures. Foam in porous media is considered *weak* when the number of the lamella is not large enough to resist the gas flow [56,57].

In order to interpret these observations we need to recall that foams are thermodynamically meta-stable. They evolve irreversibly over time because the interfacial area in the lamella diminishes in order to minimize interfacial free energy [58]. The longevity of foam in porous media essentially relies on the stability of single foam films or lamellae. The stability of foam films depends on quantities and processes like surfactant concentration, salt concentration, adsorption kinetics, gravitational drainage, gas diffusion through foam films, surface forces (or capillary pressure) and fluctuations [59,60]. Before we assert the dominant factor responsible for the difference between CO<sub>2</sub> and N<sub>2</sub> foams it is worth reviewing how individual mechanisms could affect foam stability.

*Coalescence and drainage:* These two processes are responsible for the changes in degree of dispersion of gas bubbles in foam as they cause: (i) the diffusion of gas through the lamellae and (ii) collapse of liquid lamellae and subsequent coalescence of contiguous gas bubbles [61]. Pressure difference between bubbles of unequal size induces gas-transfer from small to larger bubbles. Even in the ideal situation of an initially perfectly ordered foam, comprised of uniform bubbles with a uniform gas pressure, finite size perturbation in bubble shape (e.g. due to irregularities and heterogeneity in porous media) would lead to an irreversible growth of the larger bubbles at the expense of the smaller [56]. This foam coarsening, the Oswald ripening, is unavoidable [37].

The mass-transfer rate of gas through foam films can be characterized by the film permeability  $k$ . According to Princen and Mason [62] gas permeability depends on physical coefficients according to equation

$$k = \frac{k_H D}{h_w + 2D / k_{ml}} \quad (7.3)$$

where,  $D$  is the diffusion coefficient of the gas in the liquid phase,  $k_H$  is the Henry's coefficient,  $k_{ml}$  is the permeability of the surfactant monolayer to gas and  $h_w$  is the thickness of the liquid film. Eq. (3) shows that the permeation rate for thick foam films ( $2D / k_{ml} \ll h_w$ ) is mainly controlled by the liquid layer via  $D$  and  $k_H$  ( $k \sim k_H D$ ), while for thin foam films ( $2D / k_{ml} \gg h_w$ ) the permeability of the monolayer ( $k = k_H k_{ml} / 2$ ) is the limiting factor.

In our experiments the addition of NaCl does not affect the gas transfer rate of the film. As mentioned earlier Newton black films are expected to be formed with our experimental surfactant and salt concentration. Therefore the gas permeability of foam films depends on the solubility of the gas in the aqueous phase and the monolayer permeability. The solubility of the gases can be compared by comparing the value of their Henry's constant,  $k_H$ , i.e.,

$$\frac{k_{H,CO_2}}{k_{H,N_2}} = \frac{3.4 \times 10^{-2}}{6.1 \times 10^{-4}} = 55$$

This means that  $CO_2$  is about 55 times more soluble in water than  $N_2$  [46]. In the only published data, the transfer rate of  $CO_2$  through the foam films stabilized by hexadecyltrimethylammonium bromide (HDTAB) in the presence of NaBr was measured to be about 60 times larger than that of  $N_2$  [62,67].

The rather good agreement between the two ratios (solubility and film permeability ratio) suggests that coalescence rate of  $CO_2$  foam bubbles must be much higher than that of  $N_2$  foam bubbles. Therefore this could be why  $CO_2$  foam is weaker than  $N_2$  foam. This is analogous to the situation whereof steam foam where water vapor can pass through lamellae by condensing on one side and evaporating on the other side [68]. A small amount of nitrogen is added to reduce this effect in steam foam [69] and in the beer industry [37,70]. The higher solubility of  $CO_2$  could also explain why in  $CO_2$  foam more pore volumes of gas are needed before the gas becomes visible in the core and also why the speed of the foam front is lower for  $CO_2$  than for  $N_2$ . Indeed a considerable fraction of  $CO_2$  dissolved in the surfactant solution before can be foamed since the amount of available gas for foaming is reduced.

In porous media the Plateau borders are connected throughout the pore space and form a conductive network. In response to the local pressure gradient and gravity the liquid starts to flow. Liquid depletion in turn increases the capillary suction pressure on the lamella, which may result in film rupture. Coarsening also has a strong influence on foam drainage for gases of large solubilities (e.g.  $CO_2$ ) and small bubble sizes (*diameters*  $< 1$  mm) [63-65]. This coupling effect can shorten the lifetime of ( $CO_2$ )- foam.

The lamellae remain in the pore throats of porous media and ideally at equilibrium they will have no curvature and thus sustain no pressure drop. Therefore in the absence of the driving force the diffusion process stops. This may cause the foam remain *indefinitely* in the porous medium in the *absence of external disturbances* (in porous media heterogeneity and temperature fluctuations can be counted as external disturbances) [71,72].

Figure 7.10 shows a plot of the pressure drop over the entire core as a function of the average gas saturation in the core for low pressure CO<sub>2</sub> and N<sub>2</sub> foams respectively. Initially both foams show similar behavior, i.e., while the gas displaces the liquid the pressure drop remains low (weak foam). However, as time passes for similar gas fractions (above  $S_g=0.30$ ), N<sub>2</sub> foam exhibits higher pressure drop over the core. This implies that 1) while a transition from weak foam to strong foam occurs in N<sub>2</sub> foam, CO<sub>2</sub> foam always remains weak and 2) CO<sub>2</sub> foam is coarser than N<sub>2</sub> foam in porous media due to more intense rupture of the foam films (lamellae), as discussed previously. Figure 7.11 provides a similar plot for high pressure experiments. Again in this case there is a gas saturation in which the transition from weak foam to strong foam occurs in N<sub>2</sub> foam ( $S_g \sim 0.35$ ). This saturation is higher than that of the low pressure N<sub>2</sub> foam presumably due to the differences in the flowrates. Seemingly, CO<sub>2</sub> continues to flow as a weak foam (or more accurately foamulsion) in the core.

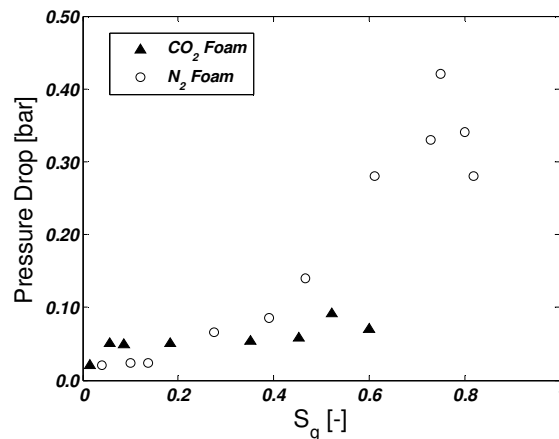


**Fig. 7.10:** Pressure drop over the core vs. average gas saturation in the core for low pressure experiments [P=1bar and T=20°C].

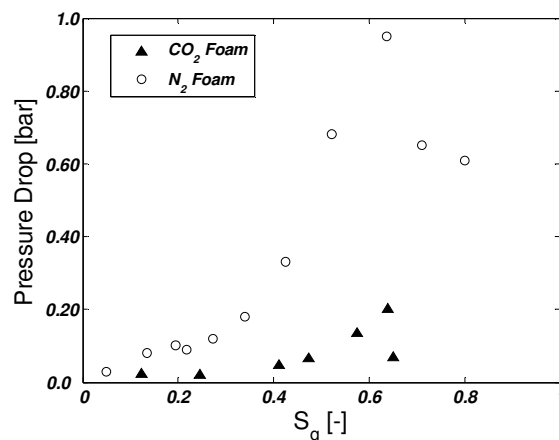


**Fig. 7.11:** Pressure drop over the core vs. average gas saturation in the core for high pressure experiments [P=90bar and T=50°C].

*Role of Interfacial tension:* The interfacial tensions of the CO<sub>2</sub>-water and the N<sub>2</sub>-water systems exhibit different behavior. The interfacial tension of the N<sub>2</sub>-water binary system does not vary considerably with pressure such that it can be assumed constant in the range of our experimental pressures [73,74]. Nevertheless, the interfacial tension between CO<sub>2</sub> and water depends strongly on pressure for pressures smaller than 10 MPa, decreasing as the pressure increases, and displays an asymptotic behavior towards a constant value for higher pressures [75-77]. Even at low pressure of 1 bar the presence of CO<sub>2</sub> above a surfactant solution may lower the interfacial tension possibly due to the surface hydrolysis of the surfactant [78]. The resistance to flow of the individual lamella in porous media is proportional to the surface tension [79]. It is interesting to mention that decrease in the interfacial tension leads to higher permeation of the gas molecules through the foam films and therefore may decrease the stability of foam [80]. Moreover, it has been observed that the relative permeability of CO<sub>2</sub> increases as the interfacial tension of the CO<sub>2</sub>-water system decreases [77].

*Wettability Alteration Effects:* Part of the observed differences in CO<sub>2</sub> and N<sub>2</sub> foam experiments may be attributed to both, differences in the interfacial tension and differences in the wetting angles of the two gases, i.e., the value of  $\sigma \cos \theta$ , where  $\sigma$  is the gas-water interfacial tension and  $\theta$  is the contact angle. Hildenbrand et al. [81] stated that for the N<sub>2</sub>-water system the product of  $\sigma \cos \theta$  exceeds the corresponding product for the CO<sub>2</sub>-water system by a factor of 1.3-2.0. This suggests that wettability of the clay part of the rock may change with injecting CO<sub>2</sub>. Foam is more stable in water-wet rock than in intermediate (or oil) wet porous media [82-84]. If the medium is not water-wet the walls may cause the lamellae to detach and collapse [9]. Our experiments are done in Bentheimer sandstone that contains 1-4 wt% of clay [85]. Therefore, injection of CO<sub>2</sub> affects the wettability of the cores. When the lamella moves across a non-wetting spot of the pores it ruptures by the pinch-off mechanism [35] lowering the resistance of foam to flow. It is important to remark that wettability and interfacial tension forces at the interface between liquid and rock may also affect bubble formation is also affected by [86]. Hence, it is possible that the rate of foam generation in CO<sub>2</sub> foam is different than N<sub>2</sub> foam due to wettability effects.

*pH effects:* Another factor that may affect the foam stability is the pH of the aqueous phase. When CO<sub>2</sub> is injected into a reservoir, CO<sub>2</sub> reacts with water and forms carbonic acid. This reaction may lower the pH of the brine down to 4.0 [87]. The value of pH may influence the foam film stability by affecting the disjoining pressure through screening of the van der Waals and electrostatic forces [60]. The pH changes could also influence the surfactant performance in porous media [88]. However, based on the experimental results it has been asserted in the literature that pH

has little effect on foam viscosity [87], foam resistivity [89] or in general foam stability when the surfactant concentration is above the CMC [90].

*Alteration of van der Waals forces:* The disjoining pressure is a measure of stability of a foam film and strongly depends on the film thickness [58,61]. According to the DLVO theory this pressure has two components: repulsive electrostatic and attractive van der Waals forces [61]. The effect of gas type on the van der Waals component of the disjoining pressure can be evaluated using Hamaker's constant, which depends on the optical and dielectric properties of the aqueous and non-aqueous phases [91]. Since these properties for CO<sub>2</sub> and N<sub>2</sub> are different it has been hypothesized that the differences in the magnitude of the attractive van der Waals forces of the lamellae in CO<sub>2</sub> and N<sub>2</sub> foams cause the differences observed in the experiments [60]. The calculations of Ref. [60] shows that the magnitude of screening of electrostatic forces for CO<sub>2</sub> is two times that of N<sub>2</sub>, while screened Hamaker's constants indicate that van der Waals forces are six time lower for CO<sub>2</sub>.

*Type of surfactant:* Different gases may show different foaming behavior with different surfactants. Although AOS surfactants have been previously used in CO<sub>2</sub> foam projects, it is possible that type of surfactant is responsible for the differences observed in the experiments.

*Temperature effects:* Temperature is another parameter that controls the foam stability by influencing the diffusion rate and adsorption of the surfactant molecules at the gas-water interface and rock surface. CO<sub>2</sub> dissolution in water is exothermic. The solution heat of CO<sub>2</sub> is given by

$$-(d \ln k_H / d(1/T))_{CO_2} = \Delta H_{CO_2} / R = 2400K \rightarrow \Delta H_{CO_2} \approx 2.0 \times 10^4 J / mol$$

This implies that CO<sub>2</sub> dissolution can cause temperature increase of

$$\Delta T_{CO_2} = \frac{\Delta H_{CO_2}}{k_H c_{p,w}} = \frac{2 \times 10^4}{3400 \times 4.2 \times 10^6} \approx 0.15 K / bar$$

A similar calculation for N<sub>2</sub> reads:  $\Delta T_{N_2} \approx 0.00015 K / bar$ . Therefore, the temperature rise in the water due to CO<sub>2</sub> dissolution is more significant, especially at higher pressures. The increase in temperature can reduce the foam stability in porous media because (i) it can initiate the inter-bubble diffusion process by causing infinitesimal perturbation and thus disturbing the equilibrium and (ii) it increases the mass transfer rate through the bubbles. However, it should be noted that the temperature effects cannot completely be responsible for the differences in foaming behavior of CO<sub>2</sub> and N<sub>2</sub> since at low pressure the temperature effect will not be significant.

## 7.5. CONCLUSIONS

The foaming behavior of CO<sub>2</sub> and N<sub>2</sub> were comparatively studied in a sandstone core by the means of a CT scanner (X-ray). It has been shown that injection of a slug of surfactant prior to CO<sub>2</sub> injection can reduce the CO<sub>2</sub> mobility, below and above its critical point. The two investigated gases exhibit different behavior in the porous medium. Foaming of CO<sub>2</sub> builds up lower pressure drop over the core at both low and high pressures when compared to N<sub>2</sub>. Both gases require a certain penetration depth to develop into foam. The penetration depth is longer for N<sub>2</sub> (large entrance effect) and increases with increasing gas velocity. The CT images and calculated water saturation profiles reveal that N<sub>2</sub> foam displaces the liquid in a front-like manner (sharp-vertical interface) while the propagation front for CO<sub>2</sub> foam is not the exact front-like displacement at low pressure. Moreover, the ultimate production of N<sub>2</sub> foam is always higher than CO<sub>2</sub> foam. The observed differences in the foaming behavior of the two gases can be related to the differences in their nature, mainly solubility in water, interfacial tensions, pH effects and the possible wettability effects. From these various factor solubility is most likely the most critical one because 1) part of the gas is dissolved in the aqueous phase and therefore when volumetric flowrates of two gases are the same the local gas velocities will be different, i.e., the amount of available CO<sub>2</sub> for foaming will be lower than N<sub>2</sub> at similar PVs and 2) it significantly affects the gas permeability coefficient and thus the foam stability.

## 7.6. REFERENCES

1. R.W. Klusman, *Energy Conversion and Management*, 44 (2003) 1921.
2. M.H. Holtz, P.K. Nance, R.J. Finley, *Environ Geosci*, 8 (3), (2001) 187.
3. H. Koide H and K. Yamazaki, *Environ Geosci*, 8 (3), (2001) 218.
4. F.M. Orr, Jr., J.P. Heller and J.J. Taber, *JAOCs*, 59 (10) (1982).
5. S.L. Wellington and H.J. Vinegar, *Surfactant-Induced Mobility Control for Carbon Dioxide Studied with Computerized Tomography*. In: *Surfactant Based Mobility Control – Progress in Miscible Flood Enhanced Oil Recovery*; Smith, D.H., Eds.; ACS Symposium Series 373; American Chemical Society: Washington, 1988; pp.344-358.
6. M. Blunt, F.J. Fayers, F.M. Orr, Jr, *Energy Convers Mgmt*, 34 (1993) 1197.
7. L.W. Lake, *Enhanced Oil Recovery*, Prentice Hall, Englewood Cliffs, NJ (1989).
8. A.N. Fried, *Foam drive process for increasing the recovery of oil*, Bureau of Mines Report of Investigation (1961).
9. W.R. Rossen, *Foams in Enhanced Oil Recovery*, In: *Foams: Theory Measurement and Applications*, R.K. Prud'homme and S. Khan (Eds), Marcel Dekker, New York City (1996).
10. D.C. Bond and O.C. Holbrook, *US Patent No. 2866507* (1958).
11. A.R. Kovscek and C.J. Radke, *Fundamentals of foam transport in porous media*, In: *Foams: Fundamentals and applications in the Petroleum Industry*, ACS Advances in Chemistry Series, N.242, American Society (1994).
12. Falls, G.J. Hirasaki, T.W. Patzek, D.A. Gauglitz, D.D. Miller, J. Ratulowski, *SPE Res. Eng.*, 176-190

- (1985).
13. G.J. Hirasaki, J. Petroleum Technology, 41 (1989) 449.
  14. R.E. Krause, R.H. Lane, D.L. Kuehne, G.F. Bain, *SPE 24191*, Presented at the 8th SPE/DOE Symposium on EOR, Tulsa, OK, Apr. 22-24 (1992).
  15. K. Preuss and J. Garcia, *Environ. Geology*, 42 (2002) 282.
  16. J.M. Nordbotten, M.A. Celia, S.B. Bachu, H. Dahle, *Environ. Sci. Technol.*, 39 (2), (2005) 602.
  17. W.R. Rossen and P.A. Gauglitz, *AIChE*, 36 (1990) 1176.
  18. S.I. Chou, *SPE 22628*, SPE Annual Technical Conference and Exhibition, Dallas, Oct. 6-9 (1991).
  19. Turta and A.K. Singhal, *SPE 48895*, SPE International Conference and Exhibition, China, Beijing, 2-6 Nov. 1998.
  20. Svortol, F. Vassenden, K. Mannhardt, *SPE 35400*, SPE/DOE tenth symposium on improved oil recovery : Tulsa OK, 21-24 April 1996.
  21. Blaker, H.K. Celius, T. Liet, H.A. Martinsen, L. Ramsussen, F. Vassenden, *SPE 56478 (SPE 78824)*, SPE annual technical conference and exhibition : Houston TX, 3-6 October 1999.
  22. M.G. Aarra, A. Skauge, H.A. Martinsen, *SPE 77695*, SPE Annual Technical Conference and Exhibition, San Antonio, Texas , 29 September-2 October 2002,
  23. C.S. Matthews, In: Enhanced Oil Recovery II, Processes and Operations, E.C. Donaldson, G.V. Chilingarian, T.F. Yen, Elsevier Science Publ. Co., New York (1989).
  24. J.P. Heller, *CO<sub>2</sub> Foams in Enhanced Oil Recovery*, In: Foams: Fundamentals and Applications in the Petroleum Industry, L.L. Schramm (ed), ACS Advances in Chemistry Series, 3, No. 242, Am. Chemical Soc., Washington, D.C. (1994). D.G.
  25. Huh and L.L. Handy, *SPE Reservoir Engineering*, February 1989.
  26. P.Q. Nguyen, *Dynamics of foam in porous media*, PhD Dissertation, Delft University of Tech., The Netherlands, 2004.
  27. D.X. Du, A. Naderi Beni, R. Farajzadeh, P.L.J. Zitha, *Ind. Eng. Chem. Res.*, 47 (2008) 6298.
  28. P.Q. Nguyen, P.K. Currie, M. Buijse, P.L.J. Zitha, *J. Petrol. Sci. Eng.*, 58 (2007) 119.
  29. T. Myers and C.J. Radke, *Ind. Eng. Chem. Res.*, 39 (8), (2000) 2725.
  30. S. Tortopidis and D.C. Shallcross, *SPE 28811*, Asia Pacific Oil and Gas Conference, Australia, 7-10 November 1994.
  31. O. Fergui, H. Bertin, M. Quintard, *J. Petrol. Sci. Eng.*, 20 (1998) 9.
  32. C.A. Irani and C. Solomon, *SPE/DOE 14962*, 5th Symposium on EOR, Tulsa, OK, 20-23 April 1986.
  33. S.H. Raza, *In. Soc. Pet. Eng.*, 10 (4), December 1970.
  34. G.C. Wang, *SPE 12645*, 4th Symposium on EOR, Tulsa, OK, 15-18 April 1986.
  35. T.J. Myers, *The role of residual oil in the mechanistic simulation of foam flow in porous media: Experiment and simulation with the population balance method*, PhD Dissertation, University of California, Berkeley, USA, 1999.
  36. R. Krastev, *Private Communication* (2008).
  37. D. Weaire and S. Hutzler, *The Physics of Foams*, Oxford University Press (1999).
  38. Saint-Jamles and D. Langevin, *Condens. Matter Phys.*, 14 (2002) 9397.
  39. M.I. Kuhlan, A.H. Falls, S.K. Hara, T.G. Monger, J.K. Borchardt, *SPE/DOE 20192*, Presented at the SPE/DOE Symposium on Enhanced Oil Recovery, Tulsa, OK, April 22-25 (1990).

40. L.W. Holm and W.H. Garrison, *SPE Reservoir Engineering*, 3 (1988) 112.
41. P.A. Gauglitz, F. Friedmann, S.I. Kam, W.R. Rossen, *SPE 75177*, SPE/DOE Improved Oil Recovery Symposium, Tulsa, Oklahoma, U.S. April 13-17, 2002.
42. R.D. Hutchins and M.J. Miller, *SPE Production & Facilities*, 20 (2005) 286.
43. R. Prieditis and G.S. Paulett, *SPE 24178*, SPE/DOE Eighth Symposium on Enhanced Oil Recovery, Tulsa, OK, 1992.
44. R. Farajzadeh, R. Krastev, P.L.J. Zitha, *Colloids Surf. A*, 324 (2008) 35.
45. D.X. Du, *Private Communication* (2007).
46. R. Sander, *Compilation of Henry's Law Constants for Inorganic and Organic Species of Potential Importance in Environmental Chemistry*, available online at: <http://www.mpch-mainz.mpg.de/%7Esander/res/henry.html>, Version 3, 1999, p57 (last date accessed September 2008)
47. R.A. Brooks, G.H. Weiss, A.J. Talbert, *J. Comput. Assist. Tomog.*, 2 (1978) 577.
48. P.L.J. Zitha, Q.P. Nguyen, P.K. Currie, M.A. Buijse, *Transport in Porous Media*, 64 (2006) 301.
49. O. G. Apaydin and A. R. Kovscek, *Transport in Porous Media*, 43 (2001) 511.
50. J.J. Douglas and R.J. Wagner, *Petrol. Transact., AIME*, 213 (1958) 96.
51. F.M.J. Perkins, *Petrol. Trans., AIME*, 210 (1957) 409.
52. M. Mahmoodi Nick, *Immiscible Foam for EOR*, MSc thesis, Delft University of Technology, The Netherlands, July 2008.
53. B.E. Poling, J.M. Prausnitz, J.P. O'Connell, *The properties of gases and liquids*, 5th Ed., McGraw Hills, (2000).
54. R. Span and W. Wagner, *J. Phys. Chem. Ref. Data*, 25 (6), (1996) 1509.
55. N. Spycher, K. Pruess, J. Ennis-King, *Geochimica et Cosmochimica Acta*, 67 (16) (2003) 3015.
56. J.P. Heller and M.S. Kuntamukkula, *Ind. Eng. Chem. Res.*, 26 (1987) 318.
57. K.R. Kibodeaux, *Experimental and theoretical studies of foam mechanisms in enhanced oil recovery and matrix acidization application*, PhD Dissertation, University of Texas at Austin, The US, 1997.
58. K.G. Kornev, A.V. Niemark, A.N. Rozhkov, *Adv. Colloid Interf. Sci.*, 82 (1999) 127.
59. R.v. Klitzing and H.-J. Müller, *Curr. Opin. Colloid In.*, 7 (2002) 42.
60. A.S. Aronson, V. Bergeron, M.E. Fagan, C.J. Radke, *Colloids Surf. A*, 83 (1994) 109.
61. A.J. de Vries, in: *Foam stability, a fundamental investigation of the factors controlling the stability of foams*, Delft (The Netherlands), Communication No. 326 (1957).
62. H. M. Princen and S. G. Mason, *J. Colloid Sci*, 20 (1965) 353.
63. S. Higenfeldt, S.A. Koehler, H.A. Stone, *Phys. Rev. Lett.*, 86 (20), (2001) 4704.
64. F.G. Gandolfo and H.L. Rosano, *J. Colloid Interf. Sci.*, 194 (1997) 31.
65. M.U. Vera and D.J. Durian, *Phys. Rev. Lett.*, 88 (8), (2002) 088304-1-4.
66. G. Maurdev, A.Saint-Jalmes, D. Langevin, *J. Colloid Interf. Sci.*, 300 (2006) 735.
67. H. M. Princen, J. Th. G. Overbeek and S. G. Mason, *J. Colloid Int. Sci*, 24 (1967) 125.
68. G.J. Hirasaki, *Private Communication* (2008).
69. A.H. Falls, J.B. Lawson, H.J. Hirasaki, *J. Pet. Tech.*, (1988) 95.
70. Teng and J.H. Dokos, *US Patent no. 4610888*, 1986.

71. D. Cohen, T.W. Patzek, C.J. Radke, *J. Colloid Interf. Sci.*, 179 (1996) 357.
72. D. Cohen, T.W. Patzek, C.J. Radke, *Transport in Porous Media*, 28 (1997) 253.
73. R. Masoudi and A. King, *J. Phys. Chem.*, 78 (1974) 2262.
74. W.L. Masterton, J. Bianchi, E.J. Slowinski, *J. Phys. Chem.*, 67 (1963) 615.
75. S.R.P. da Rocha, K.L. Harrison, K.P. Johnston, *Langmuir*, 15 (1999) 2.
76. P. Chiquet, J-L. Daridon, D. Broseta, S. Thibeau, *Energy Conversion and Management*, 48 (2007) 736.
77. S. Bachu and B. Bennion, *Environ Geol*, 54 (2008) 1707.
78. T. Gilanyi, Chr. Stergiopoulos, E. Wolfram, *Colloid and Polymer Sci*, 254 (1976) 1018.
79. G.J. Hirasaki and J.B. Lawson, *SPE J*, (1985) 176.
80. R. Krustev, D. Platikanov and M. Nedyalkov, *Colloids Surf. A*, 383 (1997) 123.
81. Hildenbrand, S. Schlomer, B.M. Kroos, R. Littke, *Geofluids*, 4 (2004) 46161.
82. F.E. Suffridge, K.T. Raterman, G.C. Russell, *SPE 19691* (1989).
83. Manhardt and J.J. Novosad, *In Situ*, 18(2), (1994) 145.
84. L.L. Schramm and K. Mannhardt, *J. Petrol. Sci and Eng.*, 15 (1996) 101.
85. G. Al-Muntasheri, *Polymer gels for water control: NMR and CT scan studies*, PhD dissertation, Delft University of Technology, The Netherlands (2008).
86. H. Kogawa, T. Shobu, M. Futakawa, A. Bucheeri, K. Haga, Takashi Naoe, *J. Nuclear Materials*, 377 (2008) 189.
87. C.N. Fredd, M.J. Miller, B.W. Quintero, *SPE 86493*, SPE International Symposium and Exhibition on Formation Damage Control, Lafayette, Louisiana, U.S. February 18-20, 2004.
88. C.J. Radke, *Private Communication* (2008).
89. T. Zhu, A. Strycker, C.J. Raible, K. Vineyard, *SPE 39680*, SPE/DOE Improved Oil Recovery Symposium, Tulsa, OK, U.S. April 19-22, 1998.
90. Y. Liu and R.B. Grigg, *SPE 93095*, SPE International Symposium on Oilfield Chemistry, the Woodlands, Texas, U.S., February 2-4, 2005.
91. J. Israelachvili, *Intermolecular and Surface Forces*, Academic Press: London, 1991.
92. R. Farajzadeh, R. Krastev, P.L.J. Zitha, *Adv. Colloid. Interf. Sci*, 137 (2008) 27.
93. Q. Xu and W.R. Rossen, *SPE 84183*, SPE Annual Technical Conference and Exhibition, 5-8 October 2003, Denver, Colorado.
94. K.R. Kibodeaux and W.R. Rossen, 67<sup>th</sup> annual Western regional meeting: a new dawn in the old West: Long Beach CA, 25-27 June 1997



---

# Chapter 8

## FOAM ASSISTED (CO<sub>2</sub>)-EOR

---

### ABSTRACT

*Application of (CO<sub>2</sub>)-foam as an Enhanced Oil Recovery (EOR) method was examined in granular porous media using X-ray Computed Tomography. In the experiments porous media were partially saturated with oil and brine (half top) and brine (half bottom). The CO<sub>2</sub> was either under sub- or super-critical conditions whereas N<sub>2</sub> remained under subcritical conditions. Prior to gas injection porous media were flooded with several pore volumes of water. In foam experiments this process was followed by injecting 1-2 pore volumes of a surfactant solution. Alpha Olefin Sulfonate (AOS) was used as foaming agent. The injection of AOS solution did not produce additional oil. We found that at low pressure experiments (P=1 bar) in the case of N<sub>2</sub>, weak foam could be formed in the oil-saturated part. An oil bank is formed ahead of the foam front, which results in additional oil recovery compared to gas injection alone. CO<sub>2</sub> injection, with the same flow rate, does not foam in the oil-saturated part of the core possibly due to its higher solubility. Above critical point (P=90 bar), CO<sub>2</sub> injection following a slug of surfactant reduces its mobility when there is no oil. Nevertheless, when foam front meets the oil the interface between gas and liquid disappears. The presence of the surfactant (foaming super-critical CO<sub>2</sub>) did not affect the oil recovery and pressure profile, indicating the detrimental effect of oil on foam stability in the medium. Our experimental results show that injection of surfactant prior to CO<sub>2</sub> injection can improve the ongoing CO<sub>2</sub>-EOR by reducing the gas mobility in the thief zones and diverting CO<sub>2</sub> into regions with higher oil saturation.*

**KEYWORDS:** *Foam, Enhanced Oil Recovery (EOR), Surfactant Alternating Gas (SAG), Carbon Dioxide (CO<sub>2</sub>), Nitrogen (N<sub>2</sub>), X-ray Computed Tomography.*

### 8.1. INTRODUCTION

A problem associated with many secondary and tertiary gas (e.g., CO<sub>2</sub>, N<sub>2</sub>, steam, air, etc.) injection projects is the inefficient gas utilization and poor recovery due to viscous fingering and gravity segregation. The fingering and segregation result from high gas mobility (displacing phase) compared to oil and water (displaced phase); gas density and viscosity are much lower than those of oil and water (even at high reservoir pressures). Unfavorable mobility ratios lead to even more severe channeling in heterogeneous reservoirs. Consequently, a large part of the reservoir is not contacted by the drive fluid and the volumetric sweep efficiency of the reservoir remains poor.

The alternation slugs of water and gas (see Fig. 8.1), i.e. Water Alternating Gas or WAG, has been common practice to get more favorable mobility ratios and improve sweep efficiency. WAG can eventually suffer from viscous instabilities and gravity segregation and therefore has not always been a successful method of controlling the gas mobility.

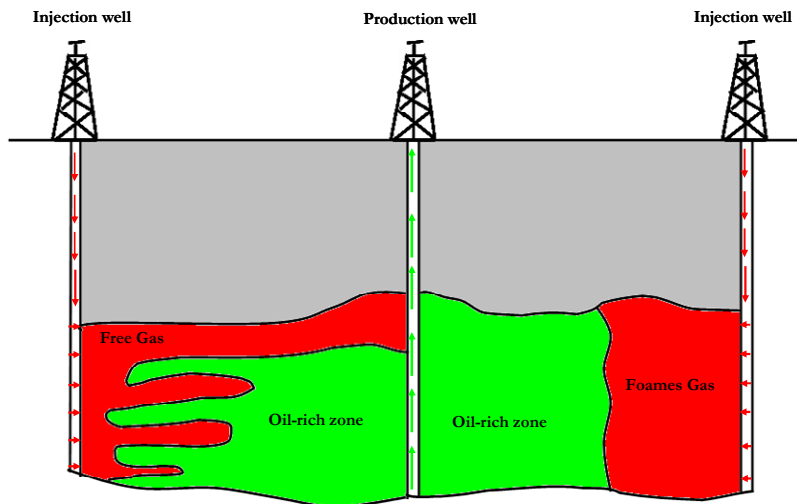


**Fig. 8.1.:** Schematic of gas flooding vs. SAG (or foam) flooding: Foaming of the gas modifies its profile by lowering gas mobility.

The addition of surfactant to water results in a process called Surfactant Alternating Gas or SAG. By foaming the gas and thus reducing its mobility especially in the swept or high permeability parts of the reservoir one can potentially overcome the problems encountered in WAG [e.g. 1-5]. Foaming reduces gas mobility by immobilizing or trapping a large fraction of the gas without compromising its efficiency. As a result, part of the gas is diverted into the oil-rich part of the reservoir and therefore enhances the oil recovery. The mechanism of oil displacement by foam differs from that for surfactant flooding due to the presence of a gas phase. Foam can affect the oil recovery in two ways: (1) by stabilizing the displacement process by increasing the displacing fluid (gas or foam) viscosity, and (2) by reducing the capillary forces via reducing the interfacial

tensions due to the presence of surfactant (this is more important in chemical foams). In addition to these two important mechanisms, since the gas is in more contact with oil, the interfacial mass transfer between gas and oil will also play an important role in mobilizing the oil in-place by dissolution, viscosity reduction and swelling. We argue that in the case of CO<sub>2</sub>, natural convection further assists these processes by enhancing the transfer rate as discussed in detail in Chapter 2.

The main concern with the application of SAG (foam) as an EOR method is the longevity of foam when it contacts the crude oil. Many experiments, both in bulk and porous media, have shown the detrimental effect of oil on foam stability. Therefore, foam in the absence of oil may behave differently than foam in the presence of oil. As discussed in the previous chapters the stability of foam in porous media essentially relies on the stability of the foam films (lamellae). This means that oil may influence the foam performance by affecting lamellae stability, a property that is desired when using oil as an antifoaming agent.

This chapter deals with foam performance in the presence of oil in porous media. Firstly, a brief review of the proposed mechanisms for explaining the anti-foaming action of oil (in bulk and porous media) is provided. Next we discuss the experiments in which a slug of surfactant is injected into a core containing water-flood residual oil and followed by injection of CO<sub>2</sub> or N<sub>2</sub>. We end the chapter with concluding remarks.

## 8.2. FOAM STABILITY

### 8.2.1. Disjoining pressure

Foam is a dispersion of gas in a continuous liquid phase, which is volumetrically the minor component. The gas is discontinuous and subdivided by thin liquid films, called lamellae, stabilized by surfactants. In foams the gas pressure,  $p_g$ , is always higher than the surrounding liquid pressure,  $p_l$ , and, therefore, a capillary suction occurs. The capillary pressure can be defined by the Young-Laplace equation as

$$p_c = p_g - p_l = 2\sigma R_c + \Pi(h), \quad (8.1)$$

where  $\sigma$  is the gas-water interfacial tension and  $R_c$  is the mean gas-water interfacial curvature (e.g., inverse of the radius for a spherical bubble). As the film becomes thinner, two surfaces of the foam film interact with each other by long-range repulsive electrostatic and short-range attractive Van der Waals forces in accordance with the classical DLVO theory. Note that the DLVO theory does not take into account the short-range repulsive steric force that becomes important in thin Newton black films [7]. These forces (or pressures) are components of the so-called disjoining pressure,  $\Pi$ , which acts on the film surfaces and balances the capillary pressure. At equilibrium

(quasi-static situation) the disjoining pressure equals to the capillary pressure, i.e.,  $\Pi = p_c$ . Disjoining pressure is a measure of stability of a foam film and strongly depends on the film thickness. Highly positive disjoining pressures imply strong repulsive forces between the film interfaces and a stable film, whereas negative attractive forces produce unstable films [8]. The three characteristics types of disjoining pressure isotherms in Fig. 8.2 correspond to (1) stable, (2) metastable, and (3) unstable films [9]. Above a critical capillary pressure, the lifetime of the lamellae and corresponding bulk foam becomes short. For sufficiently high capillary suction pressure (higher than maximum disjoining pressure) macroscopic disturbances may initiate film rupture. This means that foam stability is highly sensitive to the thermodynamics of the lamellae.

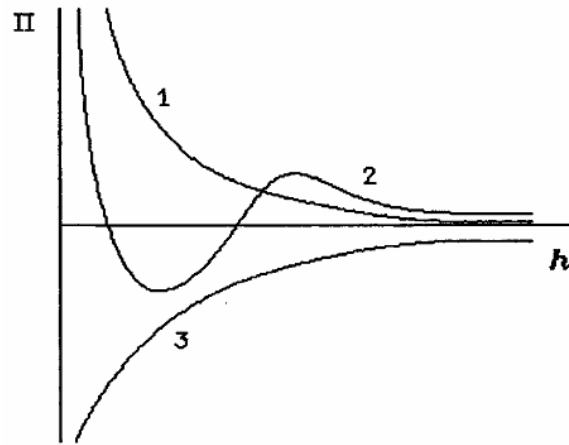


**Fig. 8.2:** Schematic illustration of disjoining pressure isotherms (1) stable, (2) metastable and (3) unstable films. The picture is taken from Ref. [9]

### 8.2.2. Effect of oil on foam stability

It is a well-known fact that addition of small traces of oil or hydrophobic particles (or mixture of both) may strongly influence foam stability. Three major mechanisms have been considered for the anti-foaming property of the dispersed oils: (1) aqueous film thinning rate during oil droplet entry (2) oil spreading on the water surface and (3) thin water film bridging. The antifoaming activity of an antifoam is usually explained in terms of the effects resulting from the surface activity of the antifoam or dewetting of the oil by the aqueous solution. In order to affect the foam stability oil must first enter to the gas-water interface [10,11].

As mentioned earlier the film ruptures when the imposed capillary pressure is higher than the maximum disjoining pressure. Some researchers have mentioned that oil reduces the foam lifetime by reducing the maximum disjoining pressure. Accordingly, two mechanisms have been proposed to explain this effect:

1. Surfactant may be adsorbed into the oil phase or transferred to the oil-water interface. This reduces the surfactant concentration at the gas-water interface, which in turn results in a dramatic decrease in the magnitude of the disjoining pressure.
2. Oil adsorbs into the micelles in the bulk surfactant solution or is co-adsorbed at the gas-water interface and hence, reduces the maximum disjoining pressure.

These mechanisms are less likely to occur because (a) pre-equilibration of the oil phase with the surfactant does not influence the antifoaming activity of oil [12], (b) most of the foam experiments are conducted at surfactant concentrations well above the CMC, and presumably the amount of surfactant is high enough to compensate for the surfactant loss to other places than the gas-water interface, and (c) oil solubilization does not significantly contribute to the foam instability [12,13, 15]. Foam is mostly destroyed in the presence of a separate immiscible oil or hydrophobic phase. This suggests that antifoaming cannot be explained by simple phase partitioning of the surfactant or the oil.

### 8.2.2.1. Entering and Spreading

An oil droplet must first enter the gas-water surface to affect foam stability. The feasibility of droplet entry,  $E_{o/w}$ , to the gas-water interface can be evaluated by an expression proposed by Harkins [15],

$$E_{o/w} = \sigma_{wg} + \sigma_{ow} - \sigma_{og} \quad (8.2)$$

In this equation  $\sigma$  is the interfacial tension and subscripts  $w$ ,  $o$  and  $g$  stand for water, oil and gas respectively. Thermodynamically, when  $E_{o/w} < 0$ , the oil remains in the bulk aqueous phase forming lenses, which also contact the gas phase. It is favorable for oil to enter the gas-water surface when  $E_{o/w} > 0$ . The original entering coefficient accommodates three partial values (the initial  $E_{o/w}^{ini}$ , the semi-initial  $E_{o/w}^{si}$  and the equilibrium  $E_{o/w}^{eq}$ ) due to the fact that the interfacial tensions are dependent on both surfactant concentration and mutual saturations of all phases [16]. The initial coefficient describes the initial non-equilibrium condition of the system; the semi-initial coefficient is calculated when one of the phases is already saturated; and the equilibrium entry coefficient defines the system when all phases are saturated. For some systems the operative entry coefficient lies between  $E_{o/w}^{ini}$  and  $E_{o/w}^{eq}$ .

It is commonly believed that when an oil droplet enters the gas-water interface it spreads over the surface. This again depends on the interfacial tensions of the phases. The spreading coefficient is defined as

$$S_{o/w} = \sigma_{wg} - \sigma_{ow} - \sigma_{og} \quad (8.3)$$

The spreading does not occur when the spreading coefficient is negative. The entering and spreading coefficients are related in the following way:  $-E_{o/w} = S_{o/w}$ . Therefore, a non-entering oil is thermodynamically equivalent to water spreading on a gas-oil interface. In the calculation of the spreading coefficient it is necessary to use the accurately measured values of the various tensions operative in pseudo-emulsion films (these films are formed whenever foam bubbles or lamellae contact oil) [17].

### 8.2.2.2. Generalized entering coefficient

Although the above equations give a rough guide to antifoaming action, they are often inadequate as they do not consider the geometry of the system or the influence of interfacial interactions within the film; hence, their application is limited. Therefore when applied to interpret the experiments involving oil-foam interaction in porous media they give contradictory results. It has been even pointed out that the results of bulk foam stability in the presence of oil cannot be related to foam stability in porous media [18,19].

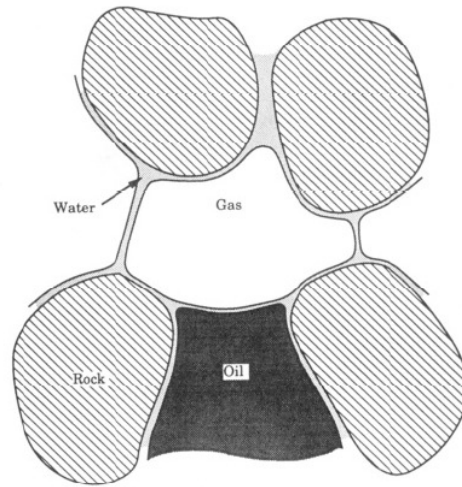


**Fig 8.3:** Schematic of foam flowing through a porous medium containing oil [12]

Bergeron et al. [12] defined a generalized entering coefficient that takes into account the effect of the porous medium, thin liquid films and capillary suction in the Plateau borders. This approach demonstrates the correspondence between the stable pseudoemulsion films, negative entering coefficients and oil-tolerant foams by applying the Frumkin-Derjaguin wetting theory. The basic assumption of this theory is that the stability of pseudoemulsion films determines the stability of foam in the presence of oil (see Fig. 8.3). The generalized entering coefficient is defined as

$$E_{o/w}^g = \sigma_{wg} + \sigma_{ow} - \sigma_f, \quad (8.4)$$

where  $\sigma_f$  is the film tension and defined as

$$\sigma_f(h_0) = \sigma_{gw} + \sigma_{ow} + \int_{\Pi=0}^{\Pi=\Pi(h_0)} h d\Pi, \quad (8.5)$$

where  $h_0$  is the equilibrium thickness of the film at a particular disjoining pressure. This reduces Eq. (8.4) to

$$E_{o/w}^g = - \int_{\Pi=0}^{\Pi=\Pi(h_0)} h d\Pi. \quad (8.6)$$

This equation relates the generalized entering coefficient to the disjoining pressure and therefore to the properties of the pseudoemulsion film. For pseudoemulsion films that are not highly curved at equilibrium it gives:  $\Pi(h_0) = p_c$ . Systems that have pseudoemulsion film isotherms with large repulsive common film branches display negative entering behavior and produce highly stable pseudoemulsion films. As a result the foam remains stable when it contacts oil.

In similar work, Lobo and Wasan [20] suggested to use the energy of interaction per unit area,  $f$ , as a criterion of the pseudoemulsion film stability

$$f = - \int_{\infty}^{h_0} \Pi dh \quad (8.7)$$

It can be concluded from Eqs. (8.6) and (8.7) that,  $f(h_0) + E_{o/w}^g(h_0) = -h_0\Pi(h_0)$ . For zero capillary pressure  $f$  and  $E_{o/w}^g$  are equivalent.

It should be noted that the idea of a generalized entry barrier is closely related to the concept of a limiting capillary pressure for foam in porous media [21]. The limiting capillary pressure in porous media without oil is close to the rupture pressure of the single foam film [8]. This means that in planar films the concept of limiting or critical capillary pressure is equivalent to the concept of critical disjoining pressure. Therefore, it can be argued that the limiting capillary pressure for foam stability when oil is present in the porous medium is close to the pressure that makes the generalized entering coefficient positive. Oil-tolerant foam in porous media can be produced by making the oil surface completely water-wet, i.e., zero contact angle.

Nevertheless, Denkov et al. [22] using the so-called film trapping technique (FTT) [23] found that the entry barrier increases with increasing surfactant concentration and micelles play a significant role in the film stabilization above a certain threshold surfactant concentration. Their calculation showed that for micron-sized oil drops there is a big difference between the values of critical

capillary pressure and critical disjoining pressure. The critical capillary pressure is a weak function of oil drop size and the asymmetric film radius while the critical disjoining pressure always scales as the inverse of drop radius. In conclusion, the critical capillary pressure is a more convenient quantity for describing the entry barriers. Moreover, Myers and Radke [24] stated that although a stable pseudoemulsion film prevents coalescence, the destruction of a pseudoemulsion film does not necessarily lead to foam coalescence. The rupture of the pseudoemulsion film allows the Plateau borders of a foam film to form a non-zero contact angle with the oil drop. The rupture mechanism depends on the foam velocity in the porous medium.

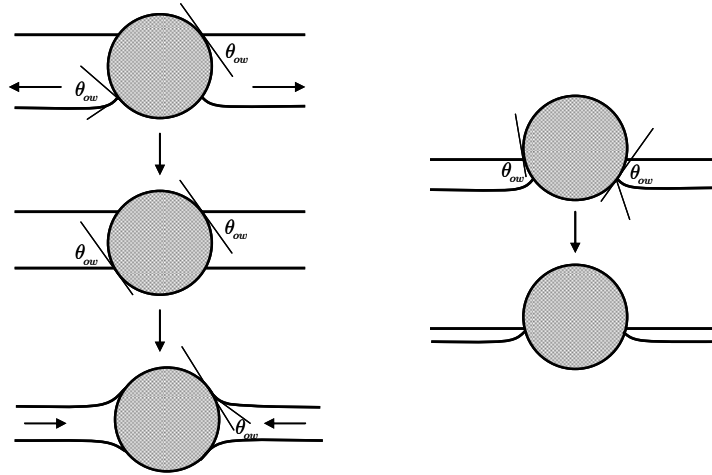


**Fig. 8.4:** Bridging of an oil droplet between two film surfaces (left): contact angle of surfactant solution with oil droplet,  $\theta_{ow} < 90^\circ$  and (right):  $\theta_{ow} > 90^\circ$ . Pictures adopted from Ref. [10].

### 8.2.2.3. Bridging of foam film by oil droplet

This mechanism was first proposed for the antifoaming effect of hydrophobic particles and later adapted to oil droplets [10]. If oil (or the hydrophobic particle) remains as a lens on one surface of the film, i.e.,  $S_{o/w} < 0$ , as the film thins the oil will enter the other surface forming a bridge across the film. The fate of the foam film depends on the contact angle between the surfactant solution and the oil droplet,  $\theta_{ow}$ . The film ruptures when  $\theta_{ow} > 90^\circ$ . The critical angle is smaller for non-spherical drops [25,26]. The bridging coefficient,  $B$ , is defined as a criterion for the effect of oil bridging on foam stability

$$B = \sigma_{wg}^2 + \sigma_{ow}^2 - \sigma_{og}^2 \quad (8.8)$$

When  $B$  is positive or zero the film is unstable, while negative values of  $B$  results in stable film. The thinning of a water film or oil droplet causes formation of a hole in the lamella [27]. When  $B \geq 0$ , capillary pressure is induced in the foam film, which drives water away from the oil drop [26]. However, Denkov et al. [22] showed that in some cases small droplets can yield a stable

bridge even if the bridging coefficient is positive. This was explained by the existence of a perturbed zone of a water film in the vicinity of an oil bridge.

Comparing Eqs. (8.2) and (8.8) one can show that when the bridging coefficient is positive the entering coefficient is also positive. However, a positive entering coefficient does not guarantee a positive bridging coefficient. Therefore, in the absence of disjoining pressure, a positive bridging coefficient is a sufficient criterion for oil to enter the gas-water interface. Considering the disjoining pressure, the generalized entering coefficient must also be positive for an oil droplet to enter the gas-water interface [12]. When the bridging coefficient is negative the spreading coefficient is also negative and therefore oil drops with negative bridging coefficients do not spread. It must be noted that a negative spreading coefficient does not guarantee a negative bridging coefficient.

#### 8.2.2.4. Oil emulsification and lamella number

Schramm and Novosad [28-30] proposed that the emulsification of oil into the foam structure is the mechanism of lamella rupture. The capillary suction in the Plateau border draws oil into lamellae, where a pinch-off mechanism produces emulsified oil. One can write

$$\Delta p_c = \frac{2\sigma_{wg}}{r_p}. \quad (8.9)$$

Here,  $r_p$  is the radius of the Plateau border. The resisting force comes from the oil tendency to minimize its interfacial area against the aqueous solution. This determines the pressure drop across that interface via:

$$\Delta p_R = \frac{2\sigma_{ow}}{r_o}, \quad (8.10)$$

where,  $r_o$  is the oil drop radius. The ratio of these pressures gives a dimensionless number called *Lamella number* that along with bulk spreading and entering coefficients can characterize foam stability in porous media when oil is present:

$$L = \frac{\Delta p_c}{\Delta p_R} = \frac{r_o}{r_p} \frac{\sigma_{wg}}{\sigma_{ow}}. \quad (8.11)$$

If the *Lamella number* is larger than unity, the oil droplets are small enough to enter to the lamella by capillary suction in the Plateau border. The most stable foams are formed when the *Lamella number* is low and entering coefficient is negative. Nevertheless, it should be mentioned

that thermodynamically emulsification is only favored for negative values of the interfacial tension, which are physically impossible! The *Lamella number* relies on the bulk measurements and fails to explain oil effects on foam stability in porous media [31]. Moreover, it is unlikely that the oil drops, as small as the thickness of a foam film (typically between 5 and 50 nm), are formed in porous media.

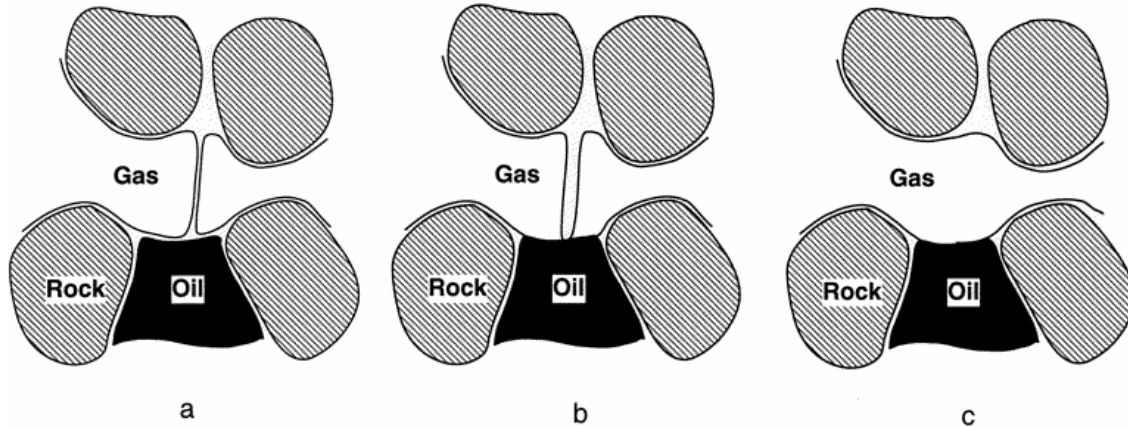


**Fig. 8.5:** Foam lamella moving across an oil droplet a) pseudoemulsion film is stable, b) pseudoemulsion film ruptures and gas bubbles directly contact oil and c) two bubbles coalesce [24].

#### 8.2.2.5. Pinch-off mechanism

Myers and Radke [24,27], using a capillary tube pore model, observed two mechanisms of rupture of foam lamellae moving across non-wetting surfaces or across portions of oil drops that enter the gas-water interface. The first mechanism, applicable for high velocity regimes (non-relevant for oil reservoirs), is Plateau border depletion. The capillary pressure in the Plateau border decreases and eventually ruptures the foam film due to the fact that the Plateau border covers the previously dry non-wetting surface. Typical velocities in the oil reservoirs are not large enough to coat a non-wetting surface or to deplete the Plateau border significantly. Therefore, a second mechanism, namely the *pinch-off mechanism* was suggested [24]. The film ruptures when oil enters the gas-water interface and gas directly contacts oil. As the lamella moves across the bare oil drops the film ruptures by pinch-off if the bridging coefficient is positive (the value of spreading coefficient is not critical). This requires the pinch-off spreading time to be less than the time required for lamellae to move across an oil drop (typically less than 0.2 sec). The different stages of this mechanism are shown in Fig. 8.5. In Fig. 8.5a, two gas bubbles separated by a foam lamella move across an oil globule. In this case, the pseudoemulsion film separates the gas bubbles from the oil globule and no rupture is observed. In Fig. 8.5b, a stable water film separating the gas bubbles from the oil droplet does not exist, and accordingly the oil globule enters the gas-water interfaces of the two bubbles. If the bridging coefficient is positive this configuration is unstable and the two

gas-water-oil three-phase contact lines move toward each other. When the two three-phase contact lines meet, the foam lamella pinches off from the oil globule, causing the two bubbles to coalesce into one as shown in Fig. 8.5c.

Based on the pinch-off mechanism the following expression was proposed for rate of foam coalescence by oil [24]:

$$r_{co} = f_1(S_o) f_2(B, v_f) f_3(\Pi / \Pi^*) v_f n_f. \quad (8.12)$$

Here,  $f_1$ ,  $f_2$  and  $f_3$  are function of the variables in the brackets. This equation states that the rate of bubble coalescence depends on the oil saturation, the bridging coefficient determined by the interfacial tensions, the lamella velocity ( $v_f$ ), the foam texture and the disjoining pressure of the pseudoemulsion films that separate gas from oil.

### 8.3. EXPERIMENTS

#### 8.3.1. Calculation of oil saturation

The set-up explained in Chapter 7 (Fig. 7.1) was used to perform the experiments. The following equation is used to calculate the oil saturation,  $S_o$ , from the measured attenuation coefficients ( $HU$ ), eliminating the contribution of the rock by the subtraction:

$$S_o = \frac{1}{\varphi} \left( \frac{HU - HU_{wet}}{HU_o - HU_w} \right), \quad (8.13)$$

where the subscripts *wet*, *o* and *w* stand for brine (or surfactant) saturated core, oil and brine respectively. The accuracy of the above equation is within  $\pm 2\%$ . This equation is valid when only two phases, i.e., water and oil or water and gas are present in porous media.

#### 8.3.2. Experimental procedure

*Saturation with brine:* The core was flushed with  $\text{CO}_2$  for at least 30 minutes to replace the air in the system. Afterwards, at least 20 pore volumes of brine with the flowrate of  $q_w = 2 \text{ ml/min}$  were injected into the core while the backpressure was set to  $P_b = 20 \text{ bar}$ . Therefore, all  $\text{CO}_2$  present in the core is dissolved into the brine and carried away. This is confirmed by the CT images.

*Drainage:* When the core was saturated with brine, it was flushed with a known amount of oil ( $q_o = 0.5 \text{ ml/min}$ ) to displace the brine. To overcome the gravity and consequently fingering (instability) effects the oil was injected from the top. Isopar H (with viscosity of 3 cP) was used as oil phase in the experiments.

*Imbibition:* The brine was injected into the core ( $q_w=2 \text{ ml/min}$ ) from the bottom until no oil was produced and the pressure drop along the core was constant within the accuracy of the measurements.

*Surfactant Injection:* After water flooding the core, 1-2 pore volumes of surfactant solution was injected ( $q_s=2 \text{ ml/min}$ ) into the porous medium from the bottom of the core. The surfactant solution contained 1 wt% of (C<sub>12</sub>)-Alpha Olefin Sulfonate (AOS) and 3.0 wt% of NaCl.

*Foam (gas) Injection:* The gas was injected into the core previously flushed with the surfactant solution (SAG foam) from the bottom of the core at the experimental pressure.

#### 8.4. RESULTS AND DISCUSSION

The images and corresponding saturation profiles of drainage and imbibition steps are similar for all of the experiments and therefore only one example is presented in Fig. 8.6. The corresponding oil saturations of the core were calculated using these images by Eq. (8.12) and are shown in Fig. 8.7. The accuracy of the last points (at  $X=17 \text{ cm}$ ) is not good due to the beam hardening effects at the edges of the core-holder [32]. As can be seen, the injected oil (brine) displaces the brine (oil) in a manner expected from the Buckley-Leverett theory, i.e., showing a rarefaction and a shock part. It should be mentioned that the residual oil saturation may vary in different axial slices made from the core as Fig. 8.7 shows the calculated saturation only for the central part of the core. The oil distribution in the core may also vary from the experiment to experiment.

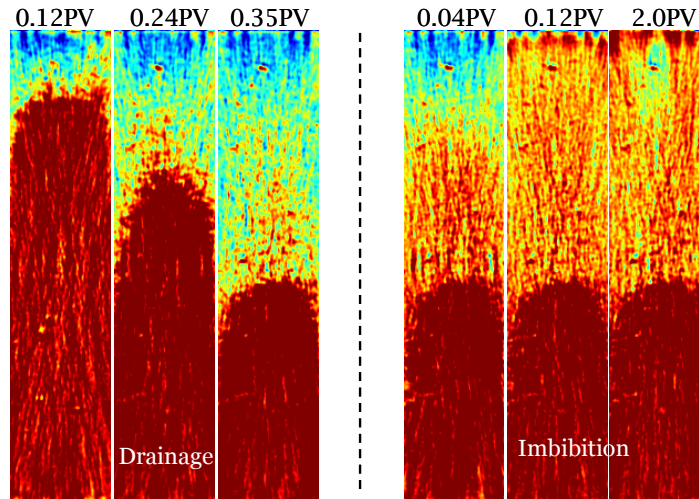


**Fig. 8.6:** CT images of an example of the drainage (left) and imbibition stages (right) of the experiments: Oil (Isopar H) is injected from top of the core initially saturated with brine (drainage). Afterwards, brine is injected from the bottom (imbibition)

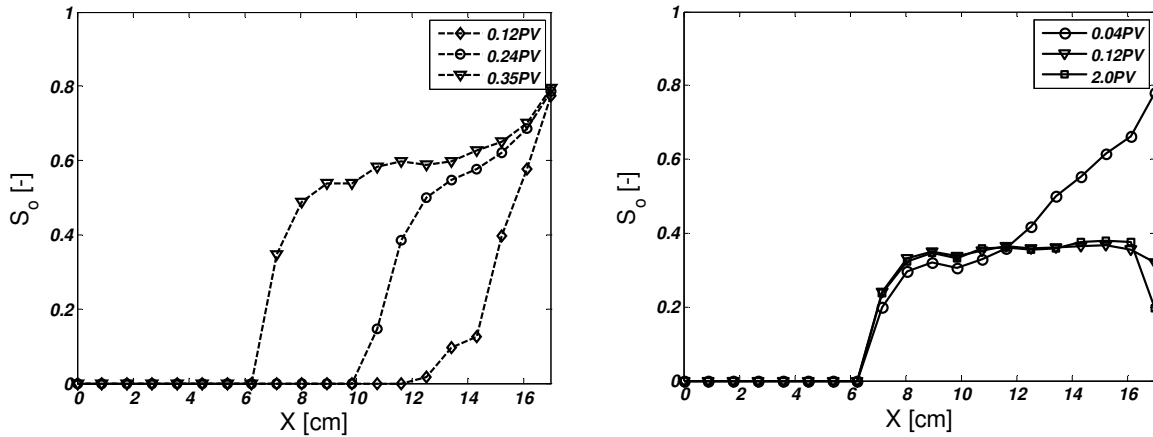


**Fig. 8.7:** Oil saturation profiles for the drainage stage (left) and imbibition stage (right), calculated from CT profiles shown in Fig. 8.6.  $X$  denotes the distance from the bottom.

### 8.4.1. Low-pressure experiments

#### 8.4.1.1. CT scan images and production data

Figure 8.8 presents the CT images of the central part of the  $N_2$  and  $CO_2$  experiments respectively. The time of each image is also shown in terms of the dimensionless time, i.e., pore volumes,  $PV$ , which is the ratio between the cumulative volume of injected fluids (in these experiments only gas) and the volume of the pore space in the porous medium. In these experiments  $N_2$  was injected at the flowrate of  $0.50$  ml/min ( $\sim 2$  ft/day) and  $CO_2$  at the flowrate of  $0.75$  ml/min into the core initially flooded with  $1.0$   $PV$  of the surfactant solution (SAG scheme). The blue, red and orange colors represent the foam (gas and surfactant solution), water  $S_w = 1$  and water-flood residual (or more accurately remaining) oil  $S_{or}$ , respectively. The green part constitutes the three phase region. The remaining oil fractions of the core are given in Table 8.1 for both experiments after water-flooding. The general features of both experiments in the water saturated part (red) are similar to the experiments discussed in Chapter 7, i.e.,  $N_2$  almost immediately appears in the core while a considerable amount of  $CO_2$  is injected into the core before it becomes visible. As time passes the orange part of the core (close to the oil-water interface) becomes more reddish implying that foam displaces the aqueous phase from the water-saturated part towards the core outlet in a way typical of a high viscosity fluid displacing a liquid. After about  $0.20$   $PV$  the  $N_2$  reaches the oil-water contact; while this time is more than  $1.0$   $PV$  for  $CO_2$ . This is likely due to the higher solubility of  $CO_2$  in water as discussed in the previous chapter. The gas breakthrough occurs earlier than  $0.30$   $PV$  for the  $N_2$  experiment. This suggests that presence of oil significantly increases the gas mobility by destroying the foam. The CT images clearly show that when  $N_2$  reaches the oil-water contact the foam front disappears, at least partially. This leaves a higher liquid saturation at the oil-water contact due to capillary effects. Part of the gas bypasses the oil and the other part channels through the oil containing part of the core.

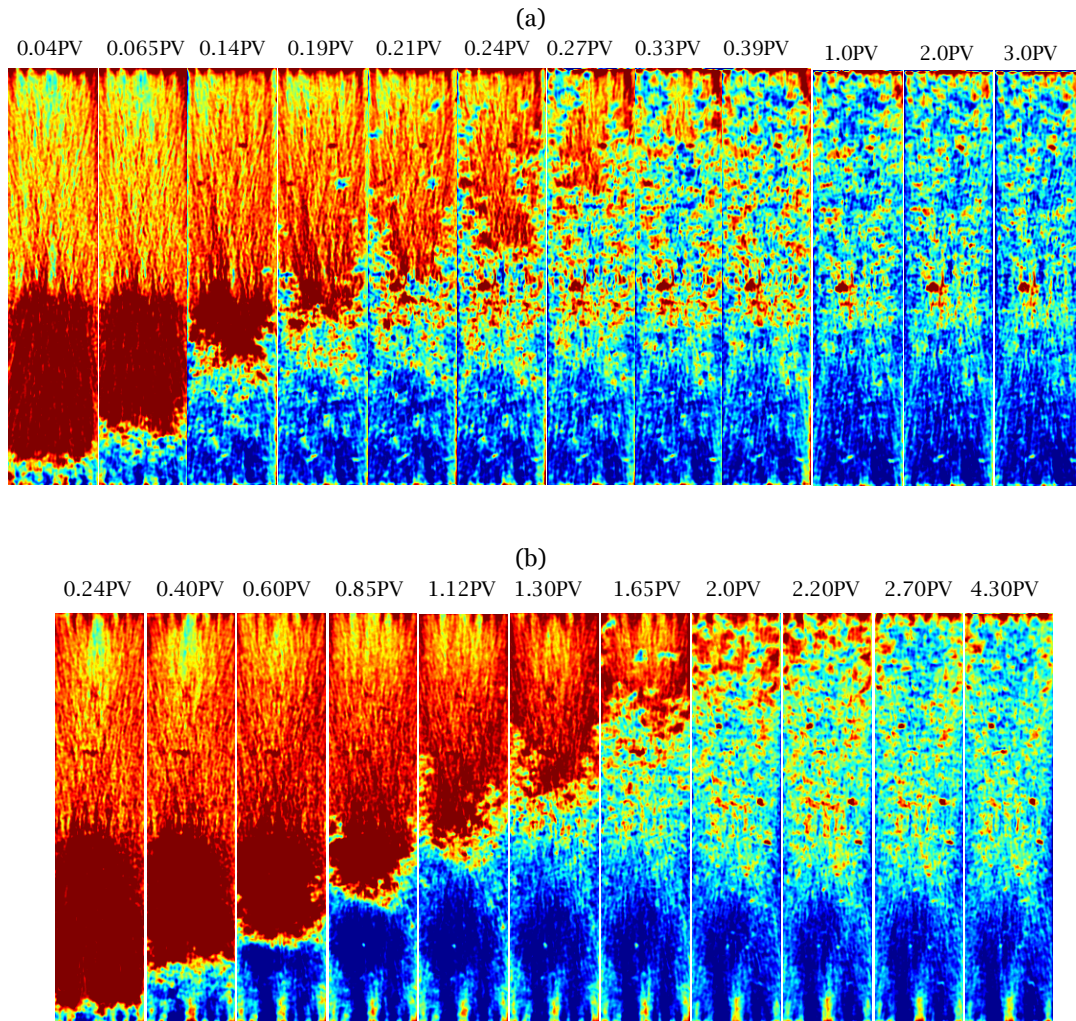


**Fig. 8.8:** CT images of (a)  $N_2$  and (b)  $CO_2$  foam flow (blue: gas and surfactant solution) in a porous medium initially saturated with surfactant solution (red) and water-flood residual oil (orange: surfactant solution and oil) at  $P=1$  bar and  $T=20$  °C. The time of each image is shown in pore volumes of the injected gas. The green part after 1.30 PV constitutes the region where there are three phases. Gas is injected from the bottom.

The interesting feature in the  $N_2$  experiment is the existence of a liquid bank ahead of the gas (foam) front. This becomes more obvious from Fig. 8.9 in which the oil and water production data are presented. It turns out from these plots that at the time when  $N_2$  occupies the entire length of the core ( $\sim 0.40$  PV) large amounts of liquid (water and oil) are already produced. Strictly speaking almost all of the oil (within the accuracy of our measurements) is produced at this time emphasizing the fact that foam pushes the oil out of the core (see Fig. 8.10).

**Table 8.1:** Summary of the experiments at atmospheric pressure

Gas	Pressure [bar]	Injected Oil [ml]	Waterflood $S_{or}$ [%]	Waterflood Recovery [%]	Surfactant Recovery	Inc. Gas Recovery [%]	Total Recovery [%]
$N_2$	1.0	15.0	$32 \pm 2$	$47 \pm 2$	-	$9.0 \pm 0.5$	$56 \pm 2$
$CO_2$	1.0	15.5	$33 \pm 2$	$46 \pm 2$	-	$4.0 \pm 0.5$	$50 \pm 2$

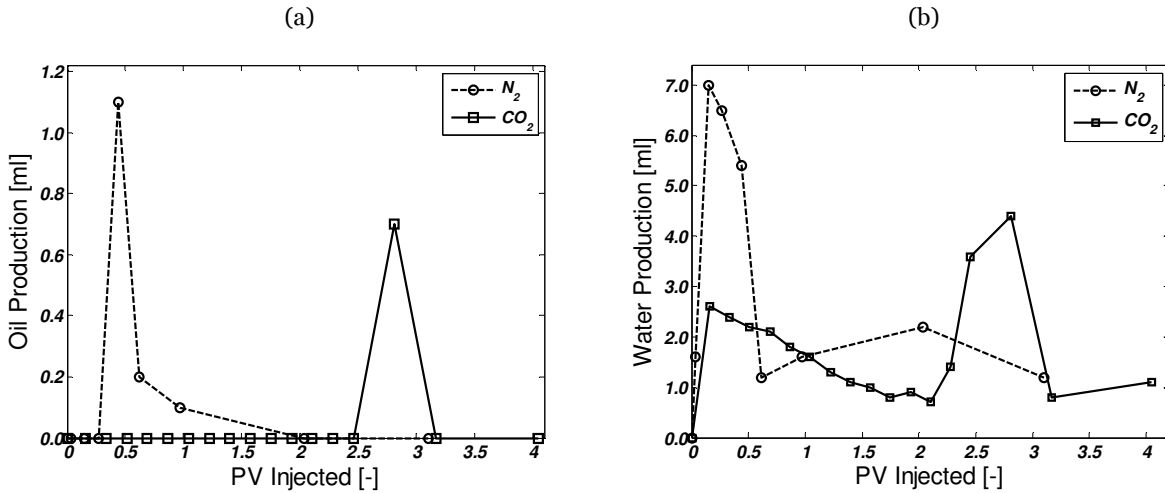


**Fig. 8.9:** Production history of (a) oil and (b) water in  $N_2$  and  $CO_2$  SAG experiments at  $P=1$  bar and  $T=20^\circ C$ . The first few points of the water production exhibit a starting up effect.

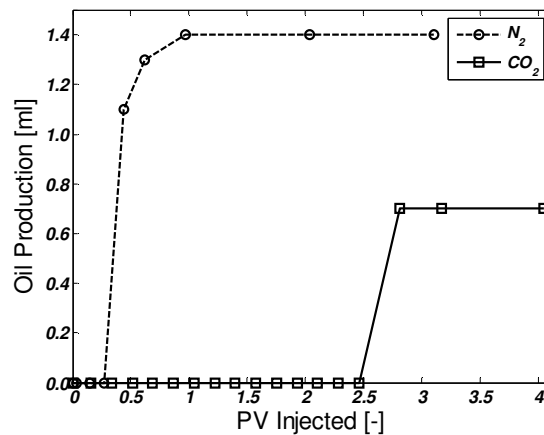


**Fig. 8.10:** Cumulative oil production history of  $N_2$  and  $CO_2$  SAG experiments at  $P=1$  bar and  $T=20^\circ C$ .

Similar to  $N_2$ , when  $CO_2$  reaches the oil-water contact (OWC) the sharp interface between the gas and the liquid is destabilized; to a smaller extent though.  $CO_2$  is not as dispersed as  $N_2$  in the oil phase. Instead similar to the water-saturated part of the core,  $CO_2$  dissolves into oil and moves slower than  $N_2$ , possibly due to its higher solubility in both water and oil compared to  $N_2$ . The production in the  $CO_2$  experiment is less than in the  $N_2$  experiment. Most likely in the  $CO_2$  experiment there is much less foam generation in the oil containing part because of (1) higher

solubility of  $\text{CO}_2$ , which leaves lesser free  $\text{CO}_2$  gas for foaming, and (2) detrimental effect of oil on foam stability as discussed in the previous section. The small oil production in the  $\text{CO}_2$  experiment can be attributed to the small amount of gas that is not dissolved.

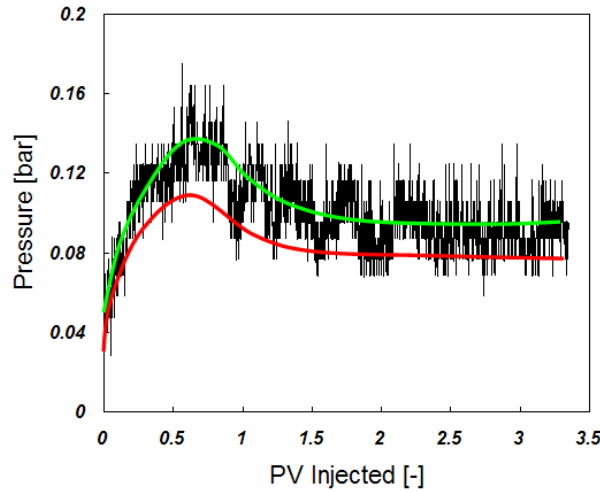


**Fig. 8.11:** Pressure drop across the entire core (green) and in the water part of the core (red) for  $\text{N}_2$  foam.

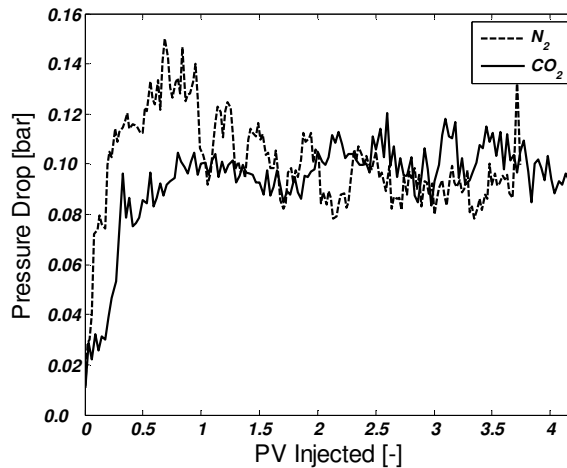


**Fig. 8.12:** Pressure drop across the entire core for  $\text{N}_2$  foam (dashed line) and  $\text{CO}_2$  foam (solid line) at  $P=1$  bar and  $T=20^\circ\text{C}$ .

#### 8.4.1.2. Pressure profiles

Figure 8.11 shows the pressure drop along the water saturated part (red line) and the entire core for  $\text{N}_2$  foam (green line). It becomes evident from this figure that although a large fraction of the pressure drop is in the water part, injection of surfactant prior to  $\text{N}_2$  slightly reduces its mobility despite the presence of oil. The pressure drop in the upper part of the core is less than one third of the total pressure drop. The pressure profile obtained in this experiment for water part is consistent with the pressure values presented in Fig. 7.5.

Figure 8.12 compares the measured pressure drops versus dimensionless time (PV) of the two experiments. Unlike the oil-free experiments of Chapter 7, the difference between the pressure drops is not large and insignificant after one PV. However, considering the differences in flowrates it appears that N<sub>2</sub> injection builds up a higher pressure drop than CO<sub>2</sub> injection, in particular prior to gas breakthrough. This could explain the slightly higher production for the N<sub>2</sub> experiment.

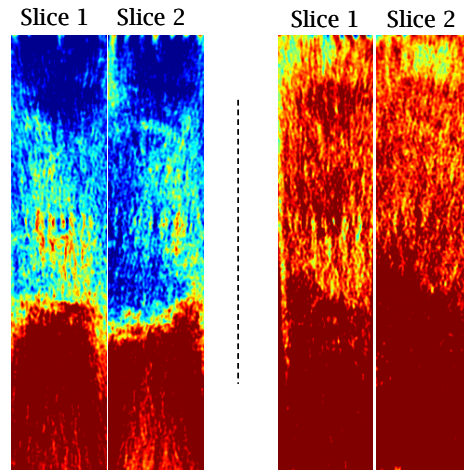


**Fig. 8.13:** Two CT images of the drainage (left) and imbibition (right) stages of the Exp-01 experiment: Blue, green and red represent gas, oil and water respectively. During the drainage part gas entered the core due to problems with the pump.

#### 8.4.2. Supercritical CO<sub>2</sub> experiments ( $P=90$ bar and $T=50$ °C )

Two experiments were carried out to investigate the effect of surfactant and foamed CO<sub>2</sub> on the oil recovery for a supercritical CO<sub>2</sub> EOR process. In these experiments the back-pressure was set to 90 bar and the core was heated up to 50 °C. The experimental procedure and materials were similar as for the low-pressure experiments.

##### 8.4.2.1. CO<sub>2</sub> injection (Exp-01)

In this experiment the core was first saturated with doped brine and oil was injected from the top afterwards. Due to some technical problems with the pump, the oil was injected at atmospheric pressure into the core. The injection was monitored by scanning the core at different time steps. During the injection it was noticed that gas was also injected into the core together with the oil. Two reasons might have caused this problem: 1) gas was already present in the pump and/or 2) the pump sucked air due to the existence of leakages in the injection line.

Figure 8.13 shows the CT images of the drainage and imbibition stages of this experiment. Gas, oil and water are respectively represented by blue, green and red. It is observed that during the

drainage stage, a substantial amount of gas unintentionally entered the core. The comparison between the two slices on the left side of the dashed line shows the uneven distribution of oil in the core. After stopping oil injection the back-pressure was increased up to  $90 \text{ bar}$  and water was injected from the bottom into the core. The two pictures at the right side of Fig. 8.13 show the fluid distribution inside the core. As can be observed, the air is trapped in some parts of the core and remains immobile. Figure 8.14 shows the calculated oil saturation along the core. From the CT calculations the maximum amount of oil inside the core is about  $6 \text{ ml}$  after water-flooding. This value is taken to compare the performance of  $\text{CO}_2$  flooding and  $\text{CO}_2$  foam, which will be described below.

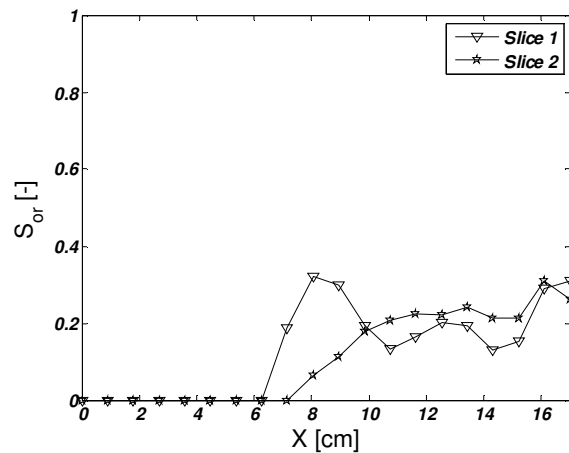


**Fig. 8.14:** Oil saturation after water-flooding in Exp-01. The total amount of oil inside the core is estimated to be about  $6 \text{ ml}$  from CT calculations.

#### 8.4.2.2. $\text{CO}_2$ foam (Exp-02)

The drainage and imbibition stages of this experiment did not suffer from any technical problems. Water-flooding produced about 44% of the initial oil, which is similar to the recovery of the low pressure experiments. Only for comparison purposes, in the following the same water-flooding recovery factor for both the Exp-01 and Exp-02 experiments will be assumed. Unlike the surfactant free Exp-01 experiment,  $1.5 \text{ PV}$  of surfactant solution was injected into the core in the Exp-02 experiment after water-flooding. The injection of surfactant did not recover additional oil. The features of the two experiments are discussed in detail here below.

#### 8.4.2.3. CT images

Figure 8.15 presents the CT images of the two experiments at corresponding times. In the Exp-01 experiment,  $\text{CO}_2$  was injected into a core without surfactant (after water-flooding) and in the Exp-02 experiment it was injected into a core, which was first flooded by surfactant solution. In both experiments  $\text{CO}_2$  was injected with a constant flowrate of  $1.0 \text{ ml/min}$  ( $\sim 1.2 \text{ m/day}$ ). The blue, red

and orange colors represent the gas, water  $S_w = 1$  and water-flood residual oil  $S_{or}$ , respectively. The green part constitutes the three phase region. The images reveal that when CO<sub>2</sub> is injected into the core initially saturated with the brine, there is no (clear) sharp interface between the gas and the brine. CO<sub>2</sub> forms channels through the brine and reaches OWC at a time between 0.04 and 0.09 PV. When CO<sub>2</sub> is injected into the core initially saturated with surfactant solution a clear interface between the moving gas and the liquid appears at the oil free part. Foaming of CO<sub>2</sub> increases the time at which CO<sub>2</sub> reaches the OWC. However, comparing the two sets of images, it seems that injection of surfactant does not have a significant effect on the CO<sub>2</sub> transfer through the oil-saturated part. In both experiments there is no clear interface between gas and liquid and the times required for CO<sub>2</sub> to travel from the OWC to the core outlet are comparable.

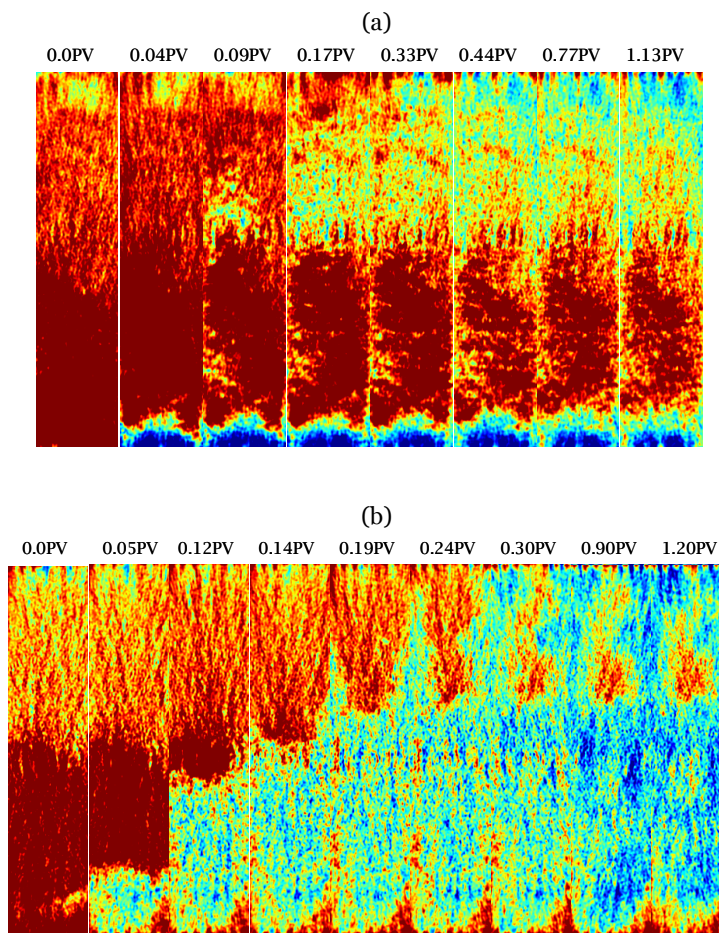


**Fig. 8.15:** CT images of (a) Exp-01 and (b) Exp-02 in a porous medium initially saturated with surfactant solution (red), gas (blue) and water-flood residual oil (orange) at  $P=90$  bar and  $T=50$  °C. The time of each image is shown in pore volumes of the injected gas. CO<sub>2</sub> is injected from the bottom.

#### 8.4.2.4. Pressure profiles

Figure 8.16 plots the measured pressure drops versus dimensionless time (PV) of the two experiments. The maximum in both curves corresponds to the gas breakthrough time. The breakthrough happens later in the Exp-02 experiment due to the foaming of CO<sub>2</sub> in the first half of the core. Moreover, Fig. 8.16 shows that injection of CO<sub>2</sub> into a core with surfactant (Exp-02 experiment) builds up a higher pressure, confirming the presence of foam. After CO<sub>2</sub> breakthrough there is no difference between the pressures of the two experiments, as the pressure curves overlap.

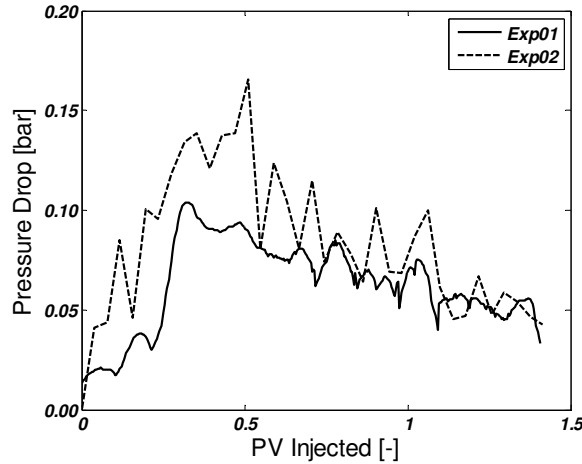


**Fig. 8.16:** Pressure drop across the entire core for the Exp-01 and the Exp-02 experiments.

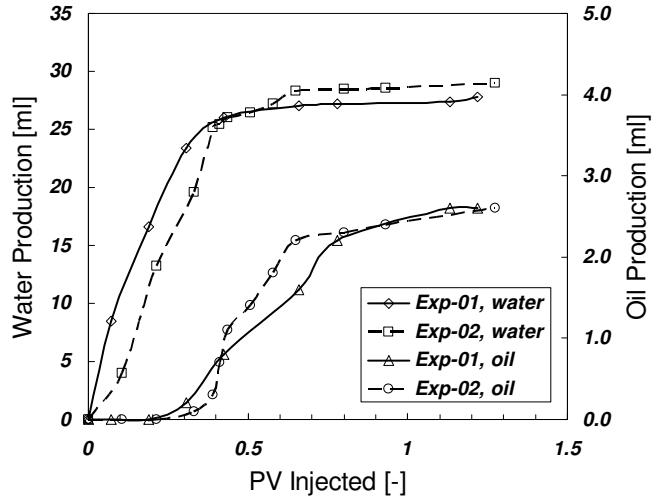
#### 8.4.2.5. Production profiles

Figure 8.17 presents the cumulative water and oil production of the two experiments. The small difference between the two water production curves can be attributed to the formation of foam. This slightly delays the water (and oil) production and more importantly sweeps more water from the first half of the core, which explains the slightly higher water production in the Exp-02 experiment. The results are consistent with the experiments of Chapter 7. The ultimate oil recoveries of the two experiments are also similar. Given the fact that the amount of oil in the Exp-01 experiment was lower than in the Exp-02 experiment prior to CO<sub>2</sub> injection, it can also be concluded that Exp-01 performs slightly better than Exp-02. However, this difference can be due to the fact that we used two different cores in our experiments.

It is possible to evaluate the CO<sub>2</sub> injection performance with the dimensionless Tertiary Recovery Factor (TRF) defined as

$$TRF = \frac{(Q_o / Q_{S_{orw}})}{PV_{g,inj}}, \quad (8.14)$$

where  $Q_o$  is the amount of produced oil,  $Q_{s_{oru}}$  is the amount of oil that is left in the porous medium after water-flooding and  $PV_{g,inj}$  is the cumulative pore volume of the gas injected. The definition is adapted from Ref. [33] and normalizes the recoveries for comparison purposes. Figure 8.18 shows the normalized oil production for two experiments. Once again there is little difference in the oil recovery of two experiments.



**Fig. 8.17:** Cumulative water and oil production of Exp-01 and Exp-02 vs. PV's of injected CO<sub>2</sub>

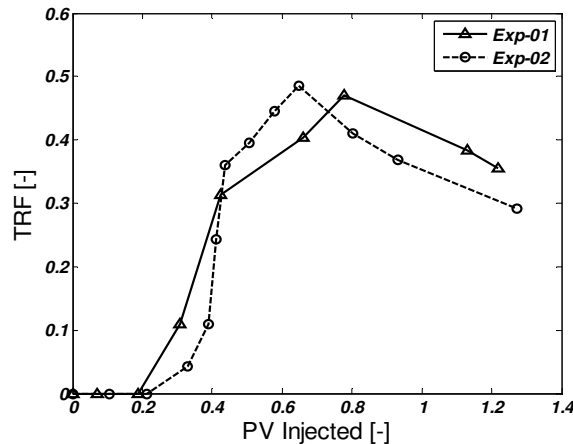


**Fig. 8.18:** Tertiary recovery factor of Exp-01 and Exp-02 calculated from Eq. (8.14) vs. PV's of injected CO<sub>2</sub>

## 8.5. CONCLUSIONS

We showed that, under gravity stable conditions and using AOS as surfactant and Isopar H as oil, injection of a foaming agent prior to CO<sub>2</sub> injection above its critical point does not produce extra oil compared with tertiary gas recovery. This is due to the fact that presence of oil does not allow formation of foam in the porous medium. Nevertheless, we observed that it is possible to reduce the mobility of sub- and super-critical CO<sub>2</sub> when there is no oil present. Moreover, we found that

N<sub>2</sub> can form weak foam zone in the presence of oil, ahead of which an oil bank moves towards the outlet of the porous medium. In this case, foaming of the gas enhances the oil recovery compared to gas injection.

On a reservoir scale, injection of surfactant followed by CO<sub>2</sub> injection (SAG or Foam) reduces the gas mobility in the regions where the oil saturation is very low. The reduction of gas mobility and blocking of the high permeable streaks will result in diversion of a portion of the injected gas into regions with higher oil saturation. Consequently, as more CO<sub>2</sub> contacts the oil in porous media and the pressure increases, extra oil will be produced by foaming CO<sub>2</sub>. Therefore, foam will considerably improve CO<sub>2</sub> utilization efficiency by reducing the amount of CO<sub>2</sub> required per unit of oil produced. Furthermore, delayed gas breakthrough and moderate gas production (lower gas to oil ratio) in the production wells will diminish the costs and problems associated with CO<sub>2</sub> handling. In conclusion, similar to steam foam, foaming of CO<sub>2</sub> can improve the ongoing (CO<sub>2</sub>)-EOR process and cannot be considered as a separate EOR process.

## 8.6. REFERENCES

1. G.G. Bernards and L.W. Holm, *SPE Journal*, September 1964, pp 267-274.
2. A.H. Falls, J.J. Musters, J. Ratulowski, SPE 16048, August 1986.
3. G.J. Hirasaki and J.B. Lawson, *SPE Journal*, April 1985, pp 175-190.
4. W.R. Rossen, *Foams in Enhanced Oil Recovery*, In: *Foams: Theory Measurement and Applications*, R.K. Prud'homme and S. Khan (Eds), Marcel Dekker, New York City (1996).
5. A.R. Kovsky and C.J. Radke, Fundamentals of foam transport in porous media, In: *Foams: Fundamentals and applications in the Petroleum Industry*, ACS Advances in Chemistry Series, N.242, American Society (1994).
6. S.L. Wellington and H.J. Vinegar, *Surfactant-Induced Mobility Control for Carbon Dioxide Studied with Computerized Tomography*. In: *Surfactant Based Mobility Control – Progress in Miscible Flood Enhanced Oil Recovery*; Smith, D.H., Eds.; ACS Symposium Series 373; American Chemical Society: Washington, 1988; pp.344-358.
7. J. Israelachvili, *Intermolecular and Surface Forces*, Academic Press: London, 1991.
8. A.S. Aronson, V. Bergeron, M.E. Fagan, C.J. Radke, *Colloids Surf. A*, 83 (1994) 109.
9. K.G. Kornev, A.V. Niemark, A.N. Rozhkov, *Adv. Colloid Interf. Sci.*, 82 (1999) 127.
10. R. Aveyard, B.P. Binks, P.D.I. Fletcher, T.G. Peck, C.E. Rucherford, *Adv. in Colloid Interf. Sci.*, 48 (1994) 93.
11. N.D. Denkov, *Langmuir*, 15 (1999) 8530.
12. V. Bergeron, M.E. Fagan, C.J. Radke, *Langmuir*, 9 (1993) 1704.
13. L.L. Schramm, *Chapter 4: Foam sensitivity to crude oil in porous media*, in: *Foams: Fundamentals and Applications in the Petroleum Industry*, L.L. Schramm, Editor, American Chemical Society, Washington D.C. (1994) 165-197.
14. P.R. Garrett, *The mode of action of antifoams*, in: *Defoaming: theory and industrial applications*: Ed.: P.R. Garrett, Marcel Dekker, New York, (1993) 1-117.
15. W.D. Harkins and A. Feldman, *J. American Chemical Society*, 44 (1922) 2665.
16. S. Ross, *J. Physical and Colloid Chemistry*, 54 (1950) 429.
17. A.D. Nikolov, D.T. Wasan, D.W. Huang, D.A. Edwards, *SPE 15443* (1986).

18. T. Meling and J.E. Hanssen, *Progress in Colloid and Polymer Science*, 82 (1990) 140.
19. M. Dalland, J.E. Hanssen, T.S. Kristiansen, *Colloids and Surfaces A*, 82 (1994) 129.
20. L. Lobo and D.T. Wasan, *Langmuir*, 9 (1993) 1668.
21. Z.I. Khatib, G.J. Hirasaki, A.H. Falls, *SPE Reservoir Eng.*, 3(3), (1988) 919.
22. N.D. Denkov, *Langmuir*, 20 (22), (2004) 9463.
23. E.S. Basheva, D. Ganchev, N.D. Denkov, K. Kasuga, N. Satoh, K. Tsujii, *Langmuir*, 16 (2000) 1000.
24. T.J. Myers and C.J. Radke, *Ind. Eng. Chem. Res.*, 39 (2000) 2725.
25. G.C. Frye and J.C. Berg, *J. Colloid Interf. Sci.*, 127 (1989) 222.
26. P.R. Garrett, *J. Colloid Interf. Sci.*, 69 (1979) 107.
27. T.J. Myers, *The role of residual oil in the mechanistic simulation of foam flow in porous media: Experiment and simulation with the population balance method*, PhD Dissertation, University of California, Berkeley, USA, 1999.
28. L.L. Schramm and J.J. Novosad, *Colloids and Surfaces*, 46 (1990) 21.
29. L.L. Schramm and J.J. Novosad, *J. Petroleum Science and Engineering*, 7 (1992) 77.
30. K. Mannhardt, J.J. Novosad, L.L. Schramm, *SPE Reservoir Eval. & Eng.*, Vol. 3, No. 1, February 2000.
31. M. Dalland, J.E. Hanssen, T.S. Kristiansen, *Colloids Surf. A.*, 82 (1994) 129.
32. Q. Ngyuen, *Dynamics of foam flow in porous media*, PhD Dissertation, Delft University of Technology, The Netherlands, 2004.
33. M. M. Kulkarni and D.N. Rao, *J. Petrol. Sci. Eng.*, 48 (2005) 1.



---

# Chapter 9

## SUMMARY & CONCLUSIONS

---

The results of this thesis give insight into the (mass)-transfer during flow of gases, especially CO<sub>2</sub>, in various gas-liquid systems. A number of experiments was performed to investigate the transport phenomena through interfaces with and without surfactant monolayers. The observed phenomena have been incorporated into physical models to predict the fate of CO<sub>2</sub> overlaying a *bulk liquid* or *liquid saturated porous media*. Moreover, dynamics of (CO<sub>2</sub>)-foam flow in oil-free and oil-saturated porous media was studied using X-ray tomography. These results are applicable in CO<sub>2</sub> sequestration and CO<sub>2</sub> EOR projects. Sections 9.1 to 9.3 summarize the main results of this thesis.

### **9.1. PART I: MASS TRANSFER ASPECTS OF CO<sub>2</sub> SEQUESTRATION**

The mass transfer of CO<sub>2</sub> into liquids was studied in a PVT cell, following the pressure history of a gas phase overlaying a liquid column. It was found that the transfer rate of CO<sub>2</sub> into water is significantly higher than predicted from diffusion based models. By extending the experimental time to a few days we showed that the transfer rate decreases over time and it is not possible to model the experiments employing Fick's law with a single (effective)-diffusion coefficient. The short-time and long-time limits of the experiments could be modeled asymptotically to obtain two effective diffusion coefficients. These coefficients are fitting parameters with no physical meaning. The measured effective diffusion coefficients for the short times were two orders of magnitude larger than the molecular diffusivity whereas long-time diffusion coefficients agree with the molecular diffusivity of CO<sub>2</sub> in water. It was suggested that at the early stages of the experiments density-driven natural convection enhances the mass transfer of CO<sub>2</sub> into water. The results of experiments show that the addition of SDS to water has no measurable effect on the transfer rate at our experimental conditions. A similar mass transfer enhancement was observed for the mass transfer between a gaseous CO<sub>2</sub> rich phase with two hydrocarbons (n-decane and n-hexadecane). The effect is less significant for n-hexadecane due to its higher viscosity.

To fully explain the measured pressure trend, a physical model based on density-driven natural convection and diffusion was formulated. The model uses a number of simplifying assumptions, e.g., that Henry's law is applicable at the interface. Simulation results show that the convective velocity increases until it reaches a maximum and then diminishes gradually as natural convection effects become less important. The maximum velocity corresponds to the time in which the CO<sub>2</sub> front reaches the bottom of the vessel. There is a strong correlation between the fluid velocity and the concentration profile with the experimental pressure decline rates. The measured and theoretically predicted pressure decline in the gas phase agree within experimental error.

Using the knowledge obtained from *bulk liquid* experiments, we demonstrated the importance of natural convection in the rate of CO<sub>2</sub> storage in aquifers. Initially the CO<sub>2</sub> front moves proportional to the square root of time (diffusion behavior) for different Rayleigh numbers and then the relationship becomes linear (convection behavior). The time, in which the switching happens, decreases with increasing Rayleigh number. The occurrence of natural convection accelerates the rate of CO<sub>2</sub> dissolution. The simulation results show that the non-linear behavior of the flow is strongly dependent on the Rayleigh number. However, as time elapses the number of the fingers decreases due to the decreasing effect of natural convection, similar to the experimental results. This effect can also be observed from the decreasing values of the stream function.

## 9.2. PART II: FOAM FILMS

The mass transfer of gases through foam films is an intriguing problem as two surfactant monolayers interact with each other through surface forces. We chose an Alpha Olefin Sulfonate (AOS) surfactant to investigate the effect of different parameters on the transfer rate of gas through foam films. Prior to these experiments, basic properties of AOS solutions and foam films made from those solutions were studied. We showed that, except for salt free solutions, the addition of salt (NaCl) does not change the adsorption at gas-liquid interface of bulk solutions  $\Gamma_s$ , calculated from surface tension measurements. The thickness of the films remains constant for a concentration range of  $c_{AOS} > 0.003 \text{ wt\%}$  at a fixed salt concentration of  $c_{NaCl} = 0.50 \text{ M}$ . However, the film thickness decreases with addition of NaCl due to the screening of the repulsive forces.

The film permeability coefficient,  $k$ , depends on the permeability and thickness of the film aqueous core and the permeability of the surfactant monolayers. We observed that  $k$  increases as the film thickness decreases until a certain value and sharply decreases afterwards. We conclude that beyond that critical point the film permeability is governed by the monolayer permeability, i.e., the adsorption density of the surfactant monolayers, and hence, the decrease of  $k$  after this

point can be explained by decreased permeability of the monolayers. The film permeability showed an unexpected increase at high surfactant concentrations well above the CMC. We hypothesize that this is a result of faster gas transport via the aqueous film core facilitated by the micelles. Experiments at different temperatures allowed the energy of the permeability process to be estimated using the simple energy barrier theory.

### 9.3. PART III: FOAM IN POROUS MEDIA

The foaming behavior of CO<sub>2</sub> and N<sub>2</sub> were compared in natural sandstone cores by means of a CT scanner (X-ray) in the absence and presence of oil. It has been shown that injection of a slug of surfactant prior to CO<sub>2</sub> injection can reduce the CO<sub>2</sub> mobility, below and above its critical point, when there is no oil present in the medium. In the oil-free porous media, foaming of CO<sub>2</sub> builds up a lower pressure drop over the core at both low and high pressures compared to N<sub>2</sub>. Both gases require a certain penetration depth to develop into foam. The penetration depth is longer for N<sub>2</sub> (large entrance effect) and increases with increasing gas velocity. The CT images and calculated water saturation profiles reveal that N<sub>2</sub> foam displaces the liquid in a front-like manner (sharp-vertical interface) while the propagation front for CO<sub>2</sub> foam is somewhat smeared out at low pressure. Moreover, the ultimate production of N<sub>2</sub> foam is always higher than CO<sub>2</sub> foam. The observed differences in the foaming behavior of the two gases can be related to the differences in their nature, mainly solubility in water, interfacial tensions, pH effects and the possible wettability effects. From these various factors solubility is most likely the most critical one.

At low pressure experiments ( $P=1\text{ bar}$ ) injection of N<sub>2</sub> after surfactant forms a weak foam when the porous medium is partially saturated with oil. As a result, an oil bank is formed ahead of the foam front and results in additional oil recovery compared to N<sub>2</sub> injection alone. CO<sub>2</sub> injection, with the same flowrate, does not foam in the core. Above its critical point ( $P=90\text{ bar}$ ), no difference was observed between CO<sub>2</sub> injection and CO<sub>2</sub> foam in terms of recovery and pressure drop over the core. Our experimental results show that injection of surfactant prior to CO<sub>2</sub> injection can improve the ongoing CO<sub>2</sub>-EOR by reducing the gas mobility in the thief zones and diverting CO<sub>2</sub> into regions with higher oil saturation. However, it is less likely that CO<sub>2</sub> foam itself produces oil from the reservoir.

### 9.4. IMPLICATIONS FOR EOR

The work described here has the following implications for CO<sub>2</sub> storage and CO<sub>2</sub> EOR.

- Natural convection effects are favorable for recovery of hydrocarbons because the mixing zone between CO<sub>2</sub> gas and the oil becomes longer, which improves the vertical sweep efficiency and the Buckley-Leverett displacement efficiency.

- 
- Permeation of gas through foam films is a strong function of salinity of the water and plays an important role in the efficiency of foam application in Petroleum Engineering.
  - Nature of the injected gas plays an important role in the efficiency of foam displacement.
  - Foaming of CO<sub>2</sub> above its critical point does not affect the oil recovery.
  - Foaming of CO<sub>2</sub> can improve the oil recovery by improving the CO<sub>2</sub> utilization efficiency, i.e., by reducing the gas mobility in the high permeable zones of the reservoir and diverting it into regions with higher oil saturation.

---

# Appendix A

## Solution of Fick's Law with a Time-Dependent Boundary Condition

---

### A.1. Physical Model

The molar flux of a gas into a liquid can be expressed by Fick's law as

$$\frac{\partial c}{\partial t} = D \frac{\partial^2 c}{\partial z^2} \quad , \quad (\text{A.1})$$

where,  $D$  is the effective diffusion coefficient of gas and  $c$  is the concentration of gas in the liquid phase. Initially there is no gas in the liquid, i.e.

$$c(z, 0) = 0 \quad , \quad (\text{A.2})$$

**B.C.1:** No-flow boundary condition can be used which means that there is no flow at the end of the liquid column,  $z = L_2$  which mathematically means:

$$\left. \frac{\partial c}{\partial z} \right|_{z=L_2} = 0 \quad . \quad (\text{A.3})$$

However, due to the fact that the diffusion process is slow and the liquid column is large, one can assume that the concentration of the gas is zero at the end of the tube ( $z \rightarrow \infty$ ). This will simplify the solution of the diffusion equation into the liquid bulk.

**B.C.2.:** One part of the changes of the total moles of the gas in the system is due to the diffusion into the liquid bulk and assuming an ideal gas behavior for the gas at the experimental pressure the mass flux of the gas at the interface can be written as:

$$\left. \frac{dn_g}{dt} \right|_{z=0} = \frac{V}{ZRT} \left. \frac{dP_g}{dt} \right|_{z=0} = -DS \left. \frac{\partial c}{\partial z} \right|_{z=0} \quad , \quad (\text{A.4})$$

where  $V$  and  $S$  are the gas volume and the cross-sectional area of the cell respectively and  $R$  is the universal gas constant.  $V$  is also assumed to be constant (fixed boundary).

The gas pressure also can be related to its concentration by assuming instantaneous thermodynamic equilibrium at the interface using Henry's law which states that the pressure of a gas above a solution is proportional to its mole fraction (concentration) in the solution, i.e.,

$$P_g(t) = kx(t) = k_H c(t) \quad (\text{A.5})$$

where  $x(t)$  is the mole fraction of the gas and  $k_H$  is taken as Henry's law proportionality constant. By substituting Henry's law for the gas pressure in Eq. (A.3) we will obtain

$$-DS \left. \frac{\partial c}{\partial z} \right|_{z=0} = \frac{Vk_H}{ZRT} \left. \frac{\partial c}{\partial t} \right|_{z=0} \quad (\text{A.6})$$

### A.2. Solution by Laplace Transform method

Equation (A.1) has a time dependent boundary condition and can be solved by Laplace transform method. Laplace form of Eq. (A.1) is

$$\frac{\partial^2 \bar{C}}{\partial z^2} - \frac{s}{D} \bar{C} = 0, \quad (\text{A.7})$$

which has the general solution of

$$\bar{C}(s) = A(s) \exp\left(\sqrt{\frac{s}{D}} z\right) + B(s) \exp\left(-\sqrt{\frac{s}{D}} z\right). \quad (\text{A.8})$$

This leads to

$$\frac{\partial \bar{C}}{\partial z} = A(s) \sqrt{\frac{s}{D}} \exp\left(\sqrt{\frac{s}{D}} z\right) - B(s) \sqrt{\frac{s}{D}} \exp\left(-\sqrt{\frac{s}{D}} z\right). \quad (\text{A.9})$$

From Eq. (A.3) we can write

$$\left. \frac{\partial \bar{C}}{\partial z} \right|_{z=L_2} = A(s) \sqrt{\frac{s}{D}} \exp\left(\sqrt{\frac{s}{D}} L_2\right) - B(s) \sqrt{\frac{s}{D}} \exp\left(-\sqrt{\frac{s}{D}} L_2\right) = 0,$$

Thus,

$$B(s) = A(s) \exp\left(2L_2\sqrt{\frac{s}{D}}\right). \quad (\text{A.10})$$

From Eq. (A.6) it follows

$$-D \frac{\partial \bar{C}}{\partial z} \Big|_{z=0} = \frac{L_1 k_H}{ZRT} \left( s \bar{C}(s) - \frac{P_i}{k_H} \right) \Big|_{z=0}, \quad (\text{A.3})$$

Using Eq. (A.9) we write

$$\sqrt{\frac{s}{D}} (A(s) - B(s)) = \frac{L_1 k_H}{ZDRT} \left( s(A(s) + B(s)) - \frac{P_i}{k_H} \right) \Big|_{z=0}, \quad (\text{A.4})$$

Substituting  $B(s)$  from Eq. (A.10) leads to

$$\begin{aligned} \sqrt{\frac{s}{D}} A(s) \left( 1 - \exp\left(2L_2\sqrt{\frac{s}{D}}\right) \right) &= \frac{L_1 k_H}{ZDRT} \left( s A(s) \left( 1 + \exp\left(2L_2\sqrt{\frac{s}{D}}\right) \right) - \frac{P_i}{k_H} \right), \\ \left[ \sqrt{\frac{s}{D}} \left( 1 - \exp\left(2L_2\sqrt{\frac{s}{D}}\right) \right) - \frac{s L_1 k_H}{ZDRT} \left( 1 + \exp\left(2L_2\sqrt{\frac{s}{D}}\right) \right) \right] A(s) &= -\frac{L_1 P_i}{ZDRT}, \end{aligned}$$

Therefore,

$$A(s) = \frac{1}{s \frac{k_H}{P_i} \left( 1 + \exp\left(2L_2\sqrt{\frac{s}{D}}\right) \right) - \frac{DZRT}{P_i L_1} \sqrt{\frac{s}{D}} \left( 1 - \exp\left(2L_2\sqrt{\frac{s}{D}}\right) \right)}. \quad (\text{A.13})$$

We define,

$$k_1(s) = \exp\left(2L_2\sqrt{\frac{s}{D}}\right) \quad (\text{A.14})$$

$$\xi = \frac{ZRT\sqrt{D}}{P_i L_1} \quad (\text{A.15})$$

$$\varsigma = \frac{k_H}{P_i} \quad (\text{A.16})$$

Therefore we can re-write

$$A(s) = \frac{1}{\zeta s(1+k_1(s)) - \xi\sqrt{s}(1-k_1(s))}, \quad (\text{A.17})$$

$$B(s) = \frac{k_1(s)}{\zeta s(1+k_1(s)) - \xi\sqrt{s}(1-k_1(s))}, \quad (\text{A.18})$$

$$\bar{C}(s) = \frac{1}{\zeta s(1+k_1(s)) - \xi\sqrt{s}(1-k_1(s))} \left[ \exp\left(\sqrt{\frac{s}{D}}z\right) + k_1(s) \exp\left(-\sqrt{\frac{s}{D}}z\right) \right]. \quad (\text{A.19})$$

### A.3. Mass Balance in the boundary

From Eq. (A.4) we can obtain:

$$\frac{V}{ZRT}(s\bar{P}_g - P_i) = -DS\sqrt{\frac{s}{D}}[A(s) - B(s)] \quad (\text{A.20})$$

$$s\bar{P}_g - P_i = -\frac{ZRT\sqrt{D}}{L_1} \frac{\sqrt{s}[1-k_1(s)]}{\zeta s(1+k_1(s)) - \xi\sqrt{s}(1-k_1(s))} \quad (\text{A.21})$$

Therefore;

$$\bar{P}_g = \frac{P_i}{s} - \frac{ZRT\sqrt{D}}{L_1} \frac{1-k_1(s)}{\zeta s^{\frac{3}{2}}(1+k_1(s)) - \xi s(1-k_1(s))} \quad (\text{A.22})$$

or,

$$\frac{\bar{P}_g(s)}{P_i} = \frac{1}{s} - \frac{1-k_1(s)}{\frac{1}{\chi} s^{\frac{3}{2}}(1+k_1(s)) - s(1-k_1(s))} \quad (\text{A.23})$$

and finally,

$$\frac{\bar{P}_g(s)}{P_i} = \frac{1}{s} - \frac{1}{\chi^{-1}s^{3/2} - s} \quad (\text{A.24})$$

where

$$\chi = \frac{ZRT\sqrt{D}}{L_1 k_H}. \quad (\text{A.25})$$

### A.4. Inverse Laplace of Eq. (A.24)

The gas pressure as a function of time can be found by Laplace inversion of Eq. (A.24), i.e.,

$$\begin{aligned}
L^{-1}[\bar{P}_g(s)] &= P_i \left[ L^{-1}(1/s) - L^{-1}\left(\frac{1}{\chi^{-1}s^{3/2} - s}\right) \right] \\
P_g(t) &= P_i \left[ 1 - L^{-1}\left(\frac{\chi}{s^{3/2} - \chi s}\right) \right]
\end{aligned} \tag{A.26}$$

In these equations  $L^{-1}$  is the inverse Laplace operator. In the following we obtain the Laplace transform of the second term in Eq. (A.26).

$$\frac{\chi}{s(s^{1/2} - \chi)} = \frac{A}{s} + \frac{B\chi}{s^{1/2} - \chi} = \frac{A(s^{1/2} - \chi) + B\chi s}{s(s^{1/2} - \chi)} = \frac{(As^{-1/2} + B\chi)s - A\chi}{s(s^{1/2} - \chi)}$$

This gives:  $A = -1$ ,  $B = \chi^{-1}s^{-1/2}$ . Thus one can write

$$\begin{aligned}
L^{-1}\left(\frac{\chi}{s^{3/2} - \chi s}\right) &= L^{-1}\left(\frac{-1}{s} + \frac{1}{s - \chi s^{1/2}}\right) \\
L^{-1}\left(\frac{\chi}{s^{3/2} - \chi s}\right) &= -1 + L^{-1}\left(\frac{1}{s + (\chi^2 s)^{1/2}}\right) = -1 + \exp(\chi^2 t) \operatorname{erfc}(-\chi t^{1/2})
\end{aligned} \tag{A.27}$$

where, we applied the following rule:

$$L^{-1}\left(\frac{1}{s + \sqrt{as}}\right) = \exp(at) \operatorname{erfc}(\sqrt{at}) \tag{A.28}$$

From Eqs. (A.26) and (A.27) an expression is obtained for gas pressure:

$$P_g(t) = P_i \left[ 2 - \exp(\chi^2 t) \operatorname{erfc}(-\chi \sqrt{t}) \right] \tag{A.29}$$



---

# Appendix B

## Formulation and Numerical Scheme of Natural Convection in Porous Media

---

### B.1. Model Equations

For the 2-D porous medium depicted in Fig. B.1, the governing equations can be written as

(a) *Continuity Equation*

$$\varphi \frac{\partial \rho}{\partial t} + \frac{\partial(\rho U_x)}{\partial X} + \frac{\partial(\rho U_z)}{\partial Z} = 0 \quad , \quad (\text{B.1})$$

(b) *Darcy's law*

$$U_x = -\frac{k_h}{\mu} \frac{\partial p}{\partial X} \quad , \quad (\text{B.2})$$

$$U_z = -\frac{k_v}{\mu} \left( \frac{\partial p}{\partial Z} - \rho g \right) \quad , \quad (\text{B.3})$$

(c) *Concentration*

$$\frac{\varphi \partial c'}{\partial t} + U_x \frac{\partial c'}{\partial X} + U_z \frac{\partial c'}{\partial Z} = \varphi D \left( \frac{\partial^2 c'}{\partial X^2} + \frac{\partial^2 c'}{\partial Z^2} \right) \quad . \quad (\text{B.4})$$

The fluid becomes denser when CO<sub>2</sub> is present at the top part of the porous medium. We assume that the liquid density changes linearly with the increasing CO<sub>2</sub> concentration, i.e.,

$$\rho = \rho_0 (1 + \beta_c (c' - c'_0)) \quad , \quad (\text{B.5})$$

from which we obtain

$$\frac{\partial \rho}{\partial X} = \rho_0 \beta_c \frac{\partial c'}{\partial X} \quad . \quad (\text{B.6})$$

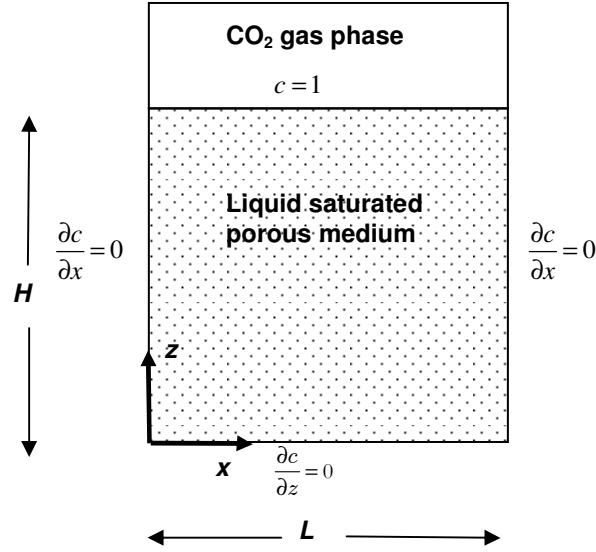


**Fig. B.1.:** Geometry of the system

Cross-differentiating Eqs. (B.2) and (B.3), Eq. (B.2) with respect to  $Z$  and Eq. (B.3) with respect to  $X$ :

$$\frac{\partial U_x}{\partial Z} = -\frac{k_h}{\mu} \frac{\partial^2 p}{\partial X \partial Z} \quad (\text{B.7})$$

$$\frac{\partial U_z}{\partial X} = -\frac{k_v}{\mu} \left( \frac{\partial^2 p}{\partial Z \partial X} - \frac{\partial \rho}{\partial X} g \right) = -\frac{k_v}{\mu} \frac{\partial^2 p}{\partial Z \partial X} + \frac{k_v g \rho_0 \beta_c}{\mu} \frac{\partial c'}{\partial X} \quad (\text{B.8})$$

Subtracting Eq. (B.8) from Eq. (B.7) and re-arranging the result will omit the pressure term:

$$\frac{\partial U_z}{\partial X} - \frac{\partial U_x}{\partial Z} = \frac{k g \rho_0 \beta_c}{\mu} \frac{\partial c'}{\partial X} \quad (\text{B.9})$$

It is assumed that the porous medium is isotropic with a single permeability of  $k$  and the height and length of the medium are equal, i.e.,  $L=H$ . Therefore, the equations to be solved are Eqs. (B.1), (B.4) and (B.9) to obtain  $U_x$ ,  $U_z$  and  $c'$ .

## B.2. Dimensionless form of the equations

We take  $H$  as characteristic length and define the following dimensionless variables

$$\begin{aligned}
 x &= \frac{X}{H}, \quad z = \frac{Z}{H}, \quad u_x = \frac{H}{\varphi D} U_X, \quad u_z = \frac{H}{\varphi D} U_Z, \quad \tau = \frac{D}{H^2} t, \quad c = \frac{c' - c'_i}{c'_0 - c'_i} \\
 u_x &= -\frac{\partial \psi}{\partial z}, \quad u_z = \frac{\partial \psi}{\partial x}, \quad \text{Ra} = \frac{k\rho_0\beta g H \Delta c'}{\varphi D \mu} = \frac{\Delta \rho g k H}{\varphi D \mu}
 \end{aligned} \tag{B.10}$$

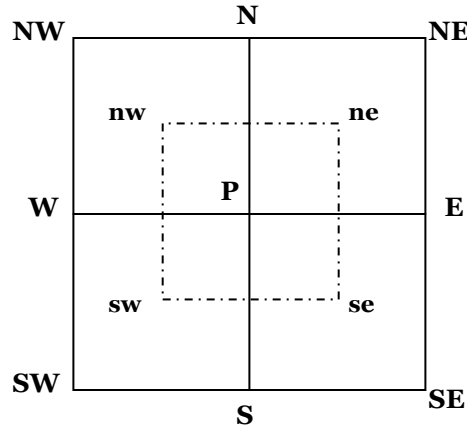
Thus, after applying the Boussinesq approximation the dimensionless form of the equations can be written as

$$\frac{\partial^2 \psi}{\partial x^2} + \frac{\partial^2 \psi}{\partial z^2} = \text{Ra} \frac{\partial c}{\partial x}, \tag{B.11}$$

$$\frac{\partial c}{\partial \tau} + \frac{\partial \psi}{\partial z} \frac{\partial c}{\partial x} - \frac{\partial \psi}{\partial x} \frac{\partial c}{\partial z} = \frac{\partial^2 c}{\partial x^2} + \frac{\partial^2 c}{\partial z^2}. \tag{B.12}$$

### B.3. Numerical Solution of the equations

The system of equations is solved by Finite Volume Method following the approach of Guçeri and Farouq.



#### B.3.1. Computation of the stream function from Eq. (B.11):

$$\int_{z_{sb}}^{z_{nb}} \int_{x_{wb}}^{x_{eb}} \left[ \frac{\partial}{\partial x} \left( \frac{\partial \psi}{\partial x} \right) + \frac{\partial}{\partial z} \left( \frac{\partial \psi}{\partial z} \right) \right] dx dz = \text{Ra} \int_{z_{sb}}^{z_{nb}} \int_{x_{wb}}^{x_{eb}} \frac{\partial c}{\partial x} dx dz \tag{B.13}$$

First term:

$$\int_{z_{sb}}^{z_{nb}} \int_{x_{wb}}^{x_{eb}} \left[ \frac{\partial}{\partial x} \left( \frac{\partial \psi}{\partial x} \right) \right] dx dz = \int_{z_{sb}}^{z_{nb}} \left( \frac{\partial \psi}{\partial x} \right)_{x_{wb}}^{x_{eb}} dz = \left( \frac{\partial \psi}{\partial x} \right)_{wb}^{eb} \Delta z = \left[ \frac{(\psi_E - \psi_P)}{\Delta x} - \frac{(\psi_P - \psi_W)}{\Delta x} \right] \Delta z \quad (\text{B.14})$$

$$= (\psi_E - 2\psi_P + \psi_W) \frac{\Delta z}{\Delta x}$$

*Second term:*

$$\int_{z_{sb}}^{z_{nb}} \int_{x_{wb}}^{x_{eb}} \left[ \frac{\partial}{\partial z} \left( \frac{\partial \psi}{\partial z} \right) \right] dx dz = \int_{x_{wb}}^{x_{eb}} \left( \frac{\partial \psi}{\partial z} \right)_{z_{sb}}^{z_{nb}} dx = \left( \frac{\partial \psi}{\partial z} \right)_{z_{sb}}^{z_{nb}} \Delta x = \left[ \frac{(\psi_N - \psi_P)}{\Delta z} - \frac{(\psi_P - \psi_S)}{\Delta z} \right] \Delta x \quad (\text{B.15})$$

$$= (\psi_N - 2\psi_P + \psi_S) \frac{\Delta x}{\Delta z}$$

*Third term:*

$$\text{Ra} \int_{z_{sb}}^{z_{nb}} \int_{x_{wb}}^{x_{eb}} \frac{\partial c}{\partial x} dx dz = \text{Ra} \frac{(c_E - c_W)}{2} \Delta z \quad (\text{B.16})$$

Replacing Eqs. (B.14)-(B.16) in Eq. (B.13) provides the following equation to calculate the stream function:

$$(\psi_E - 2\psi_P + \psi_W) \frac{\Delta z}{\Delta x} + (\psi_N - 2\psi_P + \psi_S) \frac{\Delta x}{\Delta z} = \text{Ra} \frac{(c_E - c_W)}{2} \Delta z$$

$$\psi_P = \frac{(\psi_E + \psi_W) \frac{\Delta z}{\Delta x} + (\psi_N + \psi_S) \frac{\Delta x}{\Delta z} + \text{Ra} (c_E - c_W) \frac{\Delta z}{2}}{2 \left( \frac{\Delta z}{\Delta x} + \frac{\Delta x}{\Delta z} \right)} \quad (\text{B.17})$$

### B.3.2. Calculation of concentration from Eq. (B.12):

*Accumulation term:*

$$\int_{z_{sb}}^{z_{nb}} \int_{x_{wb}}^{x_{eb}} \frac{\partial c}{\partial \tau} dx dz = \Delta x \Delta z \frac{\Delta c}{\Delta \tau} \quad (\text{B.18})$$

*Diffusion Term:*

$$\int_{z_{sb}}^{z_{nb}} \int_{x_{wb}}^{x_{eb}} \left[ \frac{\partial}{\partial x} \left( \frac{\partial c}{\partial x} \right) + \frac{\partial}{\partial z} \left( \frac{\partial c}{\partial z} \right) \right] dx dz = (c_E - 2c_P + c_W) \frac{\Delta z}{\Delta x} + (c_N - 2c_P + c_S) \frac{\Delta x}{\Delta z} \quad (\text{B.19})$$

Convection term:

$$\int_{z_S}^{z_N} \int_{x_W}^{x_E} \left[ \frac{\partial \psi}{\partial z} \frac{\partial c}{\partial x} - \frac{\partial \psi}{\partial x} \frac{\partial c}{\partial z} \right] dx dz =$$

First term of the convection part:

$$\int_{z_S}^{z_N} \int_{x_W}^{x_E} \left( \frac{\partial c}{\partial x} \frac{\partial \psi}{\partial z} \right) dx dz = \int_{z_S}^{z_N} \left( c \frac{\partial \psi}{\partial z} \right)_W^E dz = \int_{z_S}^{z_N} \left[ \left( c \frac{\partial \psi}{\partial z} \right)_E - \left( c \frac{\partial \psi}{\partial z} \right)_W \right] dz$$

$$\begin{aligned} \left( c \frac{\partial \psi}{\partial z} \right)_E \Delta z &= c_P (\psi_{ne} - \psi_{se}) = \\ &c_E \left( \frac{\psi_{ne} - \psi_{se} - |\psi_{ne} - \psi_{se}|}{2} \right) + c_P \left( \frac{\psi_{ne} - \psi_{se} + |\psi_{ne} - \psi_{se}|}{2} \right) \\ &c_E \left( \frac{\psi_{NE} + \psi_N - \psi_{SE} - \psi_S - |\psi_{NE} + \psi_N - \psi_{SE} - \psi_S|}{8} \right) + \\ &c_P \left( \frac{\psi_{NE} + \psi_N - \psi_{SE} - \psi_S + |\psi_{NE} + \psi_N - \psi_{SE} - \psi_S|}{8} \right) = \\ &c_P \left( \frac{\psi_{NE} + \psi_N - \psi_{SE} - \psi_S + |\psi_{NE} + \psi_N - \psi_{SE} - \psi_S|}{8} \right) - \\ &c_E \left( \frac{\psi_{SE} + \psi_S - \psi_{NE} - \psi_N + |\psi_{SE} + \psi_S - \psi_{NE} - \psi_N|}{8} \right) \end{aligned}$$

$$\left( c \frac{\partial \psi}{\partial z} \right)_E \Delta z = A_{EP} c_E - A_E c_P \quad (\text{B.20})$$

With a similar procedure:

$$\left( c \frac{\partial \psi}{\partial z} \right)_W \Delta z = A_{WP} c_W - A_W c_P \quad (\text{B.21})$$

$$\left( c \frac{\partial \psi}{\partial x} \right)_N \Delta x = A_{NP} c_N - A_N c_P \quad (\text{B.22})$$

$$\left( c \frac{\partial \psi}{\partial x} \right)_S \Delta x = A_{SP} c_S - A_S c_P \quad (\text{B.23})$$

$$\begin{aligned}
A_E &= \frac{\psi_{NE} + \psi_N - \psi_{SE} - \psi_S + |\psi_{NE} + \psi_N - \psi_{SE} - \psi_S|}{8} \\
A_{EP} &= \frac{\psi_{SE} + \psi_S - \psi_{NE} - \psi_N + |\psi_{SE} + \psi_S - \psi_{NE} - \psi_N|}{8} \\
A_W &= \frac{\psi_{SW} + \psi_S - \psi_{NW} - \psi_N + |\psi_{SW} + \psi_S - \psi_{NW} - \psi_N|}{8} \\
A_{WP} &= \frac{\psi_{NW} + \psi_N - \psi_{SW} - \psi_S + |\psi_{NW} + \psi_N - \psi_{SW} - \psi_S|}{8} \\
A_N &= \frac{\psi_{NW} + \psi_W - \psi_{NE} - \psi_E + |\psi_{NW} + \psi_W - \psi_{NE} - \psi_E|}{8} \\
A_{NP} &= \frac{\psi_{NE} + \psi_E - \psi_{NW} - \psi_W + |\psi_{NE} + \psi_E - \psi_{NW} - \psi_W|}{8} \\
A_S &= \frac{\psi_{SE} + \psi_E - \psi_{SW} - \psi_W + |\psi_{SE} + \psi_E - \psi_{SW} - \psi_W|}{8} \\
A_{SP} &= \frac{\psi_{SW} + \psi_W - \psi_{SE} - \psi_E + |\psi_{SW} + \psi_W - \psi_{SE} - \psi_E|}{8}
\end{aligned}$$

Collecting convective terms:

$$I_{conv} = (A_E + A_W + A_N + A_S)c_P - A_{EP}c_E - A_{WP}c_W - A_{NP}c_N - A_{SP}c_S \quad (\text{B.24})$$

Collecting all terms and substituting into Eq. (B.12) gives,

$$\begin{aligned}
\Delta x \Delta z \frac{\Delta c}{\Delta \tau} + \left( A_E + A_W + A_N + A_S + 2 \left( \frac{\Delta z}{\Delta x} + \frac{\Delta x}{\Delta z} \right) \right) c_P = \\
\left( A_{EP} + \frac{\Delta z}{\Delta x} \right) c_E + \left( A_{WP} + \frac{\Delta z}{\Delta x} \right) c_W + \left( A_{NP} + \frac{\Delta x}{\Delta z} \right) c_N + \left( A_{SP} + \frac{\Delta x}{\Delta z} \right) c_S \\
c_P = \frac{\left( A_{EP} + \frac{\Delta z}{\Delta x} \right) c_E + \left( A_{WP} + \frac{\Delta z}{\Delta x} \right) c_W + \left( A_{NP} + \frac{\Delta x}{\Delta z} \right) c_N + \left( A_{SP} + \frac{\Delta x}{\Delta z} \right) c_S}{A_E + A_W + A_N + A_S + 2 \left( \frac{\Delta z}{\Delta x} + \frac{\Delta x}{\Delta z} \right)} + \Delta x \Delta z \frac{\Delta c}{\Delta \tau}
\end{aligned} \quad (\text{B.25})$$

Equation (B.25) can be solved implicitly or explicitly to obtain concentrations.

---

# Appendix C

## Derivation of Foam Film Permeability Coefficient

---

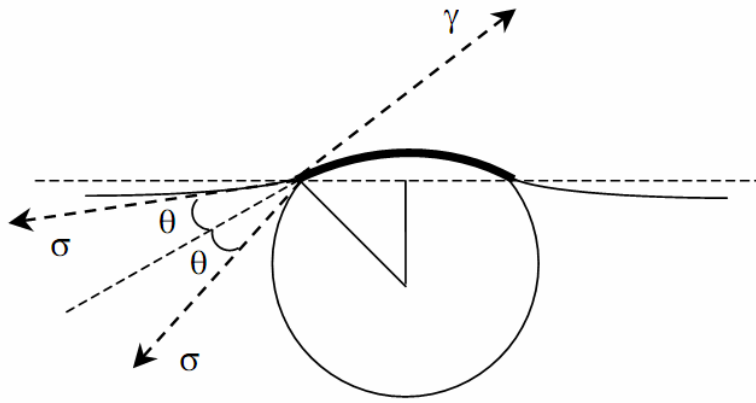


**Fig. C.1.:** Small free floating bubble at the air-aqueous solution interface and the foam film formed on top of it:  $\sigma$  (surface tension of the solution),  $\gamma$  (film tension),  $\theta$  (contact angle),  $R$  (radius of the bubble and  $r$  (radius of the film). Picture adapted from Ref. (93) of Chapter 6.

The mass flux of the gas through the foam film in Fig. C.1 can be written as:

$$\frac{dN_g}{dt} = -kA\Delta C_g \quad (\text{C.1})$$

where,  $N_g$  is the number of moles of gas passing across the film,  $\Delta C_g$  is the difference in the gas concentrations on the both sides of the film, i.e. the driving force for the diffusion process and  $k$  ( $cm/sec$ ) is the permeability coefficient for a foam film. Young-Laplace equation can be used to relate the pressure at both sides of the film by

$$P_c = \Delta P_g = P_g - P_{atm} = \frac{2\sigma}{R} \quad (\text{C.2})$$

and since  $\Delta C_g = \Delta P_g / R_B T$  one can obtain

$$\Delta C_g = \frac{1}{R_B T} \frac{2\sigma}{R} \quad (\text{C.3})$$

Replacing Eq. (C.3) into Eq. (C.1) provides

$$\frac{dN_g}{dt} = -kA \frac{1}{R_B T} \frac{2\sigma}{R} \quad (\text{C.4})$$

Since the experiments are conducted at low pressure it can be assumed that the gas follows the ideal gas rule

$$\frac{d(P_g V_g / R_B T)}{dt} = -kA \frac{1}{R_B T} \frac{2\sigma}{R} \quad (\text{C.5})$$

Therefore,

$$\frac{d\left(\left(P_{atm} + \frac{2\sigma}{R(t)}\right) \frac{4\pi}{3} R^3(t)\right)}{dt} = -k(\pi r^2(t)) \frac{2\sigma}{R(t)} \quad (\text{C.6})$$

$$\frac{d\left(\left(2P_{atm} + \frac{4\sigma}{R(t)}\right) R^3(t)\right)}{dt} = -3\sigma \frac{r^2(t)}{R(t)} k \quad (\text{C.7})$$

$$(6P_{atm} R^2(t) + 8\sigma R(t)) dR = -3\sigma \frac{r^2(t)}{R(t)} k dt \quad (\text{C.8})$$

In Eq. (C.6) we use  $A \approx \pi r^2$ , which results in an error of less than 3% in the calculation of foam film permeability. This is valid for films with areas much smaller than the area of the bubble.

Finally, one can calculate the foam film permeability coefficient from

$$k = \frac{\frac{P_{atm}}{2\sigma} (R_0^4 - R_t^4) + \frac{8}{9} (R_0^3 - R_t^3)}{\int_0^t r^2(t) dt} \quad (\text{C.9})$$

In this equation  $r$  is the radius of the formed film and  $R_0$  and  $R_t$  are the bubble radii at the beginning ( $t = 0$ ) and at the end of experiment ( $t = t$ ) respectively.

---

# Synopsis van het proefschrift

---

De resultaten van dit proefschrift geven inzicht in de (massa)overdracht van voornamelijk CO<sub>2</sub> in verschillende gas-vloeistof systemen. Een aantal experimenten zijn uitgevoerd om de transport mechanismen door grensvlakken met en zonder oppervlakte actieve monolagen te kwantificeren. Fysische modellen zijn ontwikkeld om experimenten betreffende transport van CO<sub>2</sub> liggend op een *bulk vloeistof of met vloeistof verzadigde poreuze media* te interpreteren. Bovendien wordt de dynamica van (CO<sub>2</sub>)-schuim in poreuze media zonder olie of verzadigd met olie bestudeerd met X-ray tomografie. Deze resultaten zijn toepasbaar op CO<sub>2</sub> sequestratie en CO<sub>2</sub>-EOR projecten.

Hoofdstuk 2 introduceert een eenvoudige PVT opstelling die is ontwikkeld om de overdrachts-snelheid van gassen naar vloeistoffen te kwantificeren door de druk als functie van de tijd te volgen. Met enige voorlopige berekeningen betogen wij dat, als CO<sub>2</sub> boven een vloeistoflaag wordt gebracht, de experimenteel bepaalde druk niet met de wet van Fick en een diffusie coëfficiënt kan worden gemodelleerd. Verder presenteren wij voor het eerst een aantal experimenten die het belang van door dichtheid gedreven natuurlijke convectie op de overdrachts-snelheid van CO<sub>2</sub> naar olie onderstrepen. Dit verschijnsel is van het hoogste belang voor EOR.

In hoofdstuk 3 ontwikkelen we een theoretisch model om de drukgeschiedenis van de experimenten te simuleren. Het model beschouwt een vat, gedeeltelijk gevuld met water en gedeeltelijk met CO<sub>2</sub>. We veronderstellen mechanisch evenwicht in het gedeelte gevuld met gas zodat het kan worden gemodelleerd met de wet van Fick met een voldoende grote diffusie coëfficiënt. We veronderstellen instantaan evenwicht op het oppervlak zodat daar de wet van Henry geldt. Oplossing van CO<sub>2</sub> in water doet de dichtheid toenemen leidend tot natuurlijke convectie stroming. De stroming in de vloeistof kan worden gemodelleerd door de wet van behoud van massa en de Navier-Stokes vergelijking te combineren. Dit effect is zowel van belang in watervoerende lagen als in EOR.

Hoofdstuk 4 introduceert natuurlijke convectie voor een poreus medium dat volledig met pekelwater is verzadigd.

Hoofdstuk 5 handelt over de basiseigenschappen van Alpha Olefin Sulfonate (AOS), een oppervlakte actieve stof. Het relatief goedkope AOS wordt wijd en zijd gebruikt in de petroleum industrie voor verschillende doeleinden vanwege zijn gunstige schuim en bevochtigings-eigenschappen. De oppervlakte spanning en adsorptie van de oppervlakte actieve stof worden simultaan gemeten met de dikte en contact hoek van schuim films, die van de surfactant oplossing zijn gemaakt, door de hoeveelheid oppervlakte actieve stof en electrolyt concentratie (NaCl) te veranderen. Deze kennis wordt gebruikt in hoofdstuk 6 om het onverwachte permeabiliteitsgedrag van door AOS gestabiliseerde schuim films te verklaren.

Hoofdstuk 7 vergelijkt het schuimgedrag van CO<sub>2</sub> en N<sub>2</sub> in poreuze media in afwezigheid van olie. De experimenten worden uitgevoerd in het grensvlakactieve stof – alternerend gas (SAG) schema boven en beneden het kritisch punt van CO<sub>2</sub> doormiddel van X-ray tomografie (CT scan). De mechanismen die de waargenomen verschillen veroorzaken worden in detail uitgelegd.

Hoofdstuk 8 rapporteert de resultaten van een aantal experimenten, waarin poreuze media met een residuale oliesaturatie na waterverdringing wordt doorgespoeld met een oplossing van een grensvlakactieve stof gevolgd een gas (CO<sub>2</sub> or N<sub>2</sub>).

Tenslotte, worden de belangrijkste conclusies van het proefschrift samengevat in hoofdstuk 9.

---

## چکیده پایان نامه

---

این پایان نامه به سه بخش انتقال جرم دی اکسید کربن در آب و نفت، لایه های نازک مایع (فیلمهای فوم)، و رفتار فوم (کف) در محیط متخلخل تقسیم شده و به بررسی پدیده انتقال گازها، بخصوص دی اکسید کربن، از فصل مشترک گاز-مایع در سیستمهای مختلف می پردازد.

در بخش اول با انجام یک سری آزمایشات، پدیده انتقال جرم دی اکسید کربن در آب و نفت بررسی می شود. انگیزه اصلی این آزمایشات اهمیت روزافزون مسایل و مباحث پیرامون گرمایش زمین و نقش احتمالی گازهای گلخانه ای و علی الخصوص دی اکسید کربن در وخیم تر کردن آن می باشد. در آزمایشات انجام شده، مقداری دی اکسید کربن در بالای ستونی از آب در یک لوله در فشارهای بین ۱۰ تا ۵۰ بار قرار گرفت. کاهش فشار در ستون گاز نشان دهنده و معیار انتقال مولکولهای گاز به درون مایع می باشد. در این آزمایشات مشاهده شد که در مراحل اولیه آزمایشات کاهش فشار ستون گاز بسیار بیشتر از آنی است که قانون دوم فیک بر اساس نفوذ مولکولی پیش بینی می کند. با این حال شدت انتقال جرم دی اکسید کربن در آب با افزایش زمان کاهش پیدا کرده و در نهایت پس از مدتی به شدت پیش بینی شده قانون فیک می رسد. در فصل دوم این پایان نامه با استفاده از شکل اصلاح شده قانون دوم فیک برای مراحل اولیه و پایانی این آزمایشات دو ضریب نفوذپذیری موثر (که فاقد معنای فیزیکی می باشند) به دست آمده است. این محاسبات ابتدایی نشان می دهد که ضریب نفوذپذیری مراحل پایانی آزمایشات مستقل از فشار اولیه گاز بوده و مقدار آن برابر با ضریب نفوذ مولکولی دی اکسید کربن می باشد. با این وجود ضریب موثر محاسبه شده برای مراحل ابتدایی آزمایش بین ۱۰ تا ۱۰۰ برابر ضریب نفوذ مولکولی گاز بوده و مقدار آن با افزایش فشار اولیه ستون گاز افزایش پیدا می کند.

نتایج فصل دوم نشان می دهد که گرچه با استفاده از قانون دوم فیک می توان به طور کیفی آزمایشات را مورد بررسی قرار داد با این وجود پیش بینی رفتار کلی آزمایشات با این قانون امکان پذیر نمی باشد. به همین منظور در فصل سوم، با طرح این نظریه که جابجایی آزاد یا طبیعی منتج از افزایش چگالی آب بر اثر حل شدن دی اکسید کربن باعث افزایش انتقال جرم دی اکسید کربن در آب (یا نفت) می شود، سلسله معادلاتی برای مطالعه این پدیده پیشنهاد شد. مدل پیشنهادی شامل معادلات نویر-استوکس و اصول بقای جرم و مومنتوم بوده و با استفاده از قانون هانری غلظت دی اکسید کربن در فصل مشترک آب-گاز را به فشار آن مرتبط می کند. با وجود یک سری فرضیات ساده کننده (مثلا نادیده گرفتن اثر پدیده مارانگونی) بین نتایج مدل پیشنهادی و داده های آزمایشگاهی توافق خوبی مشاهده می شود.

با استفاده از دانش به دست آمده در فصل دوم و سوم، در فصل چهارم تاثیر جابجایی طبیعی یا آزاد در شدت و سرعت ذخیره سازی گاز دی اکسید کربن در مخازن آبی زیرزمینی به طور عددی مورد بررسی قرار گرفت. این مطالعه نشان می دهد که حتی در محیط متخلخل هم نمی توان پدیده جابجایی طبیعی را نادیده گرفت چرا که این پدیده همانند مایع توده، هر چند به میزان کمتر، باعث ناپایداری فصل مشترک بین گاز و مایع شده و با افزایش سرعت انتقال جرم دی اکسید کربن به مایع موجود در محیط متخلخل سرعت ذخیره سازی آن را افزایش می دهد. شدت عمل این پدیده رابطه مستقیم با ضریب نفوذپذیری محیط

متخلخل و فشار تزریق دی اکسید کربن دارد. همچنین زمان شروع ناپایداری در فصل مشترک دی اکسید کربن و مایع با عدد ریله (که عمدتاً به ضریب نفوذپذیری و فشار گاز تزریقی بستگی دارد) رابطه معکوس دارد.

در بخش دوم این پایان نامه خواص اصلی محلولهای آلفا اولفین سولفونات (آ.اس) و فیلمهای تشکیل شده از این محلول در حضور و غیاب الکترولیت بررسی می شود. آ.اس یکی از سورفکتانت‌هایی (مواد فعال سطحی) است که به دلیل خواص کف‌کنندگی و ترکندگی عالی اش در صنعت نفت از آن استفاده زیادی می شود. با اندازه‌گیری کشش سطحی محلولهای این سورفکتانت مشاهده شد که غلظت مایسلی بحرانی محلولها با افزایش غلظت الکترولیت (کلرید سدیم) کاهش می یابد. همچنین مشاهده شد که به دلیل وجود ناخالصی‌ها در سورفکتانت منحنی کشش سطحی بر حسب لگاریتم غلظت سورفکتانت دارای یک نقطه کمینه است. نکته جالب اینکه تمام داده‌های کشش سطحی (به جز داده‌های محلول بدون الکترولیت) بر حسب  $C^*$  (به فصل پنجم مراجعه کنید) از یک شاه-منحنی عبور می کنند. به این ترتیب با دانستن این کمیت و اندازه‌گیری کشش سطحی تنها یک محلول دارای نمک به راحتی می توان کشش سطحی سایر محلولهای نمک دار را پیش بینی کرد. در ادامه در فصل ششم ضریب عبورپذیری یا ضریب انتقال جرم گاز هوا از لایه‌های نازک (فیلم) فوم اندازه‌گیری شد. در این آزمایشات مشخص شد که ضریب انتقال جرم گاز از فیلم فوم بستگی شدیدی به خواص فیزیکی-شیمیایی محلول (غلظت سورفکتانت و غلظت الکترولیت، دما و ...) و نوع گاز دارد. بر خلاف پیش بینی مدل‌های موجود که پس از غلظت مایسلی بحرانی ضریب انتقال جرم گازها را ثابت در نظر می گیرند، داده‌های ما نشان می دهد که پس از یک غلظت معین (بسیار بالاتر از غلظت مایسلی بحرانی) ضریب انتقال جرم گاز از فیلمهای فوم افزایش پیدا می کند. همچنین افزایش غلظت نمک نتایج غیرمنتظره‌ای را به همراه دارد. افزایش نمک از باعث کم شدن ضخامت لایه‌های فوم و کم اثر شدن نیروهای الکترواستاتیک می شود. با کاهش ضخامت فیلم انتظار این است که بر اساس قانون فیک انتقال جرم از فیلمها تسریع شود در حالیکه در آزمایشات خلاف این مشاهده می شود. به این ترتیب مشاهده می شود که خواص انتقال جرم فیلمهای فوم به شرایط ترمودینامیکی آنها بستگی دارد.

در بخش سوم به مقایسه خواص کف‌کنندگی دی اکسید کربن و نیتروژن در محیط متخلخل در حضور و غیاب نفت می پردازیم. برای مشاهده رفتار و نحوه جریان فوم در محیط متخلخل از سی.تی. اسکر استفاده شد. محیط متخلخل مورد استفاده در این بخش هسته‌ای به طول ۱۷ سانتی متر، شعاع ۴ سانتی متر، ضریب تراوایی ۱/۲ داری و ضریب تخلخل ۰/۲۲ ابتدا با تزریق دی اکسید کربن هوازدایی شده و سپس با تزریق آب در فشار بالا دی اکسیدکربن موجود از سیستم تخلیه شد. پس از آن هسته با محلول سورفکتانت اشباع شده و گاز به درون هسته تزریق شد. به دلیل وجود سورفکتانت در سیستم با تزریق گاز شاهد تولید فوم در محیط متخلخل هستیم. فوم تشکیل شده در نهایت تحرک گاز را کم کرده و باعث بهبود تولید آب می شود. به دلیل تفاوت‌های فیزیکی و شیمیایی گازهای مورد آزمایش (دی اکسید کربن و نیتروژن) دو گاز رفتار متفاوتی را به نمایش می گذارند. فوم نیتروژن قوی تر از فوم دی اکسید کربن می باشد بدین معنا که با تزریق نیتروژن بعد از محلول سورفکتانت اختلاف فشار بیشتری در طول هسته ثبت می شود. همچنین محاسبات درجه اشباع آب نشان می دهد که مقدار معینی از نیتروژن در مقایسه با همان مقدار دی اکسید کربن آب بیشتری را از محیط متخلخل تولید می کند. عوامل مختلف توضیح دهنده این مشاهدات در متن پایان نامه توضیح داده شده اند. در فصل هشتم کاربرد فوم به عنوان یک روش ازدیاد برداشت نفت مورد بررسی قرار گرفت. نتایج آزمایشات نشان می دهند که با وجود تشکیل فوم در نواحی بدون نفت زمانی که فوم به نفت می رسد ناپایدار شده و در نتیجه قدرت اثر خود را از دست می دهد. در فشارهای بالای نقطه بحرانی دی اکسید کربن تزریق سورفکتانت قبل از تزریق دی اکسید کربن تاثیر چندانی در ضریب بهره روی ایجاد نمی کند. بدین ترتیب نتایج ما نشان می دهد که تزریق فوم در مخازن می تواند نواحی که دارای نفت کمتری می باشند (یا نواحی با درجه نفوذپذیری بالاتر) را مسدود کرده و گاز را به سمت نواحی با درجه اشباع نفت کمتر سوق دهد. این عمل نهایتاً باعث افزایش تولید نفت می شود.

---

# Acknowledgements

---

Finally, in the “to be the most-visited page” of this thesis, I would like to express my gratitude and appreciation to all individuals, who supported me academically, technically, mentally and socially during my PhD study in TU Delft.

I have been fortunate enough to work with Prof. Hans Bruining and further my understanding of not only science but also of *life, peace and humanity*. No words can express my gratitude for this. I would also like to thank Maria for the sacrifice she makes for the sake of science.

I am indebted to Prof. Pacelli Zitha for providing me the opportunity to be part of his research group, his advice and many discussions we had on foam project. I thank Dr. Rumen Krastev for his teachings on *foam films* and also on Communism during our lunch-time in Max Planck Institute. My special thanks go to Prof. Bill Rossen, Dr. Doxing Du and Dr. Sussane Rudolph for their encouraging interest in my project and the knowledge they shared with me. I thank all committee members for careful reading of draft of this thesis, their participation in the PhD defense and their valuable comments, which truly improved the quality of this thesis.

DelftEarth Research and Shell International Exploration and Production are acknowledged for the financial support of this project. I thank Prof. Möwald for partial support of my three-month stay in Max Planck Institute in Golm, Germany. I thank my colleagues in Shell, in particular our foam team Alexey, Mohand and Carlos, for their enthusiasm, encouragement and “*bubbly outlook*”.

I am thankful to the MSc students that I supervised during my stay at Delft, Harm Delil, Ashkan Banaei, Joao Kinkela and Mahmood Mahmoodi, for their contribution in enriching the contents of this thesis.

Much of content of this thesis owes its existence to the technical staff of the Dietz Laboratory of Geotechnology department. Henny, Henk, Adri, Ellen, Karl, Jolanda, Dik, Jan-Etian, Peter, Leo, Monj, Kees and Paul are sincerely appreciated for their assistance, effort, time and support in solving many technical problems encountered during this study. I thank Lydia, Marlijn, Margot

and Hannie for their help with the most difficult work in any place on the earth, the administrative paper work.

Collective and individual acknowledgements are also owed to my colleagues and friends in Delft. Many thanks go in particular to Renato, Patrick van Hemert, Hein, Koen, Bert-Rik, Firas, Saikat, Ghaithan, Yufei, Nikolai, Willem-Jan, Ali Vakili and Elaheh, Morteza, Ali Naderi, Patrick Tardy and Julie, Farzad Farshbaf, Hamidreza and Maryam, Fariba, Maziar, Nasim and Farzad, Ehsan, Mohammad, Ahmad, Pedram, Omid, Arman, Rouzbeh, Mehdi, Alireza Asadi, Amirreza, Hamed and Sanaz, Amir Majlesi, Ali Moradi, Ali Barati, Reza, Ata, Teymour, Ali Mojaddamzadeh, Navid, Sobhan, Amirhossein, for their feedback, support and pleasant times we had together. I thank my friend Pooya for his help in printing the thesis and my brother Hassan for his persistence in assuring a quality cover design.

Yet again words fail me to express my appreciation to my sweet Renée for her support, understanding, help and her persistent confidence in me. I cannot thank her enough for being there for me all the time and for listening to me carefully during the stressful times of my PhD.

... and where would I have been without my family and their support?

لحظه لحظه زندگی ام را مدیون خانواده ام هستم؛ آنهایی که به من اطمینان دادند هر کجای دنیا که باشم به یاد من هستند و بدون هیچ چشمداشتی حمایت می کنند و چقدر دلگرم کننده و امیدبخش است این. از تک تک اعضای خانواده ام، بخصوص پدر و مادرم، که همواره مایه افتخار من بوده اند به خاطر تمام زحمتهایشان تشکر و قدردانی می کنم و امیدوارم که بتوانم ذره ای از محبت های آنها را جبران نمایم. نهایت ناسپاسی خواهد بود اگر در پایان تحصیلات خویش از معلمان و استادانم در دبستان شهید اکبر رضازاده اهر، مدرسه راهنمایی شهید دکتر حسن آیت اهر، دبیرستان نمونه سعدی تبریز و دانشگاه صنعتی امیرکبیر (پلی تکنیک تهران) تشکر نکرده باشم.

---

# Scientific Contribution

---

## I. Journal Papers

1. R. Farajzadeh, A. Andrianov, P.L.J. Zitha, "Foam assisted enhanced oil recovery at low and high pressures", submitted to Ind. Eng. Chem. Res. (May 2009).
2. R. Farajzadeh, R. Krastev, P.L.J. Zitha, "Gas permeability of foam films stabilized with an alpha olefin sulfonate surfactant", Langmuir, 25(5), 2881-2886 (2009).
3. R. Farajzadeh, P.L.J. Zitha, J. Bruining, "Enhanced mass transfer of CO<sub>2</sub> into water: experiment and modeling", accepted for publication in Ind. Eng. Chem. Res. (April 2009).
4. R. Farajzadeh, A. Andrianov, J. Bruining, P.L.J. Zitha, "Comparative study of CO<sub>2</sub> and N<sub>2</sub> foams in porous media at low and high pressures and temperatures", Ind. Eng. Chem. Res., 48(9), 4542-4552 (2009).
5. F. Farshbaf Zinati, R. Farajzadeh, P.L.J. Zitha, "Foam modeling in heterogeneous reservoirs using Stochastic Bubble Population approach", submitted to Transport in Porous Media, (January 2009).
6. D. Du, A. Naderi Beni, R. Farajzadeh, P.L.J. Zitha, "Effect of Water Solubility on Carbon Dioxide Foam Flow in Porous Media: an X-Ray Computed Tomography Study", Ind. Eng. Chem. Res., 47, 6298-6309 (2008).
7. R. Farajzadeh, R. Krastev, P.L.J. Zitha, "Properties of foam films stabilized by AOS surfactant", Colloids and Surfaces A: Engineering Aspects, 324, 35-40 (2008).
8. F. Farshbaf Zinati, R. Farajzadeh, P.K. Currie, P.L.J. Zitha, "Modeling of external filter cake build-up in radial geometry", Petroleum Science and Technology, 27(7), 746-763 (2008).
9. R. Farajzadeh, R. Krastev, P.L.J. Zitha, "Foam film permeability: theory and experiment", Advances in Colloid and Interface Science, 137(1), 27-44 (2008).
10. R. Farajzadeh, A. Barati, H.A. Delil, J. Bruining, P.L.J. Zitha, "Enhanced mass transfer of CO<sub>2</sub> into water and surfactant solutions", Petroleum Science and Technology, 25(12), 1493-1511 (2007).

11. R. Farajzadeh, H. Salimi, P.L.J. Zitha, J. Bruining. "Numerical simulation of density-driven natural convection in porous media with application for CO<sub>2</sub> injection projects", Int. J. Heat Mass Trans., 50(25-26), 5054-5064 (2007).

## II. Conference Proceedings

1. R. Farajzadeh, P.L.J. Zitha, J. Bruining, "Enhanced mass transfer of CO<sub>2</sub> into water: Experiment and modeling", SPE 121195, EUROPEC 2009, Amsterdam, The Netherlands, June (2009).
2. R. Farajzadeh, J. Bruining, P.L.J. Zitha, "New insights into application of foam for acid diversion", SPE 122133, European Formation Damage Conference, The Netherlands, May (2009).
3. R. Farajzadeh, A. Banaei, J. Kinkela, Th. de Loos, S. Rudolph, R. Krastev, J. Bruining, P.L.J. Zitha, "Surfactant induced solubilization and transfer resistance in gas-water and gas-oil systems", EAGE conference, Shiraz, Iran, May (2009).
4. M. Simjoo, M. Mahmoodi, R. Farajzadeh, S.A. Mirhaj, P.L.J. Zitha, "A CT scan study of foam flooding in porous media", EAGE conference, Shiraz, Iran, May (2009).
5. R. Farajzadeh, F. Farshbaf Zinati, P.L.J. Zitha, J. Bruining, "Density driven natural convection in layered and anisotropic porous media", Proc. 11th European Conference on Mathematics in Oil Recovery (ECMOR X1), Bergen, Norway, 8-11 September (2008).
6. R. Farajzadeh, R. Krastev, P.L.J. Zitha, "Gas permeability and properties of foam films stabilized by AOS surfactant", The XV international congress on Rheology: The Society of Rheology 80th Annual Meeting. AIP Conference Proceedings, Volume 1027, pp. 845-847 (2008).
12. F. Farshbaf Zinati, R. Farajzadeh, P.L.J. Zitha, "Foam modeling in heterogeneous reservoirs using Stochastic Bubble Population model", SPE 113358, SPE IOR symposium, Tulsa, The US April (2008).
7. R. Farajzadeh, H.A. Delil, P.L.J. Zitha, J. Bruining. "Enhanced mass transfer of CO<sub>2</sub> into water and oil by natural convection", SPE 107380, EUROPEC London, The UK, June (2007).
8. R. Farajzadeh, H. Salimi, P.L.J. Zitha, J. Bruining. "Numerical simulation of density-driven natural convection in porous media with application for CO<sub>2</sub> injection projects", SPE 107381, EUROPEC London, The UK, June (2007).

9. F. Farshbaf Zinati, R. Farajzadeh, P.K. Currie, P.L.J. Zitha, “*Modeling of external filter cake build-up in radial geometry*”, SPE 107638, , European Formation Damage Conference, The Netherlands, May (2007).
10. F. Farshbaf Zinati, R. Farajzadeh, P.L.J. Zitha, “*Modeling and CT scan study of the effect of core heterogeneity on foam flow for acid diversion*”, SPE 107790, , European Formation Damage Conference, The Netherlands, May (2007).
11. M.D. Carretero Carralero, R. Farajzadeh, D.X. Du, P.L.J. Zitha, “*Modeling and CT scan study of foams for acid diversion*”, SPE 107795, , European Formation Damage Conference, The Netherlands, May (2007).
12. R. Farajzadeh and P.L.J. Zitha, “*Critical review of foam film permeability*”, EU Foam Conference, Potsdam, Germany, July (2006).
13. R. Farajzadeh, P.L.J. Zitha, “*Thickness measurement of foam films by microinterferometry; a review*”, First Iranian Petroleum Engineering Congress, Tehran, Iran, 30-31 May 2006.

### III. Poster Presentations

1. R. Farajzadeh, M. Mahmoudi Nick, A. Andrianov, P.L.J. Zitha, “*CO<sub>2</sub>-N<sub>2</sub> foams in porous media*”, GRC on transport and flow in permeable media, Oxford, The UK (2008).
2. M. Mahmoudi Nick, R. Farajzadeh, A. Andrianov, P.L.J. Zitha, “*Stability of foam in the presence of clean and crude oils*”, EU Foam conference, Noordwijk, The Netherlands (2008).
3. R. Farajzadeh, H.A. Delil, P.L.J. Zitha, J. Bruining, “*Density-driven natural convection of CO<sub>2</sub> into water and oil*”, GRC on transport and flow in permeable media, Oxford, The UK (2008).



---

## About the author

---

<b>Name</b>	Rouhollah (Rouhi) Farajzadeh
<b>Dater of birth</b>	20 <sup>th</sup> March 1979
<b>Place of birth</b>	Ahar, Iran
<b>Sept. 1993-June 1997</b>	High school diploma in Mathematics and Physics, <i>Sa'di</i> high school (special school for talented students), Tabriz, Iran.
<b>Sept. 1997-Sept. 2001</b>	Petro-Chemical Engineering, Amirkabir University of Technology (Tehran Polytechnic), Tehran, Iran. <b>Final thesis:</b> Separation of oil and water emulsion using demulsifiers
<b>Sept 2001-Aug. 2002</b>	Sandwich courses in Petroleum Exploration Engineering, Petroleum University of Technology, Tehran, Iran.
<b>Sept. 2002-Aug. 2004</b>	M.Sc. degree with Cum Laude in Petroleum Engineering, Delft University of Technology, The Netherlads. <b>Final thesis:</b> An experimental investigation into internal filtration and external cake build-up. <b>Supervisor(s):</b> Dr. Al-Abduwani, Dr. v.d. Broek, Prof. P. K. Currie
<b>Nov. 2004-May 2005</b>	Reservoir Engineer in National Iranian Oil Company (NIOC), Tehran, Iran.
<b>May 2005-Oct. 2008</b>	Ph.D in Petroleum Engineering, Delft University of Technology, The Netherlands. <b>Title:</b> Enhanced transport phenomena in CO <sub>2</sub> sequestration and CO <sub>2</sub> EOR <b>Advisors:</b> Prof. J. Bruining and Prof. P.L.J. Zitha
<b>Nov. 2008-Present</b>	Reservoir Engineer, Shell International Exploration and Production, Rijswijk, The Netherlands